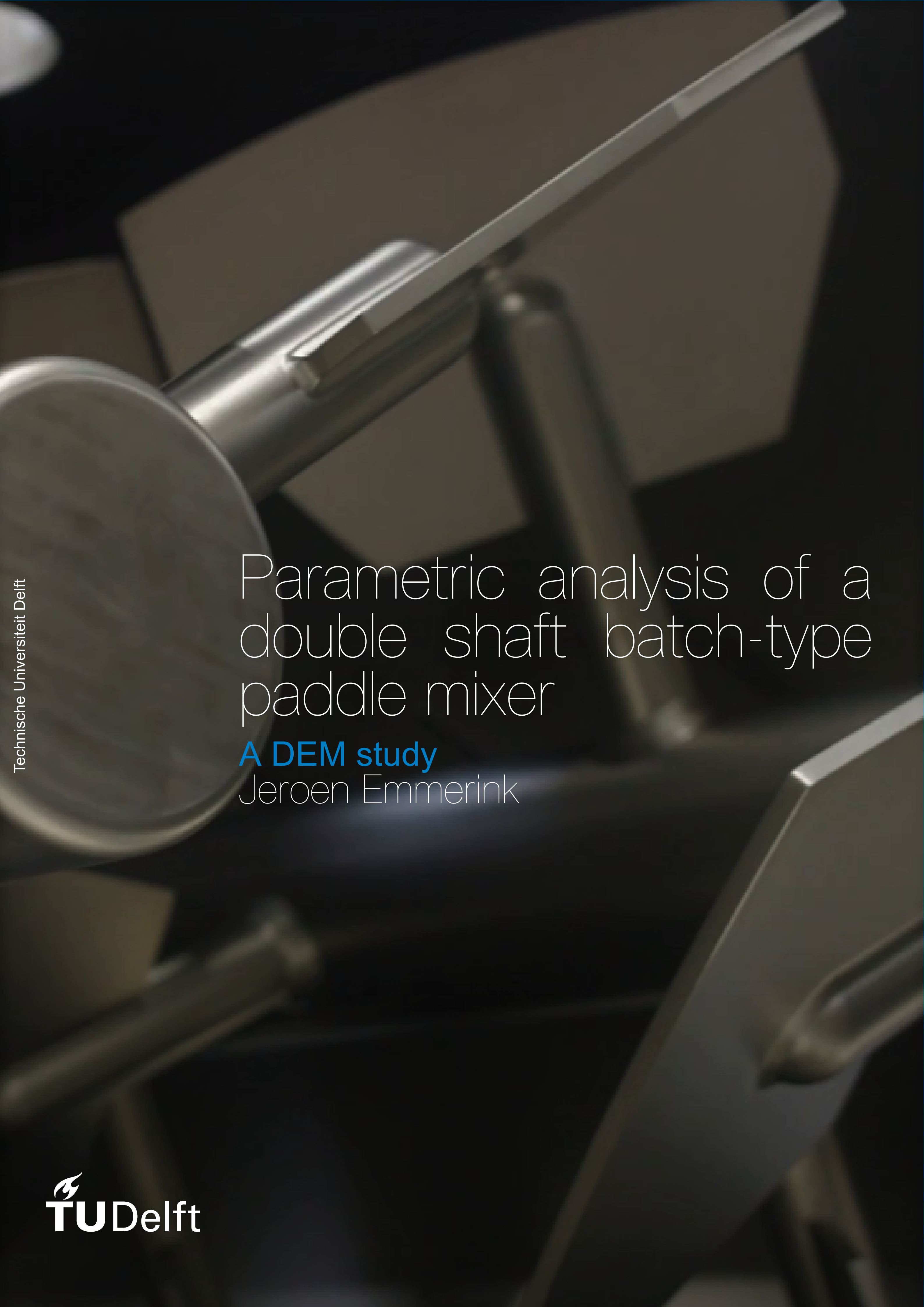

Technische Universiteit Delft

Parametric analysis of a double shaft batch-type paddle mixer

A DEM study

Jeroen Emmerink

TUDelft

Parametric analysis of a double shaft batch-type paddle mixer

A DEM study

by

Jeroen Emmerink

to obtain the degree of Master of Science
at the Delft University of Technology,
to be defended publicly on Wednesday December 14, 2022 at 12:30 PM.

Student number:	4492293	
MSc track:	Multi-Machine Engineering	
Report number:	2022.MME.8737	
Thesis committee:	Dr. Ir. D.L. Schott	TU Delft, chair
	Ir. A. Hadi	TU Delft, supervisor
	Dr. J. Jovanova	TU Delft, supervisor
	Ir. C.G.P. Cleven	Dinnissen, supervisor
Project duration:	February 21, 2022 – December 14, 2022	

This thesis is confidential and cannot be made public until December 14, 2025

Preface

'A step on its own stands never alone'

What a journey it has been. In December 2021 my graduation project started to develop what had to be the great ending of my two-year master program Multi-Machine Engineering at the Delft University of Technology. Gratitude goes out to the University that allowed me to grow professionally and personally. In particular, I want to thank my academic supervisors Ahmed Hadi, Jovana Jovanova, Javad Mohajeri and Dingena Schott which provided supervision where needed to make the right choices at the right moments in time. Their scientific contribution to my work brought the project to a higher academic level. In addition, I am glad that I had the opportunity to attend the two-weekly colloquiums where relevant insights, opinions and thoughts are shared by researchers in related research fields. I learned a lot from held discussions.

Furthermore, like it was fate the company's interests aligned perfectly with my wishes to spend the graduation period on the topic of Discrete Element Method (DEM) in combination with their paddle mixer. In particular, I want to thank my company supervisor Chris Cleven for providing me the opportunity to graduate at Dinnissen. The initiative taken for housing and a fixed workplace at the company's office has certainly contributed to the success of my graduation project. In addition, the shared practical point of view during the weekly progress meetings kept me on track. Lastly, I want to thank all my colleagues from Dinnissen for the warm welcome during the initial phase of my project. I have experienced the Limburg culture as very pleasant.

Last of all, many thanks to my family, friends and housemates who were all part of my graduation project, both consciously and unconsciously. The listeners, the advisors, the critics and even the non-interested people around me formed my project. No matter in what role they contributed to my project, they were all highly appreciated.

Jeroen Emmerink
Delft, December 2022

Abstract

The Discrete Element Method (DEM) in combination with an One Factor At a Time (OFAT) experimental simulation plan were employed to investigate the effect of a selection of factors on the mixing performance of a double shaft, batch-type paddle mixer. Most influential factors on the mixing performance of the paddle mixer are desired for optimization purposes. Selected factors are the three material characteristics (particle size, particle density, composition), three operational conditions (initial filling pattern, fill level, impeller rotational speed) and three geometric characteristics (paddle size, paddle angle and paddle number).

A 175L paddle mixer is converted into a simulation model and the material model adopted from literature. The material model comprises of free-flowing, perfectly spherical glass beads. The Hertz-Mindlin contact model is used to simulate the granular material. Furthermore, the simulation strategy consists of the filling process and mixing process. In the former, all input settings are specified. The latter process uses the filling process results to mix the 2-component mixture for a total real-time of 30 seconds. To ensure robust, stable and fit-for-purpose DEM simulations, a 'worst-case scenario' simulation is built for the filling process. By variations in shear modulus and time step, the simulation time is being reduced without compromising the stability or realistic behavior of the material. The output is then used in both processes for all simulations in the experimental simulation plan.

The mixture quality is assessed by the mixing index Relative Standard Deviation (RSD), where both the mixing effectiveness (mixture quality after 30 seconds) and the mixing efficiency (the time it takes to reach a RSD lower than or equal to 0.2) are evaluated. The particle size and particle density have a significant effect on the final mixture quality after 30 seconds of mixing (KPI 1). Moreover, screenshots in x, y and z directions at predefined time steps are generated to serve as visual feedback to understand the mixing mechanisms and flow patterns qualitatively. And, the RSD only stipulates the global mixing performance of the system. To be able to observe local differences in mixture quality, heat maps are generated. Additional local grid systems derived from the global 14x14x9 are designed such that the mass concentration of one of the components can be visualized in x, y or z direction.

The particle size and particle density have a significant effect on the final mixture quality after 30 seconds of mixing (KPI 1). Moreover, the composition, initial filling pattern, fill level, impeller rotational speed and paddle size have a significant effect on how fast a steady-state mixture quality is reached (KPI 2). Finally, the paddle angle and paddle number have a significant effect on both KPIs and therefore holds most potential with respect to optimization purposes.

Contents

Nomenclature

Abbreviations

Abbreviation	Definition
AoR	Angle of Repose
CFD	Computational Fluid Dynamics
CoDF	Coefficient of Dynamic Friction
CoR	Coefficient of Restitution
CoSF	Coefficient of Static Friction
CoV	Coefficient of Variance
DEM	Discrete Element Method
DM	Degree of mixedness
DSD	Definitive Screening Design
EEPA	Edinburg Elasto-Plastic Adhesive
ESI	Intensity of Segregation
FB	Front-Back
FEM	Finite Element Method
KPI	Key Performance Indicator
LI	Lacey Index
LSD	Linear Spring-Dashpot
LWB	Lacey, Weidenbaum and Bonilla
MCDA	Multi-Criteria Decision Analysis
ME	Mixed Entropy
MSI	Mixing Segregation Index
OFAT	One Factor At a Time
PB	Placket-Burman
PEPT	Positron Emission Particle Tracking
PSD	Particle Size Distribution
RPM	Rotations Per Minute
RSD	Relative Standard Deviation
SS	Side-by-Side
TB	Top-Bottom
VBBC	Variance amongst Bimodal Bin Counts
VRR	Variance Reduction Ratio

Symbols

Symbol	Definition	Unit
a	Particle size ratio	[-]
b	Particle density ratio	[-]
c	Composition	[-]
C_n	Normal contact damping coefficient	$[kg/s]$
C_R	Coefficient of Restitution (CoR)	[-]
C_t	Tangential contact damping coefficient	$[kg/s]$
d_p	Particle diameter	$[m]$
$D1$	Shaft diameter paddle mixer	$[mm]$
$D2$	Paddle pair diameter paddle mixer	$[mm]$

Symbol	Definition	Unit
e	Fill level of mixing chamber	[-]
E	Young's modulus	$[N/m^2]$
E_{kin}	Kinetic energy	[J]
E_{pot}	Potential energy	[J]
E^*	Equivalent Young's modulus	$[N/m^2]$
$F_{n,ij}$	Normal component of the contact force between particle i and particle j	$[N]$
$F_{t,ij}$	Tangential component of the contact force between particle i and particle j	$[N]$
f	Impeller rotational speed	$[rpm]$
F	Space between paddles	$[mm]$
$F_{g,i}$	Gravitational force on particle i	$[N]$
g	Paddle size	[-]
G	Shear modulus	$[Pa]$
G^*	Equivalent shear modulus	$[Pa]$
H	Height of paddle mixer	$[mm]$
i	Paddle number	[-]
I_i	Moment of Inertia of particle i	$[kg \cdot m^2]$
j	Total height of paddle surface	$[mm]$
k_n	Normal contact stiffness coefficient	$[N \cdot m^{-3/2}]$
k_t	Tangential contact stiffness coefficient	$[Pa \cdot m]$
L	Length of paddle mixer	$[mm]$
m_i	Mass of particle i	$[kg]$
m^*	Equivalent mass	$[kg]$
$M_{t,ij}$	Rotational torque between particle i and particle j	$[Nm]$
$M_{r,ij}$	Rolling resistance torque between particle i and particle j	$[Nm]$
M_2	Average mass concentration of particle 2 over all taken samples	[-]
$M_{2,i}$	Mass concentration of particle 2 in bin i	[-]
n_g	Height dimension of general paddle	$[mm]$
n_t	Height dimension of transfer paddle	$[mm]$
N_c	Number of particles in contact with particle i	[-]
o_g	Height dimension of general paddle	$[mm]$
o_t	Height dimension of transfer paddle	$[mm]$
p	Initial filling pattern	[-]
q_g	Height shaft to general paddle surface	$[mm]$
q_t	Height shaft to transfer paddle surface	$[mm]$
r_g	Width of general paddle	$[mm]$
r_t	Width of transfer paddle	$[mm]$
R^*	Equivalent radius	$[m]$
R_i	Radius of particle i	$[m]$
R_{min}	Smallest particle radius in system	$[m]$
R_{nbr}	Neighborhood radius	$[m]$
s	Standard deviation	[-]
t_{cr}	Critical time step	$[s]$
T	Projected width in radial direction of paddle	$[mm]$
T_R	Rayleigh time step	$[s]$
$\|v_i\|_{max}$	Highest particle velocity in the system	$[m/s]$
U	initial velocity of particle	$[m/s]$
v_i	Translational velocity of particle i	$[m/s]$
V_p	Total volume particles of granular material	$[m^3]$
V_{voids}	Total volume voids in granular material	$[m^3]$
V_b	Total volume bulk material	$[m^3]$

Symbol	Definition	Unit
W	Width of paddle mixer	$[mm]$
x	Horizontal travelled distance	$[m]$
α_1	Paddle angle general paddle	$[deg]$
α_2	Paddle angle transfer paddle	$[deg]$
β_1	Angle general paddle shape	[°]
β_2	Angle transfer paddle shape	[°]
$\delta_{n,ij}$	Normal overlap between particle i and particle j	$[m]$
$\delta_{n,ij}^{'}$	Normal velocity between particle i and particle j	$[m/s]$
$\delta_{t,ij}$	Tangential overlap between particle i and particle j	$[m]$
$\delta_{t,ij}^{'}$	Tangential velocity between particle i and particle j	$[m/s]$
ζ	Damping coefficient	[-]
Δt	Simulation time step	$[s]$
μ	Viscosity of the fluid	$[Pa \cdot s]$
ν	Poisson's ratio	[-]
ρ_p	Particle density	$[g/cm^3]$
ω_i	Angular velocity of particle i	$[s^{-1}]$

List of Figures

List of Tables

1

Introduction

1.1. Background

This research is executed in collaboration with the company Dinnissen. In Section 1.1.1, the company is described. Section 1.1.2 introduces the paddle mixer that will be subjected to a thorough research.

1.1.1. The company

Company Dinnissen is one of the front runners in the process technology of powders and granulates. Because of a combination of know-how including in-house production facilities and test facilities, they can offer top-level service in almost all sectors of process technology. They serve many renowned clients worldwide by providing well-thought-out customized solutions that guarantee the high and uniform quality, and guaranteed production continuity. An overview of all industrial processes Dinnissen provides solutions for is given in Figure 1.1. The company is specialized in creating machines that can process powders, particles and granules in all kinds of markets, namely Dairy, Food & Pharma, Chemicals & Minerals, Petfood and Feed & Aquafeed industries.

One of their solutions is the mixing machines able to mix any type of powder, granule or extruded product quickly and effectively. In Section 1.1.2 the mixing machine will be highlighted in more detail.

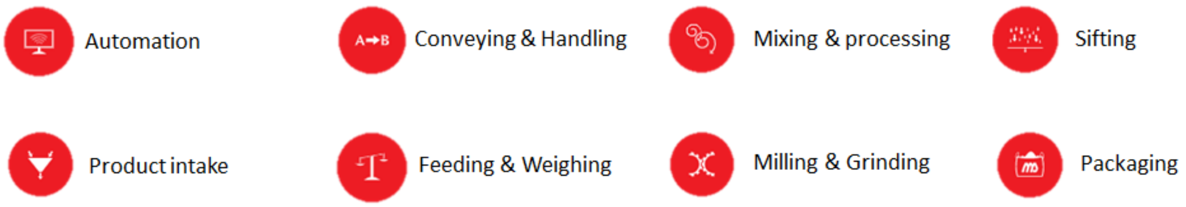

Figure 1.1: An overview of all industrial processes Dinnissen provides machinery solutions for. Reprinted from Dinnissen website.

1.1.2. Paddle mixer

The batch-type, double shaft mixing machine engineered, produced and sold by the company Dinnissen is based on a design invented in the '70s by Halvor Forberg [25]. Over the years, the design has evolved by empirical methods and in-house knowledge into a fit-for-purpose machine for Dinnissen's customers. In Figure 1.2, a double shaft batch-type paddle mixer is shown. Therewithal, the paddle mixers can be equipped with additional features like a guidance system for shaft extraction such that the machine can be cleaned easily. Especially in the food and pharmaceutical industries with high hygiene demands, such supplementary features offer great solutions.

Normally, the paddle mixer is part of a greater system including other product handling equipment. Via top inlets are the mixture components being transferred into the paddle mixer. After the mixing process, swing doors at the bottom of the mixing chamber open up and let the final mixture drop down to be further processed.

The shafts are positioned horizontally, each with 14 paddles evenly distributed over four radial quadrants. The double teardrop-shaped chamber in combination with counter-rotating shafts forces

Figure 1.2: Double shaft, batch-type paddle mixer manufactured by Dinnissen. Reprinted from Dinnissen website.

the multi-component bulk material towards the center of the chamber, just above the shafts. At this location, a so-called fluidized zone is formed [25]. Here, two or multiple material components are blended together as one bulk material by reconfiguration of the individual particles, hereby dictating the system's performance. Additionally, the paddles are configured in such a way that they force the granular material to move in a circular pattern through the chamber (Figure 1.3). Thus, not only radial mixing but also axial mixing occurs in this type of paddle mixer. A study on particle motion in double shaft paddle mixers done by Hassanpour et al. (Hassanpour et al., 2011) confirms the aforementioned flow pattern. Consult Section 3.2 for a detailed description.

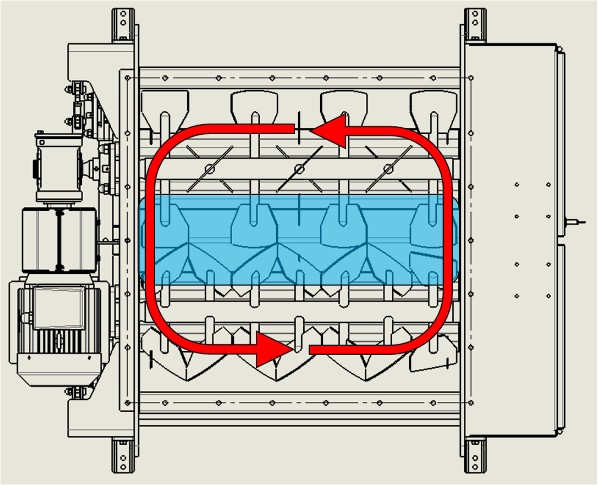

Figure 1.3: Top view of the paddle mixer with the fluidized bed indicated by blue color and the circular motion of particles indicated by red arrows.

1.2. Problem definition

Recent findings from test reports generated by external partners of Dinnissen about the mixture quality and real-time fluidized zone observations show opportunities for improvement of the mixing process. During mixing, the movement of the particles seems to be more or less stagnant in the top part of the fluidized zone. The occurrence of this phenomenon increases at higher fill rates of the granular material in the mixing chamber. Consequently, it is expected that the components in the fluidized zone do not mix as efficiently as can be possible, indirectly affecting the mix quality negatively. Except for the limited real-time fluidized zone observations, it is not possible to observe mixing patterns and flow patterns with the naked eye. The main reasons are the fast and dynamic behavior of the granular material and the non-transparent geometric machine parts.

Only the effect of the operational factors impeller rotational speed, initial filling pattern and fill level on the mixing performance of a double shaft, batch-type paddle mixer are investigated. But, the significance of material characteristics (e.g. particle shape, particle size, particle density) and geometric properties (e.g. paddle size, mixing chamber shape, paddle number) is not yet clearly understood for this particular mixing application. Due to a lack of understanding and theoretical knowledge concerning last mentioned factors, in practice long lasting trial and error procedures are conducted according to the customer's demands to make sure desired mixture quality will be reached.

1.3. Objectives & scope

To support the company with scientific background about their paddle mixers this research is initiated. First of all, to understand the mixing patterns inside the paddle mixer, a model is required. Secondly, according to an in-depth literature review knowledge about the influence of material characteristics and geometric properties on the mixing performance of the double shaft, batch-type paddle mixer is limited. Therefore, the main focus will be on screening a selection of factors identified by literature and consulting with the company. The research aim is to improve understanding on factor significance on the mixing performance of the batch-type, double shaft paddle mixer by analyzing the flow patterns and mixing mechanism. It is important to identify the most influential factors for optimization purposes. The full research will be performed using Discrete Element Method (DEM) simulations. In short, the two research objectives are:

1. Develop a model that can present flow behavior and mixing patterns inside the paddle mixer.
2. Identify and evaluate the influence of material, operational condition and geometry factors on the mixing performance of a double shaft batch-type paddle mixer.

The following bullet points describe the research boundaries to delineate the project; what is included and what is not.

Geometry

- A 175L batch-type, double shaft paddle mixer (Figure 3.5) is the system under investigation. As this particular paddle mixer is present at the Dinnissen Test Center and thus available for physical experiments, the machine is a perfect candidate for further research.

Operational conditions

- Based upon practice, a total mixing time of 30 seconds is determined (over-mixing not considered). It is expected this time length is broad enough to observe potential trends coming out of the experimental simulation plan.
- Mixing the components via a batch principle. Handling prior to and after batch mixing not considered (like moving, pouring and conveying of bulk material)
- The mixing process simulations are conducted from a stationary initial particle bed
- The initial loading pattern is a front-back configuration which is in practice the most realistic case.

Material

- Binary, free-flowing (non-cohesive) spherical glass beads represent the material model.

- Composition up to 1 % volume fraction for one of the components is investigated. Mixing of additives is not considered.

1.4. Research question and sub-questions

The main research question is:

- What is the *main effect* of a selection of *factors on* the *mixing performance* of a batch-type, double shaft paddle mixer?

The sub-questions are:

1. What kind of *modelling method* is suitable for this research?
2. How should the *current system* be converted into a *simulation model*?
3. How to ensure a *robust and fit-for-purpose simulation model* for the system?
4. What type of *experimental simulation plan* to use for investigating the influence of selected factors on mixing performance of the system?
5. Which *factors* could *influence the mixing performance* of the system?
6. What *factor values* to be chosen for the experimental simulation plan?
7. How to *assess* the *mixing performance* of the system?

1.5. Methodology

In Figure 1.4, a graphical representation of all facets of the (custom-built) research methodology is presented. Each facet is elaborated in a separate section.

Figure 1.4: Graphical representation of all facets of the followed methodology.

Research aim

The research aim is to discover what the influence is of a selection of factors on the mixing performance of the double shaft, batch-type paddle mixer. Detailed description of the research objectives and research scope can be found in Section 1.3.

Research Method

Research was conducted by using the software EDEM 2022.1 which is easily accessible via the university. and does not contain any physical experiments. Performing DEM simulations instead of physical experiments is the most time and cost-efficient way to fulfill the research objectives. First a fit-for-purpose simulation model is being built (objective 1). Then, the experimental simulation plan is designed and executed (objective 2). It consists of an One Factor At a Time (OFAT) approach, where selected factors are subjected to a parametric analysis to assess the mixing performance of the paddle mixer. The mixing performance is assessed both quantitatively and qualitatively.

- **Quantitative analysis**: In related literature, to assess quantitatively the performance of a mix application is by calculating a so-called mixing index. Most suitable mixing index for this particular research is the Relative Standard Deviation (RSD). To assess both mixing efficiency and mixing effectiveness, two KPIs are defined:

  KPI 1: The mixing index RSD after 30 seconds of mixing
  KPI 2: The time it takes to reach a RSD smaller than or equal to 0.2

- **Qualitative analysis**: To be able to understand the mixing mechanisms and patterns inside the paddle mixer, screenshots are taken of the particle bed in x, y and z directions. Additionally, in the same directions heat maps are created to assess the local mixture quality. The normalized mass concentration in every bin in a local grid system is visualized by a color based on a fixed color bar.

Data collection

The Analyst section of the software EDEM 2022.1 was used for data extraction. All data is stored in CSV-files to be post-processed.

Data analysis

The acquainted data is analyzed by the programming language Python (Section 1.5 for more detail).

Material & equipment

Commercial software EDEM 2022.1 from umbrella organization Altair and Python 3.9.12 in IDE Spyder v5.

Difficulties encountered

As with all research, some obstacles appeared on the road. Below some of them are mentioned with explanation of how they were overcome.

- Lack of storage capacity did require an external hard disk.
- Visualization of mass concentration for one of the components for designed local grid systems is not possible in EDEM. Eventually, a Python script was built to show local differences of the mass concentration by using a heat map.
- For this particular case, the EDEMpy example (available on the Altair Community website) for calculating the mixing index was not time efficient retrospectively speaking. Instead, the EDEM data extraction tool is used and data post-processing is done via a manually created Python script to obtain the mixing index.

Evaluation research methodology

The obtained results were conclusive. However, some things could have been more efficient. Below a couple of points for improvement:

1. Calculation of the RSD mixing index can be done by mass or volume fraction, or by the number of particles. In this research, the composition which is one of the evaluated material factors is based upon volume fraction, while the RSD is calculated by a mass fraction. Thus, a conversion between volume to mass fraction was required for every simulation to be able to calculate the RSD. To be more consistent next time, one choice in mass/volume/number of particles should be made to simplify the research process.

2. The grid system analysis should be more comprehensive next time. The effect on the RSD caused by a low number of particles was not accounted for while the number of particles in a bin is crucial to obtain statistically valid results. For instance, the fill level and composition contains simulations with very small number of particles that caused erronous results.
3. Acquainted results are only valid for millimeter scale, free-flowing spherical glass beads. In comparison with powders, other material factors should be taken into account as well. For example, material characteristics like particle shape and/or cohesive forces between particles caused by moisture, hydrostatics, 'Vanderwaals' forces etc.

1.6. Thesis outline

In Figure 1.5 an overview of the thesis outline is given. After a thorough literature review in Chapter 2, state-of-the-art knowledge about paddle mixers is processed to find the knowledge gap. The gap serves as the fundamental, scientific basis for the research. Thereafter, in Chapter 3 the suitable modeling method is identified and the current system is converted into a simulation model. And, in Chapter 3 the reference case is described. To ensure the simulation model is robust and fit-for-purpose, a stability analysis is performed which is also explained in Chapter 3. In Chapter 4, results from the stability analysis are used in an experimental simulation plan. In this chapter, the screening method is chosen, factor (levels) are identified, the mixing assessment strategy is determined and the experimental simulation plan is shown. Last, the results are presented and discussed by graphs, screenshots and heat maps in Chapter 5. Based upon the aforementioned chapter, conclusions are drawn and an answer is given to the research question in Chapter 6.

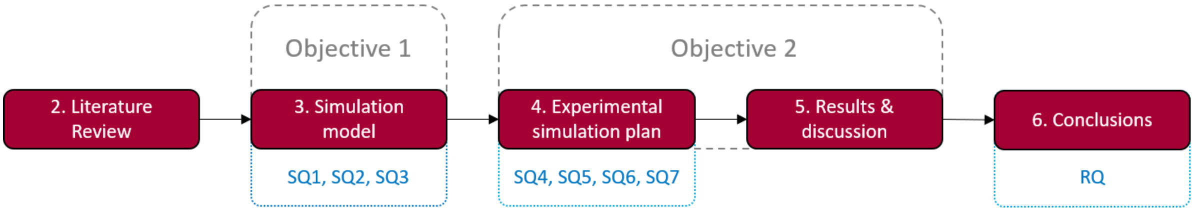

Figure 1.5: An overview of the thesis outline incorporated with research objectives, sub-questions (SQ) and research question (RQ)

2

Literature Review

This literature review built a bridge between known knowledge and knowledge gaps to be filled. First, scientific information with respect to a batch-type, double shaft paddle mixer is gathered and analyzed. Second, research on other mixing applications is reviewed to gain a broader perspective on research possibilities. Discrepancies in research development for one particular application compared to a paddle mixer can be of value, because one can learn from followed methodology or chosen factors to investigate for instance.

This chapter should be read as stand alone document and is the fundamental basis of initiated research. For guidance, the following research question has been set up. Be aware the introduced research and sub-questions differ from the questions introduced in Chapter 1.

- *What is the state-of-the-art knowledge for mixing granular materials with a double-shaft, batch-type paddle mixer?*

Following sub-questions are meant to provide general background on mixing and guide the review towards answer formulation of the research question.

1. What is the definition of a mixture concerning (two-component) granular materials?
2. What kind of (de-)mixing mechanisms exist?
3. What type of industrial mixing applications are currently available?
4. Which (sub)domains are already been investigated by the scientific community with respect to paddle mixers?

In Section 2.1, answers are given on the first two sub-questions, supported by general theory about different types of mixture, mixing mechanics and segregation (de-mixing). Next, Section 2.2 provides an overview of common mixing applications hereby answering sub-question 3. Accordingly, all published papers related to single and double shaft paddle mixers are reviewed separately in Section 2.3. Last but not least, a thorough answer is given on the research question in Section 2.4. Consequently, knowledge gaps are identified based upon given answer on the research question, serving as a fundamental basis for conducted research.

2.1. Mixing technology

Generally accepted classifications of mixture types are presented in Section 2.1.1. Consequently, common mixing mechanisms are described in Section 2.1.2. The de-mixing mechanisms, also known as segregation, can be found in Section 2.1.3.

2.1.1. Type of mixtures

Mixing two non-interacting components (free-flowing) with similar properties (size, shape, elasticity etc.) can theoretically result in different mixtures. The perfectly uniform mixture (a) as presented in Figure 2.1 is characterized by a highly ordered state wherein the particles are configured along a lattice structure. Samples that are taken arbitrarily from the mixture will contain the same number of each particle as the number present in the mixture as a whole [52, 58]. Such an perfect mixture will never be achieved unless putting much effort in building up the mixture particle by particle. Realistically speaking, the best possible mixture quality that can be achieved is the random (or stochastic) mixture (b) as shown in Figure 2.1. The mix quality reaches an asymptotic limit of random mixing after a certain amount of time, characterized by a statistical process. In a random mixture, the probability of finding a single particle of any component is the same for all possible locations and equal to the portion of that particular component in the mixture as a whole [58].

Note that for particles with different material properties (e.g. shape, size, density), achieving a random mixture is not always possible. Moreover, in case particles are subjected to inter-particle forces a random mixture is not possible at all. In the latter situation, a so-called ordered mixture can be formed consisting of agglomerates where a small-sized particle sticks to a larger particle. However, such mixture types are out of scope for this research as cohesive granular material is not considered. [52, 54]

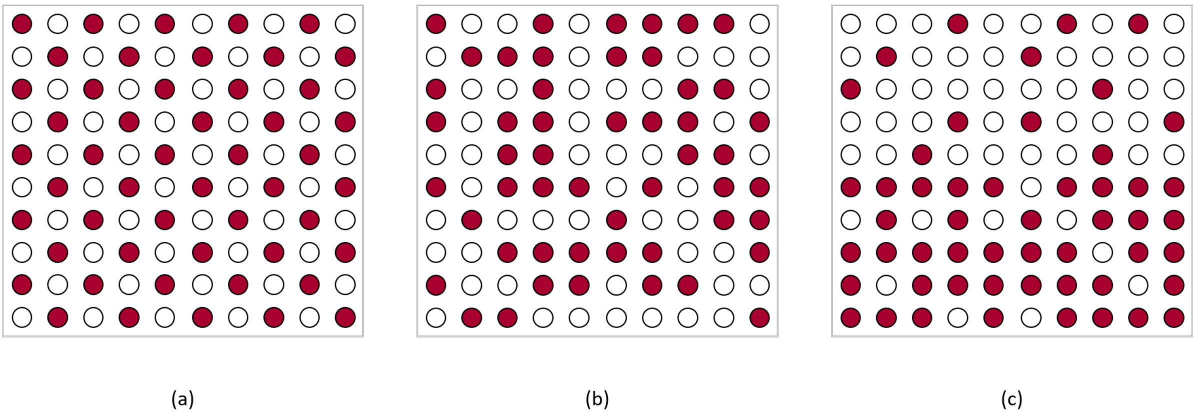

Figure 2.1: (a) A perfect mixture, (b) a random mixture and (c) a segregated mixture

2.1.2. Mixing mechanisms

In Figure 2.2 and Figure 2.3, a graphical representation is shown of the mixing process of both free-flowing and cohesive granular materials. In the former, a random reconfiguration of every individual particle is the main transport mode, while in the latter, formation of agglomerates due to surface forces between particles is clearly visualized. Note here that the schematics do not take into tertiary (or higher) component mixtures. For the sake of simplicity, also particle size and shape are kept identical for both components. [31]

Already in 1954, Lacey identified three main transportation modes of particles during the mixing process [39]:

- Convection - Deliberately caused flow patterns or currents within the batch to transport portions from one place to another. By relative displacement to one another and size reduction, the contact area created between the different components carries out mixing on a large scale. Due to low mobility of particles, the possibility of segregation (Subsection 2.1.3 is minimal.

- Diffusion - Randomized transport of individual particles where each particle moves arbitrarily, often assisted by gravity, and is spread out over the mixture. A high degree of particle mobility is required to ensure mixing on a fine scale.

- Shear - External input like mechanical agitators or internal input like a shell's rotating movement causes exchange of particles across the shear planes. This mechanism is often considered to be a combination of above mentioned mechanisms.

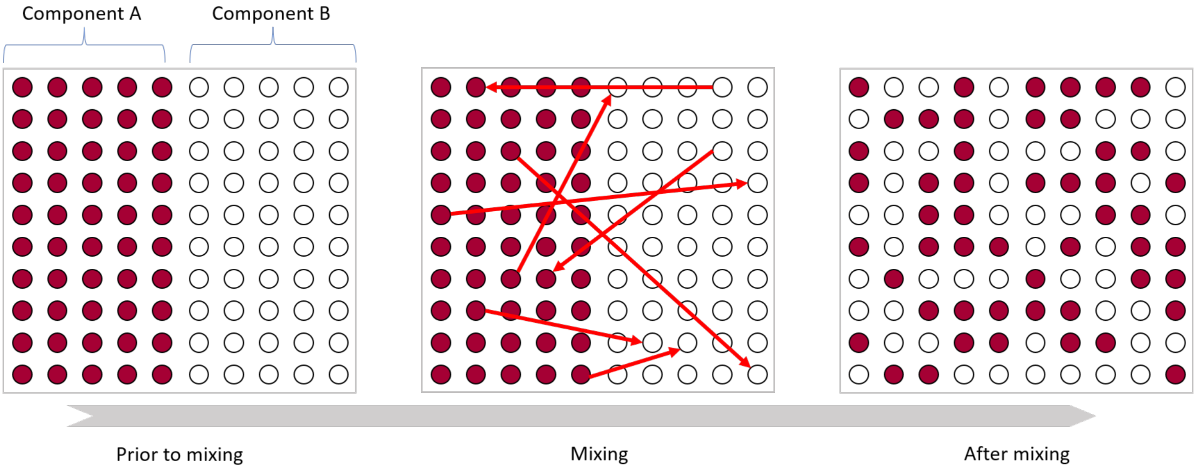

Figure 2.2: Mixing process of a free flowing bulk material.

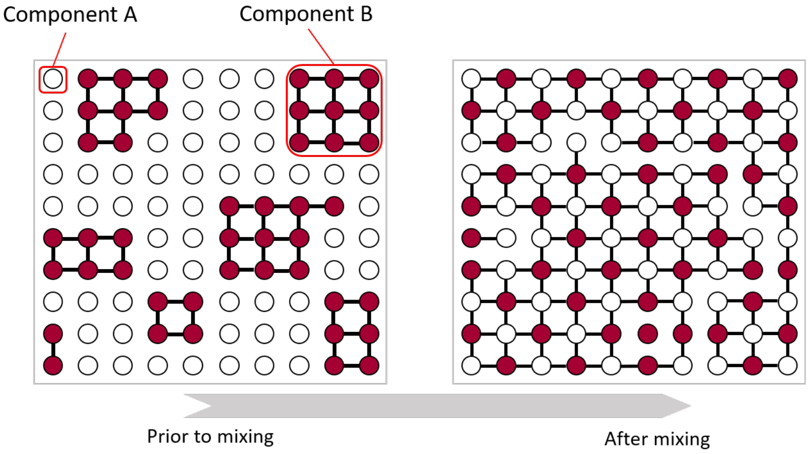

Figure 2.3: Mixing process of a cohesive bulk material.

Every mixing application has a dominant type of mechanism, but normally all three occur together to some extent. For powders, diffusion movements require an external energy input.

2.1.3. Segregation

In Figure 2.1 is a graphical representation shown for a segregated mixture (c). Segregation is the opposite of mixing and can be caused by discrepancies in physical characteristics of the material like particle size, particle density, particle shape, and/or particle roughness. The urge to obtain an optimized mixture quality during a general mixing process goes hand in hand with segregation. The two phenomena can be seen as opposites and constantly in competition with one another. Particularly free-flowing or slightly cohesive bulk materials are susceptible to segregation because of high mobility of individual particles. The final state is an equilibrium between the two and is a reversible and dynamic process [54].

Empirical and application-based values to determine at what moment segregation will occur do exist in literature. For example, for a binary mixture in a rotating drum segregation will occur at a particle diameter ratio above 1.3 [11]. Nonetheless, the segregation mechanisms depend not only on material characteristics but on many other parameters as well, like the operational conditions and the geometric design parameters of the mixing application [16]. Regardless of the complex processes concerning segregation, five different segregation mechanisms can be distinguished. Here, only mechanisms related to the mixing process of the investigated paddle mixer will be explained in coming paragraphs. A side note, although each segregation mechanism is dealt with individually, often more than only one appear simultaneously [60].

Percolation/sifting

With the percolation segregation mechanism, a disturbance of the bulk material in such a way that particles start to move results in reconfiguration of particle packing arrangement. The gaps that form during the reconfiguration is the main cause of percolation, especially for fine particles. In case bulk material consists of different particle sizes, it will be easier for the smaller particles to fall down through the gaps based upon gravitational force they are subjected to (Figure 2.4). Even a small discrepancy in particle size will give rise to this phenomenon. Ironically, dynamics like stirring, shaking or vibration promote percolation in free-flowing bulk materials while such mechanisms are sometimes utilized to mix materials. [58]

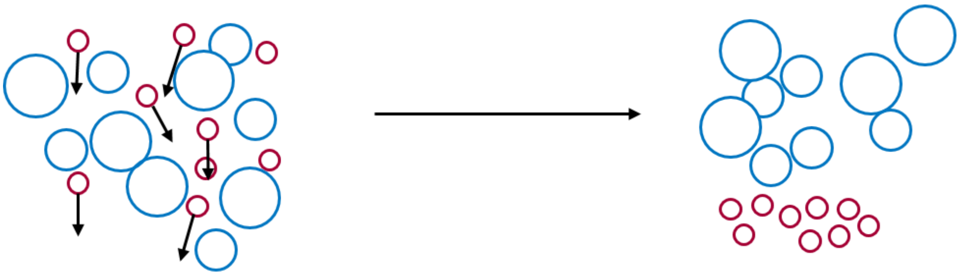

Figure 2.4: Segregation by percolation.

Another segregation mechanism that is quite similar to percolation is sifting, but it does happen at different circumstances. For instance, in dynamic conditions when particles are sliding downwards on the surface of a bulk material, the probability a small particle is caught by a sufficiently large cavity is relatively high compared to larger particles. Thus, large particles roll (in case of round particles) or slide (in case of irregular shaped particles) down, while the small particles remain in the cavities. Most often, particle size is the main factor that causes percolation and/or sifting. However, in some cases, also the particle shape is of importance. [58]

Rise of coarse particles

Rise of coarse particles can be caused by vibration of the bulk material. During vibration, large particle(s) move upward resulting in a reorientation of particles due to gaps formed beneath the larger particle(s). Once landed, the large particles rest on the smaller ones. End result is a small upward displacement. Even when the large particles do have a higher density than the smaller particles [52]. In Figure 2.5 a graphical illustration of the rise of course particles in a fine particle bed is visualised.

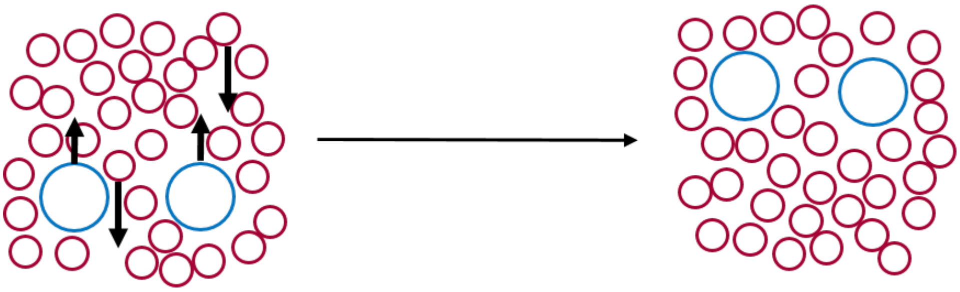

Figure 2.5: Segregation by rise of coarse particles.

Buoyancy segregation

Particulate systems where particles differ in densities, the buoyancy segregation mechanism can become active [35]. In such mechanism, the heavier particles sink and the lighter particles rise causing segregation in the vertical direction of a particle bed. In Figure 2.6 an animation is presented of the buoyancy segregation mechanism.

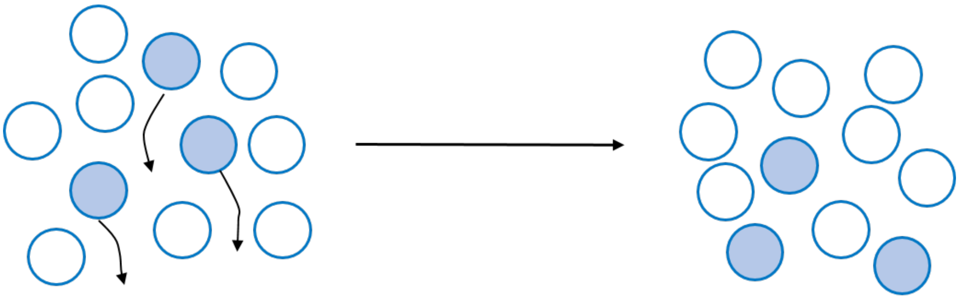

Figure 2.6: Buoyancy segregation mechanism where the shaded particles represent the heavier particles.

Push-away segregation

Another mechanism that causes segregation is called push-away [63]. Heavier particles that collide with lighter particles tends to push away the lighter ones caused by a higher momentum. In Figure 2.7 an illustration is provided.

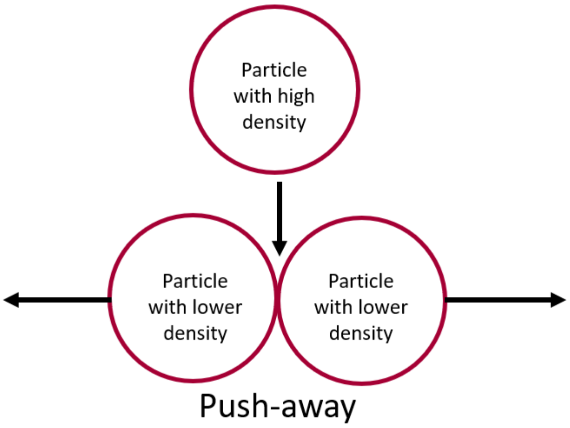

Figure 2.7: Segregation by push-away.

Trajectory segregation

In case the bulk material consisting of different particle sizes is transported via the air with an initial horizontal velocity (component), trajectory segregation could occur. The fine particles tend to drop directly downwards while the coarse particles keep on going in horizontal direction for a longer time period. The air resistance for finer particles is much higher than for coarser particles, explaining the smaller travel distance [58]. Figure 2.8 shows a graphical representation.

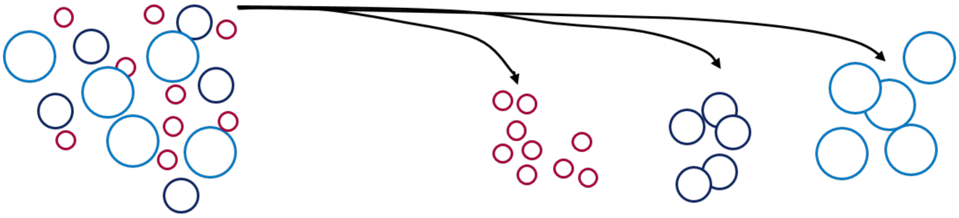

Figure 2.8: Trajectory segregation.

This can also be explained by means of an equation. The maximum horizontal travel distance of a particle can be calculated by Equation 2.1 [58]. Accordingly, one can deduce that a larger particle diameter result in a larger travel distance and vice versa [52, 58, 60]. For the complete derivation of Equation 2.1, consult chapter 2 of the book *'Introduction to Particle Technology'* from Martin Rhodes [58].

$$x = \frac{U \cdot \rho_P \cdot d_p^2}{18 \cdot \mu} \tag{2.1}$$

where

x is the horizontal travelled distance

U is the initial velocity of the particle

ρ_P is the particle density

d_p is the particle diameter

μ is the viscosity of fluid

2.2. Mixing applications

This section provides an overview of all common types of mix applications and outline to which group the paddle mixer belongs.

Currently, many different mixing designs exist that all serve its own purpose based upon specific industry-related requirements (Table 2.1 and Figure 2.9).

In literature, different classifications have been proposed. Bridgewater [11] subdivides mix applications into two groups, which are:

1. A shell rotates and the bulk material slops around inside. Primarily, mixing is dominated by diffusion and shear mechanisms.
2. Shell is stationary and bulk material is mixed by an internal rotor or rotors fitted with ribbons, blades, screws and/or paddles.

Rhodes [58] suggested a classification of four groups:

1. Tumbling mixers - Closed vessel rotating about its axis.
2. Convective mixers - Closed vessel with circulation patterns set up by rotating blades or paddles.
3. Fluidized bed mixers - Bubble motion within the bed causes circulation pattern.
4. High shear mixers - Local high shear stresses created by devices similar to those used in comminution.

Another classification is given by Cleary et al. [16]:

1. Gravity controlled mixers
2. Stirred mixers
3. High shear (or high energy) mixers

Accordingly, an own interpretation of mix application classification is given in Table 2.1. In which group 1 and group 2 in the *Class 1* column represents the rotating vessel and fixed vessel + rotary blades/paddles. The *Class 2* group represents the classification defined by Clear et al. [16].

Table 2.1: Overview of common mix applications classified in distinct groups.

Class 1	Class 2	Mixer	Predominating mechanism	Source
Group 1	Gravity	Cylindrical mixer	Shear/diffusion	[11]
		V-mixer	Diffusion	[54]
		Double cone blender	Shear/diffusion	[54]
		Tote mixer	Diffusion	[11]
Group 2	Stirred	Plough share mixer	Convection	[11]
		Ribbon mixer	Convection	[54]
		Paddle mixer	Diffusion	[54]
		Planetary mixer	Convection	[11]
		Nauta mixer	Convection/diffusion	[54]
	High shear	Disc impeller	Shear	[11]
		Blade impeller	Shear	[11]
		Muller mixer	Shear	[54]

Gravity controlled mixers like cylindrical mixers [8, 70], V-mixers [65], Double cone blenders [56] and Tote mixers [6] are rotary shells where the material falls down in a random fashion characterized by a diffusive mix mechanism. Secondly, stirred mixers consists of a fixed vessel where the material is mixed by a horizontal or vertical impeller in the form of blades, ribbons and/or paddles. Typical applications are plough share mixers [23], ribbon mixers [26, 37, 66, 71], paddle mixers [29, 34], planetary mixers [42] and Nauta mixers [12]. Last but not least, high shear are similar to the stirred class of mixers but use very high rotational speeds to mix the granular materials. Examples are disc/blade impellers [13, 70] and Muller mixers.

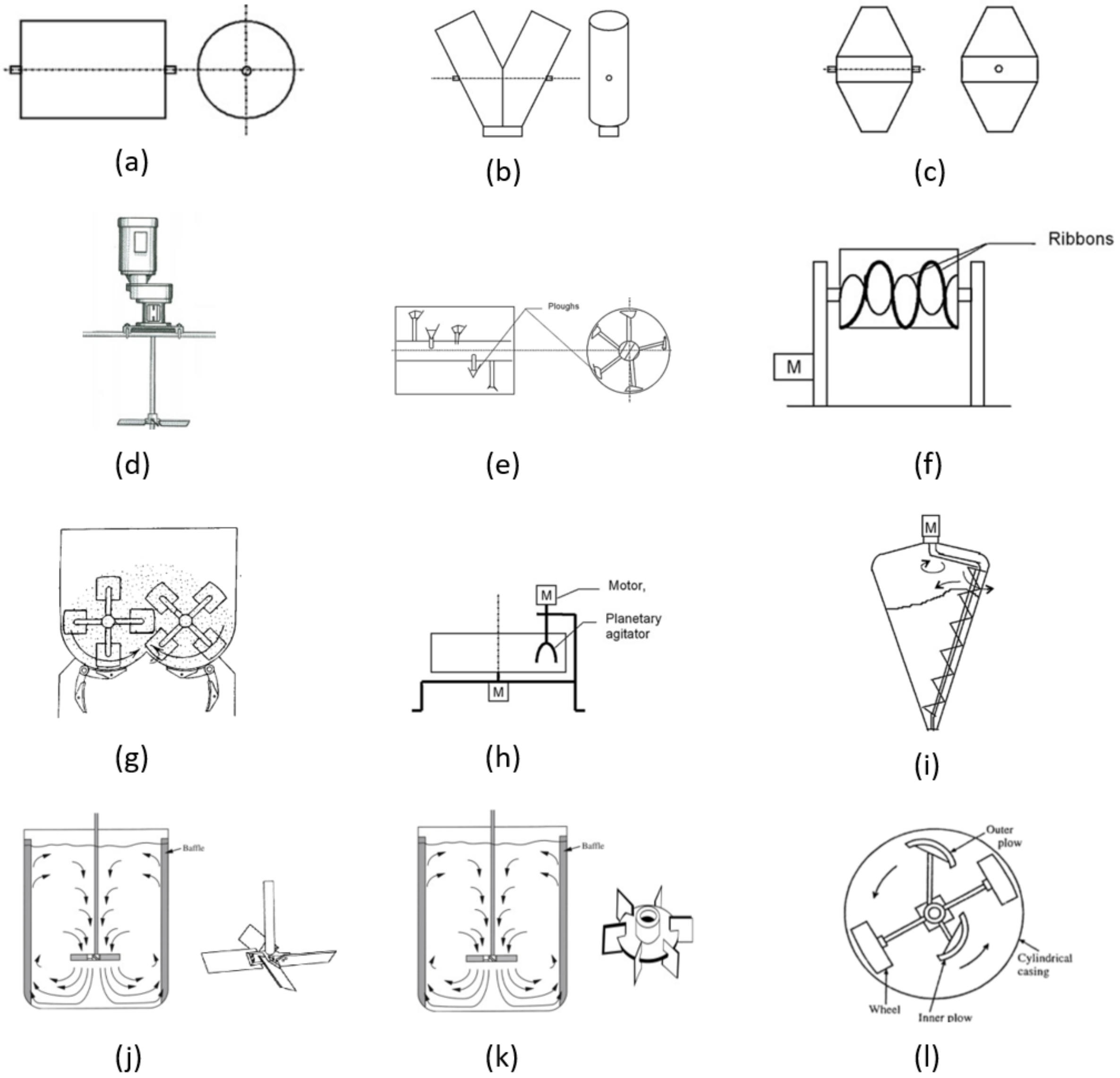

Figure 2.9: (a) Cylindrical drum, (b) V-mixer, (c) Double cone blender, (d) Tote mixer, (e) Plough share mixer, (f) Ribbon mixer, (g) Paddle mixer, (h) Planetary mixer, (i) Nauta mixer, (j) Disc impeller, (k) Blade impeller, (l) Muller mixer. Reprinted from [11, 54].

In Figure 2.9 an overview of most common mixer applications is presented by simple animations. As this research focuses on a double shaft, batch-type paddle mixer, further elaboration on showcased mixing applications is out of scope. In Section 2.3, published papers related to the paddle mixer will be explained in more detail.

2.3. Paddle mixer

Only a small number of papers is published about paddle mixers, both in combination with DEM simulations and without. In 2018, Ebrahimi et al. [21] investigated impeller configurations on mixing performance in a single shaft, horizontal batch-type paddle mixer. In subsequent years, Ebrahimi et al. [22] and Yaraghi et al. [69] also investigated rotational speed, fill level and initial loading pattern of both mono-sized and bi-disperse particles for a single shaft paddle mixer. Both DEM and experimental measurements were used to assess the mixing performance of the mixer.

Concerning double-shaft, batch-type paddle mixer only a few papers are published that relates to DEM. Hassanpour et al. [29] was the first to investigate this particular application in relation to DEM. The study consists of an analysis of particle motion by using experiments in the form of Positron Emmission Particle Tracking (PEPT) and DEM simulations. In 2013, Li et al. [40] looked into the effect of Particle Size Distribution (PSD) on segregation and coating uniformity. Subsequently, as a follow up study on the research done by Hassanpour et al. a more thorough research was done by tracking multiple particles with PEPT and DEM simulations [51].

Furthermore, Shenoy et al. [61, 62] utilized a custom built double shaft paddle mixer to investigate the effect of particle density, particle size, particle shape, water content and composition on a binary food powder mixture. Hereby the researchers did not make use of the DEM approach but conducted experiments.

Last of all, recently Jadidi et al. [34] published an paper about mixing performance analysis of a double shaft, paddle mixer by doing a sensitivity analysis on the impeller speed, initial loading pattern and fill level. Supplementary, they also touched upon the influence of particle shape on the mixing performance [32].

In next subsections, all above mentioned papers are condensed in chronological order. Note that only information that is believed relevant for this research is highlighted. Consult respective paper(s) for more information. Major findings are summarized in Table 2.2 and presented in Section 2.4.

2.3.1. Analysis of particle motion in a paddle mixer using Discrete Element Method (DEM) - Hassanpour et al. [29]

A study executed by Hassanpour et al. in 2010 [29] has shown how to utilize DEM simulations in combination with the PEPT measurement technique to understand the powder kinematic behavior in a double shaft paddle mixer. A geometric model of the mixer is shown in Figure 2.10. Each shaft consists of five paddle pairs, mounted in an angled fashion. The paddle pair at the end of the shaft has a different angle. The latter is due to its function as 'transfer' paddle, where the granular material is transferred from one side of the mixing chamber to the other.

Due to confidentiality reasons not all data is provided in the published paper which makes it rather hard to draw conclusions. Nevertheless, a valuable insight on the material's flow dynamics in a double shaft, batch type paddle mixer is given by means of a qualitative analysis as shown in Figure 2.11. The counteracting rotation of the shafts forces the material to move towards the center of the chamber as visualized in the upper two illustrations (a) and (b). The angled paddles cause the bulk material to move in axial direction which is clearly shown by the lower illustrations (c) and (d). The qualitative analysis as presented in Figure 2.11 is in good agreement with PEPT measurements.

2.3.2. Multi-scale modeling of a spray coating process in a paddle mixer/coater: The effect of particle size distribution on particle segregation and coating uniformity - Li et al. [40]

Among other subjects, Li et al. [40] researched the effect of particle size distribution (PSD) on the flow dynamics and segregation in a double shaft paddle mixer as shown in Figure 2.12. This paddle mixer consists of 7 angled paddle pairs per shaft, with the last one under a different angle functioning as a 'transfer' paddle.

The poly-disperse mixture is prone to segregation caused by the typical geometric characteristics and operational conditions of the double shaft paddle mixer. Small particles accumulate in the bottom and in the center of the mixing chamber. Moreover, concentration of larger particles decreases in radial direction further away from the shaft. Looking from the top view onto the particle bed it can be observed that the larger particles tend to accumulate where the transfer paddles are located, at the end of the shafts. It is assumed by the author that this phenomenon is caused by the front and back wall that block the continuous flow over to the other side of the mixer. In Figure 2.12 a visual representation is provided.

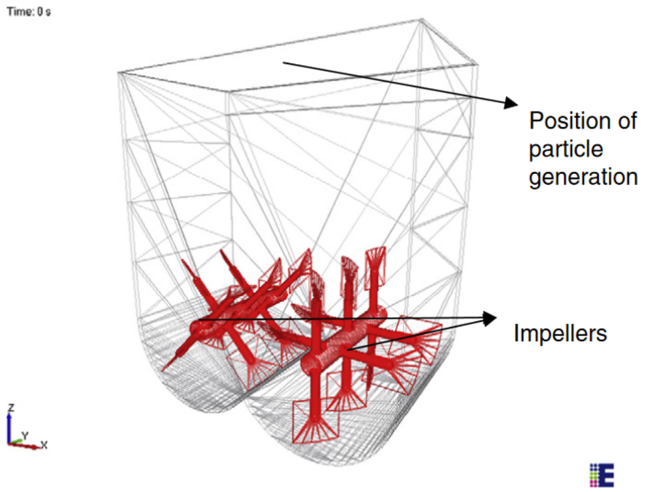

Figure 2.10: The imported geometry of the 6L paddle mixer simulated by the DEM. Reprinted from [29].

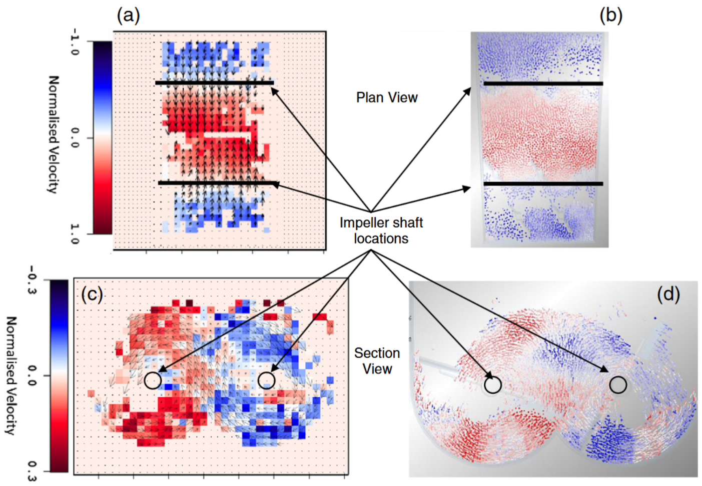

Figure 2.11: Time-averaged velocity profiles. Top view (red up and blue down). (a) PEPT and (b) DEM simulation. Front view (red out of page and blue into page) (c) PEPT (d) DEM simulation. Velocities are normalized by the paddle tip speed. Reprinted from [29].

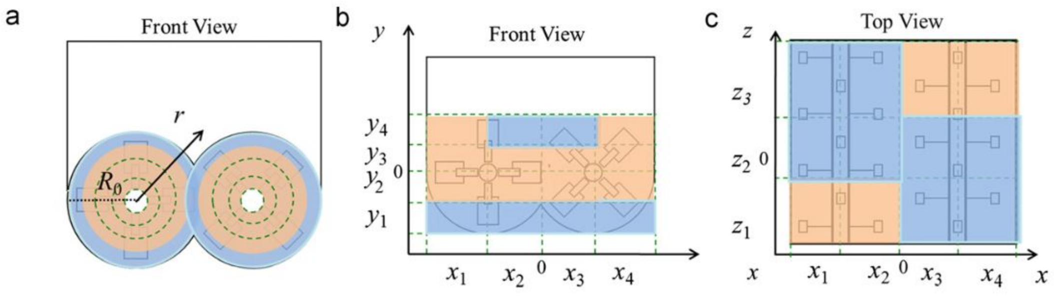

Figure 2.12: Front and top view of spatial segregation at steady state for binary mixture with rotational speed of 158 rpm and D/d = 1.3 (with D large particle diameter and d small particle diameter). Orange color represent large particle dominated areas and blue small particle dominated areas. Reprinted from [40].

2.3.3. A comparative analysis of particle tracking in a mixer by discrete element method and positron emission particle tracking - Pasha et al. [51]

This is an extended research of the paper published by Hassanpour et al. [29] in 2010. An attempt is made to simulate the mixing process with a double-shaft, paddle mixer with DEM simulations aiming at good agreement with PEPT experiments. Main focus is on increasing the number of PEPT tracers on their time-averaged velocity distribution to eventually investigate if it can approve data representation.

In short, it takes 251 seconds for one tracer to move adequately through the mixing chamber. Comparison of the data of one single tracer with DEM simulation one could say they are in good agreement. However, increasing the number of tracers in the paddle mixer system does not influence average velocity distribution.

2.3.4. Effect of powder densities, particle size and shape on mixture quality of binary food powder mixtures. - Shenoy et al. [62]

In this paper, the effect of particle size and bulk density on the mixture homogeneity is investigated by means of experimenting with various food powder mixtures. Researchers made use of a custom-built 2L double shaft paddle mixer to mix the components.

Particle size ratios up to a ratio of 4.45 mixed very well, but higher ratios cause a decrease in mixture quality. Compared to bulk density, the particle size ratio has a higher influence on mixture quality. At bulk density ratios higher than 6 segregation was observed. However, it is believed by the author that the irregular shaped mix components (thyme and oregano) are the main cause for observed segregation. Due to the irregular shapes of aforementioned components, the naturally generated voids between particles caused downward movements of rectangular shaped particles, which lead to segregation.

2.3.5. Dry mixing of food powders: Effect of water content and composition on mixture quality of binary mixtures. - Shenoy et al. [61]

As a sequel on previous research done by Shenoy et al. [62], they now focused on the effect of water content and composition on the mix performance of the same 2L double shaft paddle mixer.

The mixture composition in the range 20-80% did not affect the mixture quality much, however mixture compositions with component concentrations less than 1% did effect the quality. Generally, the effect of composition was higher for mixtures that were hard to mix (e.g. caused by shape irregularities). A final remark, the flowability of a powder plays a key role in assessing how well the paddle mixer is able to mix the researched substances.

2.3.6. The effect of impeller configurations on particle mixing in an agitated paddle mixer - Ebrahimi et al. [21]

The paper is about a single shaft, batch-type paddle mixer with main focus on the effect of impeller configuration on the mixing performance of the system. Remy et al. [57] pointed out the relevance of the impeller configuration and could be seen as the origin of this research.

Six individual paddle blades alternating in 90° are connected to a shaft (Figure 2.13). Free flowing, mono-disperse glass beads with similar properties were loaded in a top-bottom configuration prior to the experiments/DEM simulations with 40% fill level. The mixer rotates with 40 rpm. In Figure 2.13 a graphical representation of the mixer is showcased and in Figure 2.14 associated dimensional values are presented.

After calibrating the DEM model by comparison with experiments, the influence of different paddle configurations on degree of mixing is analyzed by comparing their RSD values. Figure 2.15 present a front view of the single shaft paddle mixer with variable α indicating the adjustable paddle angle. Figure 2.16 presents a graphical representation of the RSD mixing index plotted against number of revolution for various impeller configurations. Evidently, the impeller's angle has a significant influence on the mixing performance of the system.

This is also qualitatively confirmed by snapshots taken after 10 revolutions for all paddle configurations (Figure 2.17). The 30°-angle and 45°-angle impeller configurations show better mixtures than the other three.

In conclusion, the RSD values for 60°-angle were in most of cases worst of all impeller configurations. At the end of the mixing time, the RSD of respective configuration approached the RSD from 0°-angle and rectangular configurations due to high axial convection. The 30°-angle and 45°-angle

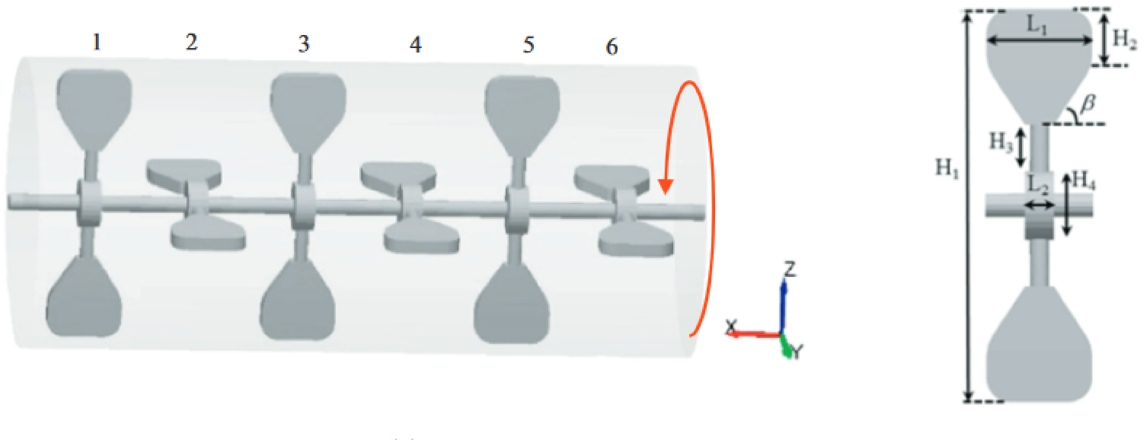

(a)

(b)

Figure 2.13: (a) Front view of the mixing system equipped with 0°-angle paddle, and (b) Dimensions of individual paddle blade. Reprinted from [21].

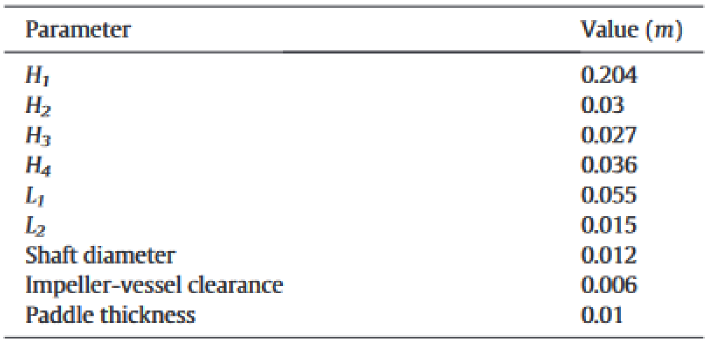

Parameter	Value (m)
H_1	0.204
H_2	0.03
H_3	0.027
H_4	0.036
L_1	0.055
L_2	0.015
Shaft diameter	0.012
Impeller-vessel clearance	0.006
Paddle thickness	0.01

Figure 2.14: Dimensions of the impeller as defined in Figure 2.13. Reprinted from [21].

(a)

(b)

Figure 2.15: Graphical illustration of single shaft paddle geometry. (a) Paddle blade configuration with angle α and (b) Rectangular paddle configuration. Reprinted from [21].

performed best due to diffusive and convective axial mixing mechanism. On the other hand, mixing in radial directions performed worse for these two configurations compared to 0°-angle and rectangular configurations. Furthermore, increasing the paddle angle from 30° to 45° to 60° resulted in deterioration of mix quality at all times. Diffusion was the dominant mixing mechanism for all paddle configurations.

2.3.7. Mixing assessment of non-cohesive particles in a paddle mixer through experiments and discrete element method (DEM) - Yaraghi et al. [69]

In a second study the same research group investigated the mixer's performance by varying the key parameters rotational speed (10, 40 and 70 rpm), fill level (40, 50 and 60%) and particle loading

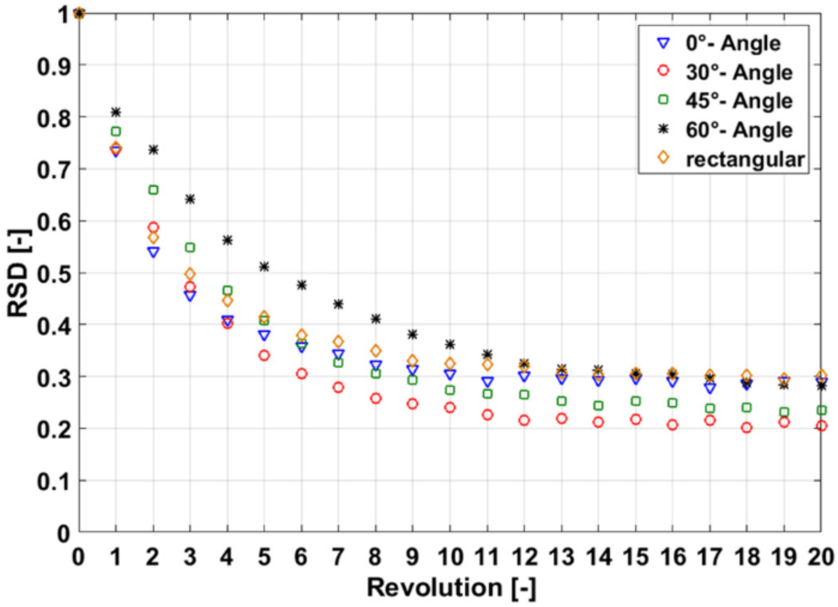

Figure 2.16: Graphical illustration of RSD mixing index against number of revolution for various impeller configurations. Reprinted from [21].

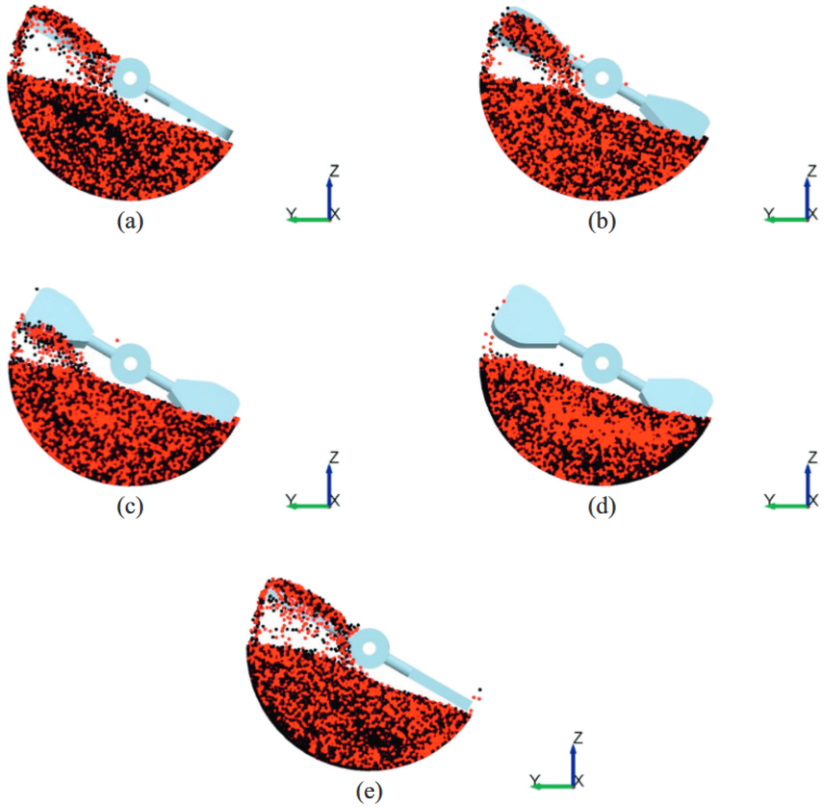

Figure 2.17: A side view of the mixer after 10 revolutions of mixing. (a) 0°-angle, (b) 30°-angle, (c) 45°-angle, (d) 60°-angle and (e) rectangular paddles. Reprinted from [21].

arrangement of mixing components (Top-Bottom and Front-Back). The same material (free-flowing, mono-disperse glass beads) was used as in previous study done by Ebrahimi et al. [21].

In short, for all particle loading arrangements and fill levels, the mixing performance did improve by increasing rotational speed from 10 to 40 rpm. However, this was not the case when increasing rotational speed to 70 rpm with fill levels 40% and 50%. For the 60% fill level, at first the mixing performance enhanced with rotational speed of 70 rpm for both loading arrangements, but decreased when time progressed compared to the 40 rpm case. Moreover, independent of the loading arrangement with rotational speeds 40 rpm and 70 rpm, increasing fill level from 40% to 50% to 60% improved the mixing performance. One could deduce from aforementioned concluding remarks that the two loading arrangements did not influence the system's performance. The rotational speed has the strongest effect on the mix quality as chaotic motion of particles is stimulated caused by an increase of rotational speed.

2.3.8. Assessment of bi-disperse solid particles mixing in a horizontal paddle mixer through experiments and DEM - Ebrahimi et al. [22]

In the third study of research group Ebrahimi et al. [22] on the single shaft, paddle mixer they investigated the effect of a binary mixture on the mixing performance. The material consisted of 2 components with two different particle diameters. The critical operating parameters that were defined are impeller rotation speed (40rpm, 70rpm and 100rpm), two vessel fill levels (40% and 60%), particle number ratio (r_n = N_s/N_l with r_n is equal to 4, 1 and 0.25. Where N_s is the number of small particles and N_s is the number of large particles) and particle loading arrangement.

It was found that an r_n of 0.25 and 40 rpm yielded the best mixing performance for both fill levels. For the other two particle number ratios (r_n of 1 and 4) with 40% fill level and 40 rpm resulted in best mixing performance after the reaching steady state condition. But, during initial mixing stages the high rotational speeds (70 and 100 rpm) provided better mix quality. For a value of r_n = 1 and 60% fill level, the rotational speeds 40 rpm and 70 rpm performed slightly better when the steady state was reached compared to the rotational speed of 100 rpm. Furthermore, for a value of r_n = 4 and 60% fill level, with rotational speed of 70 rpm and 100 rpm the steady state condition was reached faster compared to rotational speed of 40 rpm. Additionally, the particle number ratio had a major influence on the mixing performance. An increase in particle number ratio resulted in a decrease in RSD values for all rotational speeds and fill levels. In general, the higher fill level of 60% resulted in better mixing performance of the system compared to the lower fill level of 40%. Finally, the particle loading arrangement did not have a significant influence on the mixing performance.

2.3.9. Mixing performance analysis of non-cohesive particles in a double paddle blender using DEM and experiments - Jadidi et al. [34]

In January 2022, Jadidi et al. [34] published an paper about thorough research on a 80L double shaft, batch-type paddle mixer (Figure 2.18).

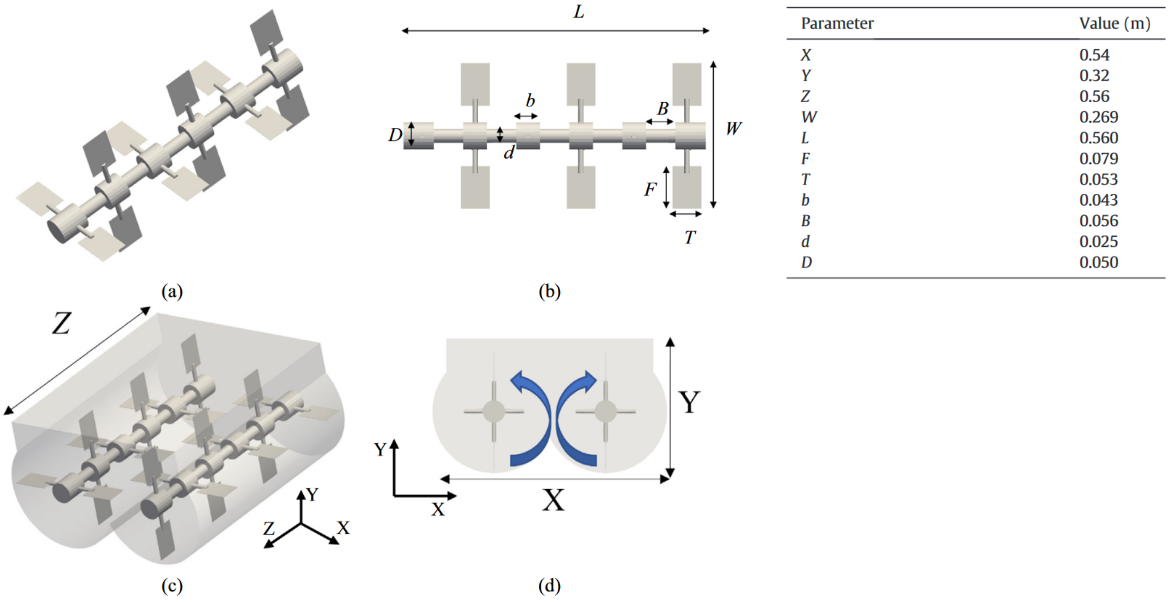

Parameter	Value (m)
X	0.54
Y	0.32
Z	0.56
W	0.269
L	0.560
F	0.079
T	0.053
b	0.043
B	0.056
d	0.025
D	0.050

Figure 2.18: Double shaft paddle mixer with dimensions. Reprinted from [34].

Mono-disperse, non-cohesive glass beads were used in the experiments and DEM simulations with a total real-time of 20s. After calibration of the material model, a sensitivity analysis has been executed on the influence of the fill level (40%, 50% and 60%), impeller speed (10 rpm, 40 rpm and 70 rpm) and initial loading pattern (Top-Bottom, Side-by-Side and Front-Back) on the mixing performance of the system. Prematurely, the Front-Back (FB) loading pattern is eliminated due to poor mixing performance in all cases. Main conclusions are enumerated below:

1. For all fill levels in the Top-Bottom (TB) loading pattern, increasing the impeller speed from 10 to 70 rpm improved the mixing performance of the system. As mixing time continued, the impeller speed of 40 rpm reached the RSD value of the 70 rpm impeller speed at the end of the mixing process, irrespective of the fill level.
2. For all fill levels in the Side-by-Side (SS) loading pattern, increasing the impeller speed enhanced mixing performance for the entire mixing time.
3. The SS loading pattern achieved steady-state conditions slower compared to simulation cases with TB initial loading pattern.
4. An increase in impeller speeds resulted in an increase in forces acting on particles. The forces experienced by the particles could in some cases damage the final product.
5. Influence of fill levels for both loading patterns did not impact the mixing performance of the system considerably. For the impeller speed of 10 rpm, a fill level of 60% led to a slight decrease in mixing performance.
6. The TB loading pattern resulted in the best mixing performance compared to the other two loading patterns.
7. According to Peclet number calculations, the dominant mixing mechanism in all cases was diffusion.
8. The diffusivity coefficient and granular temperature analysis explained the improvement in mixing performance with increasing impeller speed values.
9. Response Surface Methodology (RSM) confirmed the major influence of impeller speed and initial loading pattern on the mixing performance.
10. Interaction between operating parameters did not affect mixing performance

2.3.10. Investigation of Mixing Non-Spherical Particles in a Double Paddle Blender via Experiments and GPU-Based DEM Modeling. - Jadidi et al. [32]

This relatively concise research is about the effect of non-spherical particles onto the mixing kinematics and flow patterns of a double shaft paddle mixer (same as in [34] with both DEM and experiments. The calibrated DEM model was subjected to a number of simulations to do both a qualitative and quantitative analysis on the effect of particle shape on the mixing performance. It was found that simulations with spherical particles gave the best mixing performance of the system compared to cubical and cylindrical shaped particles. The cubical shaped particles performed better than the cylindrical ones as the former comes closer to the spherical shaped particles.

2.3.11. Mixing and segregation assessment of bi-disperse solid particles in a double paddle mixer. - Jadidi et al. [34]

The impact of the particle number ratio, vessel fill level, impeller rotational speed on the mixing performance of a double shaft paddle mixer was investigated with DEM and experiments [33]. The utilization of a bi-disperse particle mixture made this research unique compared to research done by the same research group in January 2022 [34] where they only conducted experiments on mono-disperse particles mixtures. Besides the discrepancy in particle size ratio and particle number ratio, all other settings compared to their previous research is similar.

The impeller rotational speed and the particle number ratio did affect the mixing performance of the system. Changing the speed from 10rpm to 40rpm improved the mix quality regardless of what fill level was chosen. Despite the fact an increase in mixing performance could be observed when the impeller speed increased in the initial stage of mixing from 40rpm to 70rpm, in the end they both provided the same mixing quality for all fill levels.

Furthermore, increasing the particle number ratio affected the mixing performance positively for all impeller rotational speed and fill levels. Especially for high speeds and fill levels, the final mixture quality increased with an increase in particle number ratio meaning that a higher percentage of smaller particles in the mixing chamber would lead to a better mixing performance.

2.4. Conclusion

The main findings of published papers about paddle mixers are presented in Table 2.2. One can observe, not many papers are published in relation to paddle mixers. The main knowledge gap present in this relatively new research field is an in-depth understanding of which factors affect the mixing performance of the system and which do not. Although a couple of material (particle size, density etc.), operational conditions (fill level, impeller rotational speed etc.) and geometric characteristics (impeller configuration) are investigated for both single and double shaft paddle mixers, the number of factors are tremendous in many different possible combinations. In conclusion, screening a selection of factors to investigate their effect on the mixing performance of a double shaft, batch-type paddle mixer is a necessity to improve understanding of the dynamics and interaction of material and paddle mixer.

Table 2.2: Relevant results from the literature review on the paddle mixer.

Source	Type	DEM	Characteristics	Main findings
[29]	Double shaft	Yes	Mono-sized Spherical Free-flowing d_p = 4.52 mm ρ_p = 1000 kg m^{-3} v_{shaft} not given (confidential) V_{mixer} = 6 L	- Comparison DEM simulations of particle flow to experimental measurements using Positron Emission Particle Tracking (PEPT). - Qualitative agreement between DEM and PEPT in terms of flow patterns inside the paddle mixer. - Quantitative analysis show reasonable agreement between DEM and PEPT in terms of velocity distribution.
[40]	Double shaft	Yes	Bi-disperse Spherical Free-flowing d_p = 10.52 mm ρ_p = 750 kg m^{-3} v_{shaft} = 158 rpm V_{mixer} = 6 L	- Investigation of Particle Size Distribution (PSD) on flow dynamics, segregation and coating uniformity. - A DEM model is created to do analysis on particle motion and coating growth. - Small particles accumulate in the fluidized zone in the center of the mixer, while large particles collect at the end wall regions.
[51]	Double shaft	Yes	Mono-sized Spherical Free-flowing d_p = 4.52 mm ρ_p = 1000 kg m^{-3}	- Investigation on the effect of increasing number of tracers on their time-averaged velocity distribution and whether it can represent the data on whole population of particles. - It takes 251 seconds for one tracer to travel adequately in all active space of the system. - Data of the PEPT experiment with one tracer with those of DEM with one tracer are in good agreement. - DEM simulations suggest that increasing the number of tracers in the paddle does not influence the average velocity distribution.

[62]	Double shaft	No	Poly-disperse Food powders d_p = 24-1600 μm ρ_p = 1360-1760 $\mathrm{kg\,m^{-3}}$ V_{mixer} = 2 L	- Effect of particle size and bulk density on mixture homogeneity are investigated for different food powders like salt. - By conductivity analysis the Coefficient of Variation (CoV) was determined to assess the homogeneity. - Powders mixed very well up to a particle size ratio of 4.45. Mixture quality decreased for higher ratios, but no segregation was observed. - Bulk density had a larger effect on segregation compared to the particle size, however it is believed this had mainly to do with the irregular particle shape of the oregano particles.
[61]	Double shaft	No	Binary Non-spherical (food powders) d_p = 225-1600 μm ρ_p = 1210-2160 $\mathrm{kg\,m^{-3}}$ V_{mixer} = 2 L	- Effect of composition and water content on mixture quality of food powder mixtures is investigated. - For compositions sugar-salt and paprika-salt within 20-80% salt content range the mixture quality was not affected. - For composition oregano/salt with higher oregano content and low salt content, the mixture quality was affected negatively.
[21]	Single shaft	Yes	Mono-sized Spherical Free-flowing d_p = 3 mm ρ_p = 2500 $\mathrm{kg\,m^{-3}}$ v_{shaft} = 40 rpm	- The influence of the impeller configuration on mixing performance was investigated. - Paddle configuration 30°-angle and 45°-angle provided better mixing performance compared to 0°-angle, 60°-angle and rectangular angle. - The particle-particle contact forces were less affected by alterations in impeller configurations compared to particle-impeller contact forces. - Diffusion is the dominant mixing mechanism irrespective of the impeller configurations.

[69]	Single shaft	Yes	Mono-sized Spherical Free-flowing d_p = 3 mm ρ_p = 2500 $\mathrm{kg\,m^{-3}}$ V_{mixer} = 4 L	- Effects of impeller rotational speed, fill level and initial loading pattern on mixing performance were investigated. - Increase of impeller speed from 10 to 40 rpm resulted in better mixing quality irrespective of initial loading pattern and fill level. - Increase of impeller speed from 40 to 70 RPM resulted in better mixing quality for 60% fill level irrespective of initial loading pattern. - Increase of fill level from 40 to 60% enhanced mixing performance with rotational speeds 40 and 70 RPM. - For rotational speed of 10 RPM, mixing quality was independent of fill level and loading pattern for almost all simulations. - Loading pattern did not have major influence on mixing performance. - ANOVA showed impeller rotational speed had strongest influence on mixing performance. - Diffusion is the dominant mixing mechanism.
[22]	Single shaft	Yes	Bi-disperse Spherical Free-flowing d_p = 3 and 5 mm ρ_p = 1000 $\mathrm{kg\,m^{-3}}$	- Mixing of bi-disperse particles was investigated. Influence of impeller rotational speed, fill level, particle number ratio and initial loading pattern on mixing performance was analyzed. - The particle number ratio had the most significant effect on the mixing performance. - Diffusion is the dominant mixing mechanism. - In case diffusion coefficients of 3 and 5 mm (particle size) were close, the best mixing performance was achieved.

[34]	Double shaft	Yes	Mono-sized Spherical Free-flowing d_p = 3 mm ρ_p = 2500 kg m^{-3}	- Analysis of flow patterns and mixing mechanisms. - Influence of impeller speed, initial loading pattern and fill level on mixing performance was investigated. - Impeller speed and initial loading pattern had significant effects on mixing performance. - Diffusion and granular temperature analysis explained enhanced mixing performance due to increase in impeller speed. - Diffusion is the dominant mixing mechanism. - ANOVA results revealed that the interaction between impeller speed and initial loading pattern had negligible impact on mixing performance.
[32]	Double shaft	Yes	Non-spherical Free-flowing	- Investigation of mixing kinematics, flow pattern and particle shape was investigated. - The particle shape significantly influence the mixing performance of the system.
[33]	Double shaft	Yes	Bi-disperse Spherical Free-flowing d_p = 3 and 5 mm ρ_p = 2500 kg m^{-3} V_{mixer} = 80 L	- Experiments and a calibrated DEM model were used to analyse the flow patterns and mixing mechanisms of the mixer. - The impact of the particle number ratio, vessel fill level and paddle rotational speed was investigated. - The mixing performance was effected by variations of the particle number ratio and the paddle rotational speed. - A change in speed from 10 to 40 rpm improved the mixing performance. Moreover, an increase from 40 to 70 rpm improved the performance in the initial mixing stage. But, in the end both the 40 rpm and the 70 rpm simulation were performing equally well. - Mixture quality was better for the 70 rpm speed than for 10 rpm. - A decrease in particle number ratio resulted in a reduction in mixture quality, irrespective of the rotational speed and vessel fill level. Furthermore, results indicated that the effect of particle number ratio was more significant for higher speeds and fill levels. - A small increase in mixing performance was observed with a fill level of 60% compared to a fill level of 40%.

3

Simulation model

In this chapter, the modelling method is selected which is described in Section 3.1. Thereafter, the simulation model setup for the paddle mixer under investigation is elaborated in Section 3.2. The stability analysis can be found in Section 3.3.

3.1. Modelling method

After a brief introduction in Section 3.1.1, a detailed description of the selected method is in Section 3.1.2 with corresponding advantages and limitations of the method are described in Section 3.1.3.

3.1.1. Introduction

The mixing application investigated deals with material comprising of multiple solid particles. In this particular situation these solid particles can be in contact with other solid particles, or with the geometry of the mixing application. Due to geometric movement of the blades through the particle bed, interparticle forces on a micro scale change over time resulting in dynamic behavior of granular material on a macro level inside the mixing chamber.

One can imagine that for a particulate system consisting of many particles, tracking each individual particle via experimental measurements is not feasible. Although, optical imaging techniques exist like Position Emission Particle Tracking (PEPT) which are able to track one or a small selection of particles inside a particle bed [50, 68]. Still, an experimental technique that is able to capture all particles in real-time is not (yet) available. The paper of Asachi et al. [7] reviewed all available powder mixture assessment techniques currently available. A summary is presented in table 4 of the respective paper.

Alternatively, computational modelling techniques could offer great solutions. The increase in popularity of such techniques has mainly to do with technological advances in computer science. The rapid development originates from improvements in programming in combination with an increase in computational speed and power [46]. For example, Computational Fluid Dynamics (CFD) techniques have proven to be effective, able to capture the dynamic behavior of a fluid like liquids or gases. Or, the Finite Element Method (FEM) techniques that can perform analysis on solid structures by subdividing the whole system in smaller parts called 'Finite Elements'.

Whereas the FEM is perfectly suited for analysis on mechanical behavior like for instance stress or deformation evaluations on continuum materials, this method is not applicable for particulate systems as they are by nature discontinuous. A common modelling technique for particulate systems is called the Discrete Element Method (DEM), applied in many areas like mining engineering, agricultural technology, chemical engineering, pharmaceutical industry, food industry and process engineering [9, 24]. Hereby, assuming the system consists of a large number of particles. Its popularity is invigorated by Table B.1 in Appendix B where the number of published papers related to DEM is plotted over time. Evidently, this trend carries a huge potential for future solutions to typical engineering problems in industry. In Section 3.1.2, a detailed elaboration is presented of the method.

3.1.2. Discrete Element Method (DEM)

In the year 1971, Cundall introduced DEM related to rock mechanics [18]. Subsequently, the first paper published in open literature about the granular material application of DEM was in 1979 by Cundall and Strack [19].

Due to rapid increase in computer technology, shared knowledge about the method and the huge potential in many application fields have led to an increase in popularity of DEM in last decades. The method makes it possible to model complex bulk material behavior by simulating the material on a particle level. A finite number of discrete particles in a fixed, bounded system are able to interact with each other, governed by the Newton's equation of motion. In addition, contact can occur between particles or between particle and system's boundary. In the next sections, all features are elaborated upon related to DEM.

3.1.2.1. Equations of Motions

Particles experience two types of motions during simulation: Rotational and Translational. Both are governed by Newton's laws of motion. The forces and torques on an individual particle are caused by interaction with other particles, system's boundaries or non-contact forces like electric fields, van der Waals forces and particle-fluid interactions. [19]

In Equation 3.1 and Equation 3.2, the translational and rotational equations of motion are formulated. In Figure 3.1, a two-dimensional particle-particle interaction is illustrated with corresponding parameters introduced in the equations of motion. [19]

$$m_i \frac{dv_i}{dt} = \sum_{j}^{N_c} (F_{n,ij} - F_{t,ij}) + F_{g,i} \tag{3.1}$$

where:

m_i is the mass of particle i

v_i is the translational velocity of particle i

N_c is the number of particles in contact with particle i

$F_{n,ij}$ is the normal component of the contact force between particle i and j

$F_{t,ij}$ is the tangential component of the contact force between particle i and j

$F_{g,i}$ is the gravitational force on particle i

$$I_i \frac{d\omega_i}{dt} = \sum_{j}^{N_c} (M_{t,ij} + M_{r,ij}) \tag{3.2}$$

where:

I_i is the moment of inertia of particle i

ω_i is the angular velocity of particle i

N_c is the number of particles in contact with particle i

$M_{t,ij}$ is the rotational torque between particle i and j

$M_{r,ij}$ is the rolling resistance torque between particle i and j

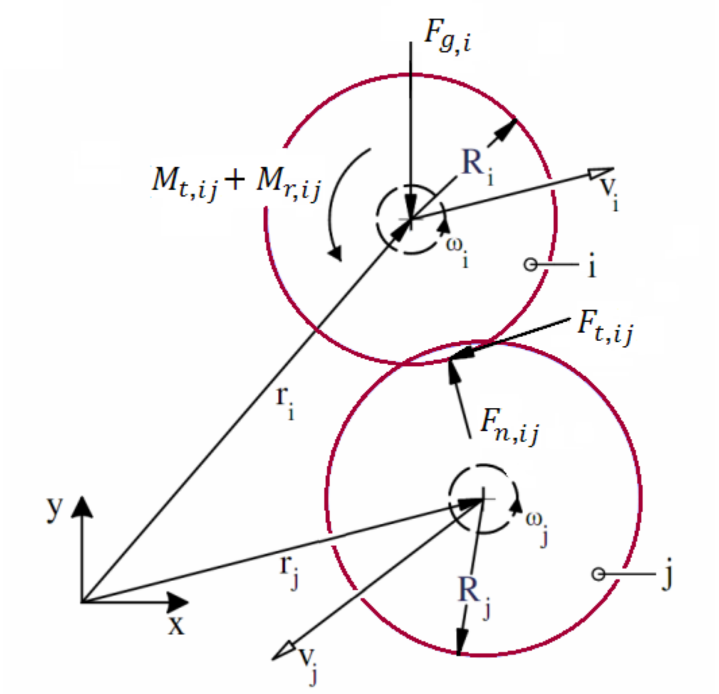

Figure 3.1: Two-dimensional particle-particle interaction with forces particle j acting forces on particle i. Reprinted from [27] and adjusted.

3.1.2.2. Contact model

The way particles interact with each other or with a system's boundary is described by a contact model. A contact model is a simplified framework where forces and torques on the moving bodies can be calculated efficiently by a set of mathematical formulas. During particle-particle or particle-boundary contact, normal and tangential forces are present which depend on the amount of overlap and rate of displacement of moving bodies. Moreover, not only tangential and normal forces play a role, but also rolling between contact surfaces. The latter influences the rolling behavior of the particle. [27]

Last few years researchers have created own contact models which are most often based upon well known contact models like the linear spring-dashpot model (LSD) [19] and the Hertz-Mindlin model [72], which was developed decades ago for elastic contact behavior between solid bodies. However, these two are considered suitable for modelling elastic granular behavior. Thus, elasto-plastic contact models are being developed to account for plastic behavior. For example, Morrissey [48] developed in 2013 the Edinburg Elasto-Plastic Adhesive (EEPA) contact model to include stress history of the cohesive granular material.

3.1.2.3. Contact detection

To detect contacts between particles or between particles and boundaries an efficient and simple algorithm is required. According to Grima [27], the chosen contact detection algorithm governs the computational efficiency and thus a conservative algorithm should be chosen to ensure all contacts are detected, especially in large systems with a high amount of particles.

In short, there are two algorithms that are most popular [27] which will be explained in coming paragraphs. Which one to choose depends on the type of motion of the system (quasi-static or dynamic), the particle shape/type and packing of the particles.

Grid method

The system's space is divided into a grid of cells. For an individual particle, contacts between other particles within its own cell and with neighboring cells is checked. Because of these contacts, the method is sometimes called neighboring cells method. Within every cell a list of the particles is maintained. Consequently, the size of the grid cells influence the computational time. When the grid cell is too small, the number of cells to search for possible contacts is too high. However, a grid cell too large will also have a negative effect on the computational efficiency as too many particles will be present in one individual grid cell.

To determine the right grid cell size one should take into account the particle size, number of particles and computational capacity. A balance must be found between two options. On the one hand, a fine grid cell size leads to a small number of particles in the cell and could thus result in a low number of contact points with other particles or boundaries, leading to frequent and quick updates of the neighboring list. On the other hand, a large grid cell size will lead to a high number of particles within each cell and thus could lead to more contact points. As a consequence, time required to search for contacts and update the neighboring list will take longer. However, the update rate of the list will be lower compared to the update rate of the list for small size grid cells.

Neighbor list method

This neighbor list method is a particular method that uses a redefined radius around an individual particle to search for contacts in its neighborhood (Figure 3.2). A so-called Verlet list is kept for each particle's neighbors to detect possible contacts or situations where a collision is likely. For systems with a high number of particles and quasi-static assemblies this method is perfectly suited. But, for systems with particles moving at high velocities the method is less efficient. The latter is true because of the Verlet list that must be updated more frequently compared to the former [55].

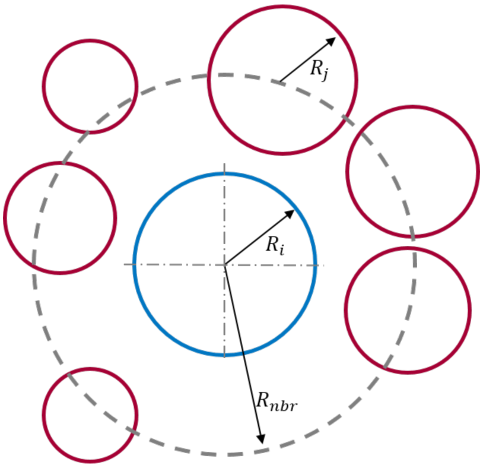

Figure 3.2: 2D illustration of Verlet method. Reprinted from [27] and adjusted.

The predefined radius called the neighborhood radius R_{nbr} should be large enough such that the algorithm is able to detect particles within its neighborhood before collision (Equation 3.3).

$$R_{nbr} \geq (R_i + R_j) \tag{3.3}$$

where:

R_{nbr} is the neighborhood radius

R_i is the radius of particle i

R_j is the radius of particle j

Another factor that should be taken into account is the velocity of particles. To ensure a sufficient neighborhood radius considering the highest particle velocity $v_{i,max}$ in the system, Equation 3.4 must be met.

$$\sum_{n=i}^{j} |v_i|_{max} \Delta t \geq \frac{R_{nbr}}{2} \tag{3.4}$$

where:

$|v_i|_{max}$ is the highest particle velocity in a system

Δt is the simulation time step interval

R_{nbr} is the neighborhood radius

In case dealing with systems with a high number of particles (greater than 10^6), this particular method can become unsuitable due to computational limitations [53].

3.1.2.4. Numerical stability

As DEM is an iterative process governed by explicit integration and central difference time integration, a suitable time step must be chosen to ensure numerical stability [27]. In general, one should select a time step which is small enough such that no new contacts take place in the current time step except those that have already been recognised at the beginning of the time step. Moreover, one wants to take the time step as large as possible to increase calculation efficiency. However, if a time step is too large several undesired situations could occur. For example, erratic behavior may occur by excessive overlap between particles. Or the contact detection algorithm would fail to detect contact(s) at all. [59]

In Figure 3.3 an illustration is provided. Here situation (a) propose a number of possible time steps while situations (b) and (c) illustrate undesired time steps.

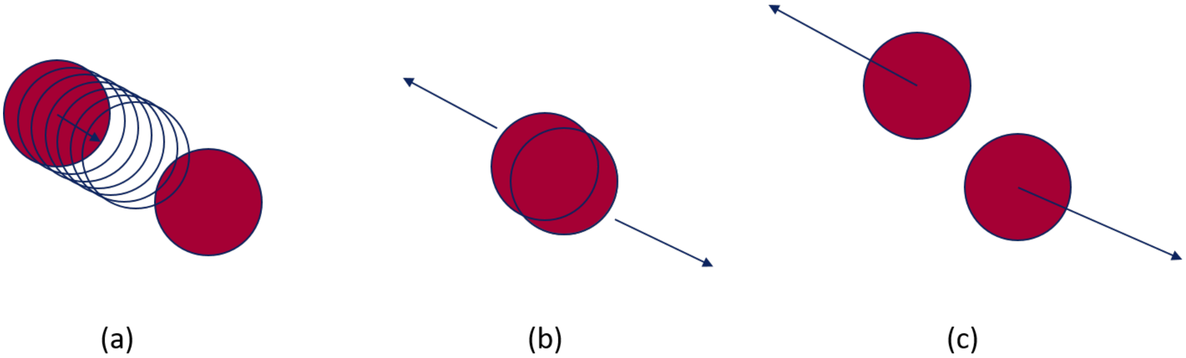

Figure 3.3: 2D illustration of different situations with respect to the chosen time step. (a) proposes several desired time steps, (b) will cause erratic behavior caused by excessive overlap between particles and (c) particles moved through each other (contact missed). Reprinted from [59] and adjusted.

As a result, the simulation will become unstable. Thus, to justify the assumption of constant acceleration within each time step and to ensure the system's stability the actual time step must be smaller than the critical time step (Equation 3.5).

$$\Delta t \leq t_{cr} \tag{3.5}$$

where

Δt is the simulation time step interval

t_{cr} is the critical time step

To calculate the theoretical maximum time step (Rayleigh time step) for coordination number (number of contacts per particle) larger than one (Equation 3.6). In practice the critical time step t_{cr} is a fraction of T_R. For high coordination numbers (4 or higher) 20% of Rayleigh time step T_R. For lower coordination numbers 40% of Rayleigh time step T_R is sufficient.

$$T_R = \frac{\pi R_{min}\sqrt{\frac{\rho_p}{G}}}{0.1631\nu_p + 0.8766} \tag{3.6}$$

where

T_R is the Rayleigh time step

R_{min} is the smallest particle radius

G is the shear modulus

ρ_p is the particle density

ν is the Poisson's ratio

3.1.2.5. Contact definition

In what way particles interact with each other, two different approaches can be distinguished: ”soft-particle” approach and ”hard-particle approach”. The former is the most used technique due to multiple advantages. For example, more than one particle contact can be tracked, inter-particle forces are easily implemented and the technique allows for a longer contact duration. Latter has a positive impact on computational time. Moreover, the ”soft-particle” approach is perfectly suited for quasi-static systems which is not the case for the ”hard-particle” approach. The latter is better suited for rapid flows where multiple collisions at the same time are not likely to occur. [27]

3.1.2.6. DEM algorithm

In Figure 3.4, a flow chart is visualized that shows all steps in the DEM algorithm. A DEM simulation algorithm always comprises following functions and features [27]:

1. Initialization of simulation environment
2. Detect contacts
3. Calculate interaction forces
4. Calculate particle positions
5. Save output data

3.1.2.7. Particle shape

Originally, only spherical or disc mono-disperse particles were utilized for all granular material simulations to simplify the system. This has major disadvantages as spherical or disk particles are not able to capture shear resistance accurately enough for irregularly shaped particles. Furthermore, the lower bulk strength and lack of dilation during shear are other drawbacks.

To represent realistic physical behavior of granular material, non-spherical shaped particles are required. Nowadays, several options exist to set up differently shaped particles. For example, one can cluster spherical particles of arbitrary size together. Even more complex structures like super-quadratic, ellipsoidal and polyhedral shapes are currently available. [43]

3.1.3. Advantages and limitations

One of the main advantages of utilization of the DEM technique is the cost and time reduction compared to physical experiments, leading to quicker innovative designs and processes. The possibility to extract information from DEM simulation software like forces, velocities and positions on particle level makes it a valuable tool for understanding bulk material behavior. Normally, a (high) number of physical prototypes are required for design improvements. Nevertheless, these prototypes can now be made virtual and analyzed accordingly, saving a lot of time and resources. [27]

Calibrating the material model used is one of the important parts of doing a DEM study. The procedure could be time intensive and require physical experiments to obtain material characteristics for material model input settings. In case a material model should represent a real bulk material in practice, calibration is key. Moreover, it is important that DEM simulations should be carefully validated with real-world experiments in case design improvement or optimization is aimed for. Validation makes sure the simulation represents the physical system (at a predefined accuracy).

Despite the fact that developments in computer technology have led to an increase in available computational power, still it is not enough to capture realistic amounts, sizes and shapes of particles in many industrial applications. To deal with this disadvantage, one could simplify the simulation by using spherical particles, consulting simpler contact models, decrease of normal/tangential stiffness, increasing the particle size, decreasing number of particles and/or using periodic boundaries. [27]

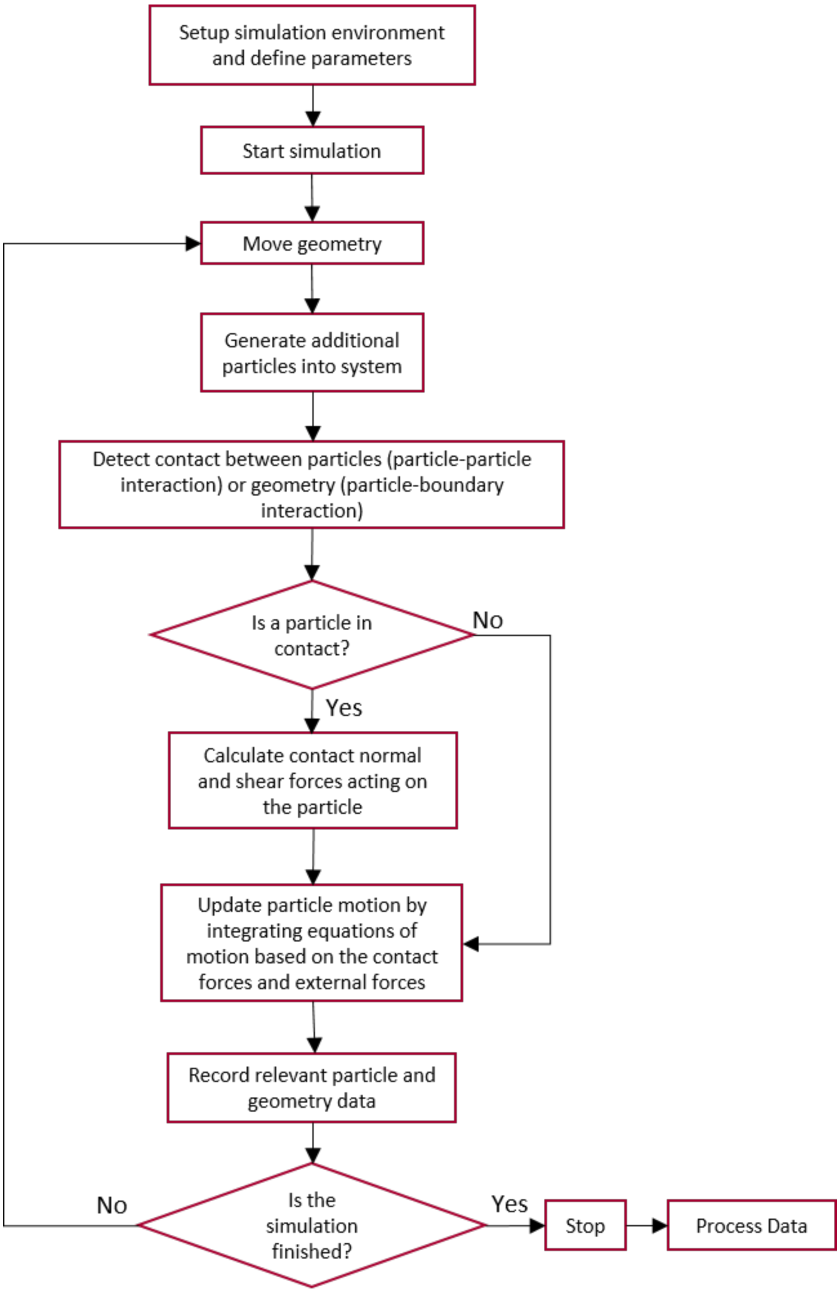

Figure 3.4: Flow chart of the DEM algorithm steps. Reprinted from [27] and adjusted.

To simulate non-spherical particles, different models like polyhedral ellipses, ellipsoids or polygons exist. However, modeling non-spherical particles require more sophisticated contact models and indirectly increases computation time. Also, so called multi-sphere method where spheres are rigidly connected to mimic realistic shapes is a possibility considering particle morphology. This method ensures computational efficiency for contact detection and force calculation. Regarding multi-sphere method for modeling particle shape, the drawback is an increase in computational memory. [44]

3.2. Simulation model setup

This section present the current system. In particular, the geometry model that will represent the double shaft paddle mixer will be discussed in Section 3.2.1, and the material model characteristics in Section 3.2.2. Thereafter, the contact model will be explained in Section 3.2.3. Last of all, the simulation strategy followed will be explained in Section 3.2.4. The commercial software EDEM™ is used to construct the simulation model.

3.2.1. Geometry model

The system under investigation is a 175L batch-type, double shaft paddle mixer engineered by the company Dinnissen. This mixer type contains two horizontally positioned, counter-rotating impellers in a double teardrop-shaped chamber. In total, each impeller consists of 7 paddle pairs welded equally spaced onto impeller shafts, in an alternate 90-degree arrangement. Moreover, 6 out of 7 paddle pairs are positioned under a 45°-angle compared to the shaft. As already described in Chapter 2, the angled paddles causing both radial and axial mixing mechanisms in the paddle mixer under investigation. To avoid accumulation in the corners of the mixing chamber, the last paddle pair is positioned under a -15°-angle and functions as 'transfer' paddles. To clarify, the paddle pair at the outermost front left and back right are transfer paddles (Figure 3.8). To avoid collisions between the paddles of shaft1 and shaft2, a phase angle of 45° is applied between the two shafts (Figure 3.6).

In Figure 3.5 and Figure 3.6, a coordinate system is presented in the lower left corner. In addition to these x, y and z directions a front/back/side orientation is given to the system. In next chapters these view definitions will be used for spatial designation.

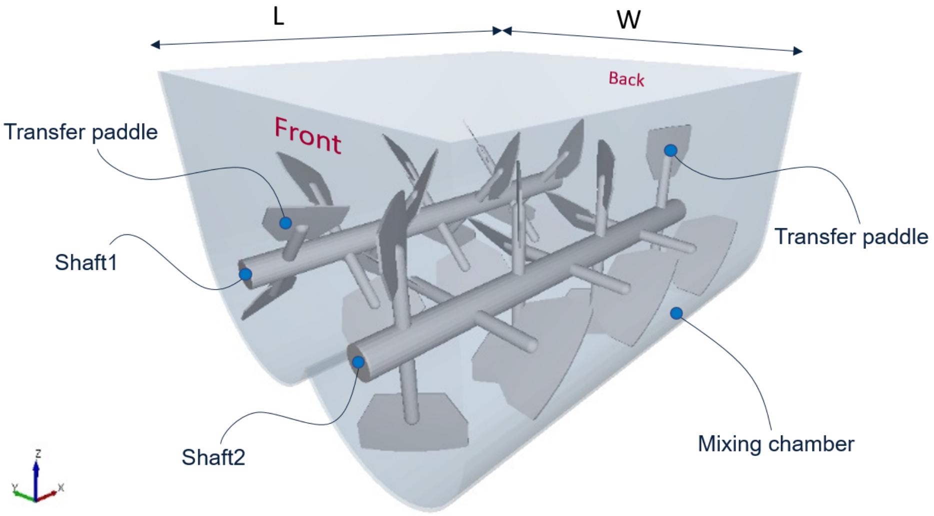

Figure 3.5: Isometric view of the double shaft paddle mixer with names and dimensions.

The configuration of the two shafts are positioned in such a way the material is transported axially besides the radial mixing mechanism [29], but they are in fact identical. Therefore, only shaft2 is highlighted in Figure 3.7 and Figure 3.8. The right side view and top view clearly shows the 45° angled paddles and -15° angled transfer paddles.

In Figure 3.9, both the normal paddle and the transfer paddle are depicted. The difference in paddle size is caused by the desire for an equal projected surface area when the paddles are welded under their respective angles in radial direction. In Table 3.1 all dimensional values are presented concerning the geometry of the system.

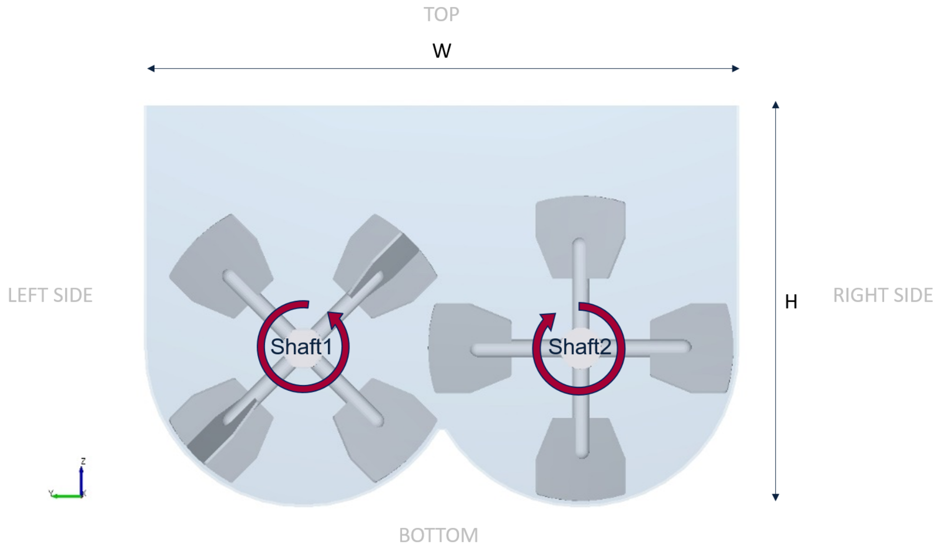

Figure 3.6: Front view of a double shaft paddle mixer with rotational directions of shafts.

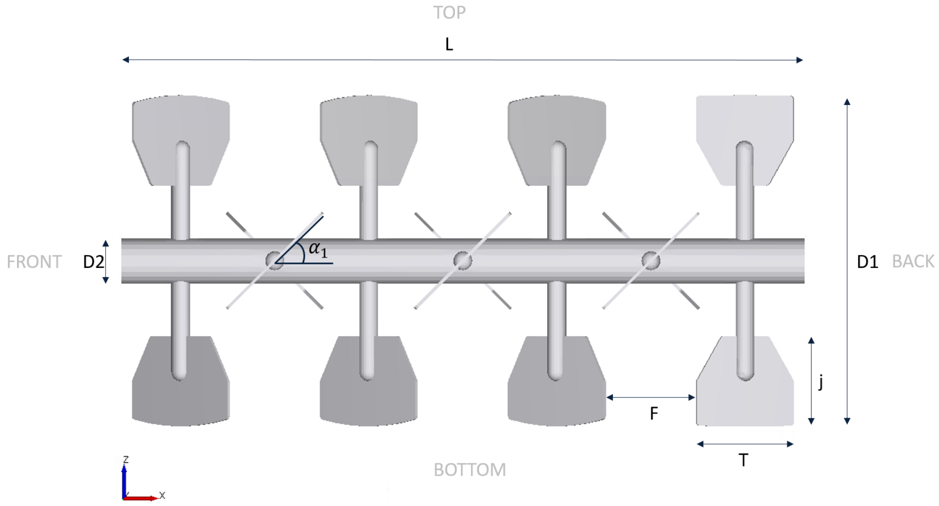

Figure 3.7: Right side view of shaft2 with dimensions.

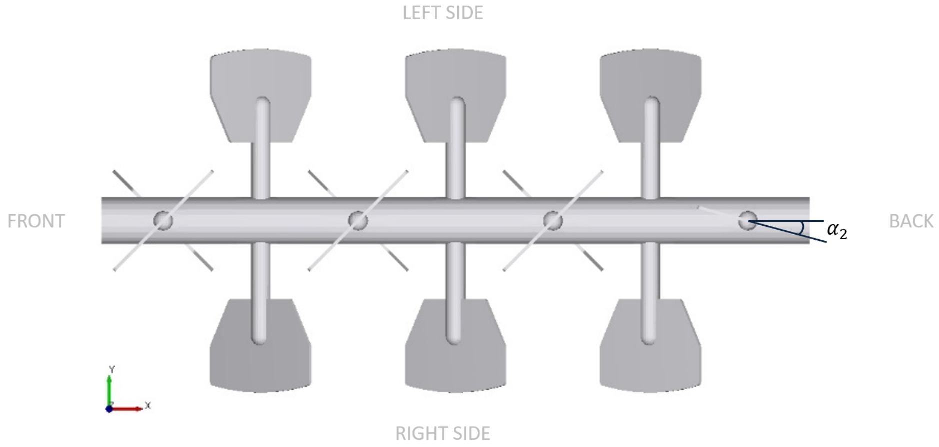

Figure 3.8: Top view of shaft2 with paddle mixer angle indicated.

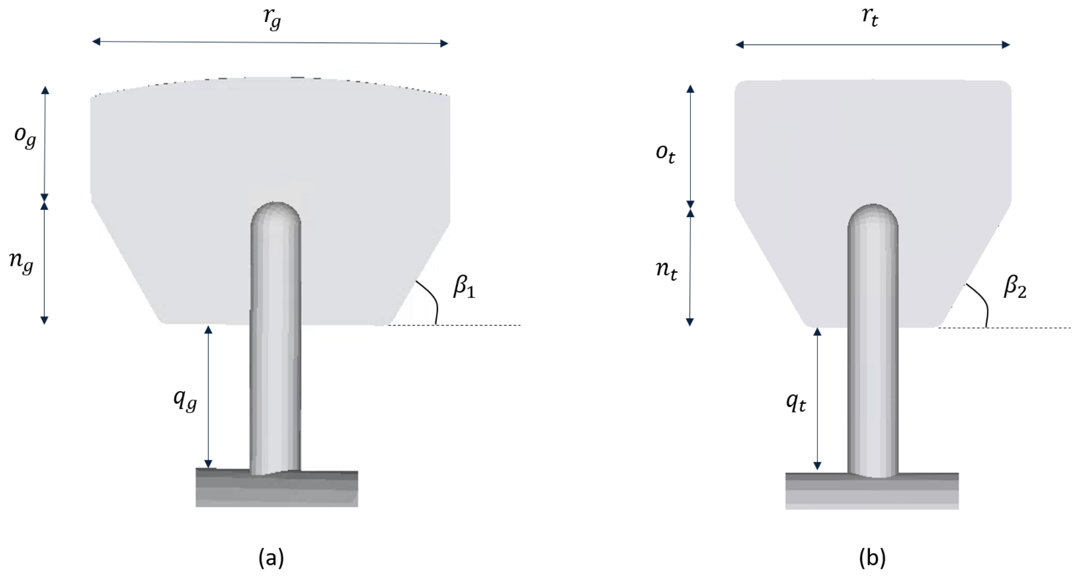

Figure 3.9: (a) General paddle and (b) transfer paddle of the paddle mixer.

Table 3.1: Dimensional values of geometric parts.

Parameter	Unit	Value	Parameter	Unit	Value
L	mm	900	n_g	mm	61.34
W	mm	850	q_g	mm	70
H	mm	570	r_t	mm	134
$D1$	mm	440	o_t	mm	58.66
$D2$	mm	60	n_t	mm	61.34
F	mm	120	q_t	mm	70
T	mm	130	α_1	°	45
j	mm	120	α_2	°	-15
r_g	mm	180	β_1	°	60
o_g	mm	58.66	β_2	°	60

3.2.2. Material model

In addition to the defined geometry in Section 3.2.1, a material model is the other part necessary to simulate the system. The material model used by Jadidi et al. [34] is adopted as starting point. The reasoning behind this choice is three-fold. Firstly, in this stage of research its about screening factors and understanding trends, not about calibrating the material model or optimizing a real-world problem. Second, chosen material model consists of perfect, free-flowing spherical glass beads with a particle size on millimeter level. Because the computation time is still one of the drawbacks in DEM simulations, a low computation time is desired. This particular material model is one of the best models one can choose with respect to computation time efficiency. Third, glass beads are easy to obtain which could be of value in case real-world experiments have to be conducted in future research. The particle properties are visualized in Table 3.2. Note that the particle diameter, particle density and shear modulus will be subjected to a sensitivity analysis which will be explained in Section 3.3.

The interaction properties are visualized in Table 3.3. Here, both the interaction between particles and particles with the inner chamber wall, paddles and shafts is considered.

The geometry properties are visualized in Table 3.4. Note that the geometry properties are not adopted from the paper of Jadidi et al. [34]. Dinnissen uses stainless steel for their double shaft paddle mixers mainly because of the high hygiene demands from the food and pharmaceutical industries [64].

Table 3.2: Adopted material properties from Jadidi et al. [34].

Parameter	Unit	Value
Particle diameter	mm	5
Particle density	$\mathrm{kg\,m^{-3}}$	2500
Poisson's ratio	-	0.3
Shear modulus	Pa	7e6

Table 3.3: Adopted interaction properties from Jadidi et al. [34].

	Particle-Particle	Particle-Geometry
Coefficient of Restitution (CoR)	0.75	0.75
Coefficient of Static Friction (CoSF)	0.5	0.35
Coefficient of Dynamic Friction (CoDF)	0.01	0.005

Table 3.4: Geometry properties according to Dinnissen's double shaft paddle mixer.

Parameter	Unit	Value
Density	$\mathrm{kg\,m^{-3}}$	7850
Poisson's ratio	-	0.265
Shear modulus	Pa	7.4e10

3.2.3. Contact model

The contact model consists of a set of equations which estimate the contact forces between particles, as described in Section 3.2.3. In this research, the Hertz-Mindlin contact model was used to calculate the particle-particle and particle-geometry interaction contact forces.

Hertz-Mindlin contact model is a nonlinear model which comprises the theory of Hertz [30]. Hertz' theory suggested a displacement - force relationship in the normal direction to describe the elastic contact between two spheres. The actual contact model is developed in the year 1953 by Mindlin and Deresiewicz [47]. They added the effects of tangential force-displacement for elastic spheres under frictional contact. [38]

According to literature, it is the most popular DEM contact model for free-flowing elastic granular material. The major difference with the LSD contact model is its non-linearity; The elastic terms are non-linear and the damping term is a function of velocity and displacement [27]. Thus, it is assumed the Hertz-Mindlin contact model is most suitable for the free-flowing, spherical glass beads.

In Figure 3.10 the rheological schematic is shown for the contact model for both particle-particle interaction and particle-geometry interaction.

The normal component of the contact force between particle i and j can be calculated by Equation 3.7.

$$F_{n,ij} = k_n \cdot \delta_{n,ij}^{\frac{3}{2}} + C_n \cdot \delta'_{n,ij} \tag{3.7}$$

$$k_n = \frac{4}{3} \cdot E^* \cdot \sqrt{R^*} \tag{3.8}$$

$$C_n = -2 \cdot \sqrt{\frac{5}{6}} \cdot \zeta \cdot \sqrt{m^*} \tag{3.9}$$

$$\frac{1}{E^*} = \frac{(1-\nu_i^2)}{E_i} + \frac{(1-\nu_j^2)}{E_j} \tag{3.10}$$

$$R^* = \frac{1}{\frac{1}{R_i} + \frac{1}{R_j}} \tag{3.11}$$

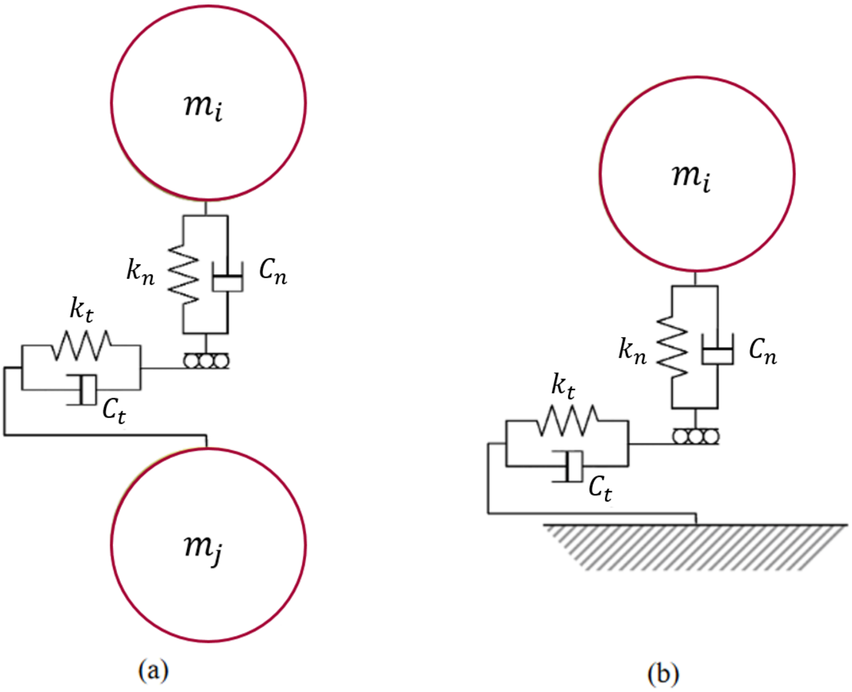

Figure 3.10: Graphical representation of Hertz-Mindlin contact model. (a) Particle-particle interaction and (b) Particle-geometry interaction. Reprinted from [27].

$$m^* = \frac{m_i m_j}{m_i + m_j} \tag{3.12}$$

$$\zeta = \frac{ln(C_R)}{\sqrt{ln^2(C_R) + \pi^2}} \tag{3.13}$$

where

$F_{n,ij}$ is the normal component of the contact force between particle i and j

k_n is the normal contact stiffness coefficient

E^* is the equivalent Young's modulus

R^* is the equivalent radius

$\delta_{n,ij}$ is the normal overlap between particle i and j

C_n is the normal contact damping coefficient

$\delta'_{n,ij}$ is the normal velocity between particle i and j

E is the Young's modulus

ν is the Poisson's ratio

R_i is the radius of particle i

m^* is the equivalent mass

m_i is the mass of particle i

ζ is the damping coefficient

C_R is the Coefficient of Restitution (CoR)

The tangential component of the contact force between particle i and j can be calculated by Equation 3.14.

$$F_{t,ij} = k_t \cdot \delta_{t,ij} + C_t \cdot \delta'_{t,ij} \tag{3.14}$$

$$k_t = 8 \cdot G^* \cdot \sqrt{R^* \cdot \delta_{n,ij}} \tag{3.15}$$

$$C_t = -2 \cdot \sqrt{\frac{5}{6}} \cdot \zeta \cdot \sqrt{m^*} \tag{3.16}$$

$$\frac{1}{G^*} = \frac{(2 - \nu_i)}{G_i} + \frac{(2 - \nu_j)}{G_j} \tag{3.17}$$

where

$F_{t,ij}$ is the tangential component of the contact force between particle i and j

k_t is the tangential contact stiffness coefficient

$\delta_{t,ij}$ is the tangential overlap between particle i and j

C_t is the tangential contact damping coefficient

$\delta'_{t,ij}$ is the tangential velocity between particle i and j

G^* is the equivalent shear modulus

G is the shear modulus

R^* is the equivalent radius

3.2.4. Reference case

The reference case used for the experimental simulation plan is explained in this section. Two different processes are distinguished; filling and mixing. During the filling process particles are generated according to the characteristics as shown in Table 3.5. The parameters are explained in detail in Chapter 4. In Section 3.2.4.1 the filling process is explained. After the filling process, the two mixture components will be mixed according to the output of the filling process (Section 3.2.4.2).

3.2.4.1. Filling process

The filling process is an important part of the research because the outcome will be used as starting point for the mixing process. Here, all material properties, operational conditions (excluding impeller rotational speed) and geometry are defined.

First of all, before the paddle mixer can start mixing the granular material, the chamber should be filled with particles. In practice, the filling procedure of the mixer differs from client to client, highly dependent on mixture characteristics like material types, mixture composition and number of components. Therefore, the filling process can be seen as an important part of the simulation strategy whereby the correct configuration is determined. This research focuses on binary mixtures as explained in Section 1.3, so two components are generated. *The red particles represent component 1 (or sometimes referred to as particle 1) and the blue particles represent component 2 (or particle 2).*

In the EDEM™ software, a factory can be utilized to generate particles. Two types of factories are available, a dynamic one and a static one. In the former, the particles will be generated over time up to a certain mass or number of particles. In case of the latter option, all particles are generated at one particular time step.

To evaluate which factory is most suitable for the filling process, both a dynamic factory and static factory for particle generation is analyzed. The KPI in this process is the total computation time required to run one simulation. It is desired to minimize the computation time of the filling process as much as possible, to ensure its contribution to the total computation time (consisting of both filling process and

Table 3.5: Characteristics of reference case.

Parameter	Unit	Value
Diameter particle 1 $d_{p,1}$	mm	10
Diameter particle 2 $d_{p,2}$	mm	5
Density particle 1 $\rho_{p,1}$	$\mathrm{kg\,m^{-3}}$	2500
Density particle 2 $\rho_{p,2}$	$\mathrm{kg\,m^{-3}}$	357
Composition c	-	80/20
Initial filling pattern p	-	Front-Back
Fill level e	%	100
Impeller rotational speed f	rpm	60
Paddle size g	-	1.0 (Original, Figure 3.9)
Paddle angle α_1	°	45
Paddle number i	-	14
Number of particle 1	-	149,427
Number of particle 2	-	298,855
Total number of particles	-	448,282

Table 3.6: Computation time and simulation time (real time) of the filling procedure for a dynamic factory and static factory.

Factory type	Computation time	Simulation time
Dynamic	48 minutes	10 seconds
Static	24 minutes	4 seconds

the actual mixing process) is small. The filling process is an important part of the research, but it is not the main focus.

According to Table 3.6, filling the mixing chamber with static or dynamic factory takes approximately an equal amount of computation time in case the same simulation (real) time is considered. However, the static factory only needs half of the simulation time to get the mixing chamber filled. Furthermore, because of the static factory's simplicity, this type of factory is chosen as filling method. In Figure 3.11, an illustration is given of the filling process with a static factory.

When a filling process simulation is finished, a check is executed on the number of particles present in the mixing chamber for both components. Sometimes the particle generation input does not always align with the actual outcome of generated particles in the simulation.

3.2.4.2. Mixing process

The mixing process is the second part of the two-fold simulation strategy. After the system is configured with a certain material and geometry, next step is to start mixing. In practice, a mixing time of 30-60 seconds is enough to obtain a desired homogeneity irrespective of the industry sector (pharmaceutical, food, feed etc.). Considering this time span and the computational limits of DEM simulation, a total simulation time of 30 seconds is chosen. It is expected this time length is broad enough to observe possible trends coming out of the experimental simulation plan.

The impeller rotational speed is the only factor that will be varied in this part of the simulation strategy. All other factors are already defined in the filling process. Additionally, the rotational acceleration and deceleration of the shafts experienced in practice during the initial and final stage of mixing are not taken into account. The effect of these speed rates on the mixing patterns and mechanisms are considered insignificant for this research.

As already explained in Section 3.2.1, the mixing machine consists of two shafts and the mixing chamber. Normally, the machine is covered with a top plate during mixing to prevent the product from escaping. In the simulations concerning the mixing process, a simple top plate is added to the geometry. The top plate is not shown in Figure 3.5. In Figure 3.12, an illustration is given of the mixing process.

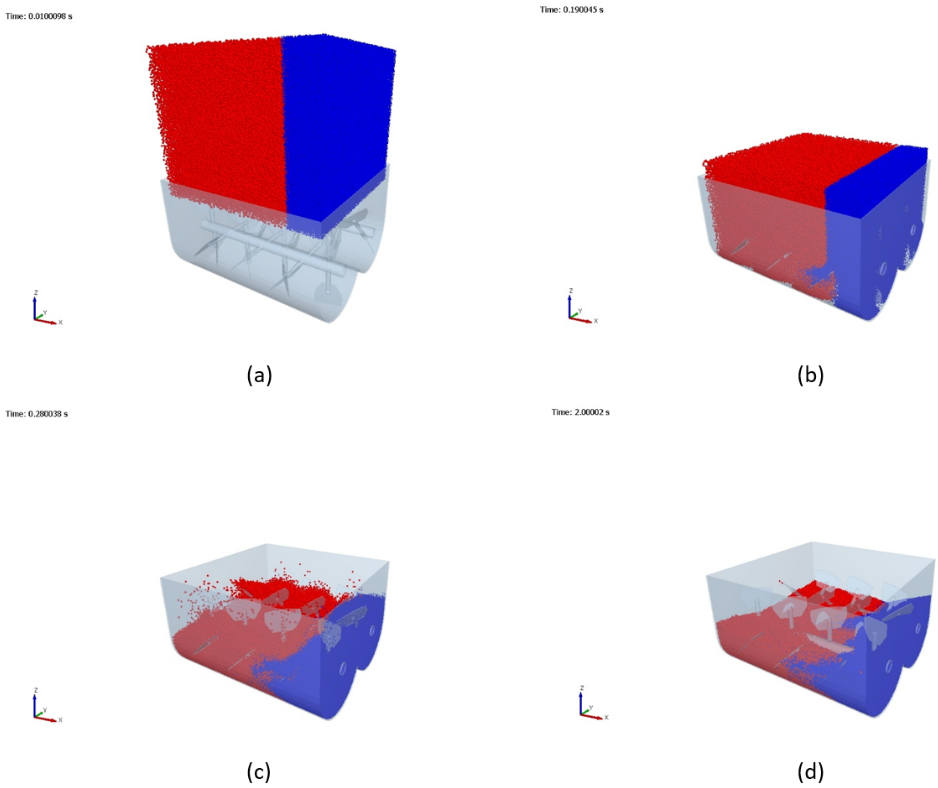

Figure 3.11: (a) Particles generated in a box located above the mixing chamber, (b) particles falling down caused by gravitational force and (c) particles settle in the mixing chamber and (d) the final steady-state particle bed

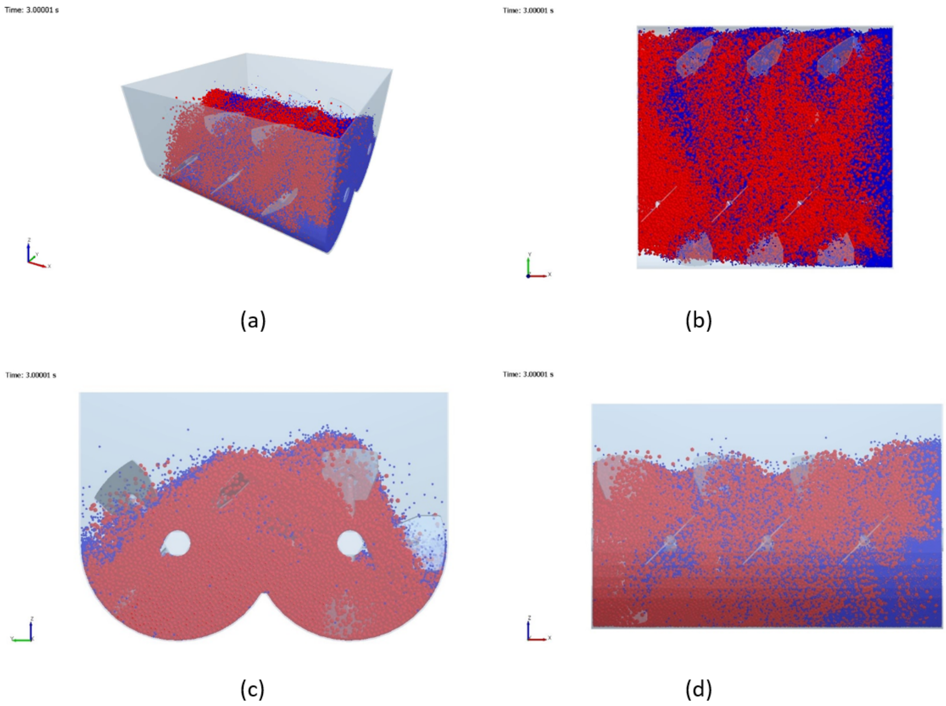

Figure 3.12: (a) Isometric view, (b) top view, (c) front view and (d) side view of a mixing process for an arbitrary configuration at time step t=3s.

3.3. Stability analysis

To ensure stability and time efficiency for all DEM simulations that are part of the experimental simulation plan, a 'worst-case scenario' simulation is generated. This simulation configuration should be set up in such a way that whatever comes out of the stability analysis, the output values can also be applied to all other simulations. Hereby, the stability and exhibition of realistic material behavior should not be compromised. Important to note here is that the stability analysis is executed on the filling process of the mixing chamber as described in Section 3.2.4.1. The result of the stability analysis will be used for both filling and mixing processes in the experimental simulation plan.

The 'worst-case scenario' simulation is designed with the independent factors in mind (as explained in Section 4.2) and the equation for calculating the Rayleigh time step as described in Section 3.1.2.4 (Equation 3.18). The latter describes the theoretical maximum time step of the granular system when the coordination number (number of contacts per particle) is greater than 1. The Rayleigh time step is dependent on the smallest particle radius, particle density, shear modulus and Poisson's ratio present in the simulation.

$$T_R = \frac{\pi R_{min} \left(\frac{\rho}{G}\right)^{1/2}}{0.1631\nu + 0.8766} \tag{3.18}$$

where:

T_R is the Rayleigh time step

R_{min} is the smallest particle radius

ρ_p is the particle density

G is the shear modulus

ν is the Poisson's ratio

By an increase in the Rayleigh time step also the actual simulation time step goes up, meaning less time steps are required. Consequently, fewer calculations will lead to a quicker run time.

According to Lommen et al. [41] and Marigo et al. [45], the shear modulus is one of the most influential parameters that affects the computational expenses of a simulation. Therefore, for the 'worst-case scenario' lowest particle radius R and particle density ρ_p based upon the factor levels as presented in Section 4.2 will be fixed. In Table 3.7 the input settings are presented. *Important to note here is that all other settings (besides the particle diameters and densities) are chosen arbitrarily as they do not affect the stability of the system.*

Consequently, a two-step stability analysis shown in Figure 3.13 is followed. As mentioned earlier the shear modulus has the highest effect on the computation time [41, 44]. The lower the shear modulus, the lower the total computation time of one simulation. Moreover, obviously increasing the actual time step would also reduce the total computation time. In Section 3.3.1 and Section 3.3.2, the two step approach will be explained in more detail. In Section 3.3.3, the outcome of the stability analysis will be pointed out in a concise manner.

3.3.1. Shear modulus

First of all, the first step of the simulation plan (Figure B.2 in Appendix B) is followed wherein the influence of the shear modulus on the simulation time and stability is investigated. A realistic shear modulus of glass beads is equal to approximately 3e10 Pa [49]. However, in Jadidi's paper [34] a shear modulus of 7e6 Pa was adopted. Probably, main reason for the discrepancy is a reduction in computation time. To investigate if the considerable reduction in magnitude can also be applied in this research, a simulation time reduction analysis will be executed. According to Janda et al. [36] a particle bed can be classified as stable with an energy ratio E_{kin}/E_{pot} of approximately 1e-6. Also, Ebrahimi et al. [22] defined an upper limit of 10e-7 J kinetic energy which comes down to approximately the same ratio. An energy ratio E_{kin}/E_{pot} = 1e-6 will be taken as upper limit in the analysis. After the mixing chamber is filled with particles, the particle bed may not exceed the specified upper limit. Furthermore, reduction of the shear modulus can lead to undesirable effects, like a change in granular material properties on both a macroscopic and microscopic level. Therefore, besides the evaluation of the

Table 3.7: Input settings for the stability analysis.

Parameter	Unit	Value
Diameter particle 1 $d_{p,1}$	mm	5
Diameter particle 2 $d_{p,2}$	mm	5
Density particle 1 $\rho_{p,1}$	$\mathrm{kg\,m^{-3}}$	2500
Density particle 2 $\rho_{p,2}$	$\mathrm{kg\,m^{-3}}$	125
Composition c	-	50/50
Initial filling pattern p	-	Top-Bottom
Fill level e	%	140
Impeller rotational speed f	rpm	60
Paddle size g	-	1.0
Paddle angle α_1	°	45
Paddle number i	-	14
Number of particle 1	-	1,045,990
Number of particle 2	-	1,045,990
Total number of particles	-	2,091,980

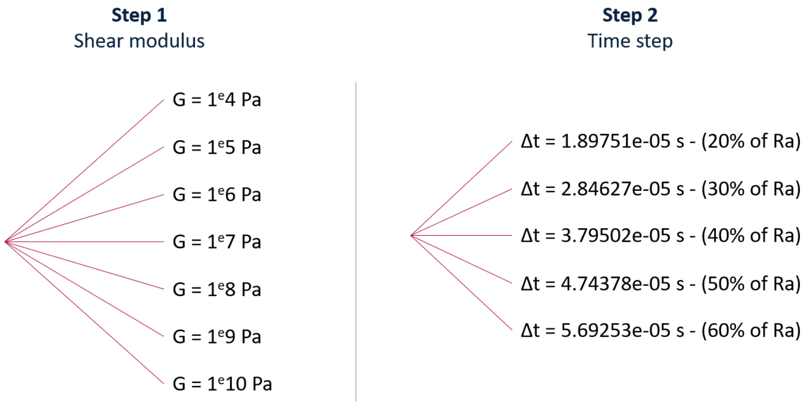

Figure 3.13: Two-step approach for simulation time reduction and stability analysis.

energy ratio of the particle bed also the voidage of the particle bed in the form of a boundary condition is assessed.

According to the simulation plan, the two KPIs are the total computation time per simulation and the ratio between the kinetic energy E_{kin} and the potential energy E_{pot}. Both KPIs are aimed to be minimized, the former for research feasibility and the latter for simulation stability.

In Figure 3.14, the computation time is plotted for each shear modulus. Results of the particle bed stability are visualized in Figure 3.15 and Figure 3.16.

The figures show the importance of the shear modulus during the computation time reduction process and stability analysis. With respect to Figure 3.14, it confirms the positive correlation between both parameters. Figure 3.16 comprises of all shear moduli except G=1e4 Pa at time period 2.5-3 seconds. At this stage in the filling process, the particle bed should become stationary and not exceeding an energy ratio of 1e-6. It can be concluded that all shear moduli except G=1e4 Pa and G=1e5 Pa suffice.

The only thing that is left is checking if the particle bed has the voidage that matches with typical voidage values of glass beads. After a particle is generated by the static factory, each particle will find its way downward driven by gravity till it hits the stationary geometry or already existing particle bed. After a certain amount of time, each particle will settle and should reach a steady-state. It is expected the particles are not deformed or broken after impact and will also not do so under their own weight. In other words, they are in-compressible. Main reason for this assumption is the free-flowing characteristic on a bulk level (partly) caused by a high shear modulus on particle level. Consequently,

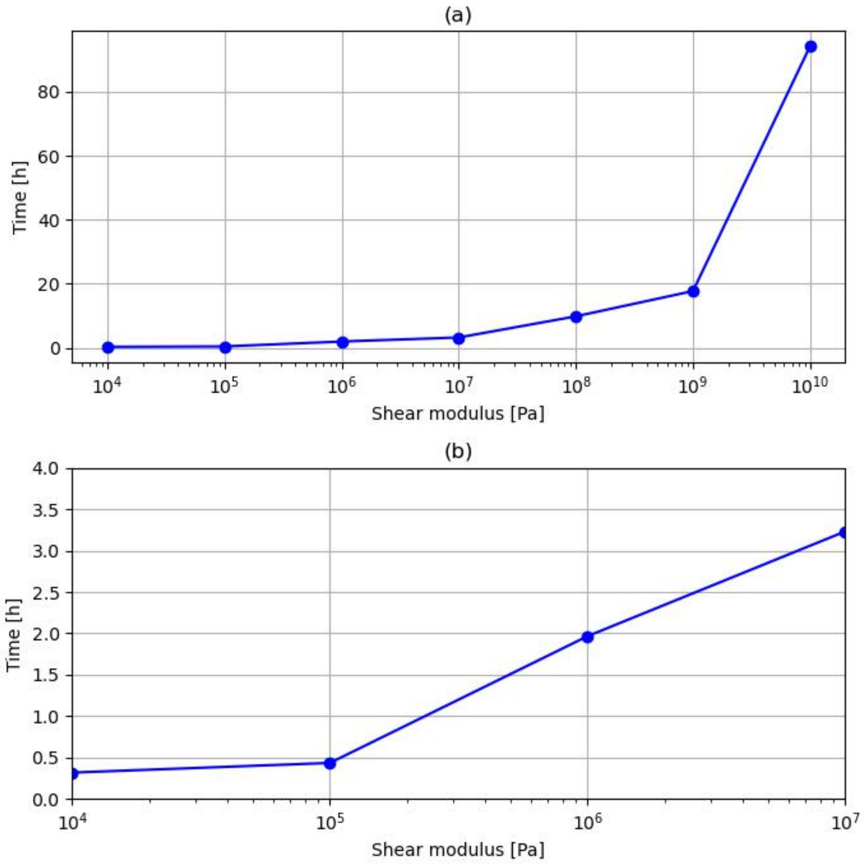

Figure 3.14: (a) Effect of all shear moduli on total computation time for one simulation and (b) effect of G=1e4 Pa up to G=1e7 Pa on total computation time for one simulation.

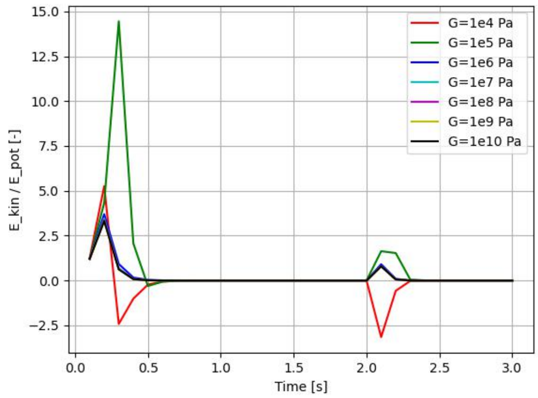

Figure 3.15: Stability analysis for filling process of the ’worst-scenario scenario’ simulation for all shear moduli.

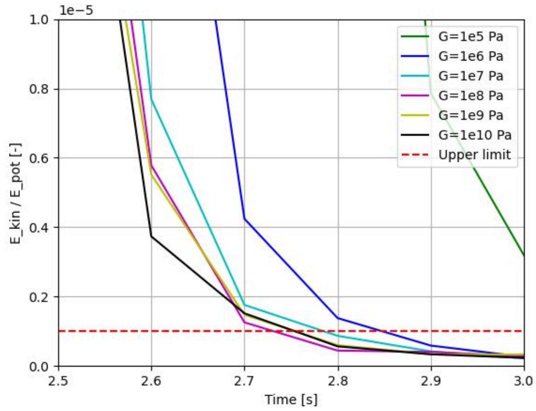

Figure 3.16: Stability analysis for filling process of the ’worst-scenario scenario’ simulation excluding G=1e4 Pa at time period 2.5-3s.

the state of compaction (or packing density) can be seen as a constant, independent of measurement location in the mixing chamber. A quantity to measure the state of compaction is the voidage, calculated by Equation 3.19.

$$Voidage = \frac{V_{voids}}{V_b} \times 100 \tag{3.19}$$

where

$Voidage$ represents percentage of empty space between particles

V_{voids} is total volume taken up by the voids

V_b is total volume of bulk material

Moreover, the way in which the particles are positioned compared to one another is completely arbitrary. The perfect or densest packing of hard, equally sized spheres takes up 74% of the total volume which comes down to a voidage of 26%. The random configuration of the particles could take a value up to 63.5% which comes down to a voidage of 36.5% [67].

A voidage of 40±5% is assumed to be acceptable based upon the voidage for a random configuration of particles (equal to 36.5%). The 40±5% voidage value will serve as a reference.

In Figure 3.17 different views indicate the strategically chosen locations of three equally sized bins of 30x30x30 mm to quickly assess the voidage of the particle bed. With particle sizes equal to 5 mm, the bin size is assumed to be large enough to represent the voidage accurately. The height difference is meant to observe any consolidation of the granular material by self-weight. Also, any wall effects on the granular material's voidage can be investigated with this particular bin configuration.

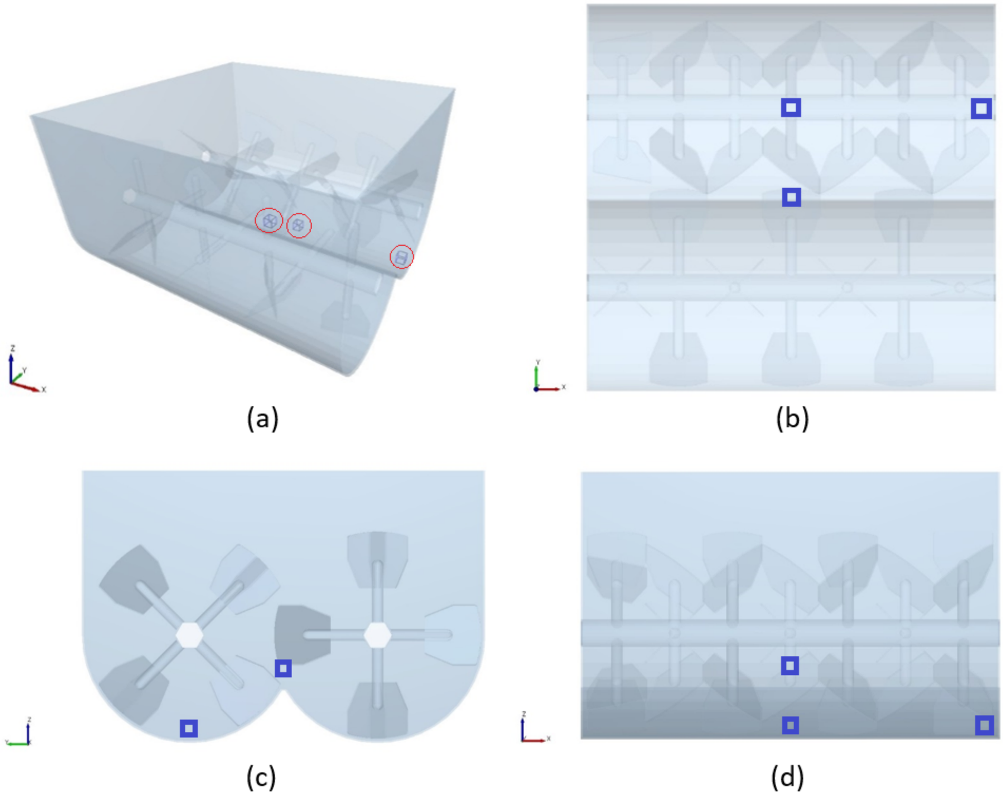

Figure 3.17: (a) Isometric view, (b) top view, (c) front view and (d) right side view to indicate bin locations for voidage analysis.

In Figure 3.18 the voidage over time for all shear moduli during the filling of the chamber is presented. The results show that both a shear modulus of G=1e4 Pa and G=1e5 Pa do not represent realistic voidage values when the particle bed reaches a steady-state between 2.5 and 3 seconds. As the benchmark voidage is equal to 40±5%, the lowest two investigated shear moduli are assessed unsuitable.

In conclusion, a **shear modulus of 1e6 Pa** is chosen as input parameter for all simulations. Both simulations with shear moduli 1e4 Pa and 1e5 Pa are evaluated unstable according to Figure 3.16. A similar approach is followed for the second step of this 2-step stability analysis approach where the time step will be the center of attention.

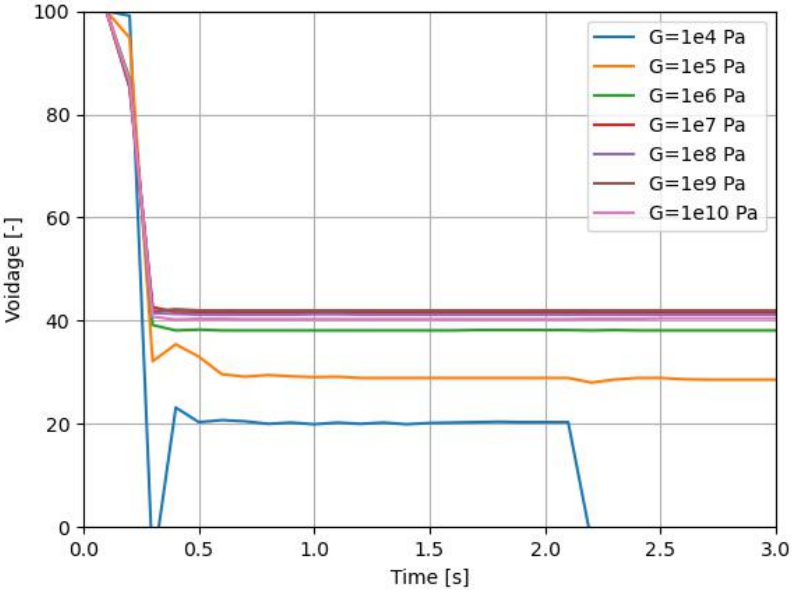

Figure 3.18: Effect of all shear moduli on voidage.

3.3.2. Time step

Secondly, as soon as a suitable shear modulus is found, the second step is increasing the time step. As Stephen Cole [17] also stated "selecting a suitable time step is critical". On the one hand, the time step should be small enough to ensure stability but on the other hand it should be as large as possible to reduce calculation time of the simulation. Figure B.3 in Appendix **??** shows the second step of the simulation plan.

In Figure 3.19 the computation time is plotted for each time step. As expected, the time required to run one simulation decreases with increasing time step.

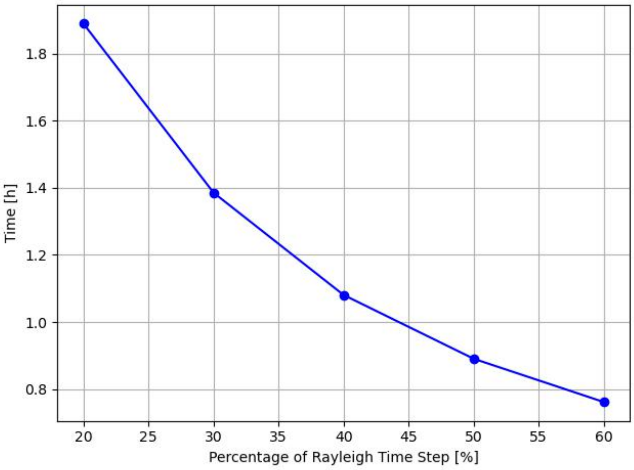

Figure 3.19: Effect of time step on total computation time for one simulation.

Next, the effect of the time step on the stability of the simulation is investigated. Results are showcased in Figure 3.20 and Figure 3.21. All time steps except '60% of the Rayleigh time step' do suffice.[1]

Lastly, the effect of the time step on the voidage is analyzed. In Figure 3.22 the results are presented. No matter what time step is chosen, the particle bed represents realistic behavior in terms of voidage.

---

[1] All plots are displayed in Figure 3.20 but lay very close to one another.

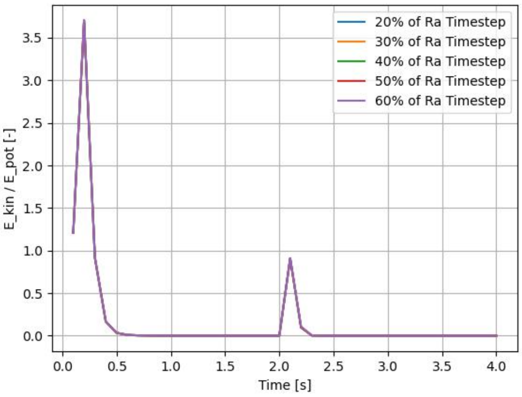

Figure 3.20: Stability analysis for filling process of the 'worst-scenario scenario' simulation for all time steps.

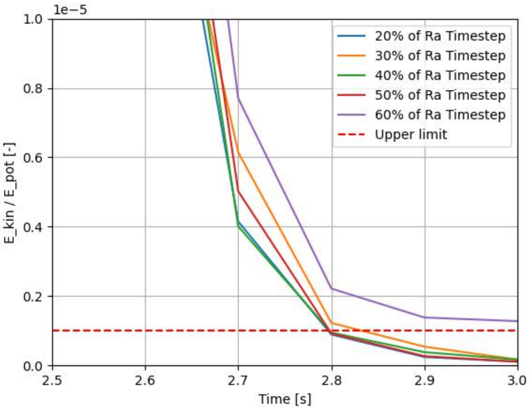

Figure 3.21: Stability analysis for filling process of the 'worst-scenario scenario' simulation for all time steps at time period 2.5-3s.

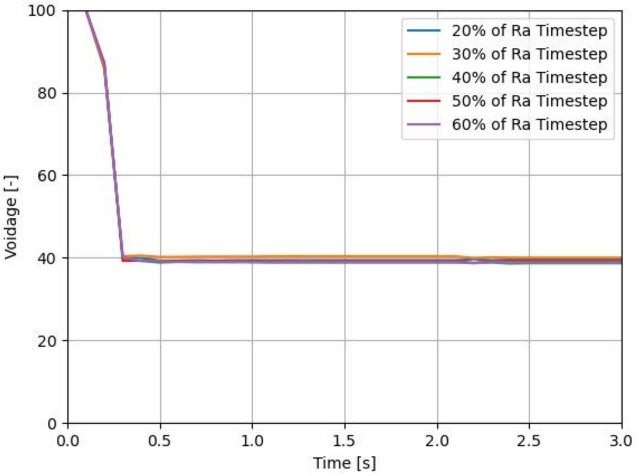

Figure 3.22: Effect of all time steps on voidage.

Finally, 50% of the Rayleigh time step is evaluated most suitable. That comes down to a **time step of 4.74378e-05 seconds** chosen as input parameter for all simulations.

3.3.3. Conclusion

In conclusion, the followed two-step approach led to values for the shear modulus (**1e6 Pa**) and time step (**4.74378e-5 s**) that will be used for the experiments in the experimental simulation plan. It is made sure all experiments that are part of the experimental simulation plan will be stable.

Besides quantitative analysis, also a qualitative assessment by means of visual observation is applied to both the filling and mixing process. The discrepancy in colour of both mixture components, made possible by the Analyst section of EDEM™, helps to confirm the desired initial filling pattern is successfully created. In addition, visual observations of the mixing process of the glass beads show expected mixing mechanisms and flow patterns.

4

Experimental simulation plan

This chapter is meant to explicate the followed experimental simulation plan for investigating the influence of selected factors on the mixing performance of the system. To optimize the system effectively, most influential factors that could influence the system should be identified. This can be done by a so called screening procedure that will be explained in more detail in Section 4.1. Thereafter, chosen factors will be explained in Section 4.2 substantiated with literature and company's interests, followed by a more detailed description of factor levels in Section 4.3. Thereafter, Section 4.4 will shine a light on how to assess the mixing performance of the system. Lastly, the experimental simulation plan is showcased in Section 4.5.

4.1. Screening design

In general, a system's output can be influenced by many factors that can be controlled or not controlled. (Figure 4.1). The uncontrollable ones with respect to practice can be dedicated to climatic conditions of where the paddle mixer is operating, causing variability to its performance. Nevertheless, the controllable factors can be varied during experiments. As this research only comprises of simulation experiments, uncontrollable factors can be neglected. [3]

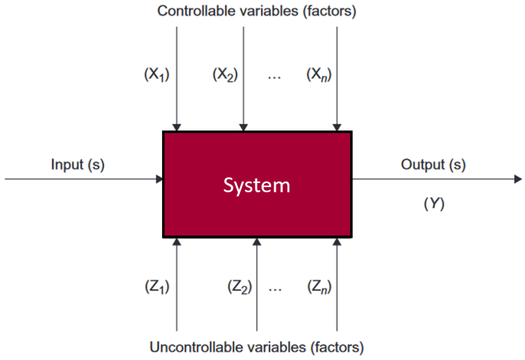

Figure 4.1: Abstraction of generic system model. Reprinted from [3] and adjusted.

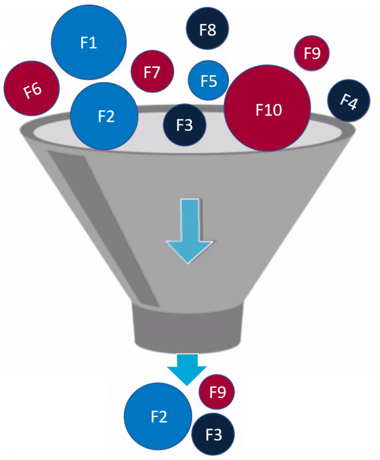

Figure 4.2: General visual representation of the screening method principle.

With respect to the controllable factors, it is of great importance to gain understanding of which factors have a high influence on the system's output and which factors do not. To optimize a system's output effectively and efficiently, focus should lay on most influential factors. A screening-like experimental simulation plan helps to concentrate on process improvement efforts on the few most important factors. Graphical representation of a screening procedure is shown in Figure 4.2.

Different kinds of screening procedures do exist like the One Factor At a Time (OFAT), the Placket-Burman (PB) or Definitive Screening Design (DSD) [4]. The PB and DSD screening Design of Experiments (DoE) are based upon statistics. The OFAT approach is examined most suitable to investigate the selected factors. In Table 4.1, both advantages and disadvantages of OFAT are shown. Because research on a relatively high number of factors (nine in total) could become cluttered, simplicity of the experimental simulation plan is key. Generated results should be easy to understand. Therefore, the decisive factor is the ability to evaluate the particle bed in a qualitative way. It is desired to understand mixing mechanisms and flow patterns, preferably by visual observations of the particle bed. Because multiple factors will be varied for one simulation with respect to the statistics-based methods like the PB and DSD, it will be harder to observe what factor is responsible for the system's output for the simulation of interest. Additionally, as research on this particular mixing application is scarce, results generated by the OFAT experimental simulation plan are assumed to be a good starting point for further research.

However, the OFAT approach does also has drawbacks. A relatively high number of runs are required, no interactions between factors will be caught and confounding effects will occur. Drawn conclusions about investigated factors are only valid for all other factor values fixed at their center point values (column '0' in Table 4.2).

Table 4.1: Advantages and disadvantages of the One Factor at a Time (OFAT) approach for particular situation [4].

Advantages	Disadvantages
Relatively simple method	No interactions between factors
No external software required to built DoE	High number of runs
Qualitative analysis of main effect factor possible	Confounding effects

4.2. Factors

Most influential factors on the mixing performance of the double-shaft paddle mixer are currently unknown. The identified factors that will be investigated in this research can be subdivided in three categories. The first category is related to the material which is by nature versatile. In practice, the mix components are determined by the customer. The operational conditions of the paddle mixer represent the second category. Compared to the material category, factors in this category can be adjusted easily before mixing a new batch. Ultimately, the geometrical factors of the system like the mixing chamber shape or paddle dimensions are. These factors can also be adjusted however not that effortless compared to the second category. In case geometrical changes are desired it should be implemented in the manufacturing process already. A complete overview of selected factors in respective categories is shown in Figure 4.3. Reasons to include selected factors will be explained in coming paragraphs.

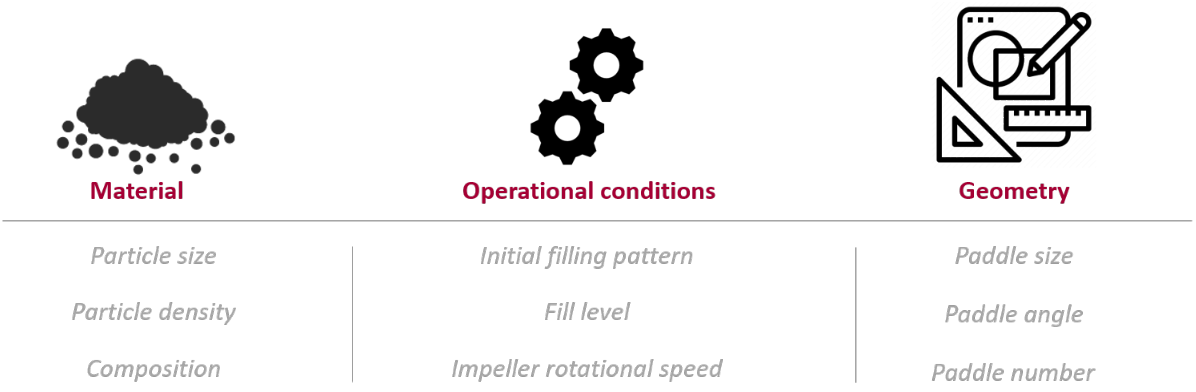

Figure 4.3: Overview of selected factors within corresponding category.

Particle size

First material factor is the particle size. Multiple researchers have investigated the effect of particle size on the mixing performance. Not only with respect to paddle mixers, but also other types of mixing applications like bladed mixers, rotating drums and plowshare mixers [1, 2, 14, 28, 73]. For example, Halidan et al. [28] found that for a bladed mixer there is an optimum small-to-large particle size ratio for a particular volume fraction and particle density ratio that can provide the maximum mixing index. Thus, research popularity of poly-disperse mixtures has led to the inclusion of particle size as material factor in this research.

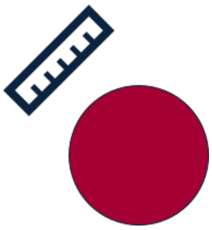

Particle density

Second material factor is the particle density. Despite the fact this material factor has not (yet) been part of research related to paddle mixers, it is still an important one to consider. As explained in Section 2.1.3, particle density differences can cause undesired segregation effects. The significance of particle density in relation to mixing is underlined in a number of scientific publications [14, 28, 73].

Composition

The last material factor is composition (mass/volume/number ratio between the two components). In 2015, Shenoy et al. [61] investigated (among other domains) the effect of composition on the mixing performance of a custom-built double shaft paddle mixer. This is the only paper discovered to be related to a paddle mixer that investigate composition. Nevertheless, composition is ought to be of importance as the paper concludes the mixture quality is affected by this factor.

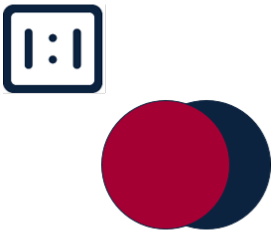

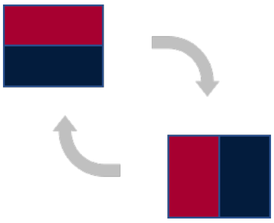

Initial filling pattern

The first operational condition identified for this research is the initial filling pattern which tells something about the way components are oriented compared to one another. Recently, Jadidi et al. [34] investigated the effect of Top-bottom, Side-by-Side and Front-Back initial filling patterns on the mixing performance of a double shaft paddle mixer. The paddle mixer in respective research has quite some similarities with the paddle mixer in this research. However, one major difference is the paddle configuration in Jadidi's paper with 0°-angle, rectangular paddles. Aforementioned discrepancy is the main reason to include the initial filling pattern as one of the three operational condition factors. Besides, research on other mixing applications has shown significance of the initial filling pattern as well [2, 26].

Fill level

The fill level is the second factor belonging to the operational condition category. This factor is also investigated by Jadidi et al. [34]. The same reasoning holds for the fill level; discrepancy in paddle configuration of the paddle mixer investigated by Jadidi et al. had led to inclusion of the fill level as second factor belonging to the operational condition category. In addition, researchers that investigated the effect of initial filling pattern on mixing performance of a plowshare mixer and ribbon mixer also included fill level [2, 26].

Impeller rotational speed

The last factor belonging to the operational conditions is the impeller rotational speed. This is the third factor investigated by the research group Jadidi et al. [34]. Also, Zhou et al. [73], Alian et al. [2] and Golshan et al. [26] investigated the impeller rotational speed on other mix applications. Besides the aforementioned scientific relevance, the company is also interested in this particular factor because the speed can be easily adapted in practice.

Paddle size

In consultation with the company, the size of the paddle is one of the geometric factors. Here, the effective paddle surface is meant with the paddle size. It is assumed that the moving surface of the paddle through the particle bed hereby relocating the material will influence the mix mechanisms and indirectly the mixing performance of the system.

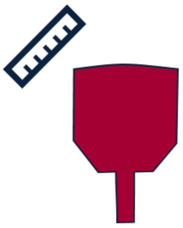

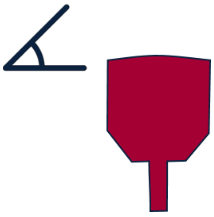

Paddle angle

The second factor belonging to the geometry category is the paddle angle. As shown in Chapter 3, the paddles in this particular double shaft paddle mixer are positioned under an angle of 45° compared to the shaft (with the exception of the transfer paddles). It is believed that the paddle angle would affect the mixing performance of the system. Main reason to substantiate this thought is based upon research done by Ebrahimi et al. [21]. Ebrahimi et al. investigated the effect of impeller configuration on the mixing performance of a single shaft paddle mixer. Disparities in paddle angle showed a considerable impact on mixing performance.

Number of paddles

The number of paddles welded onto the shaft represents the last geometrical factor. As the rotating paddles cause the material to move from one place to another, more or less paddles should unarguably result in more or less transported material through the mixing chamber. Consequently, it is believed that the mixture quality would be affected because of this.

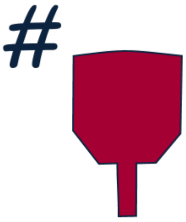

4.3. Factor levels

First of all, the number of levels are determined. To be able to grasp potential quadratic relationships between factor and KPI's, at least three data points are required. In this way, any curvature in the factor-KPI plots would indicate a non-linear relationship. Secondly, the level values are defined. An overview of all factor levels is shown in Table 4.2. Here level column '0' represent the reference case (or center-point). In next sections, an explanation for all factor levels is provided.

Table 4.2: Overview of all selected factors with corresponding levels for screening procedure.

Factor	Unit	-1	0	1
a - Particle size ratio	[-]	1	2	3
b - Particle density ratio	[-]	1	7	20
c - Composition	[-]	99/1	80/20	50/50
p - Initial filling pattern	[-]	TB	FB	SS
e - Fill level	[%]	40	100	140
f - Impeller rotational speed	[rpm]	40	60	80
g - Paddle size	[-]	0.67	1.00	1.50
α_1 - Paddle angle	[°]	30	45	60
i - Paddle number	[#]	7	14	28

Particle size ratio

The effect of the particle size will be investigated by the size ratio between the two components of the mixture (Equation 4.1). The particle size equal to 5 mm from Jadidi et al. [34] as explained in Section 3.2.2 is used as smallest particle diameter. Main reason is the simulation feasibility with respect to computation time. With respect to the upper extreme, the largest particle diameter from practice is approximately 15 mm. From here, the middle particle diameter is determine to be equal to 10 mm. The particle size ratios that follow from these three particle diameters are considered to be sufficient to explore its influence on the mixing performance.

$$a = \frac{d_{p,1}}{d_{p,2}} \tag{4.1}$$

where:

a is the particle size ratio

$d_{p,1}$ is the diameter of particle 1

$d_{p,2}$ is the diameter of particle 2

Particle density ratio

The effect of the particle density will be investigated by the particle density ratio between two components of the mixture (Equation 4.2). The particle density equal to 2500 $\mathrm{kg\,m^{-3}}$ from Jadidi et al. [34] as explained in Section 3.2.2 is used as largest particle density. Similar to the reasoning of the particle size is the simulation feasibility with respect to computation time key here. Moreover, in particle density ratios equal to 20 are encountered. Therefore, the particle densities 125 $\mathrm{kg\,m^{-3}}$, 357 $\mathrm{kg\,m^{-3}}$ and 2500 $\mathrm{kg\,m^{-3}}$ will be used to create particle density ratios of 20, 7 and 1.

$$b = \frac{\rho_{p,1}}{\rho_{p,2}} \tag{4.2}$$

where:

b is the particle density ratio

$\rho_{p,1}$ is the density of particle 1

$\rho_{p,2}$ is the density of particle 2

Composition

The effect of composition will be investigated by the total volume ratio between the two components of the mixture (Equation 4.3). The compositions 99/1, 80/20 and 50/50 are the three volume ratios subjected to the parametric analysis. It is assumed that these three values are sufficient to explore its influence on the mixing performance. In Figure 4.4 the three different compositions are shown.

$$c = \frac{V_{p,1}}{V_{p,2}} \tag{4.3}$$

where:

c is the composition

$V_{p,1}$ is the total volume of component 1

$V_{p,2}$ is the total volume of component 2

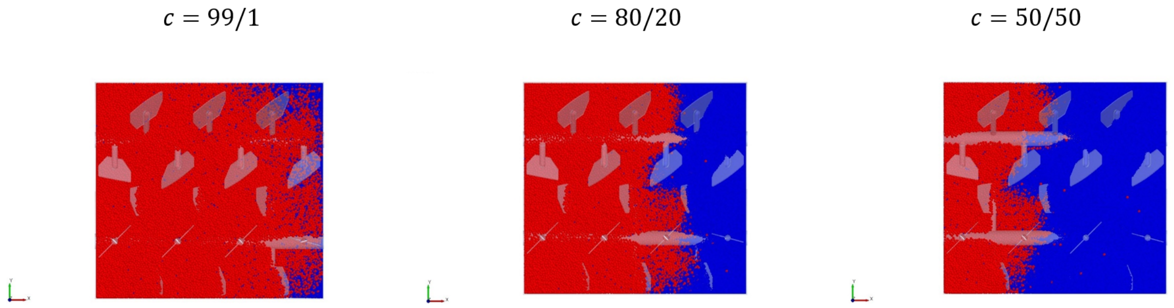
$c = 99/1$ $c = 80/20$ $c = 50/50$

Figure 4.4: Illustration of the three different compositions.

Initial filling pattern

In practice, there is not one systematic way of filling the mixing chamber with mixture components. To simplify the filling procedure, three different initial filling patterns are introduced: Top-Bottom (TB), Front-Back (FB) and Side-by-Side (SS). These patterns are based upon the published paper by Ebrahimi et al. [34]. In Figure 4.5 an illustration of the three different initial filling patterns is provided.

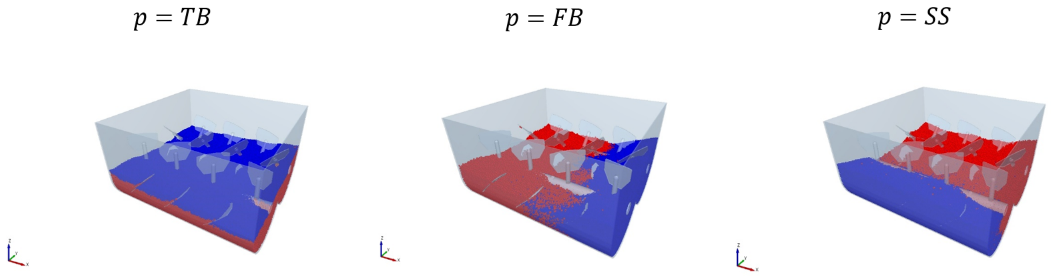
$p = TB$ $p = FB$ $p = SS$

Figure 4.5: Illustration of the three different initial filling patterns.

Fill level

The double shaft paddle mixer under investigation has a total volume of 175L. This volume is assumed to be 100% filled. From here, a lower level of 40% and an upper level of 140% is determined. The fill level of the mixing chamber is determined in consultation with the company. It is assumed that this factor range is sufficiently broad to explore its influence on the mixing performance. In Figure 4.6 an illustration of the three different fill levels is provided.

Impeller rotational speed

The impeller rotational speed both both shafts is equal to 60 rpm for the center-point simulation. The lower level value is equal to 40 rpm and the upper level equal to 80 rpm. The impeller rotational speed

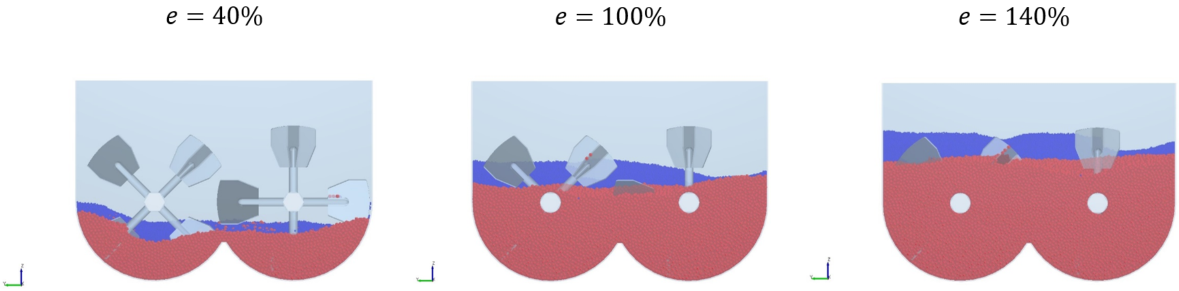
$e = 40\%$ $e = 100\%$ $e = 140\%$

Figure 4.6: Illustration of the three different fill levels.

of the shafts is determined in consultation with the company. It is assumed that this factor range is sufficiently broad to explore its influence on the mixing performance.

Paddle size

The paddle size in terms of effective surface currently used in the industrial paddle mixer under investigation is utilized as a benchmark. The lower level value is equal to 2/3 times the center-point value. And the upper level equal to 3/2 times the center-point value. The width of the most outer part of the paddle is kept the same for all three paddle sizes and material is removed or added from inside out, meaning closest to the shaft. The motivation is based upon the desire to ensure that the paddles' rotating ranges of motion are aligned, close to the inner wall of the chamber. An illustration is provided in Figure 4.7. The original paddle size of the transfer paddles is kept the same.

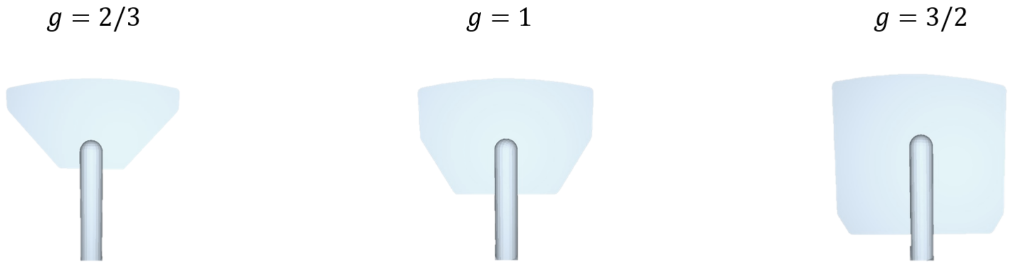
$g = 2/3$ $g = 1$ $g = 3/2$

Figure 4.7: Illustration of the three different paddle sizes.

Paddle angle

According to Jadidi et al. [34] causes a 0° paddle angle poor results, especially for a FB initial filling pattern. And, a paddle angle equal to 90° would probably perform even worse because no effective surface is present to relocate the granular material. With these two extremes in mind, it is chosen to set a lower level equal to 30° and an upper level equal to 60°. The current paddle angle is equal to 45°. In Figure 4.8 an illustration of the three different paddle angles is provided. The angle of the transfer paddles stays the same.

Paddle number

Current number of paddles is equal to 7 paddle pairs welded onto each shaft, thus a total number of 14 paddles. The lower level equals 7 paddles in total and the upper level equals 28 paddles in total. These amounts are determined after consultation with the company. In Figure 4.9 an illustration of the three different paddle numbers is provided.

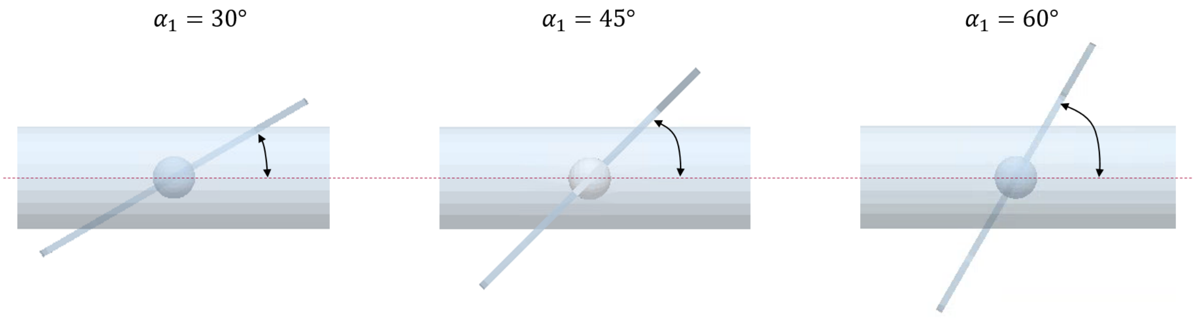

$\alpha_1 = 30°$ $\alpha_1 = 45°$ $\alpha_1 = 60°$

Figure 4.8: Illustration of the three different paddle angles.

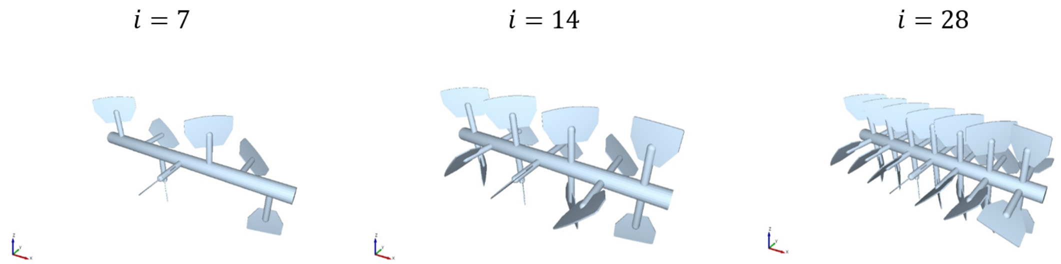

$i = 7$ $i = 14$ $i = 28$

Figure 4.9: Illustration of the three different paddle numbers.

4.4. Mixing performance assessment

In Figure 4.10, a graphical representation is presented where is shown which responses are evaluated both qualitatively and quantitatively. The Key Performance Indicators (KPI's) are further elaborated in Section 4.4.1. The qualitative responses are elaborated on in Section 4.4.2

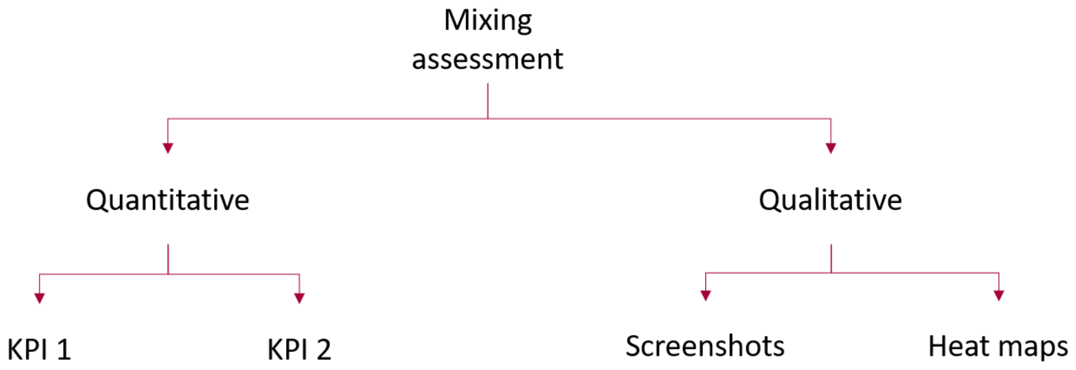

Figure 4.10: A graphical representation of investigated responses to determine the system's mixing performance.

4.4.1. Quantitative assessment

In this section, the mixing assessment in a quantitative manner is being described. Both KPI's from Figure 4.10 are described in Section 4.4.1.3 and will follow from Section 4.4.1.1 and Section 4.4.1.2.

4.4.1.1. Relative Standard Deviation (RSD)

To be able to assess the overall mixing performance of the system in a quantitative manner by means of KPI 1 and KPI 2, a so called mixing index is required. Typical characteristics for such an index are its mixing process independence, simplicity for determination and accurate representation of the final mixture quality [54]. Already in the year 1991, over 40 different mixing indices were available and this number is still growing [54]. The vast spectrum of various mixing indices originates from complexity of mixing processes. Every mixing application comes with its own set of criteria that needs to be satisfied. Consequently, different mixing indices are brought to the table that fits its purpose of respective application.

Mix quality assessment via a computational model like DEM is much easier compared to experimental methods. The latter often implies sampling on a limited number of locations in the particle bed concerning batch-type mix applications, often inaccessible from the outside. One could not simply take samples on hard-to-reach spots without disturbing the final product. Non-invasive methods like the DEM offer therefore a great solution. [16]

Still, selecting a suitable metric to assess the (final) mixture quality is a challenge due to the abundance of mixing indices available. To investigate which mixing index should be deployed that fits perfectly with the model of the double shaft paddle mixer characteristics, a Multi Criteria Decision Analysis (MCDA) is executed on a selection of mixing indices. In first section, a set of criteria is defined. Thereafter, a selection of mixing indices are compared to one another according to predefined criteria to evaluate its suitability.

As mentioned earlier, many mixing indices are available at present day. For this research, the selection as proposed by Bhalode et al. [10] has been assessed sufficient because of its broad and varied characteristics. A detailed overview of all mixing indices can be found in [10]. The classification of mixing indices as discussed in this paper indicate three categories: Variance-based, Distance-based and Contact-based (Figure 4.11).

Variance-based indices evaluate the concentration of tracer particles in a mixture. This category is highly dependent on the grid size of the system. A small grid size could overlook a sufficient mixture on a macro-scale level, while a coarse grid could miss micro-mixing effects. Furthermore, they can be used for real-time mixing measurement and quick evaluation. [10]

Moreover, the distance-based indices evaluate the distance between particles belonging to different mixture components to measure the mix quality of the (final) product. For most indices belonging to this category, computational effort to measure the location of each particle as a function of time is one of the major drawbacks. Moreover, they are grid independent and direction dependent. [10]

In case of contact-based indices, the contacts of a singular particle with neighboring particles is measured. They are easy and quick to calculate. Moreover, mixing systems where the granular material stays intact during mixing are typical applications that can be subjected to mixing indices belonging to this category. In other words, if particles separate from each other which is the case in fluidized beds/zones, measurements with contact-based indices become erroneous. [10]

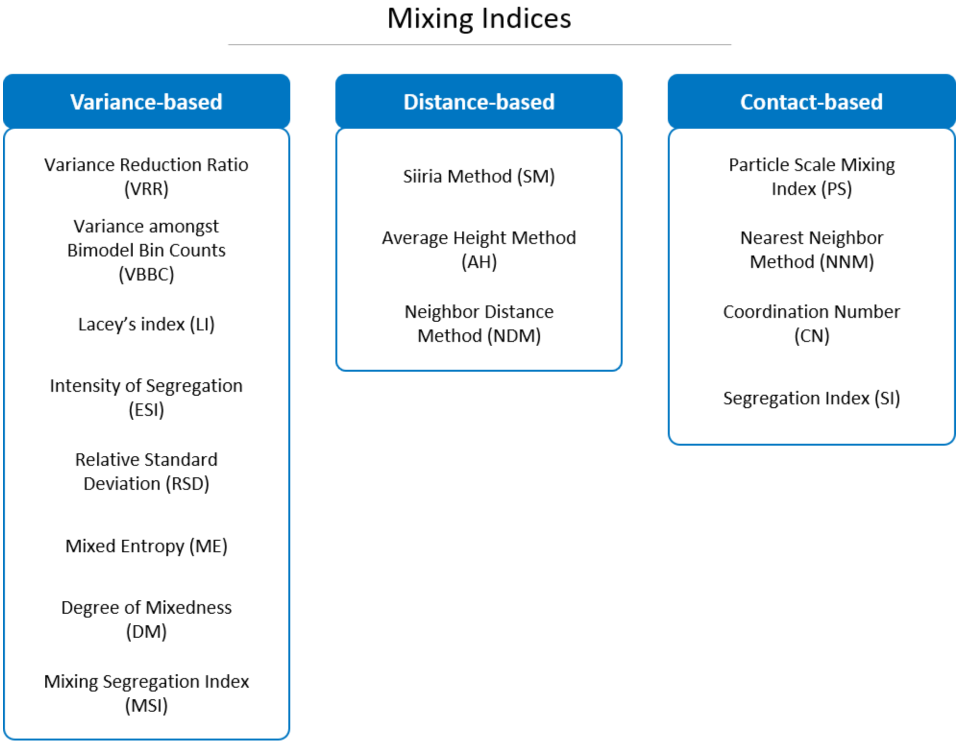

Figure 4.11: Mixing index classification. Reprinted from [10] and adjusted.

In conclusion, the distance-based and contact-based mixing indices will not be further evaluated in this analysis. The distance-based category comprise a high computational expense and cannot be utilized to assess a mixture in multiple directions. In addition, the diffusive nature of particles in the fluidized zone in the centre of the double shaft paddle mixer, where particles separate from each other, provoke in-applicability of contact-based mixing indices. Thus, only the variance-based mixing indices will be included in the MCDA.

To select the most suitable mixing index, four criteria are being set up as shown in Table 4.3. The criteria are based upon the paper published by Bhalode et al. [10], but reformulated to serve the needs of this research.

All the assumptions made during the mixing index analysis are listed below.

- No modifications of mixing indices are considered
- A computational approach (DEM) is followed to do mixing index analysis
- Only a small selection of all mixing indices available is analyzed.
- Derivate or correlated mixing indices with selected indices are not considered. For example, as elaborated on in [15], the Kramer's Mixing Index or LWB Mixing Index (Lacey, Weidenbaum and Bonilla) are derivatives of the Lacey's Index and therefore not taken into account.

Every mixing index belonging to the variance-based class are individually evaluated by means of a MCDA, visualized by Table 4.4. It can be concluded that all indices except the Mixing Segregation Index (MSI) are suitable mixing indices. As all mixing indices are suitable for the mix application under

Table 4.3: Decision criteria for mixing index analysis with a short explanation.

#	Criteria	Explanation
1	Computational complexity	The DEM simulations are time consuming and due to time constraints of the research, a brief mixing index assessment afterwards is desired. Moreover, the aim to conduct real-time mixing evaluation on multiple time periods is another argument why the computational complexity should be low.
2	Direction	To ensure mixing homogeneity of the final product, the mix quality has to be analyzed in all directions (x, y and z). Besides, it is expected both axial and radial mixing occurs in the double shaft paddle mixer according to Hassanpour et al. [29].
3	Size	One of the factors that will be varied during the screening design is the particle size ratio of the mixture. Thus, a size independent mixing index is required.
4	Parameter dependency	To simplify the search for an appropriate mixing index, the index should be independent of external parameters. Since, in this manner the extra computational efforts deciding for the correct external parameter values are avoided.

Table 4.4: Multi Criteria Decision Analysis (MCDA) on variance-based Mixing Indices ('+' means advantageous and '-' means disadvantageous for this particular application).

	Variance-based							
Criteria	**LI**	**RSD**	**VRR**	**VBBC**	**ESI**	**ME**	**DM**	**MSI**
1	+	+	+	+	+	+	+	+
2	+	+	+	+	+	+	+	+
3	+	+	+	+	+	+	+	-
4	+	+	+	+	+	+	+	+

investigation after evaluation, the Relative Standard Deviation (RSD) mixing index is chosen. The company is familiar with this particular index when determining mixture quality of a final product. To make sure the results are interpreted correctly, the index should be understood easily. Another reason to select this mixing index in particular is the utilization frequency in research papers related to paddle mixers [21, 22, 34]. It is believed by the author that an uniform statistical method generally improves understanding of findings coming from multiple scientific sources.

The RSD is a common mixing index deployed to assess the quality of a mixture. Another term called Coefficient of Variance (CoV) can also be found in literature, basically meaning the same. One can calculate this index by Equation 4.4 [10], tailored to the paddle mixer under investigation.

$$RSD = \frac{s}{M_2} \tag{4.4}$$

The standard deviation s can be calculated by Equation 4.5.

$$s = \sqrt{\frac{\sum_{i=1}^{Z} (M_{2,i} - M_2)^2}{Z - 1}} \tag{4.5}$$

where:

RSD is the mixing index Relative Standard Deviation

s is the standard deviation over all taken samples

M_2 is the average mass concentration of component 2 over all taken samples

$M_{2,i}$ is the mass concentration of component 2 in bin i

Z is the number of bins

As the composition of the 80/20 center point value is based upon volume, the mass concentration is determined by converting the volume fraction into a mass fraction.

4.4.1.2. RSD calculation

To assess the evolution of the mixing performance of the system by the RSD, a grid system is designed. This 3-dimensional grid spans out over the whole machine and consist of discrete elements called bins. The number of bins in x, y and z direction is dependent on mixture dimensions and particle diameter of the component(s).

Theoretically speaking, a RSD of 1 would mean the two mixture components are completely segregated. On the other hand, a RSD of 0 would mean the components are perfectly mixed. Ideally, the RSD over time should follow a global trend from high to low. More specific, as the bins would always capture the interface of a two-component mixture already a number of bins is filled with both components. Consequently, the RSD should begin from a value slightly lower than 1.0 and start decreasing the moment the shafts are beginning to rotate. Depending on the mixing configuration of the system, eventually the RSD should reach a steady-state value.

In relation to variations in bin sizes, the accuracy and reliability of the RSD value can be affected. A small bin size could result in inaccurate results caused by too few particles inside a bin. However, a bin that is too large would cause misconception of the RSD values because the effect of micro-mixing is not captured. It is desired to get a bin size as low as possible to showcase local differences in mass concentrations, besides the global mixing performance indicated by the RSD.

The settings of the simulations are presented in Table 4.5. The bin size should be designed based upon the largest particle diameter in the system [34]. Thus, simulation 3 (Table 4.8) is chosen as initial configuration. As no larger particles than d_p=15mm will be simulated during the screening design of experiments, this particular simulation is chosen. Upfront, its assumed the binned number of particles is sufficient to obtain accurate RSD results.

Table 4.5: Input settings for the grid system analysis.

Parameter	Unit	Value
Diameter particle 1 $d_{p,1}$	mm	15
Diameter particle 2 $d_{p,2}$	mm	5
Density particle 1 $\rho_{p,1}$	$\mathrm{kg\,m^{-3}}$	2500
Density particle 2 $\rho_{p,2}$	$\mathrm{kg\,m^{-3}}$	357
Composition c	-	80/20
Initial filling pattern p	-	Front-Back
Fill level e	%	100
Impeller rotational speed f	rpm	60
Paddle size g	-	1.0
Paddle angle α_1	°	45
Paddle number i	-	14
Number of particle 1	-	44,275
Number of particle 2	-	298,855
Total number of particles	-	343,130

To determine the grid size of the grid bin system, scientific papers related to both paddle mixers and other types of mixing applications in relation to DEM are consulted. A brief summary of a selection of reviewed papers is presented in Table 4.6.

The result presented in the fourth column in Table 4.6 called *Bin Size Factor* is built up from two terms. The first term is equal to the smallest length of the LxWxH expression as shown in the third column of Table 4.6. The second term is the maximum particle radius that is present in the simulations. Dividing the first term with the second term results in the *Bin Size Factor* as shown in the fourth column. In other words, this column presents multiples of the maximum particle diameter that will be present in the simulations.

Table 4.6: An overview of a selection of applications with corresponding grid bin systems.

Mixer type	Number of bins LxWxH [-]	Bin size LxWxH [mm]	Bin size factor	Source
Paddle mixer	28x28x16	19.3x20x20	4	[34]
Plowshare mixer	15x10x10	43x27x27	3.8	[2]
Horizontal rotating drum	25x70x70	1x12x12	1.9	[5]
Horizontal rotating drum	1x10x10	30x20x20	3.3	[14]
Horizontal rotating drum	1x10x10	200x40x40	2	[20]
Horizontal rotating drum	1x12x12	229x8.7x8.7	1.7	[1]
Vertical ribbon mixer	-	-	3	[26]
Intensive mixer	18x18x6	17.2x17.2x16.7	4.2	[8]

As shown in Table 4.6, the bin size is spread over a range of 1.7 up to 4.2 times the maximum particle size. However, Cleary et al. [16] mentioned a bin size of five times the average particle diameter to ensure statistical significance. To investigate what bin size is most suitable for the paddle mixer application, an experimental simulation plan is followed as shown in Appendix C, Figure C.1. The factors 4, 5 and 6 times the largest particle diameter are chosen based upon Table 4.6, the statement made by Cleary et al. [16] and the paper published by Jadidi et al. [34] where a suggestion is made to keep a bin size of greater than 4*d_p. It is of great importance that the grid system will be kept the same for all simulations, as the outcome of the RSD is grid dependent.

The results of the three different grid size systems are presented in Figure 4.12 and Table 4.7. All three graphs show the expected trend and they do not differ much besides a slight discrepancy in steady-state RSD values. What can also be observed is the RSD reaching a value of greater than 1. The wide spread in mass concentration values of component 2 over the evaluated bins causes an increase in RSD higher than 1. As the graph shows the expected trend after approx. 3.8 seconds, the part where the RSD exceeds a value of one is not considered.

Table 4.7: Analysis on grid system with number of bins, average number of particles in each cell and the RSD.

Bin size	Grid size	Bin number	Average number of particles in each bin	RSD (t=30s)
6*d_p	9x9x6	486	351	0.105
5*d_p	11x11x7	847	201	0.131
4*d_p	14x14x9	1764	97	0.167

To conclude, local differences in mass concentration of one of the components in x, y or z direction is one of the desired outputs of this research, besides the global mixture quality showcased by the RSD. Therefore, the bin size of 4*d_p is chosen for this research to also be able to capture micro-mixing effects in the particle bed (Figure 4.13). In addition, in simulations where the mass fraction of one of the components is relatively low, it could happen the number of particles present in the bins is too low to keep results statistically valid. In that case, further analysis is required.

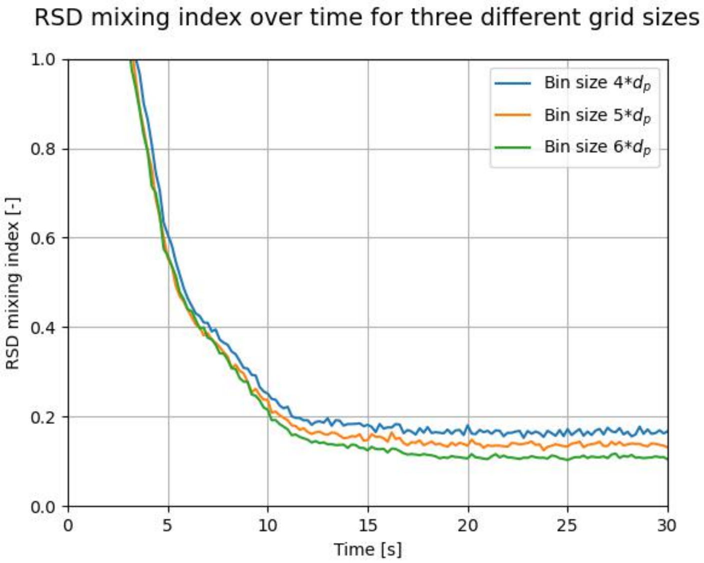

Figure 4.12: RSD mixing index over time for different grid sizes.

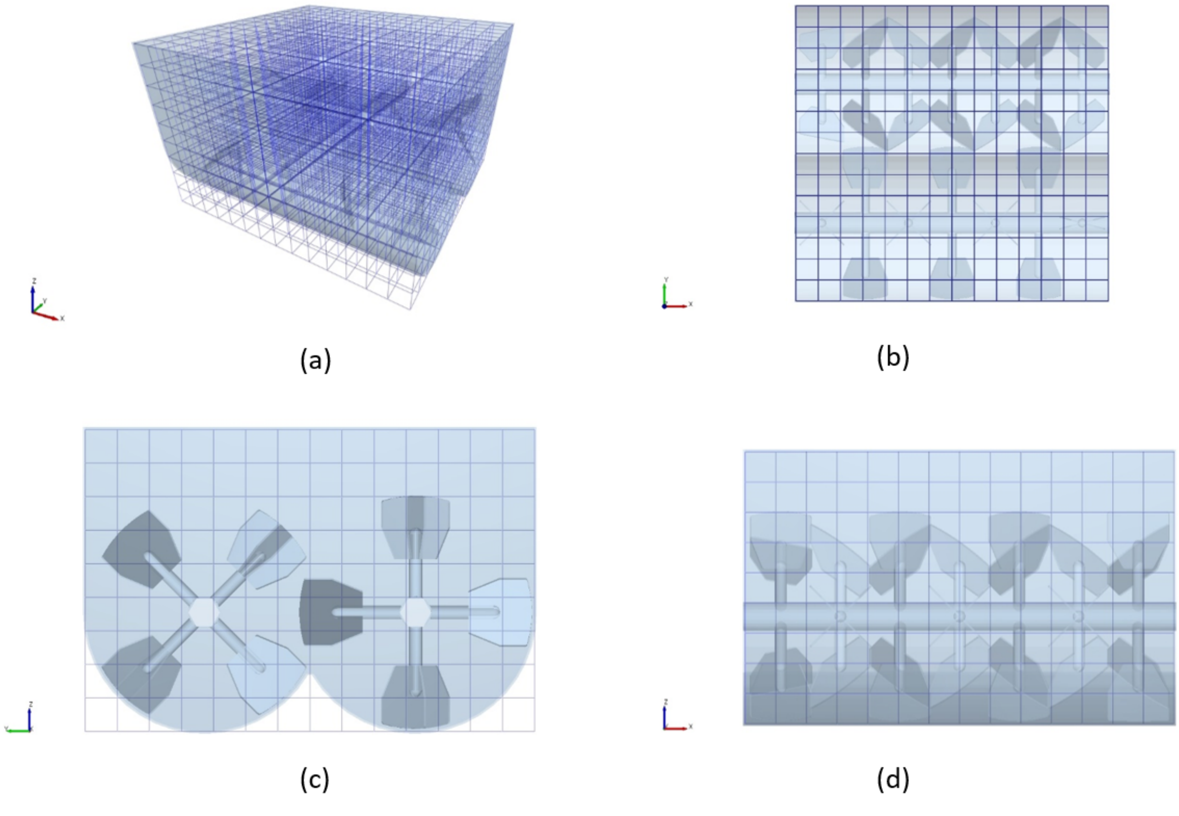

Figure 4.13: (a) Isometric view, (b) top view, (c) front view and (d) right side view of 14x14x9 global grid system with bin size equal to 4*d_p.

4.4.1.3. Key Performance Indicators (KPI's)

Now that the mixing performance of the simulation model can be quantified by the RSD, KPI's are required to be able to compare factor levels with each other in a quantitative way. The following two KPI's are determined, tailored to the paddle mixer:

KPI 1: The RSD after 30 seconds of mixing - The first KPI indicate the *mixing effectiveness* of the system for investigated factor level. Reason to choose a mixing time of 30 seconds is explained in Section 3.2.4.2.

KPI 2: Time it takes to reach a RSD lower than or equal to 0.2 - The second KPI indicate the *mixing efficiency* towards the steady-state RSD value. In other words, how fast does the mixture quality of one factor level evolve over time compared to another. The value 0.2 is chosen on a trial-and-error basis with the aim to get a KPI 2 for most of the simulations. As such, all simulations can be compared to one another concerning mixing efficiency.

In Figure 4.14, an example graph is shown where the two KPI's are visualized.

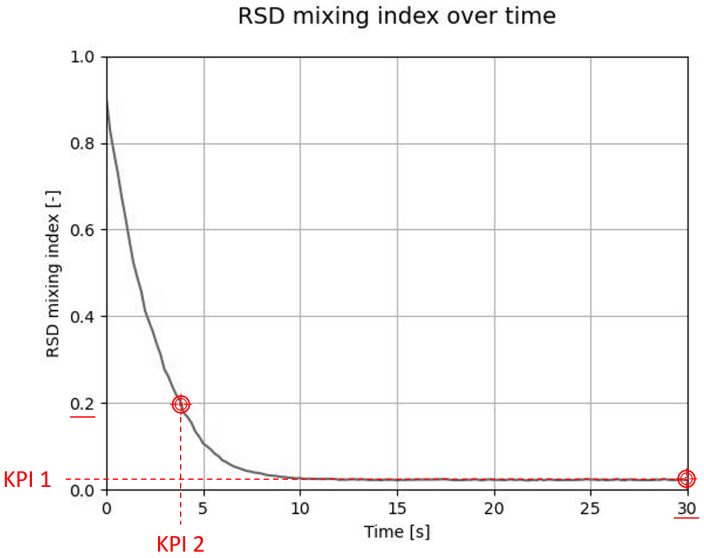

Figure 4.14: Visualization of KPI 1 and KPI 2 in an example RSD-time graph.

With respect to visualization, both KPI's will be presented in tabular form for every factor level. Additionally, RSD-time plots (as is shown in Figure 4.14) and KPI-factor plots will be generated. The former is meant to compare the mixing performance of different factor levels with each other. The latter is useful to show the factor's significance with respect to mixing effectiveness (KPI 1) and/or mixing efficiency (KPI 2).

4.4.2. Qualitative assessment

It is chosen to show screenshots of eight time steps. The initial t=0s to t=5s will be depicted, the last time step at t=30s when the impellers are still rotating and at t=31s when the impellers are stationary. These screenshots will provide sufficient information about the mixing mechanism and flow patterns of the two-component mixture in a qualitative way.

Furthermore, to be able to qualitatively assess the mixing performance of the system on a local level, three additional grid systems are derived from the global one described in Section 4.4.1. These grids are shown in Figure C.2, Figure C.3 and Figure C.4 in Appendix C. The mass concentration of particle 2 (particles of mixture component 2) for every elongated bin is extracted from EDEM™, normalized with the average mass concentration of particle 2 in the whole system and visualized by means of a heat map. The elongated bins can have the color blue, grey or red. Compared to the average mass concentration of component 2, a deficiency of component 2 in an arbitrary elongated bin is indicated by the blue color and a surplus indicated by the red color. Grey indicate the mass concentration of particle 2 in respective elongated bin equals the average mass concentration of particle 2 in the whole system.

To evaluate the local mixture quality of the particle bed both during mixing and when the impeller rotational speed is equal to zero, heat maps are generated on the time steps t=30s and t=31s.

4.5. Experimental simulation plan

A complete overview of the OFAT screening design composed with all factor level values is shown in Table 4.8. The letters in the first row represent the factors illustrated by Table 4.2. No repetitions are performed, because a brief analysis on the reference case showed negligible deviation between multiple repetitions.

Table 4.8: Experimental simulation plan with factor levels and number of particles (particle1, particle2 and total)

Run	a	b	c	p	e	f	g	α_1	i	Particle1	Particle2	Total
Ref.	2	7	80/20	FB	100%	60	1	45°	14	149,427	298,855	448,282
2	**1**	7	80/20	FB	100%	60	1	45°	14	1,195,419	298,855	1,494,274
3	**3**	7	80/20	FB	100%	60	1	45°	14	44,275	298,855	343,130
4	2	**1**	80/20	FB	100%	60	1	45°	14	149,427	298,855	448,282
5	2	**20**	80/20	FB	100%	60	1	45°	14	149,427	298,855	448,282
6	2	7	**99/1**	FB	100%	60	1	45°	14	184,916	14,943	199,859
7	2	7	**50/50**	FB	100%	60	1	45°	14	93,392	747,137	840,529
8	2	7	80/20	**TB**	100%	60	1	45°	14	149,427	298,855	448,282
9	2	7	80/20	**SS**	100%	60	1	45°	14	149,427	298,855	448,282
10	2	7	80/20	FB	**40%**	60	1	45°	14	59,771	119,542	179,313
11	2	7	80/20	FB	**140%**	60	1	45°	14	209,198	418,397	627,595
12	2	7	80/20	FB	100%	**40**	1	45°	14	149,427	298,855	448,282
13	2	7	80/20	FB	100%	**80**	1	45°	14	149,427	298,855	448,282
14	2	7	80/20	FB	100%	60	**0.67**	45°	14	149,427	298,855	448,282
15	2	7	80/20	FB	100%	60	**1.5**	45°	14	149,427	298,855	448,282
16	2	7	80/20	FB	100%	60	1	**30°**	14	149,427	298,855	448,282
17	2	7	80/20	FB	100%	60	1	**60°**	14	149,427	298,855	448,282
18	2	7	80/20	FB	100%	60	1	45°	**7**	149,427	298,855	448,282
19	2	7	80/20	FB	100%	60	1	45°	**28**	149,427	298,855	448,282

5

Results & discussion

The reader should interpret these results with the following in mind. In Chapter 4 the experimental simulation plan is designed which is based upon an OFAT approach. Generated results explicate the main effect of every factor on the paddle mixer's response. Drawn conclusions about evaluated factors are only valid with all other values fixed at their center point values, as shown in Table 4.2. In other words, interactions between factors is not captured. Moreover, some general remarks can be stated according to the results:

- It can be observed by the screenshots in Appendix D that for every simulation the 2-component mixture is being mixed in the first 5 seconds. While, the RSD in the initial stage of mixing ends up higher than a value of one for every simulation according to the RSD-Time graphs. As an RSD of 1 describes a completely separated mixture, the results of RSD greater than 1 are determined to be erroneous in the initial stage of mixing. The faulty results are caused by a wide spread of the concentration of particle 2 in evaluated bins. In the initial stage of mixing, some bins are completely filled with particle 2 and others only contain a few particles of component 2. The wide spread in mass concentration over all bins cause a high standard deviation. And, as the standard deviation is divided by a constant average total concentration of particle 2 to obtain the RSD, consequently the RSD ends up higher than one.
- In this chapter, only the top view heat maps are shown. The side view and front view are put into Appendix D. Looking from the top of the system, all elongated bins in z-direction are filled with enough particles to draw valid conclusions (excluding 99/1 composition and 40% fill level simulations). With respect to the front and side views, the opposite is true where some bins are filled with too few particles.
- According to the heat maps, the mixture quality is relatively lower near right and left side walls than in the center of the mixing chamber for almost all simulations. Driving force(s) that cause this phenomenon is not yet clearly understood and could be an interesting topic for further research.
- Table D.1 in Appendix D presents all values for KPI 1 and KPI 2. Because the factors composition (simulation 6 and 7), fill level (simulation 10 and 11) and paddle number (simulation 18 and 19) required further analysis, new KPI's are displayed in Table D.2 and Table D.3.

For every factor, results are being discussed based upon presented plots and heat maps. Thereafter, interpretation of the results is given according to literature or the author's perception. Additional tables, screenshots and plots can be found in Appendix D.

5.1. Particle size

The influence of the particle size on the mixing performance of the paddle mixer is shown in Figure 5.1. The plots shown in Figure 5.2 present the KPI 1 and KPI 2 values for the researched levels.

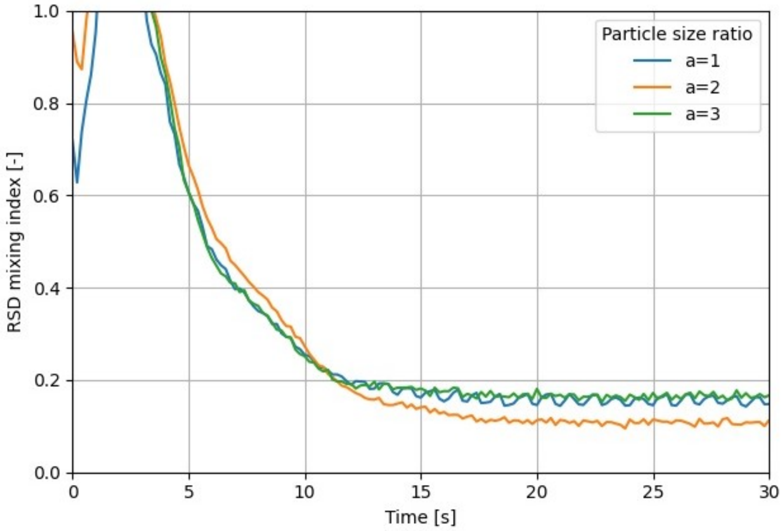

Figure 5.1: RSD mixing index over time for different particle size ratios.

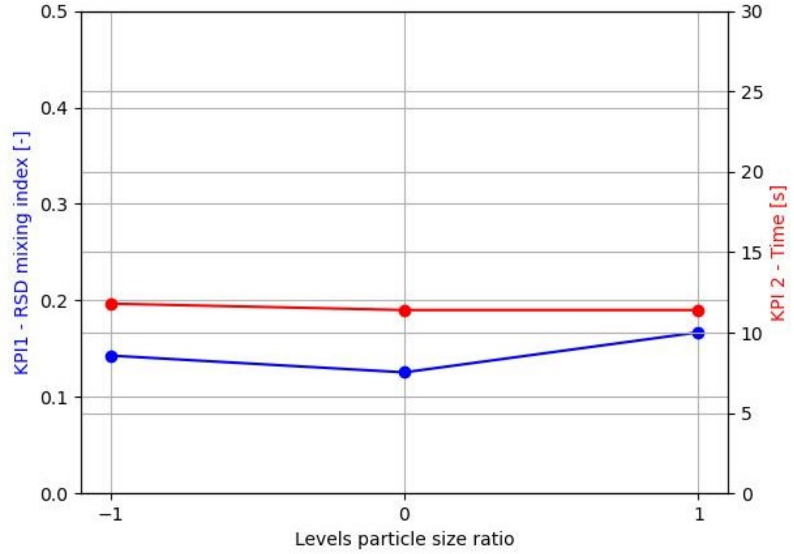

Figure 5.2: Main effect particle size ratio on KPI 1 and KPI 2.

In Figure 5.1 one can observe that the particle size ratios a=1 and a=3 perform comparable, and the particle size ratio a=2 performs slightly better than the other two when the steady-state RSD is reached. Besides that the particle size ratio has no significant effect on the mixing efficiency (KPI 2), as shown in Figure 5.2, the results are not in line with the hypothesis related to the mixing effectiveness (KPI 1).

As explained in Section 2.1.3, particle size is one of the main culprits concerning segregation. The percolation segregation mechanism occurs when a poly-disperse particle bed is being disturbed causing a reconfiguration of the particle packing arrangement. The smaller particles will fall down between the gaps of the larger particles due to gravitational force. And, rise of coarse particles explained in the same section is another segregation mechanism that could come into play. With this in mind, it is expected that an increase in particle size ratio would lead to a decrease in final mixture quality.

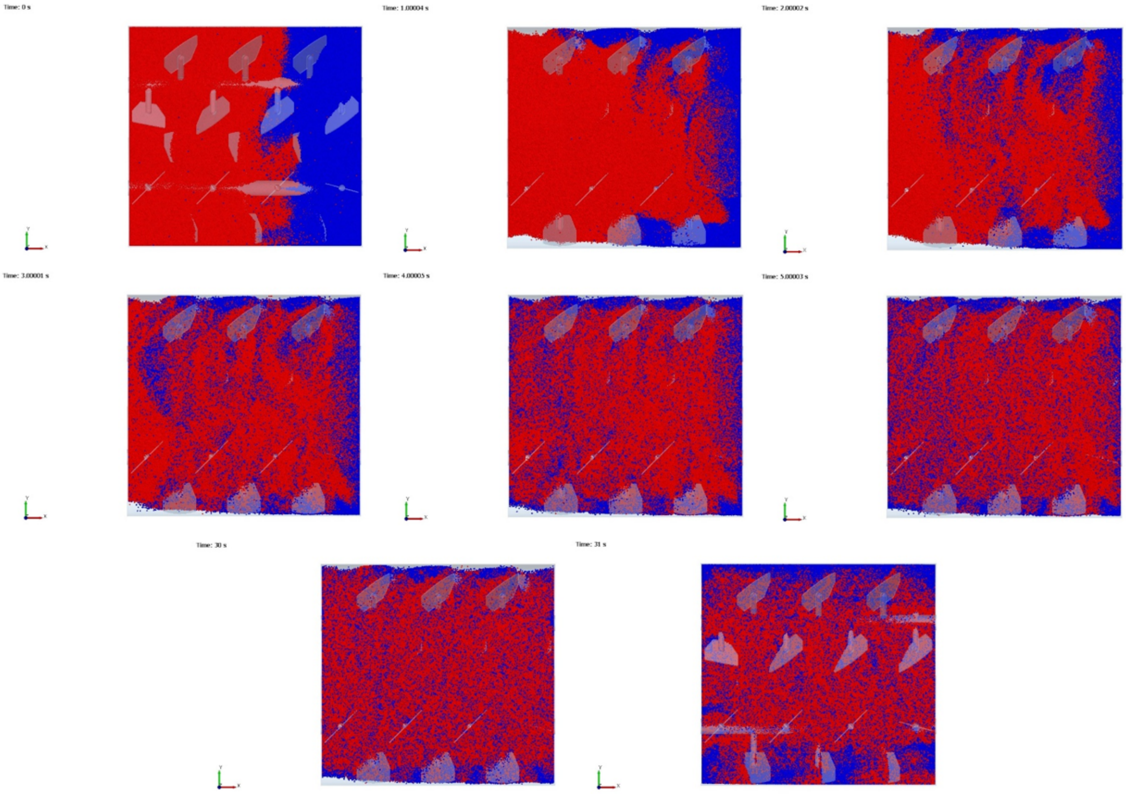

Figure 5.3: Top view of simulation 2 - Particle size ratio (α=1) for time step t=0s, t=1s, t=2s, t=3s, t=4s, t=5s, t=30s and t=31s.

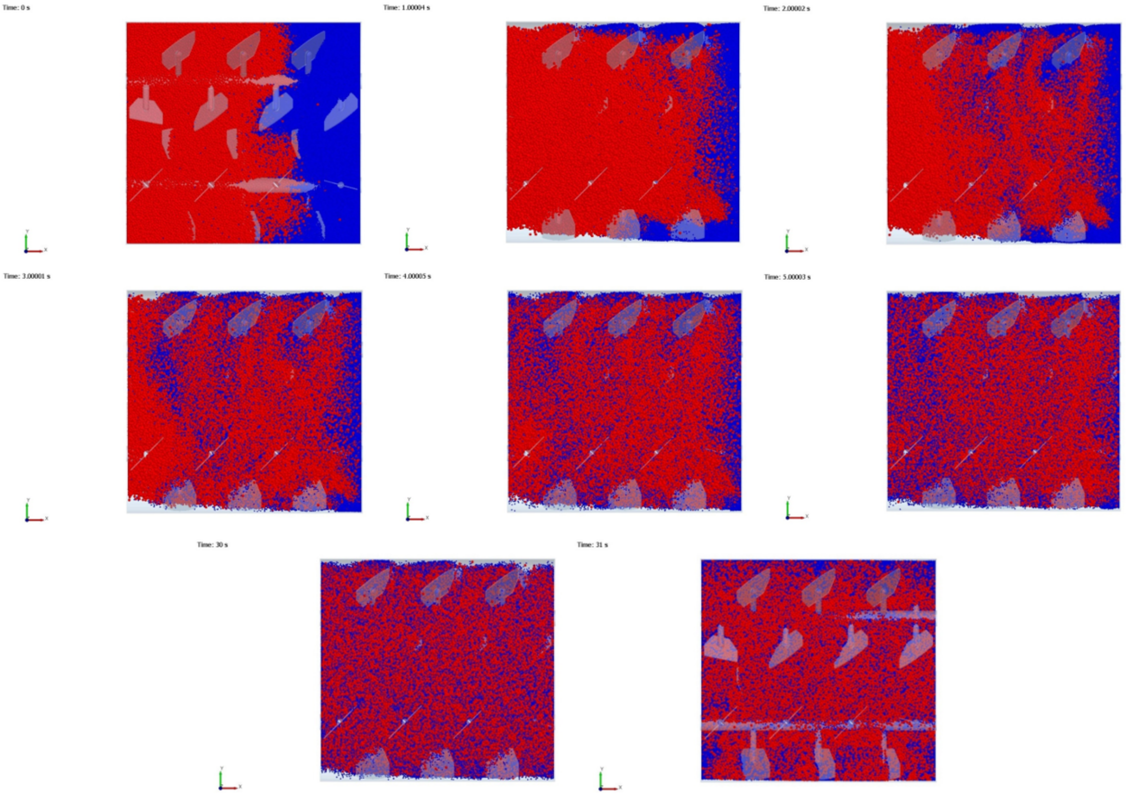

Figure 5.4: Top view of simulation 1 - Center point for time step t=0s, t=1s, t=2s, t=3s, t=4s, t=5s, t=30s and t=31s.

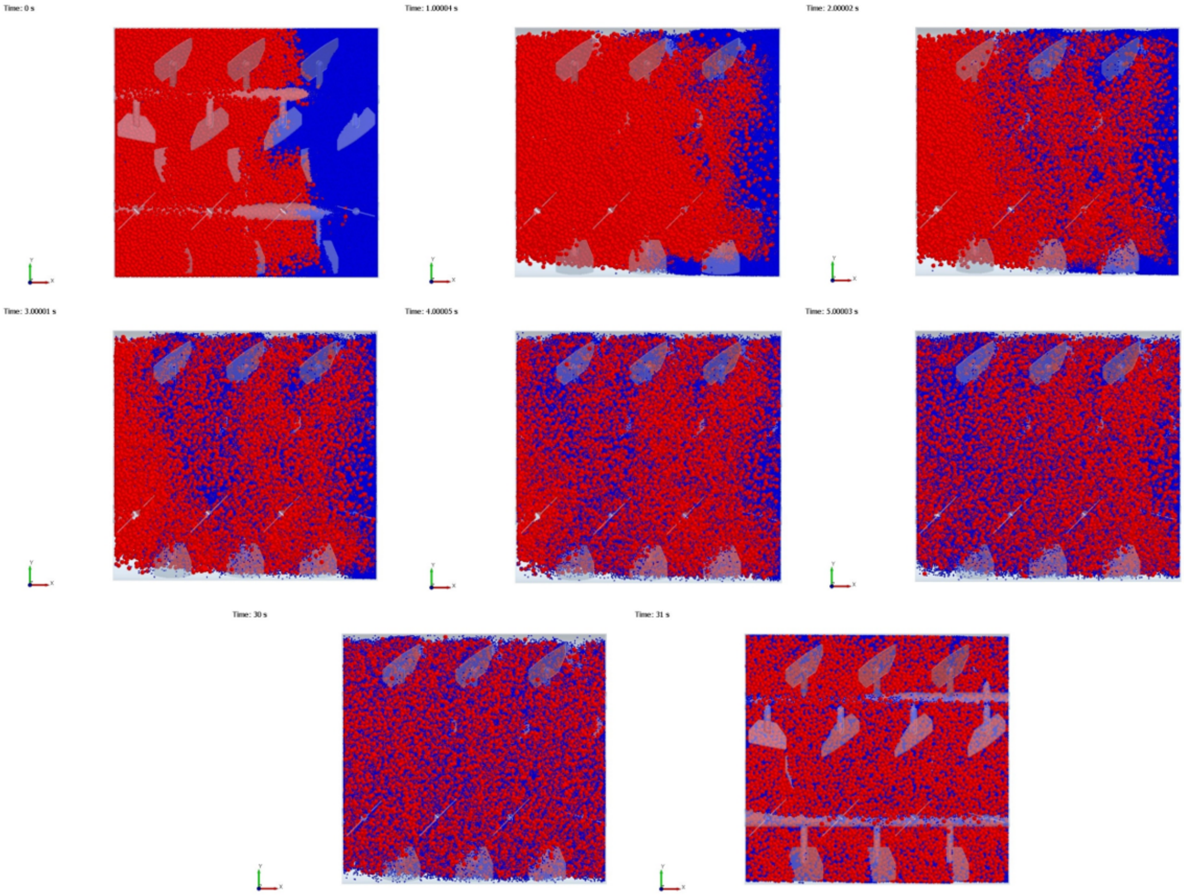

Figure 5.5: Top view of simulation 3 - Particle size ratio (a=3) for time step t=0s, t=1s, t=2s, t=3s, t=4s, t=5s, t=30s and t=31s.

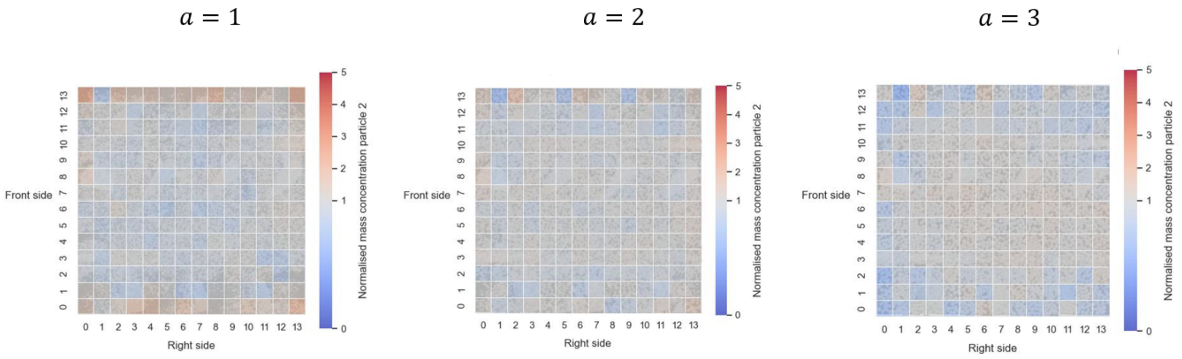

Figure 5.6: a. Particle size ratio - Heat map of 14x14x1 grid with normalized concentrations of particle 2 at time=31s.

Looking at the heat map in 5.6, and the screenshots visualized in Figure 5.4, Figure 5.3 and Figure 5.5, for particle size ratio of a=1 component 2 particles (blue) accumulate at the wall of the mixing chamber at t=31s, while this phenomenon is not observed for a=2 and a=3.

The observed phenomenon can be explained by the interplay between different segregation mechanisms. It is assumed the push-away effect is the most dominant segregation mechanism present here (as explained in Section 2.1.3). The difference in particle density (center point value of b=7 in Table 4.2) causes the heavier particles to push away the lighter particles towards the sides of the mixing chamber.

With respect to particle size ratios a=2 and a=3, the accumulation of component 2 particles (blue) at the wall edges is observed less. Now that the particle size differs between the two components, it is assumed the percolation segregation mechanism becomes the more dominant mixing mechanism. This assumption is backed up by screenshots shown in Figure 5.8, Figure 5.7 and Figure 5.9, where the larger particles (red) accumulate at the top of the particle bed at t=31s.

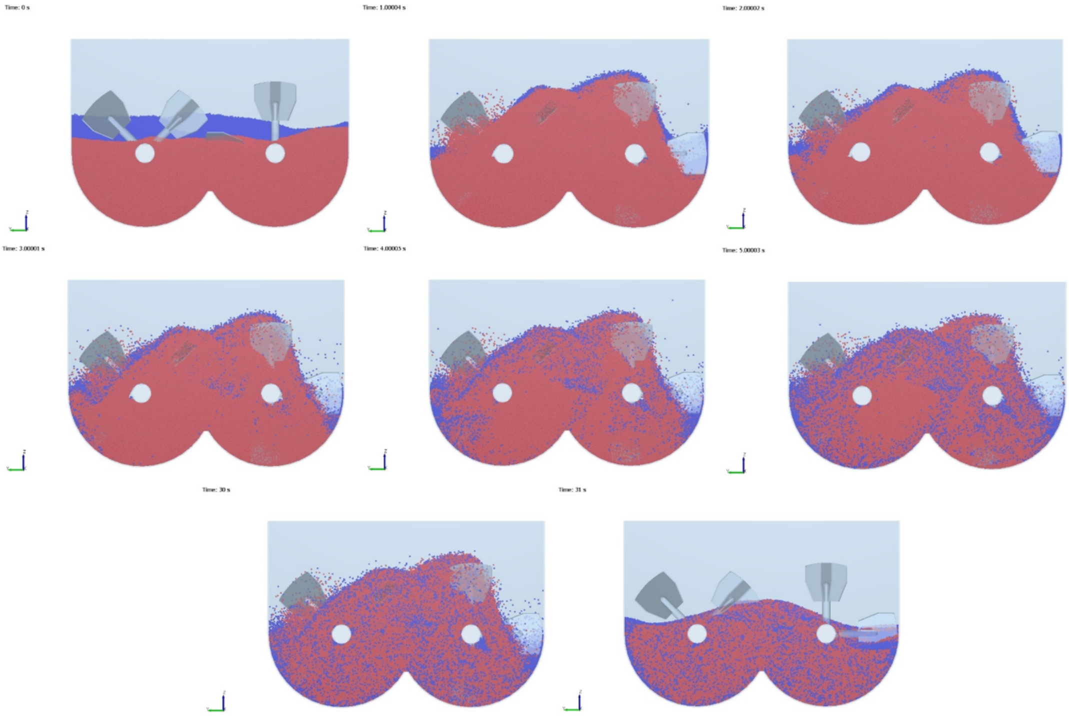

Figure 5.7: Front view of simulation 2 - Particle size ratio (b=1) for time step t=0s, t=1s, t=2s, t=3s, t=4s, t=5s, t=30s and t=31s.

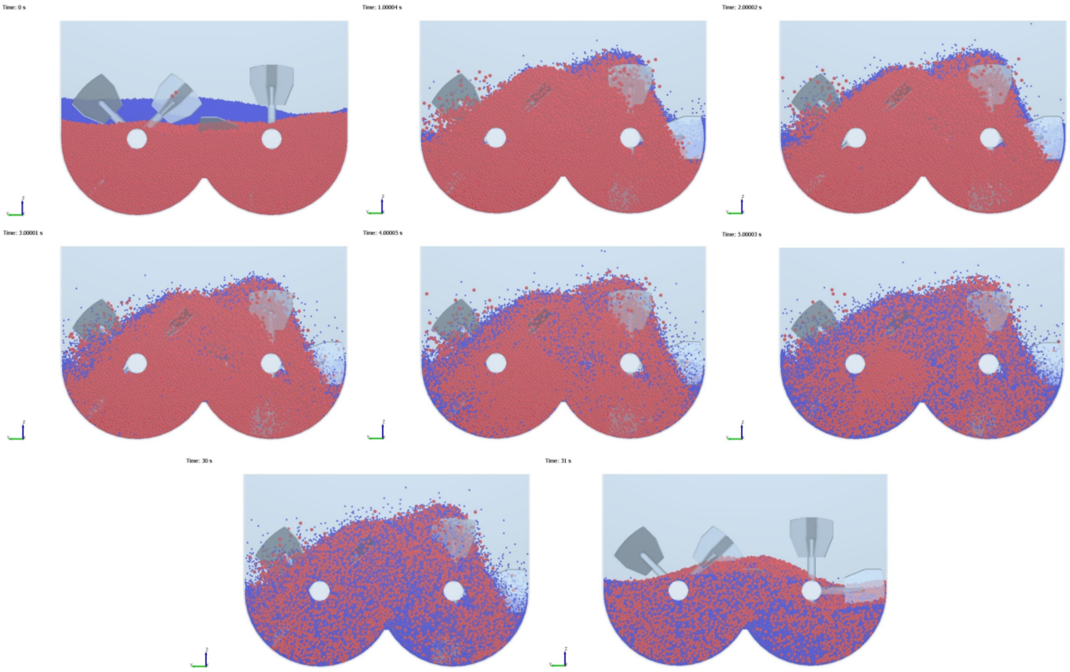

Figure 5.8: Front view of simulation 1 - Center point for time step t=0s, t=1s, t=2s, t=3s, t=4s, t=5s, t=30s and t=31s.

Moreover, in section 2.1.3 in the literature review, the buoyancy segregation mechanism is explained. Jain et al. [35] investigated the effect of both particle size and density on the segregation in a rotating drum. Especially the interaction between the two material characteristics on segregation,

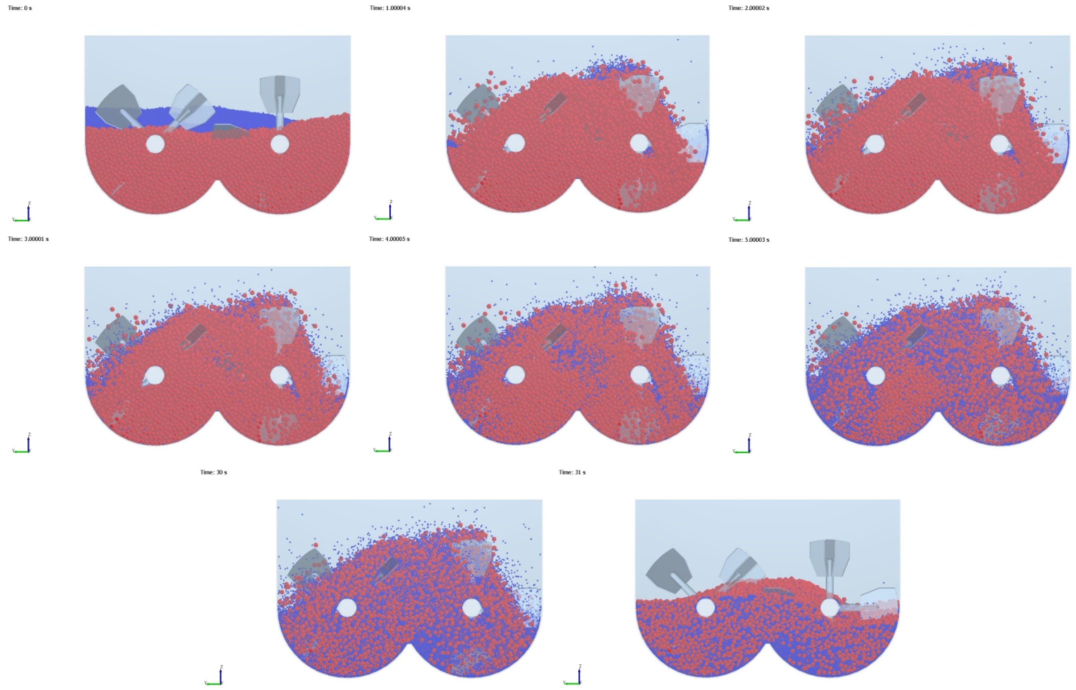

Figure 5.9: Front view of simulation 3 - Particle size ratio (b=20) for time step t=0s, t=1s, t=2s, t=3s, t=4s, t=5s, t=30s and t=31s.

where the two mechanisms compete or reinforce each other, were of interest. The conclusion states that segregation can be reduced if the denser particles also have a bigger particle size and if the particle size ratio is greater than the particle density ratio. Relating the conclusion to this research, the first statement is true where the bigger particles have a particle density $\rho_{p,2}$ = 2500 kg m^{-3} compared to the smaller particles with a particle density $\rho_{p,1}$ = 357 kg m^{-3}. However, the second statement is not true because the particle size ratio (a=2 and a=3) is not greater than the particle density ratio (b=7). To summarize, if the drawn conclusion by Jain et al. [35] is also valid for the double shaft paddle mixer is yet to be discovered.

It is believed by the author that the difference in particle density for the center point simulation (Section 4.3) interact with the varying particle size ratio. In what way the mentioned mechanisms percolation, buoyancy and push-away interact for this particular type of mixing application is not yet known and needs further research.

5.2. Particle density

The influence of the particle density on the mixing performance of the paddle mixer is shown in Figure 5.10. The plots shown in Figure 5.11 present the KPI 1 and KPI 2 values for the researched levels.

In Figure 5.10, all three investigated levels show a more or less equal development of the mixing quality over time and end up approximately on the same RSD after 30 seconds of mixing.

As explained in Section 2.1.3, buoyancy will cause particles with different densities to segregate; heavier particles sink and lighter ones rise. However, as was already mentioned in Section 5.1, interactions between particle size and particle density ratios could cause an increase or decrease in segregation. The relation between the existing segregation mechanisms is unknown and requires further research.

Moreover, what can be observed from the heat map shown in Figure 5.12, is that with an increase in particle density ratio b, the lighter particles (blue) end up near the wall of the mixing chamber. It is expected the push-away segregation mechanism is causing observed phenomenon. As already mentioned, besides the push away segregation mechanism it is assumed that also mechanisms buoyancy and percolation are causing segregation, one more dominant than the other. It is not yet clearly understood which one is more dominant over the others.

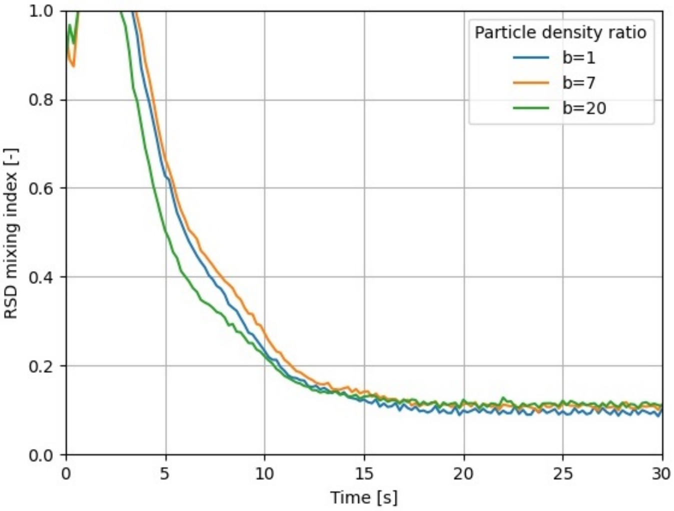

Figure 5.10: RSD mixing index over time for different particle density ratios.

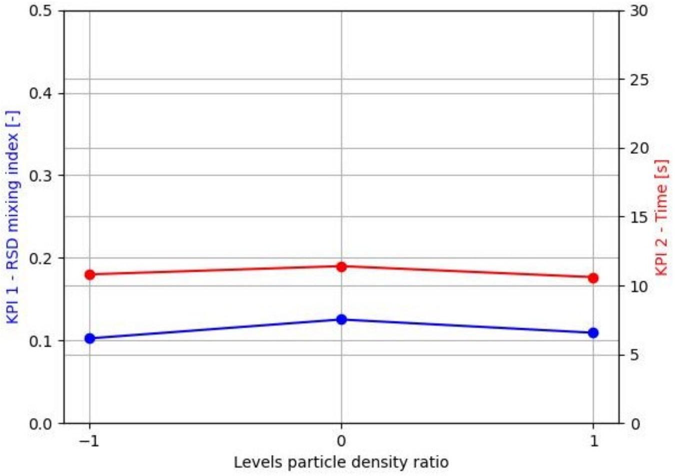

Figure 5.11: Main effect particle density ratio on KPI 1 and KPI 2.

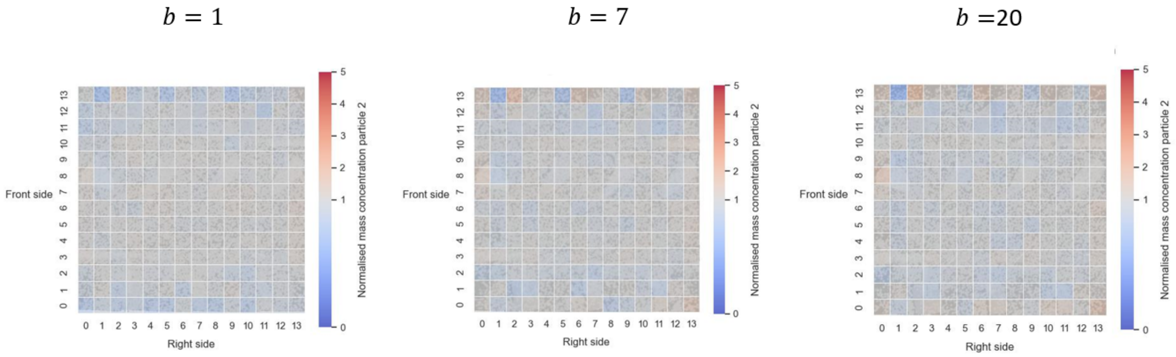
$b = 1$ $b = 7$ $b = 20$

Figure 5.12: b. Particle density ratio - Heat map of 14x14x1 grid with normalized concentrations of particle 2 at time=31s.

5.3. Composition

The influence of the composition on the mixing performance of the paddle mixer is shown in Figure 5.13. The plots shown in Figure 5.14 present the KPI 1 and KPI 2 values for the (initial) researched levels.

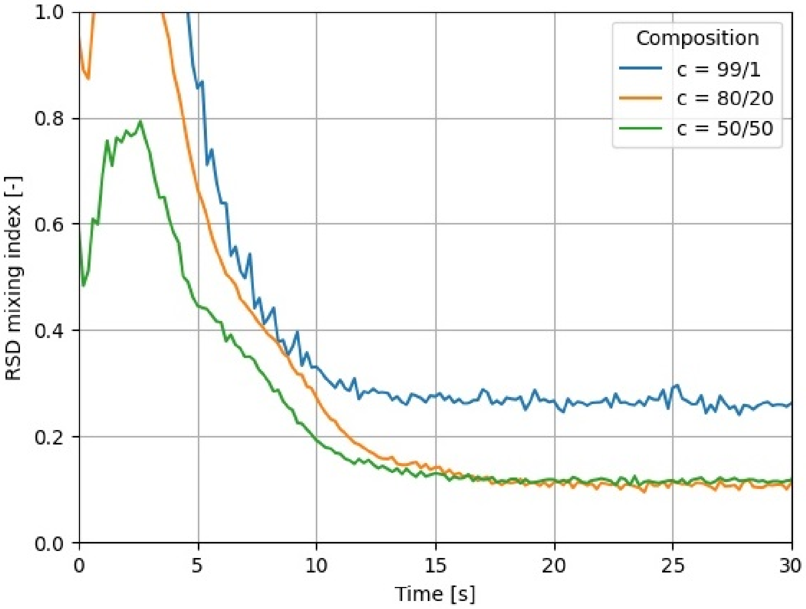

Figure 5.13: RSD mixing index over time for different compositions.

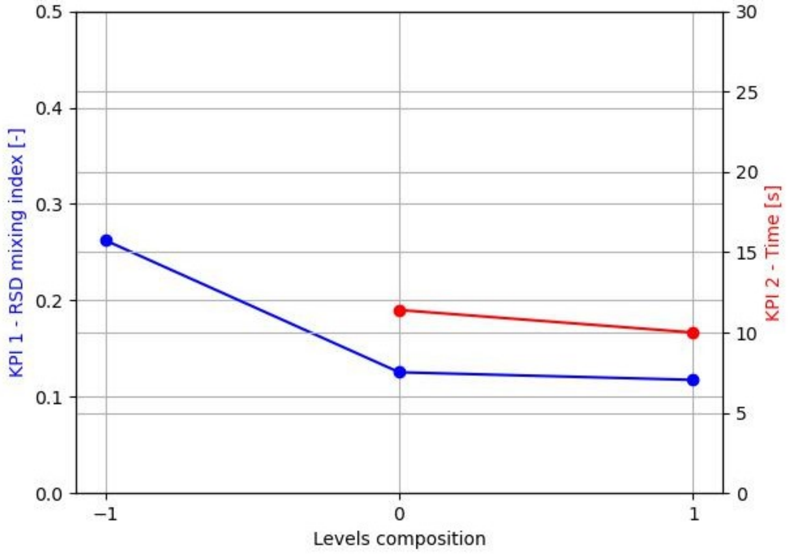

Figure 5.14: Main effect composition on KPI 1 and KPI 2.

According to Figure 5.13, the c=80/20 and c=50/50 compositions perform better than the c=99/1 composition, as was expected upfront. Among other subjects, Shenoy et al. investigated the effect of composition on mixtures like sugar/salt and paprika/salt mixtures [61]. For salt concentration equal to or lower than 1%, the mixing performance of respective mixtures decreased. The final RSD after 30 seconds of mixing for c=99/1 is caused by the disproportional distribution of mass concentration of component 2 over evaluated bins, as shown in Figure 5.17. However, the substantial difference in final steady-state mixture qualities of c=99/1 compared to c=80/20 and c=50/50 raises some questions. Because the grid system analysis (explained in Section 4.4.1.2 is performed with c=80/20, it could be for the c=99/1 too few particles of component 2 are present in each bin to obtain an accurate RSD.

To further analyze the effect of the grid system on the c=99/1 result, another grid system is designed consisting of larger bins (7x7x4 bins in x, y and z directions respectively). Figure 5.15 and Figure 5.16 show the results.

Figure 5.15 and Figure 5.16 show the grid system has an effect on the RSD over time for all three

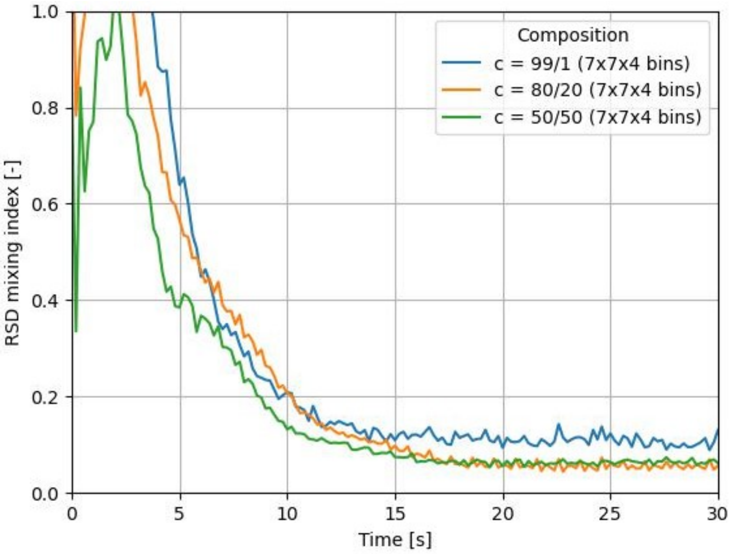

Figure 5.15: RSD mixing index over time for different compositions with a grid system consisting of 7x7x4 bins

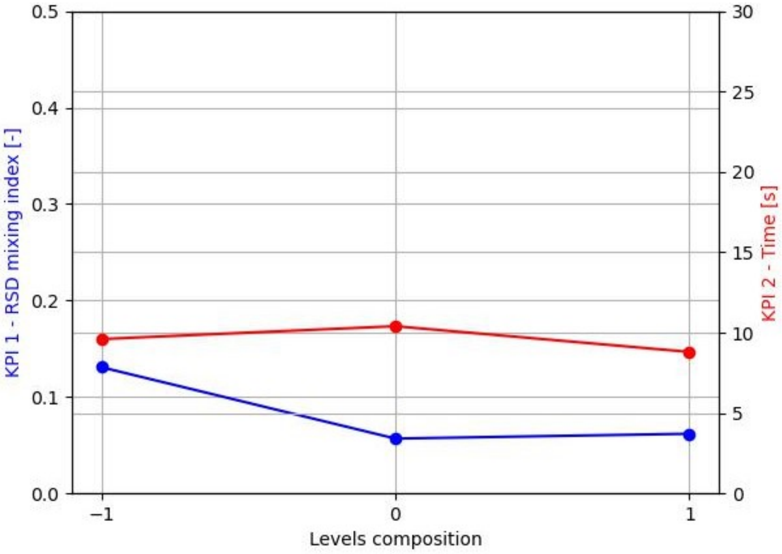

Figure 5.16: Main effect composition on KPI 1 and KPI 2 with adapted grid system from 14x14x9 to 7x7x4 bins.

composition levels which is in line with the statement that the RSD is grid dependent (mentioned in Section 4.4.1.1). Furthermore, the c=99/1 steady state RSD lays closer to the other two levels. The larger bins in the 7x7x4 grid system results in more particles per bin. This is beneficial for the analysis on the c=99/1 simulation, as the results can be assumed more accurate from a statistical point of view. However, further research is required to proof the c=99/1 simulation converges to the other two composition levels when the bin size further increases. As all other factors besides the composition should be evaluated with the same grid system to compare KPI's, further analysis is not included.

5.4. Initial filling pattern

The influence of the initial filling pattern on the mixing performance of the paddle mixer is shown in Figure 5.18. The plots shown in Figure 5.19 present the KPI 1 and KPI 2 values for the researched levels.

Looking at Figure 5.18, the TB initial filling pattern is the best performing pattern followed by SS and FB filling patterns. And, the mixing performance of the FB filling pattern ends up close to the SS filling

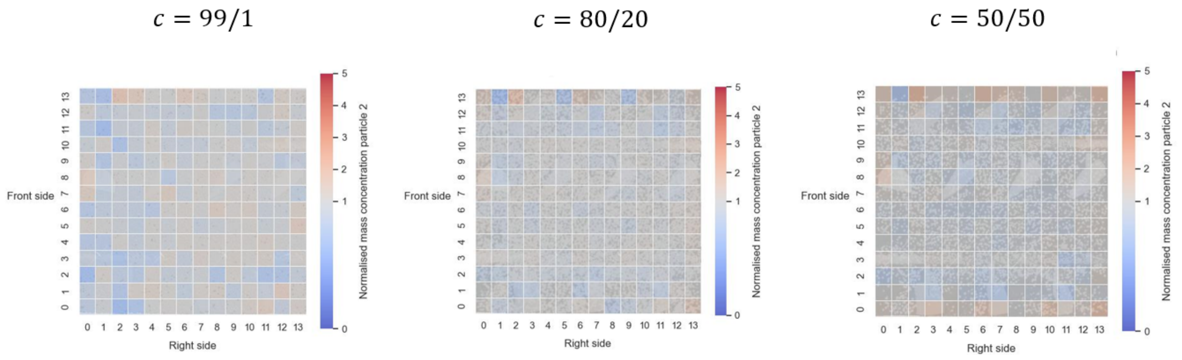

Figure 5.17: c. Composition - Heat map of 14x14x1 grid with normalized concentrations of particle 2 at time=31s.

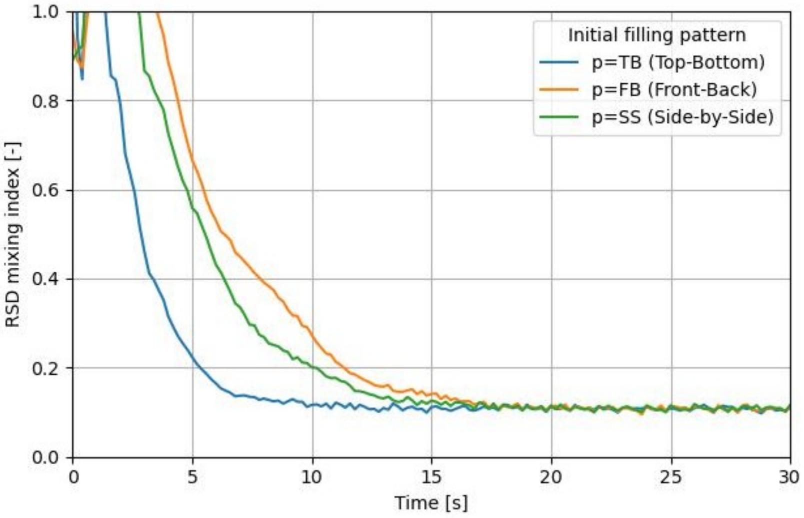

Figure 5.18: RSD mixing index over time for different initial filling patterns.

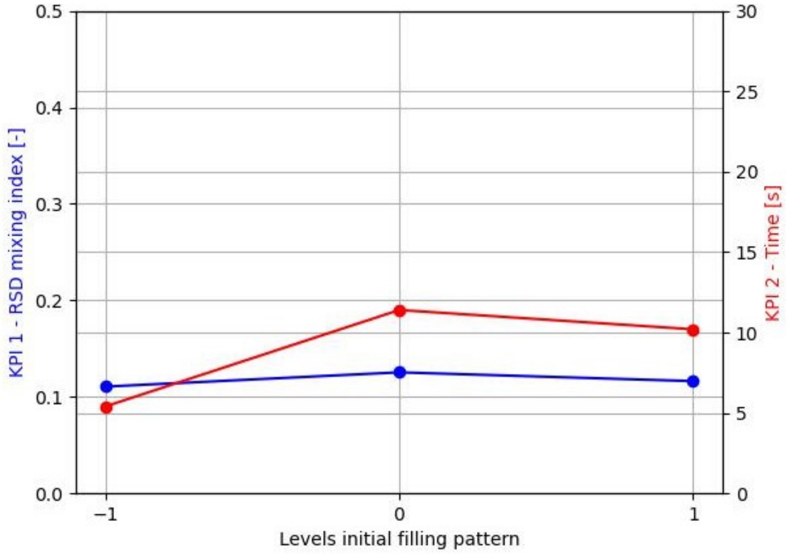

Figure 5.19: Main effect initial filling pattern on KPI 1 and KPI 2.

pattern. Upfront, it was expected that the Top-Bottom filling pattern will show the best performance according to the paper published by Jadidi et al. [34]. Jadidi et al. [34] found that the TB configuration performed better than the Side-by-Side (SS) and Front-Back (FB) filling patterns. It is believed this has mainly to do with the initial interface between the two mixture components in combination with its orientation in the mixing chamber. A larger interface would mean the average distance between the two components is less compared to a smaller interface. Thus, a smaller travelling distance would be beneficial with respect to a quick mixing process. In combination with the rotating shafts with angled paddles that forces the particles to be moved in both axial and radial directions, the TB filling pattern should perform best. Moreover, as Jadidi et al. [34] used a mixing application with non-angled paddles (Section 2.3.9), axial mixing was curtailed. Consequently, the FB initial filling pattern was eliminated from the research because of poor mixing performance. It was expected that the FB pattern would still cause the worst mixing performance, although the results will be closer to the other two patterns because of the angled paddles for the paddle mixer under investigation. Lastly, all three levels reach the same steady-state RSD which underline the presence of both axial and radial mix mechanisms caused by the angled paddles (Figure 5.19). The latter can be confirmed by research from Hassanpour et al. [29], explained in Section 2.3.1.

In Figure 5.20, the heat maps show similar results for all three investigated initial filling patterns which are in line with Figure 5.18. And, the screenshots shown in Figure 5.21 and Figure 5.22 clearly illustrate differences in mixture development for the first five seconds of mixing, compared to Figure 5.4 presented in Section 5.1.

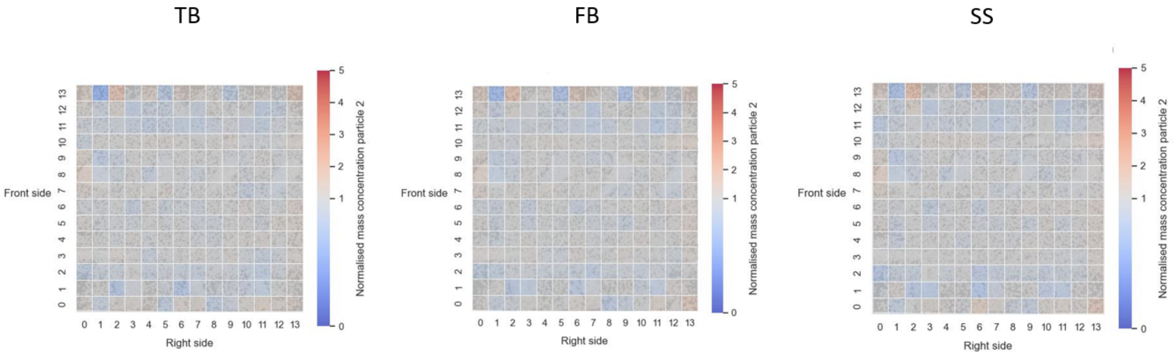

Figure 5.20: d. Initial filling pattern - Heat map of 14x14x1 grid with normalized concentrations of particle 2 at time=31s.

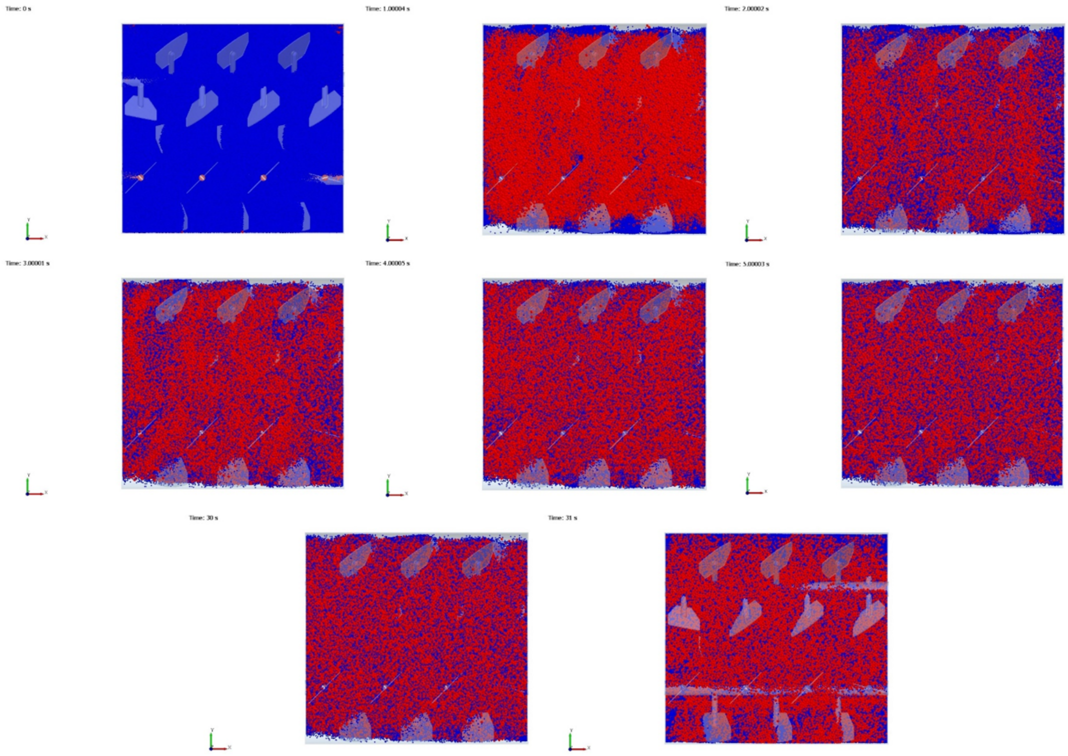

Figure 5.21: Top view of simulation 8 - Initial filling pattern (d=TB) for time step t=0s, t=1s, t=2s, t=3s, t=4s, t=5s, t=30s and t=31s.

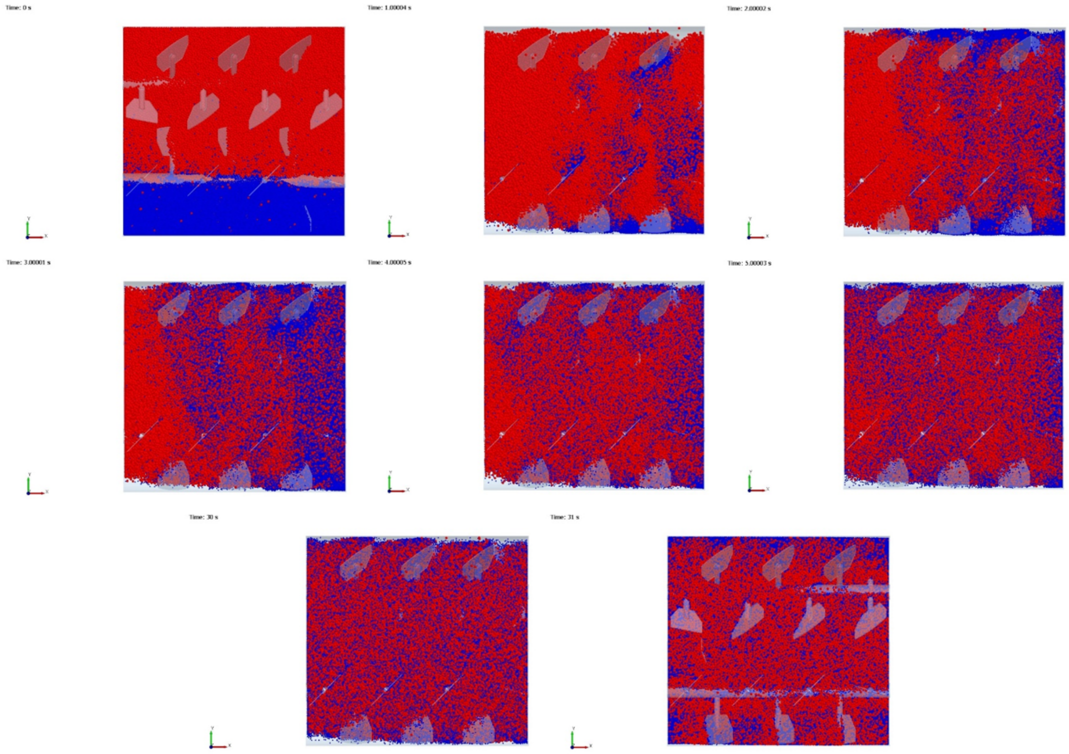

Figure 5.22: Top view of simulation 9 - Initial filling pattern (d=SS) for time step t=0s, t=1s, t=2s, t=3s, t=4s, t=5s, t=30s and t=31s.

5.5. Fill level

The influence of the fill level on the mixing performance of the paddle mixer is shown in Figure 5.23. The plots shown in Figure 5.24 present the KPI 1 and KPI 2 values for the (initial) researched levels.

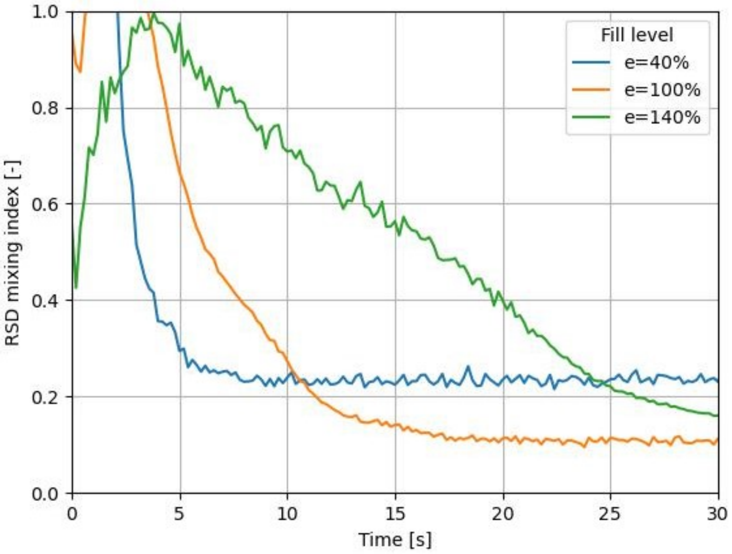

Figure 5.23: RSD mixing index over time for different fill levels.

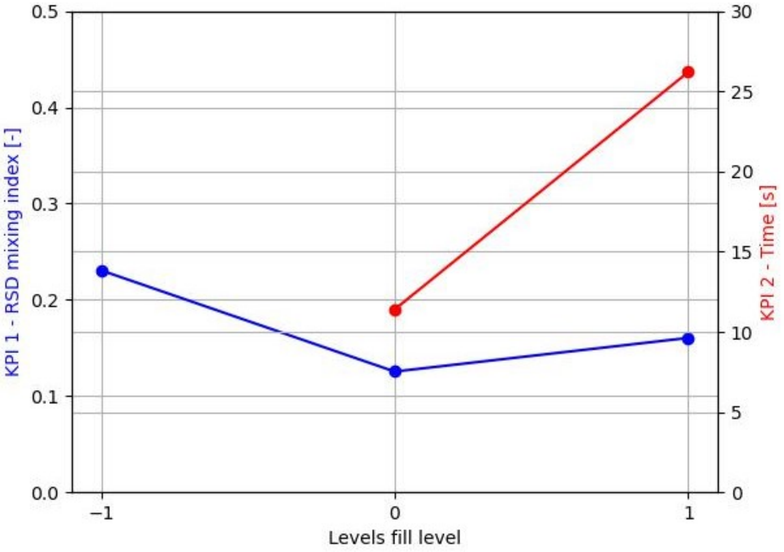

Figure 5.24: Main effect fill level on KPI 1 and KPI 2.

Considering the results presented in Figure 5.23, a higher fill level resulted in slower mixing. However, the steady-state mixture quality reached by e=40% fill level is unforeseen. Moreover, the mixing time for the e=140% level is too small to draw accurate conclusions, as it did not reach the steady-state RSD yet. Nevertheless, the graph suggests the e=140% level is approaching the e=100% level. Consequently, the KPI 2 for the the 40% fill level is missing in Figure 5.24 as this level did not reach a value of RSD ≤ 0.2.

According to Jadidi et al. [34], the fill level does not have a significant impact on the mixing performance. They investigated 40%, 50% and 60% fill levels with impeller rotational speeds of 10 rpm, 40 rpm and 70 rpm. All levels performed more or less equal in terms of mixing speed and final steady-state mixture quality. However, concerning the broad range of fill levels selected for this research (40%, 100% and 140%) compared to Jadidi's research, it was expected the fill level does have influence on the mixing performance of the system. The hypothesis is based upon the number of particles that have to be relocated which would lead to an increase in time before reaching a steady state mixture quality. Hereby, it is assumed that the fill level range investigated by Jadidi was too narrow to observe any variation in mixing performance.

The reason behind the unexpected result of the e=40% level has probably to do with the designed grid system. There are too few particles in every bin to get an accurate estimate of the standard deviation, and indirectly of the RSD. To test the hypothesis, a new grid system is designed consisting of 7x7x4 bins instead of 14x14x9 bins. In Figure 5.25 and Figure 5.26 the outcome is presented.

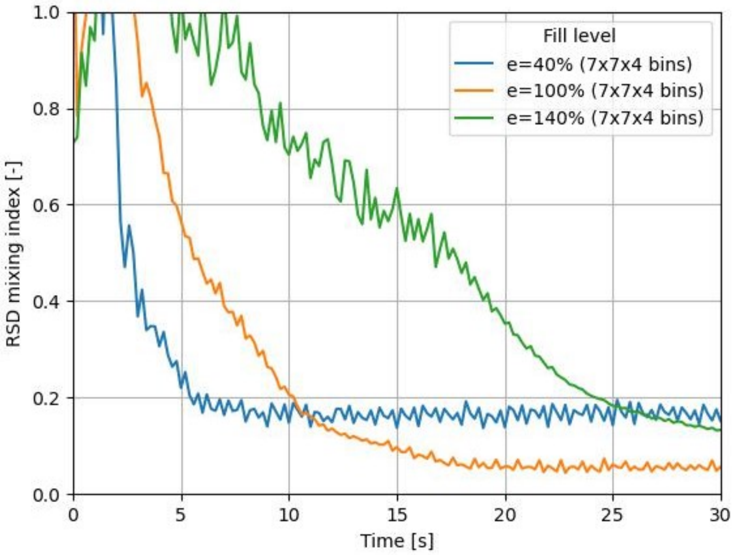

Figure 5.25: RSD mixing index over time for different fill levels with a grid system consisting of 7x7x4 bins.

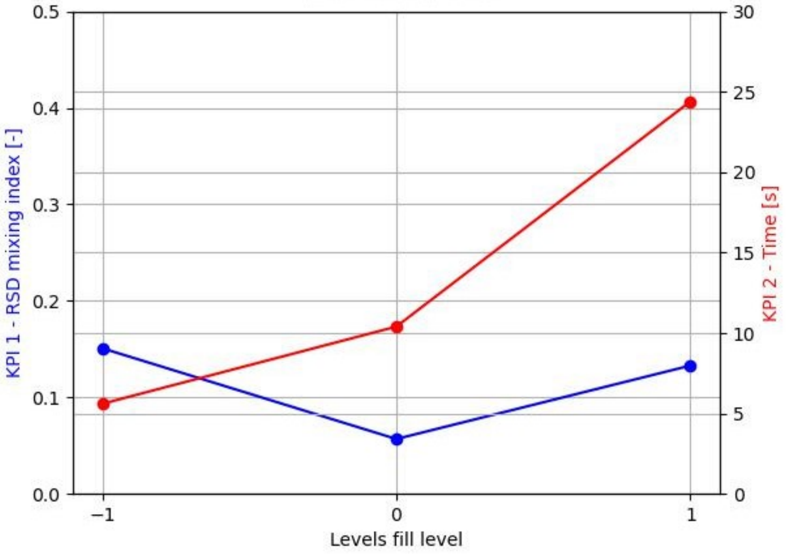

Figure 5.26: Main effect fill level on KPI 1 and KPI 2 with adapted grid system from 14x14x9 to 7x7x4 bins.

Comparison between Figure 5.25 and the original Figure 5.23, one can observe the e=40% level converges towards the e=100% level. Still, the steady-state mixture qualities are not identical, as is clearly visualized in Figure 5.26. Whether the present discrepancy of steady-state mixture quality between the 40% level and e=100% is caused by the grid system or other factors is unknown. Further analysis is not part of this research.

Moreover, what can also be perceived is the considerable fluctuations of the RSD over time for both the 40% level and the 140%. Fluctuations in each level is believed to originate from different sources.

The fluctuations in the 40% level can be explained by the highly diffusive behavior of particles in the mixing chamber. The particles do have enough space in the fluidized zone of the mixing chamber to move freely. In Figure 5.27 the particle velocity is displayed at t=30s and explicate the diffusive behavior of the particles. Consequently, concentration of particle 2 in every evaluated bin changes rapidly in time causing variation in RSD.

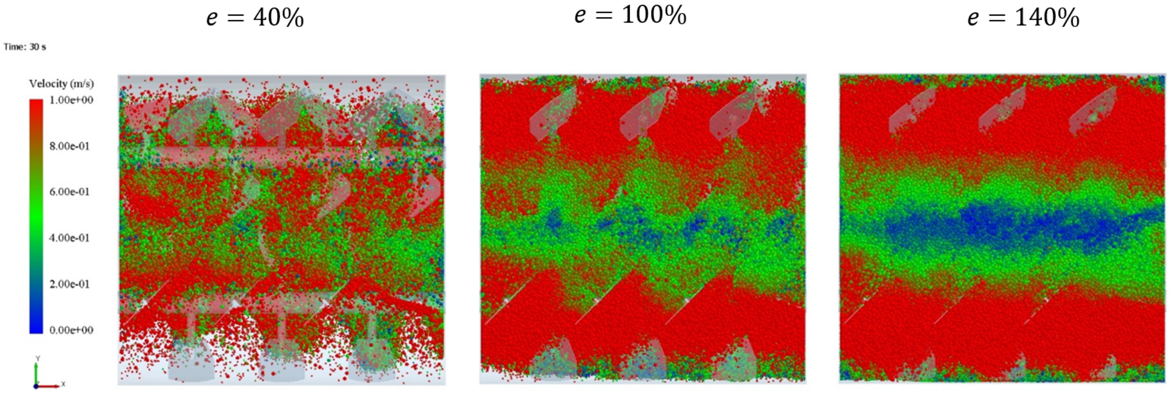

Figure 5.27: Velocity of particles from top view for all three fill levels at time=31s.

With respect to the 140% level, the origin of the fluctuations probably lays at the alteration of mixing mechanism dominance. The freedom of movement of particles in the fluidized zone is decreased causing a deterioration of the diffusive mixing mechanism. As a result, the convective mixing mechanism plays a more dominant role in the mixing process (Section 2.1.2). In other words, groups of particles are relocated by the paddles. As the paddle pairs are welded onto the shaft in an 90° alternating fashion, not all particle groups are transported equally smooth through the mixing chamber causing observed fluctuations.

Lastly, Figure 5.27 clearly shows for e=140% fill level the stagnant fluidized zone in the center of the mixing chamber with particle velocities equal to zero. This is not conducive for the mixing performance of the system as shown in Figure 5.25 where the mixing efficiency is substantially lower for the e=140% fill level compared to the e=40% and e=100% fill levels.

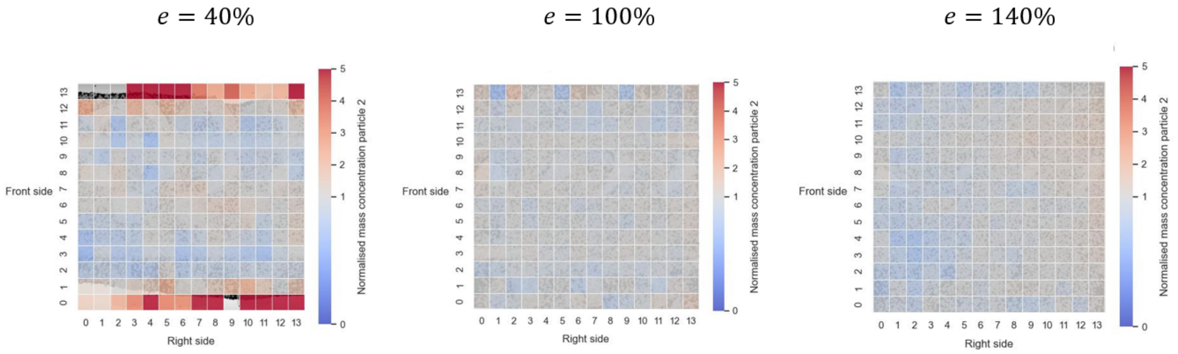

Figure 5.28: e. Fill level - Heat map of 14x14x1 grid with normalized concentrations of particle 2 at time=31s.

The local differences shown in Figure 5.28 clearly shows the lack of particles in every bin for the e=40% fill level to draw accurate conclusions, especially near the right and left side walls. Another interesting conclusion that can be drawn from these figures is the non saturated mixture after 31 seconds of mixing for the e=140% simulation. Component 2 is not yet equally distributed over the mixing chamber, but the majority of particles is still located at the back side of the mixing chamber.

5.6. Impeller rotational speed

The influence of the impeller rotational speed on the mixing performance of the paddle mixer is shown in Figure 5.29. The plots shown in Figure 5.30 present the KPI 1 and KPI 2 values for the researched levels.

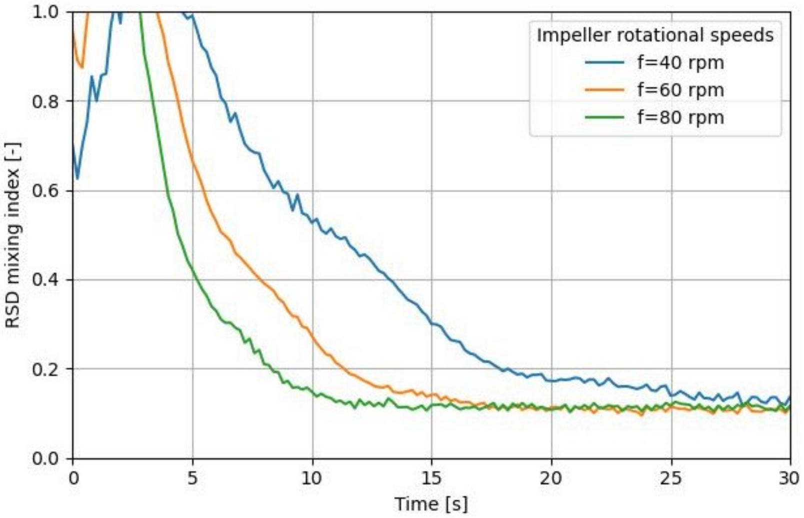

Figure 5.29: RSD mixing index over time for different impeller rotational speeds.

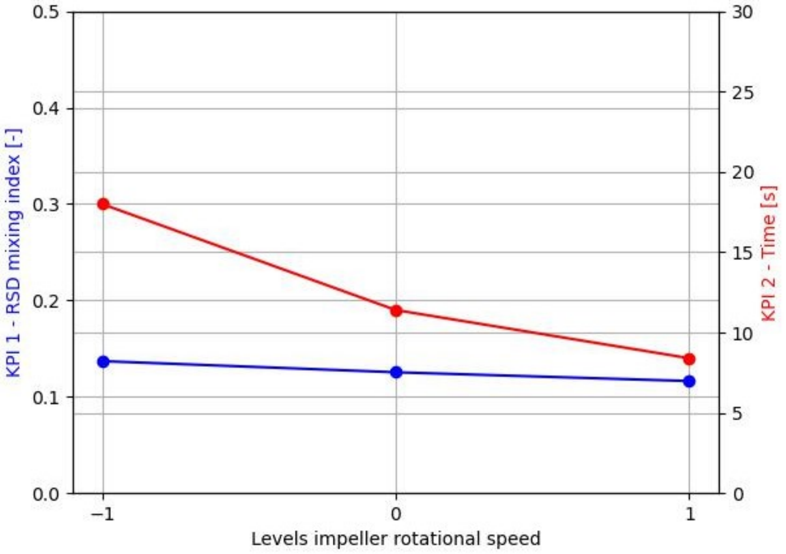

Figure 5.30: Main effect impeller rotational speed on KPI 1 and KPI 2.

Looking at Figure 5.29, the f=80 rpm impeller rotational speed causes a higher momentum to the particles compared to f=40 rpm and f=60 rpm impeller rotational speeds. Consequently, the steady-state RSD is reached faster. Figure 5.31 confirms aforementioned where an impeller rotational speed of f=80 rpm causes higher particle velocities. Eventually, the f=60 rpm level reach the same steady-state value as the f=80 rpm after 18 seconds, followed by the f=40 rpm level at 30 seconds. Figure 5.30 clearly shows the relation between impeller rotational speed and KPI 1 and KPI 2, where the mixing effectiveness is not affected by the parametric variation of the impeller rotational speed while the mixing efficiency is.

According to Jadidi et al. [34], an increase in impeller rotational speed from 40 to 70 rpm resulted in an improvement in mixing performance of the system during the initial stage of mixing, irrespective of the investigated fill levels TB and SS. After 8 seconds of mixing both impeller rotational speeds reach an identical steady-state value. The phenomenon can be explained by the amount of momentum imposed on the particles that increases with a higher impeller rotational speed. With respect to this research, a higher impeller rotational speed stimulates the diffusive movement of particles in the fluidized zone of the mixing chamber which is the main reason for the improvement of mixing efficiency in the initial stage of mixing.

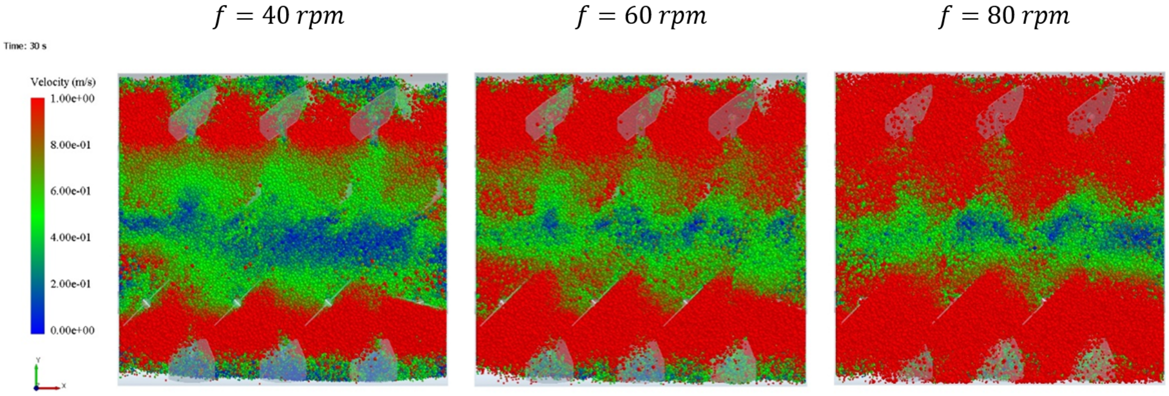

Figure 5.31: Velocity of particles from top view for all three impeller rotational speeds at time=31s.

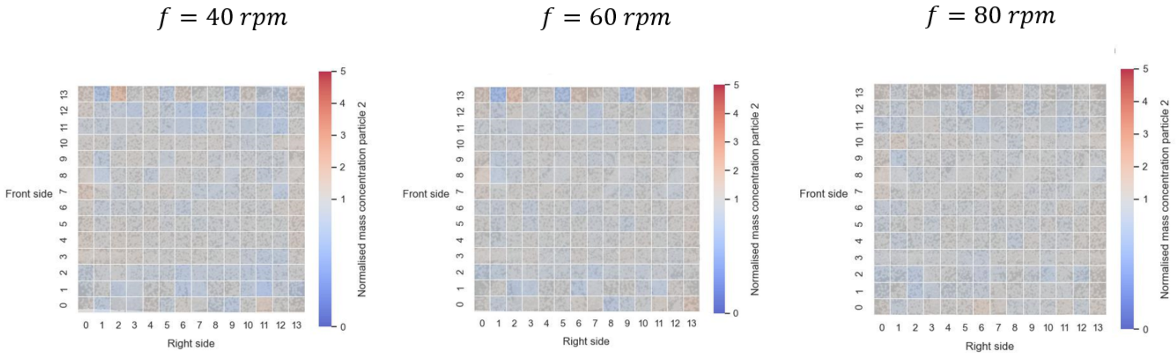

Figure 5.32: f. Impeller rotational speed - Heat map of 14x14x1 grid with normalized concentrations of particle 2 at time=31s.

The heat maps for every level in Figure 5.32 show more or less similar results which is in line with the global trend shown in Figure 5.29. Additionally, Figure 5.33 and Figure 5.34 clearly illustrate differences in mixture development for the first five seconds of mixing, compared to Figure 5.4 presented in Section 5.1.

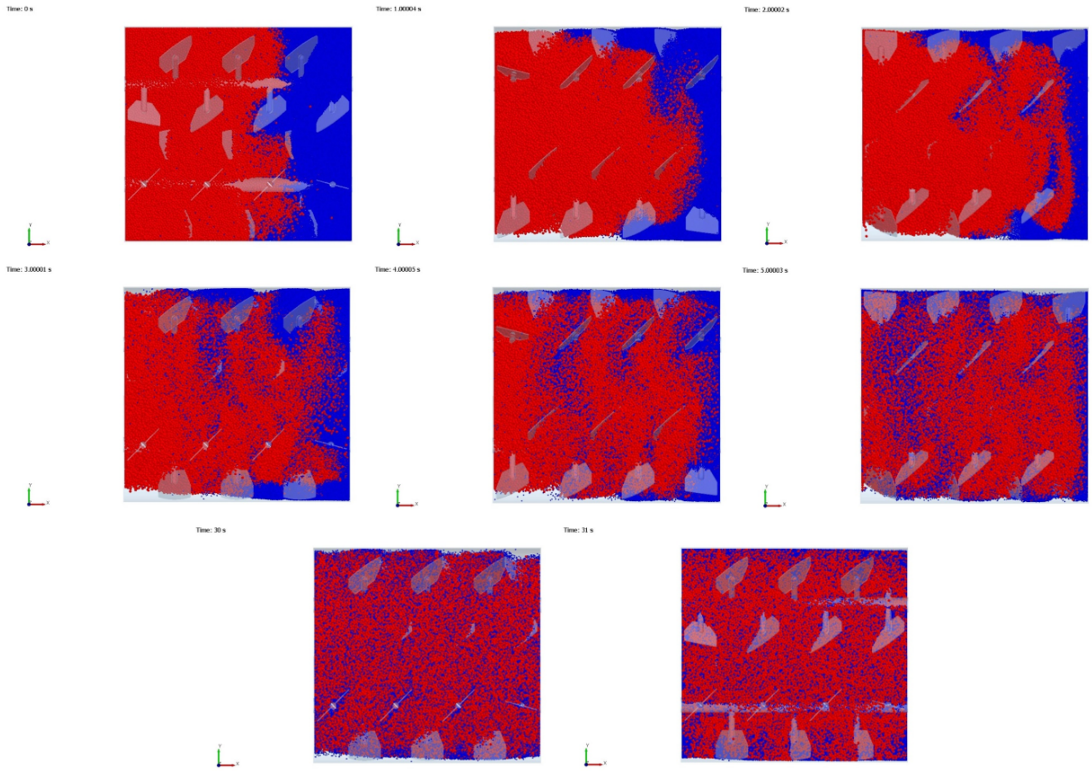

Figure 5.33: Top view of simulation 12 - Impeller rotational speed (40 rpm) for time step t=0s, t=1s, t=2s, t=3s, t=4s, t=5s, t=30s and t=31s.

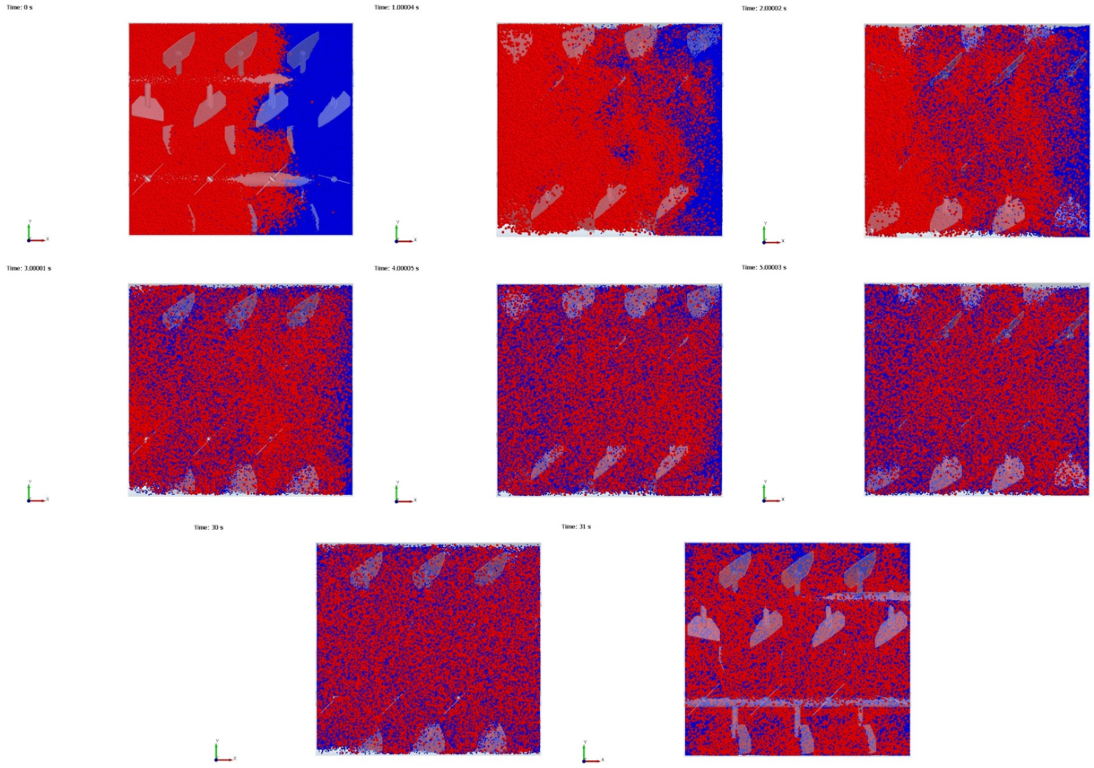

Figure 5.34: Top view of simulation 13 - Impeller rotational speed (80 rpm) for time step t=0s, t=1s, t=2s, t=3s, t=4s, t=5s, t=30s and t=31s.

5.7. Paddle size

The influence of the paddle size on the mixing performance of the paddle mixer is shown in Figure 5.35. The plots shown in Figure 5.36 present the KPI 1 and KPI 2 values for the researched levels.

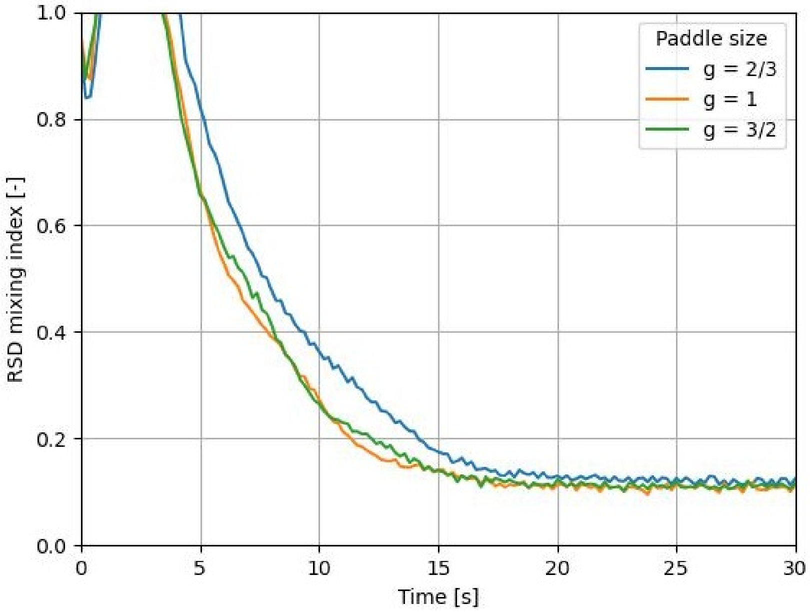

Figure 5.35: RSD mixing index over time for different paddle sizes.

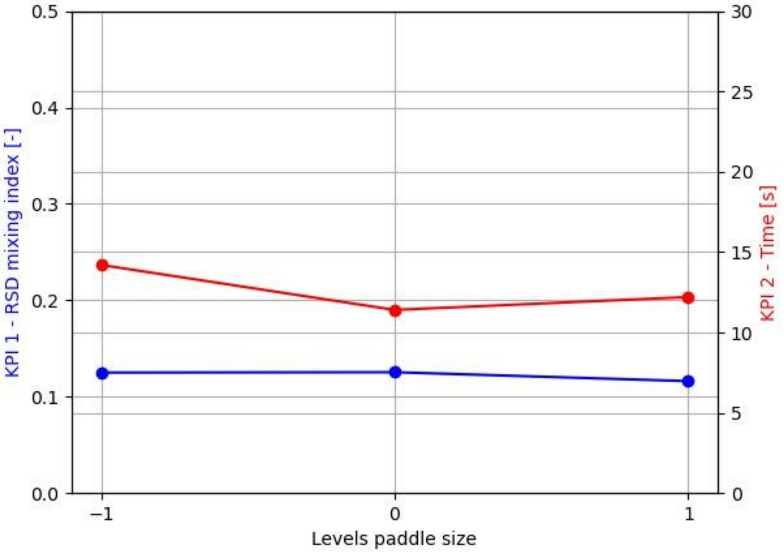

Figure 5.36: Main effect paddle size on KPI 1 and KPI 2.

According to Figure 5.35, a smaller paddle size results in a slower mixing process. It can also be observed that the paddle size g=1 and g=3/2 perform equally well. In literature, no research has (yet) been conducted on the effect of the paddle size on the mixing performance of the paddle mixer. As explained in Section 5.6, a highly dynamic and diffusive fluidized zone is beneficial for the mixing performance of the system. The paddle part that contributes most to such a fluidized zone is the outermost part of the paddle near the inner wall of the mixing chamber, because the centrifugal force is highest at this position, indirectly increasing particle velocity. As the material that is added or removed from the original paddle size (Section 4.3) is done inside out meaning in radial direction outwards, the paddle size does not affect the mixing performance significantly. The final steady-state RSD is similar for all three levels.

The heat maps shown in Figure 5.37 show no major differences between the paddle size levels.

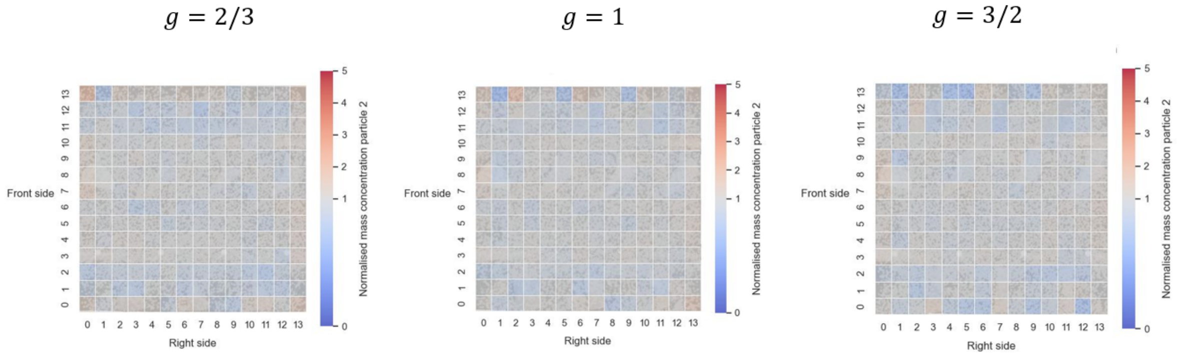

Figure 5.37: g. Paddle size - Heat map of 14x14x1 grid with normalized concentrations of particle 2 at time=31s.

5.8. Paddle angle

The influence of the paddle angle on the mixing performance of the paddle mixer is shown in Figure 5.38. The plots shown in Figure 5.39 present the KPI 1 and KPI 2 values for the researched levels.

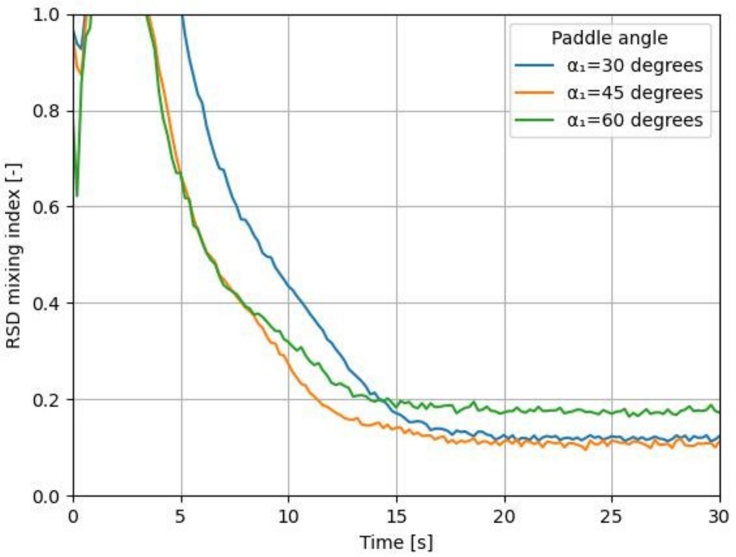

Figure 5.38: RSD mixing index over time for different paddle angles.

Looking at Figure 5.38, it can be stated the paddle angle equal to α_1=45° is the best performing one. This paddle angle outperforms the α_1=30° paddle angle in terms of mixing efficiency, and does the same for the α_1=60° paddle angle in terms of final steady-state mixing quality.

In literature, Jadidi et al. [34] used a paddle mixer with fixed, 0°-angled paddles. Consequently, radial mixing was the dominant mixing mechanism compared to the axial mixing mechanism. In 2018, Ebrahimi et al. [21] investigated the impeller configuration of a single shaft paddle mixer. From the five different impeller configurations (0°, 30°, 45°, 60° and rectangular impellers) the 30°-angled paddle resulted in the best performing paddle followed by the 45°-angled paddle.

With respect to the double shaft paddle mixer a similar result was expected. On the one hand, a 0°-angled paddle configuration lacks the ability to stimulate axial mixing. On the other hand, an angle approaching 90° would be disadvantageous for radial mixing. The optimum paddle angle will lay in between these two extremes.

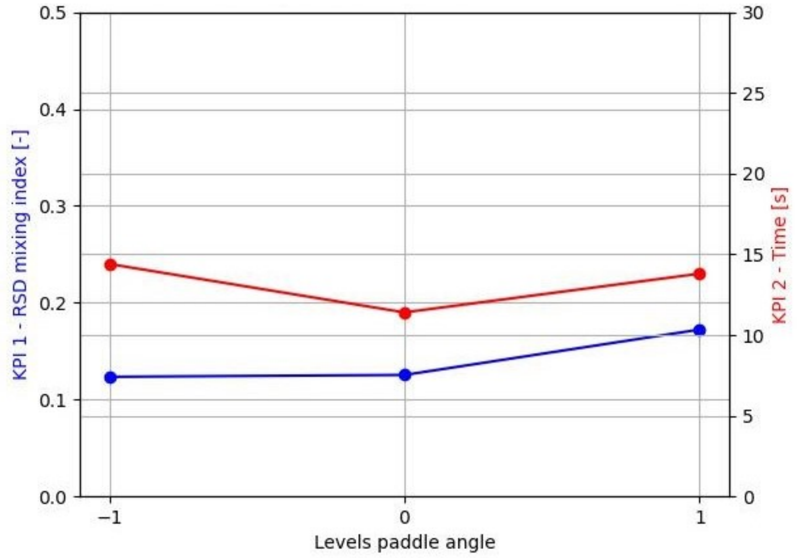

Figure 5.39: Main effect paddle angle on KPI 1 and KPI 2.

An interesting observation is the difference in final steady-state mixture quality between the 60° paddle angle compared to the α_1=30° and α_1=45° paddle angles. The paddle mixer with α_1=60° paddles is not able to perform equally well compared to the other two configurations. Figure 5.40 depict the origin of the problem. At the left and right walls of the mixing machine, many particle velocities are equal to zero or close to zero. The α_1=60° angled paddles are not able to grab all particles near the walls resulting in a lower steady-state RSD eventually.

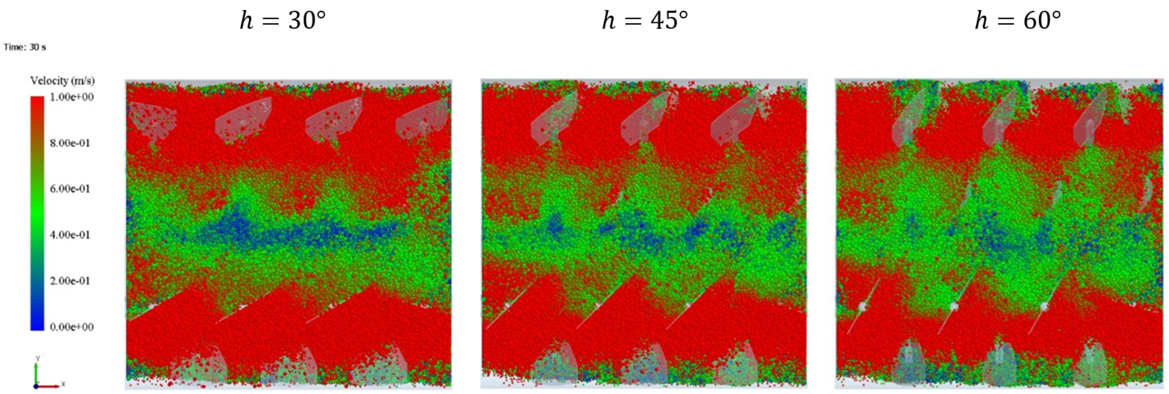

Figure 5.40: Velocity of particles from top view for all three paddle angles at time=31s.

Figure 5.41 clearly shows a pattern where the mass concentration of component 2 is low. On the height of bins 1-2 and 11-12 at the the front side, over the length of the mixing chamber there is a deficiency of component 2. According to the screenshots in Appendix D, component 2 nests itself near the wall at bin 0 and 13 from the front side. It is assumed the α_1=60°-angled paddles are not able to grasp the outermost material due to a decrease in projected paddle surface.

5.9. Paddle number

The influence of the paddle number on the mixing performance of the paddle mixer is shown in Figure 5.42. The plots shown in Figure 5.43 present the KPI 1 and KPI 2 values for the (initial) researched levels.

According to Figure 5.42 and Figure 5.43, the paddle number does have an influence on both the mixing efficiency (KPI 2) and mixing effectiveness (KPI 1). Less paddles compared to the original

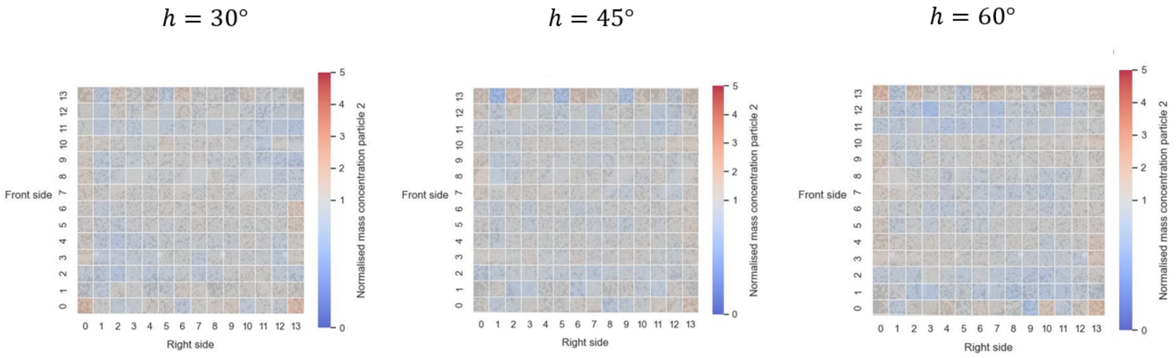

Figure 5.41: h. Paddle angle - Heat map of 14x14x1 grid with normalized concentrations of particle 2 at time=31s.

paddle number (equal to 14), would mean less particles will be relocated over time and thus slower mixing. With respect to mixing efficiency, a paddle number of 28 did not lead to expected result. More paddles do not contribute to reaching the steady-state RSD quicker. The creation of a stagnant fluidized zone is causing the slower mixing mechanism compared to the i=14 level (indicated by the blue color in Figure 5.44).

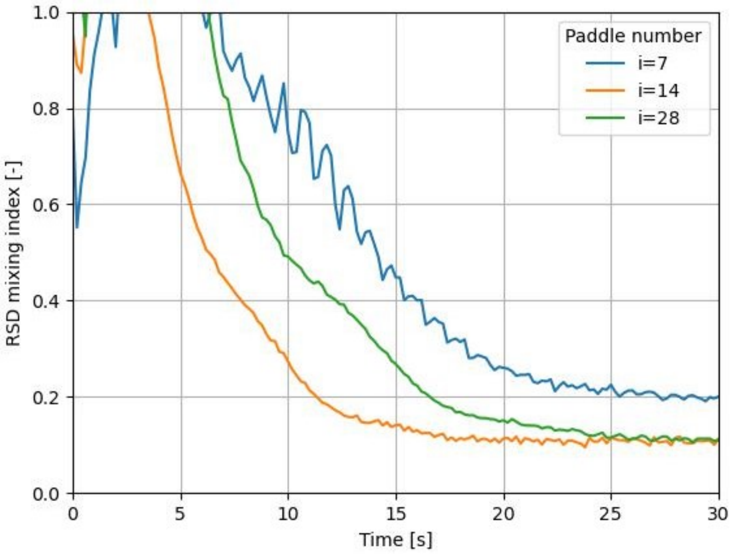

Figure 5.42: RSD mixing index over time for different paddle numbers.

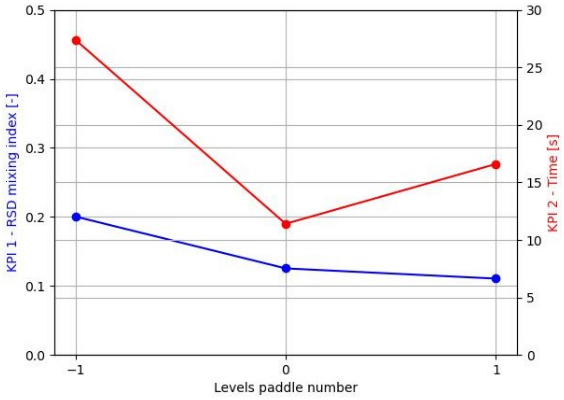

Figure 5.43: Main effect paddle number on KPI 1 and KPI 2.

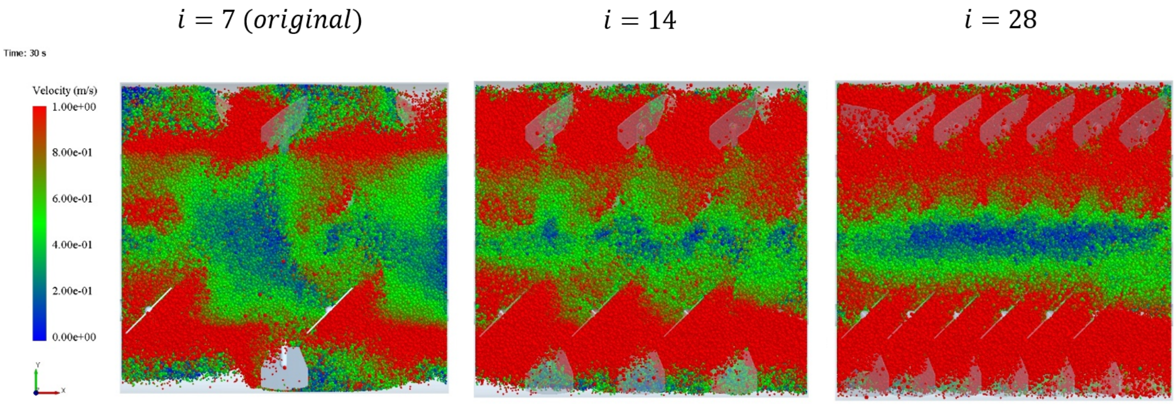

$i = 7\ (original)$ $i = 14$ $i = 28$

Figure 5.44: Velocity of particles from top view for all three paddle number levels at time=31s.

Furthermore, a dissimilarity is observed between steady-state RSD values. A paddle number i=7 ends up at a higher RSD compared to the other two. The dissimilarity in steady-state RSD values between paddle number equal to i=7 compared to i=14 and i=28 paddle numbers is caused by local differences in the particle bed as shown in Figure 5.45. It can be clearly observed that 7 paddles are not able to distribute component 2 equally well along the mixing chamber. Figure 5.46 shows the velocity of particles for the time period 29.2-30s (full rotation of the shafts). The blue color indicate the stagnant zones which are both spatially and temporally dependent. It is believed these zones are the main cause of the discrepancy in RSD after 30 seconds of mixing compared to the paddle numbers equal to i=14 and i=28.

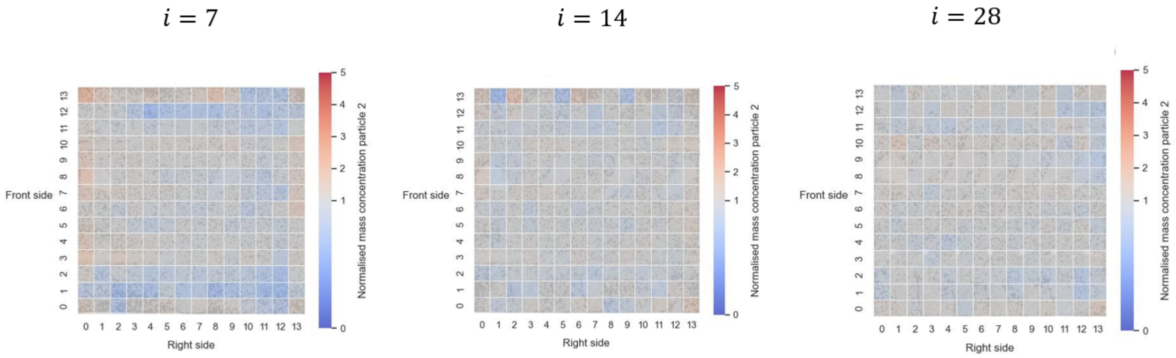

$i = 7$ $i = 14$ $i = 28$

Figure 5.45: i. Paddle number - Heat map of 14x14x1 grid with normalized concentrations of particle 2 at time=31s.

After the first analysis it is decided to also investigate two variants of the paddle number i=7 (Figure 5.47) The results are shown in Figure 5.48 and Figure 5.49.

As can be concluded from Figure 5.48, different configurations of the paddle number i=7 leads to different results, but eventually an identical steady-state RSD value is reached for all three variants of the i=7 level.

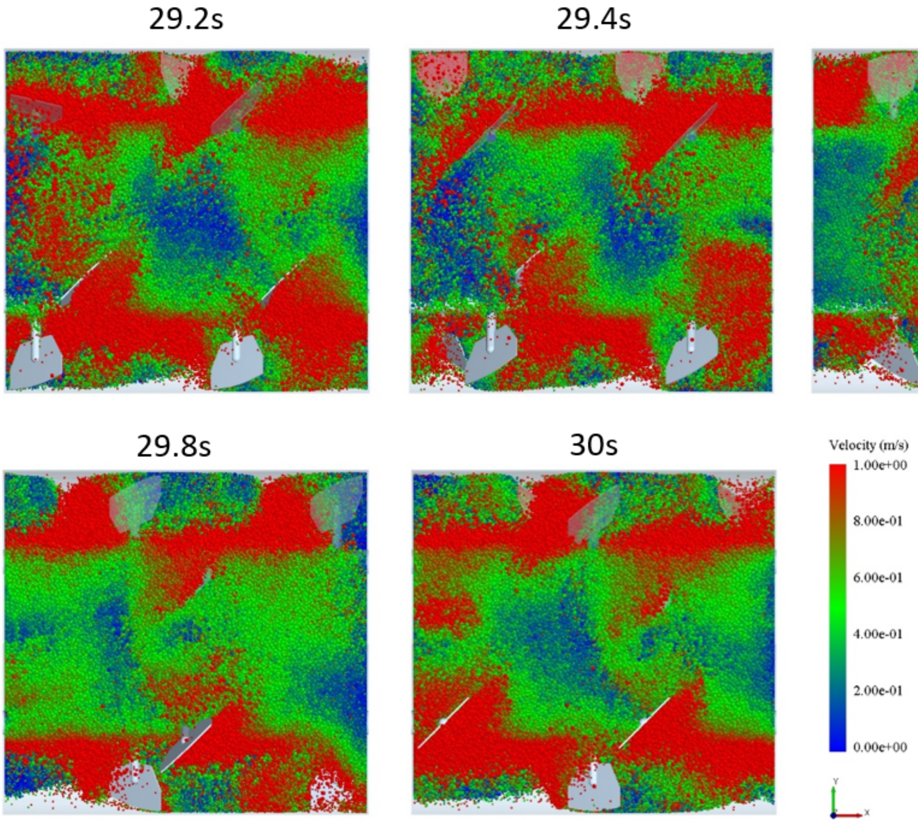

Figure 5.46: Velocity of particles from top view for the paddle number equal to 7 for time range 29.2-30s.

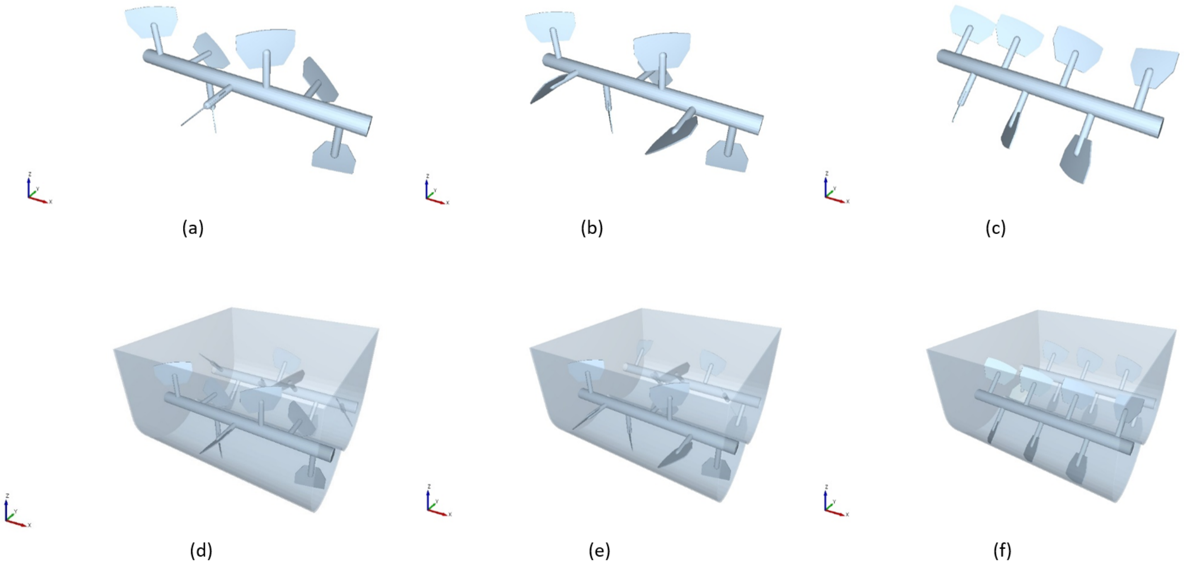

Figure 5.47: (a) Original paddle number of 7, (b) variant 1, (c) variant 2, (d) Original shaft configuration, (e) shaft configuration for variant 1 and (f) shaft configuration of variant 2. Shaft2 is used for the illustration.

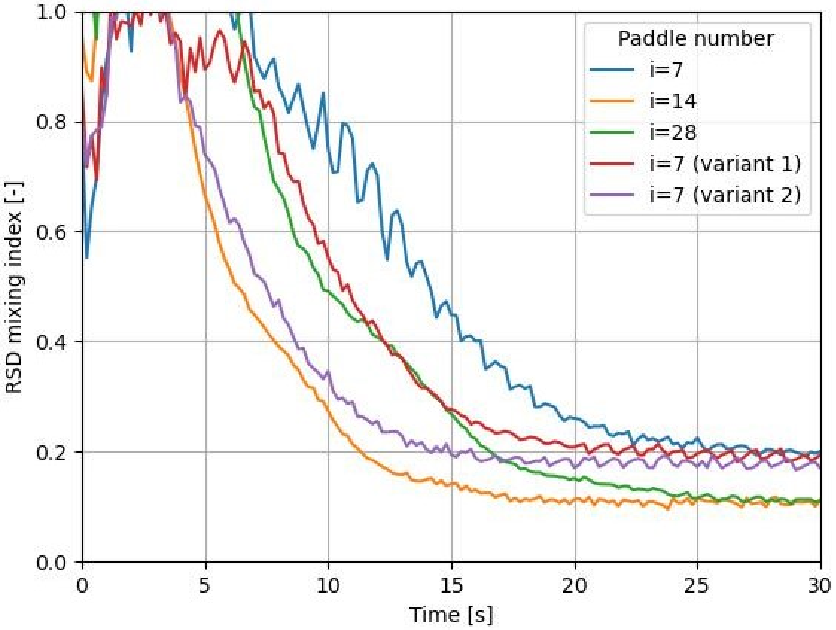

Figure 5.48: RSD mixing index over time for different paddle numbers, including variant 1 and variant 2 of the paddle number equal to 7.

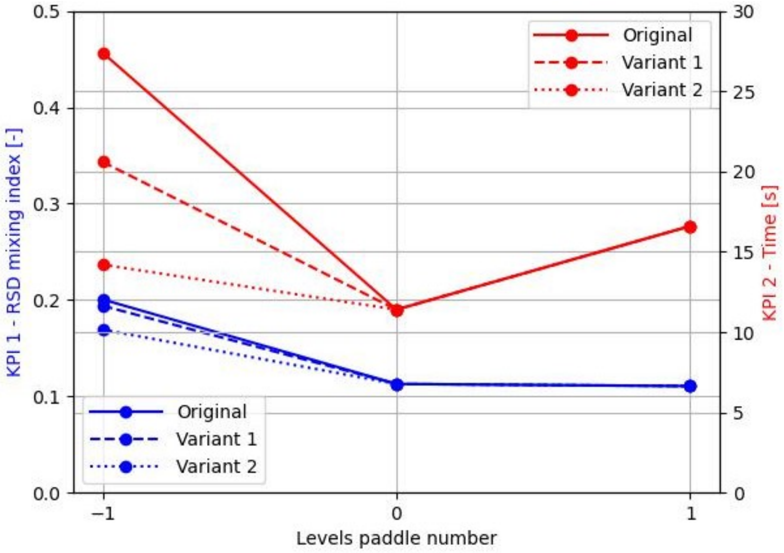

Figure 5.49: Main effect paddle number on KPI 1 and KPI 2, including two variants of the paddle number equal to 7.

6

Conclusions

The formulated sub-questions as presented in Chapter 1 are answered in this chapter. For more details about the given answers consult Chapter 3 and Chapter 4 depending on which sub-question is of interest (Figure 1.5 for an overview). Finally, the research question is answered based on the results presented in Chapter 5.

1. *What kind of modeling method is suitable for this research?*

Granular material such as powders or granules consists of many small, solid particles that come into contact with each other or with handling equipment when processed. The dynamic and complex behavior of granular material caused by the paddle mixer requires a sophisticated model that can provide insights into the mixing mechanism and flow patterns of the system. Besides, it is not possible (yet) to track every particle individually during physical experiments. The most suitable computational modeling method for particulate systems is the Discrete Element Method (DEM), applied in many different fields like the food industry, pharmaceutical industry and chemical industry. The possibility to simulate material on a particle level is one of the great advantages. The working principle of DEM lies in the ability to model a finite number of discrete particles in a fixed, bounded system that can interact with each other, governed by Newton's equation of motion. Great advantages are the reduction in time and cost compared to physical experiments leading to quicker innovative designs and processes. Still, computational expenses of DEM result in limitations with respect to simulation of realistic amounts, sizes and shapes of particles that are often encountered in industry.

2. *How should the current system be converted into a simulation model?*

A 175L double shaft, batch-type paddle mixer is chosen to be modeled in EDEM™ which is one out of the many different paddle mixers engineered, manufactured and sold by Dinnissen. Only most relevant parts are converted into the geometric model. Moreover, a material model adopted from Jadidi et al. [34] is used as starting point for the research. A two-component material model is utilized consisting of free-flowing, spherical glass beads. Lastly, the simulation strategy consists of a filling process and a mixing process. In the former, all input settings are defined. The latter is meant for the actual mixing of the material for a total time of 30 seconds from a stationary particle bed, where the filling process results are used as input for the mixing process simulation.

3. *How to ensure a robust and fit-for-purpose simulation model for the system?*

In numerical computation algorithms as DEM, one should be aware of the stability of the simulation model. To ensure stability, time efficiency and realistic behavior of the material for all DEM simulations in the experimental simulation plan, a 'worst-case scenario' is being set up. As the name already suggests, this simulation is meant to analyze the system's stability for the least beneficial situation. A two-step approach is followed where first the shear modulus is varied followed by the time step. Responses like the computation time, stability in terms of energy ratio between kinetic energy E_{kin}

and potential energy E_{pot} and the voidage of the particle bed are evaluated. Based on the outputs, a suitable shear modulus and time step is chosen such that the computation time is reduced without compromising the stability of the simulation and staying within realistic limits concerning the voidage of the particle bed.

4. What type of experimental simulation plan to use for investigating the influence of selected factors on mixing performance of the system?

The high number of selected factors to investigate has led to an OFAT approach as most suitable experimental simulation plan. First of all, this method is characterized by its simplicity. Secondly, no external software is required as is the case for more sophisticated, statistics-based methods like the Plackett-Burman (PB) and the Definitive Screening Design (DSD). Lastly, the possibility to do a qualitative analysis by visually observing the particle bed is the third advantage. The latter is the decisive factor to choose for this particular method, besides the fact no interactions are captured between factors, a high number of runs are required and confounding effects can be present. To be able to understand the mixing mechanisms and flow patterns for every investigated factor visual observations are necessary. With statistics-based DoE's, this is not possible because more than one factor will be changed for one simulation.

5. Which factors could influence the mixing performance of the system?

The factors that are selected for this research are based on literature and consultation with the company. As research about double shaft, batch-type paddle mixers is scarce, published articles about other mixing applications are reviewed. Frequently material characteristics that influence the mixing performance of various mixing applications are the particle size, particle density and composition. The operational condition factors selected are based on the published paper by Jadidi et al. [34] which are the initial filling pattern, fill level and impeller rotational speed. Finally, the geometric factors are mainly focused on the paddles of the mixer. After consultation with the company, the paddle size, paddle angle and paddle number are chosen.

6. What factor values to be chosen for the experimental simulation plan?

The factor range selected for every factor is partly based on literature and partly based on practice. Extreme but realistic factor ranges are defined that are broad enough to explore the effect of a respective factor on the mixing performance of the system. An overview is provided in Table 4.2.

7. How to assess the mixing performance of the system?

To assess the mixing performance of the system, both quantitative and qualitative analyses have been executed. Concerning quantitative analysis, first a mixing index is selected based upon a Multi Criteria Decision Analysis (MCDA). The Relative Standard Deviation (RSD) is chosen to be most suitable for this particular research. The RSD equal to one indicates a completely segregated mixture and a RSD of zero a perfectly mixed mixture. To investigate both the mixing efficiency and mixing effectiveness, two Key Performance Indicators (KPI's) are defined and tailored to the paddle mixer, which are:

KPI 1: The RSD after 30 seconds of mixing - The first KPI indicate the mixing effectiveness of the system for investigated factor level.

KPI 2: The time it takes to reach a RSD smaller than or equal to 0.2 - The second KPI indicates the mixing efficiency towards the steady-state RSD value. In other words, how fast does the mixture quality of one factor level evolve.

To be able to extract the data from EDEM™ required to calculate the RSD, a 14x14x9 grid system is designed that is spanned out over the full system. The grid system has been subjected to a thorough analysis and evaluated as suitable for most simulations.

Furthermore, qualitative analysis is done by the generation of screenshots and heat maps. The former serves the purpose of visual feedback on mixing mechanisms and flow patterns. The latter shows local differences in the particle bed by a grid system consisting of discrete elongated bins in x, y or z directions, derived from the global 14x14x9 grid system.

All answers to the sub-questions have been answered. Next, an answer is formulated on the research question, which reads as follows:

What is the main effect of a selection of factors on the mixing performance of a batch-type, double shaft paddle mixer?

After thorough data analysis and discussion in Chapter 5, conclusions can be drawn on the effect of selected factors on the mixing performance of the double shaft, batch-type paddle mixer. The results must be interpreted correctly. The main effects of selected factors will be the result of chosen OFAT approach and no factor interactions are captured. Accordingly, conclusions drawn about every individual factor in this chapter are only valid with all other factors are fixed at specific values.[1].

The mixing performance is evaluated on mixing effectiveness (KPI 1) and mixing efficiency (KPI 2). An overview of all results is shown in Figure 6.1. The partially greyed-out plots of the composition and fill level are not considered. The c=99/1 composition results are affected by the designed 14x14x9 grid system, even as the e=40% fill level and require further research to draw valid conclusions. The e=140% fill level did not reach a steady-state RSD after 30 seconds of mixing and is therefore excluded.

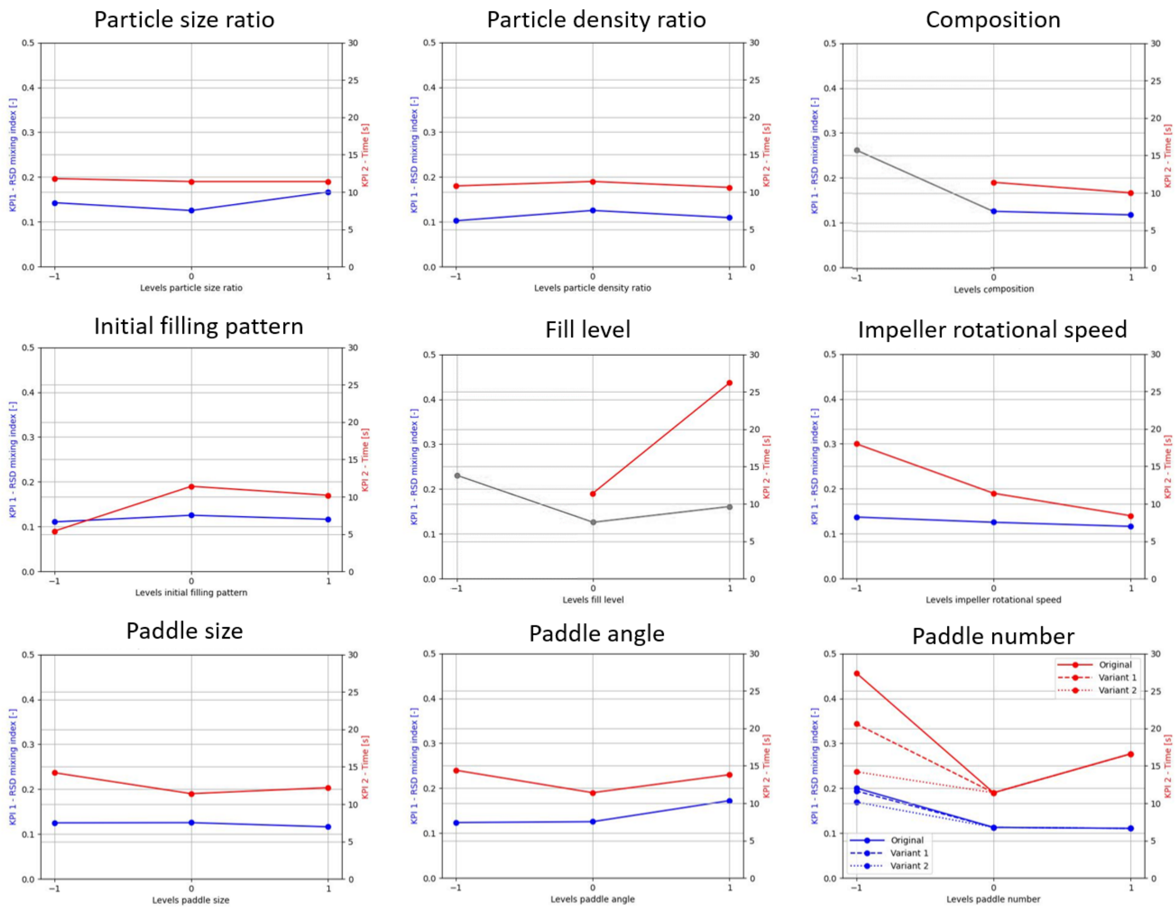

Figure 6.1: Overview of the influence of all factors on KPI and KPI 2. Greyed out plots of the composition and fill levels are not considered.

With respect to the mixing effectiveness (KPI 1) as shown in Figure 6.1, the factors particle size,

---

[1] The specific values can be found in Table 4.2 and represent the center point simulation.

particle density, paddle angle and paddle number have a significant influence on the final steady-state RSD value reached after 30 seconds of mixing.

Furthermore, it can be observed that all factors have a nonlinear relation (besides particle density) with evaluated KPI 1. Initially it was expected that an increase in particle size ratio would cause an increase in KPI 1. However, as shown in Figure 6.1 this is not true. Literature suggest that interplay of particle size and particle density can cause mixing to be enhanced or attenuated. Therefore, the non-linearity of the particle size is expected to originate from the interaction with the particle density.

With respect to the paddle angle, an optimal configuration exists between the 30 and 60 degrees. Thus, it can be concluded that the radial mixing and the axial mixing mechanisms both contribute to the mixing performance of the paddle mixer. Increasing the number of paddles will improve the mixing effectiveness up to a certain point. Eventually, the extra surface that relocates the granular material will not add value anymore. What the tipping point is concerning the addition of paddles needs further investigation. Besides, how the paddles are assembled onto the shaft could also have an effect on KPI 1 as shown by the different variants of the paddle number equal to 7 (Figure 6.1).

With respect to the mixing efficiency (KPI 2) as shown in Figure 6.1, the factors initial filling pattern, fill level, impeller rotational speed and paddle number have a major influence. The factors composition, paddle size and paddle angle have a substantial influence.

Moreover, the factors paddle size, paddle angle and paddle number do have a nonlinear relation with KPI 2. The initial filling pattern is excluded here since it is a categorical factor. But, it can be stated that the Top-Bottom (TB) initial filling pattern performs best compared to the Front-Back (FB) and Side-by-Side (SS) patterns. Additionally, increasing the impeller rotational speed results in a decrease of KPI 2. In other words, mixing of the product occurs faster. Finally, the effect of the paddle number on KPI 2 is significant. Irrespective of the i=7 paddle variants (introduced in Section 5.9), it can be observed that the mixing efficiency does not improve when eliminating 7 paddles or adding 14 paddles to the original paddle number of i=14.

In Figure **??**, the factor significance on the mixing performance is shown. The particle size and particle density have a significant effect on the final mixture quality after 30 seconds of mixing (KPI 1: Mixing effectiveness). The composition, initial filling pattern, impeller rotational speed and paddle size have a significant effect on how fast a steady-state mixture quality is reached (KPI 2: Mixing efficiency). The paddle angle and paddle number have a significant effect on both KPI's and therefore holds most potential with respect to optimization purposes.

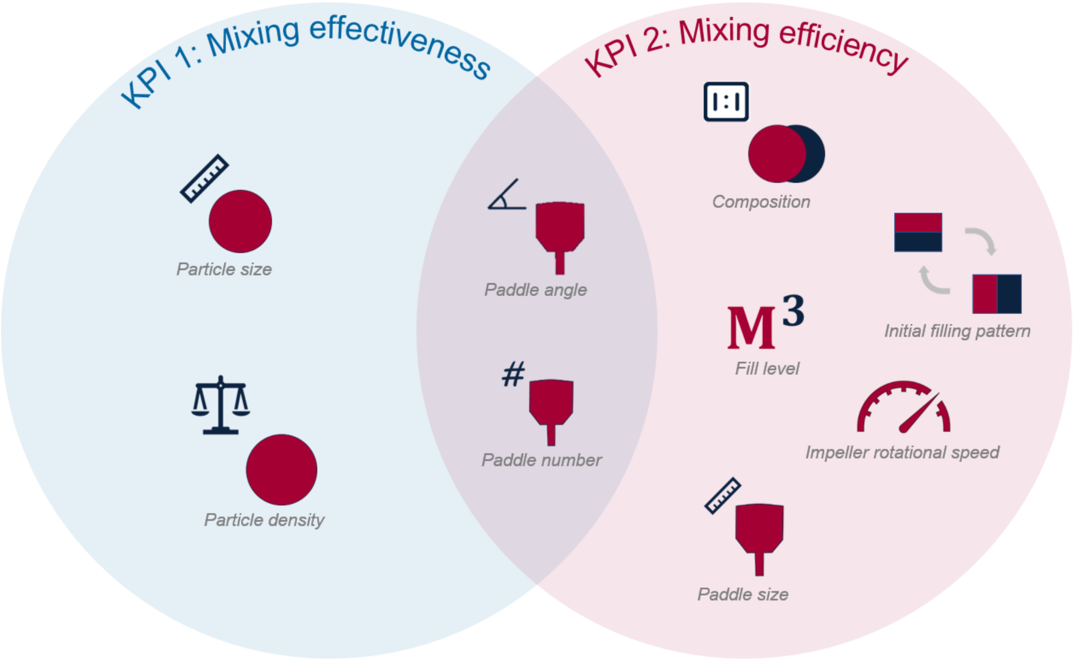

Figure 6.2: Venn diagram of factor significance with regard to KPI 1: Mixing effectiveness and KPI 2: Mixing efficiency.

7

Recommendations

The limitations of this research opens up possibilities for further research. Below, a number of recommendations are presented that is necessary and/or interesting to investigate with respect to further research.

1. Validation of the retrieved results by means of real-world physical experiments. Already during the scope definition, experimental work is taken into account by the choice of paddle mixer to analyse. The 175L paddle mixer is present at the Dinnisen Test center.
2. With the current OFAT approach, interactions between factors are missed. To be able to obtain interactions and make a deliberate choice on which factors to investigate further for optimization purposes, more simulations are required. An experimental simulation plan in the form of a Design of Experiments (DoE) could capture interaction in an efficient number of runs. It is advised to focus on the operational conditions and geometric properties of the paddle mixer.
3. The effect of cohesion or particle shape are two other important factors that could be interesting research subjects. In general, powders are being mixed with the double shaft paddle mixer. The micrometer level particle size of a powder is more prone to cohesive forces between particles. Moreover, in practice mixed granular material, regardless of whether it is powder or granules, do consists of irregularly shaped particles. Another geometric factor that is worth investigating is the form of the mixing chamber. As mentioned in the introductory text of Chapter 5, according to the heat maps the mixture quality is relatively lower near right and left side walls than in the center of the mixing chamber for almost all simulations. It is believed the mixing chamber's form contributes to this phenomenon.

Bibliography

[1] Basel Alchikh-Sulaiman et al. “Using the discrete element method to assess the mixing of polydisperse solid particles in a rotary drum”. en. In: *Particuology* 25 (Apr. 2016), pp. 133–142. ISSN: 1674-2001. DOI: `10.1016/j.partic.2015.05.006`. URL: `https://www.sciencedirect.com/science/article/pii/S1674200115001522` (visited on 03/25/2022).

[2] Meysam Alian, Farhad Ein-Mozaffari, and Simant R. Upreti. “Analysis of the mixing of solid particles in a plowshare mixer via discrete element method (DEM)”. en. In: *Powder Technology* 274 (Apr. 2015), pp. 77–87. ISSN: 0032-5910. DOI: `10.1016/j.powtec.2015.01.012`. URL: `https://www.sciencedirect.com/science/article/pii/S0032591015000224` (visited on 04/19/2022).

[3] Jiju Antony. “2 - Fundamentals of Design of Experiments”. en. In: *Design of Experiments for Engineers and Scientists (Second Edition)*. Ed. by Jiju Antony. Oxford: Elsevier, Jan. 2014, pp. 7–17. ISBN: 978-0-08-099417-8. DOI: `10.1016/B978-0-08-099417-8.00002-X`. URL: `https://www.sciencedirect.com/science/article/pii/B978008099417800002X` (visited on 08/30/2022).

[4] Jiju Antony. “5 - Screening Designs”. en. In: *Design of Experiments for Engineers and Scientists (Second Edition)*. Ed. by Jiju Antony. Oxford: Elsevier, Jan. 2014, pp. 51–62. ISBN: 978-0-08-099417-8. DOI: `10.1016/B978-0-08-099417-8.00005-5`. URL: `https://www.sciencedirect.com/science/article/pii/B9780080994178000055` (visited on 08/30/2022).

[5] M. M. H. D. Arntz et al. “Granular mixing and segregation in a horizontal rotating drum: A simulation study on the impact of rotational speed and fill level”. en. In: *AIChE Journal* 54.12 (2008), pp. 3133–3146. ISSN: 1547-5905. DOI: `10.1002/aic.11622`. URL: `https://onlinelibrary.wiley.com/doi/abs/10.1002/aic.11622` (visited on 07/06/2022).

[6] P. E. Arratia et al. “A study of the mixing and segregation mechanisms in the Bohle Tote blender via DEM simulations”. en. In: *Powder Technology* 164.1 (May 2006), pp. 50–57. ISSN: 0032-5910. DOI: `10.1016/j.powtec.2006.01.018`. URL: `https://www.sciencedirect.com/science/article/pii/S0032591006000398` (visited on 03/24/2022).

[7] Maryam Asachi, Ehsan Nourafkan, and Ali Hassanpour. “A review of current techniques for the evaluation of powder mixing”. en. In: *Advanced Powder Technology* 29.7 (July 2018), pp. 1525–1549. ISSN: 0921-8831. DOI: `10.1016/j.apt.2018.03.031`. URL: `https://www.sciencedirect.com/science/article/pii/S0921883118301298` (visited on 10/11/2022).

[8] G. Basinskas and M. Sakai. “Numerical study of the mixing efficiency of a ribbon mixer using the discrete element method”. English. In: *Powder Technology* 287 (2016), pp. 380–394. ISSN: 0032-5910. DOI: `10.1016/j.powtec.2015.10.017`.

[9] F. Bertrand, L. -A. Leclaire, and G. Levecque. “DEM-based models for the mixing of granular materials”. en. In: *Chemical Engineering Science*. 5th International Symposium on Mixing in Industrial Processes (ISMIP5) 60.8 (Apr. 2005), pp. 2517–2531. ISSN: 0009-2509. DOI: `10.1016/j.ces.2004.11.048`. URL: `https://www.sciencedirect.com/science/article/pii/S0009250904009492` (visited on 03/08/2022).

[10] Pooja Bhalode and Marianthi Ierapetritou. “A review of existing mixing indices in solid-based continuous blending operations”. en. In: *Powder Technology* 373 (Aug. 2020), pp. 195–209. ISSN: 0032-5910. DOI: `10.1016/j.powtec.2020.06.043`. URL: `https://www.sciencedirect.com/science/article/pii/S0032591020305635` (visited on 03/22/2022).

[11] J. Bridgwater. “Mixing of powders and granular materials by mechanical means - A perspective”. English. In: *Particuology* 10.4 (2012), pp. 397–427. ISSN: 1674-2001. DOI: `10.1016/j.partic.2012.06.002`.

[12] R. Cai, Z. Hou, and Y. Zhao. "Numerical study on particle mixing in a double-screw conical mixer". English. In: *Powder Technology* 352 (2019), pp. 193–208. ISSN: 0032-5910. DOI: `10.1016/j.powtec.2019.04.065`.

[13] E.L. Chan et al. "Dem investigation of horizontal high shear mixer flow behaviour and implications for scale-up". English. In: *Powder Technology* 270.PB (2015), pp. 561–568. ISSN: 0032-5910. DOI: `10.1016/j.powtec.2014.09.017`.

[14] Hui Chen et al. "Radial mixing and segregation of granular bed bi-dispersed both in particle size and density within horizontal rotating drum". en. In: *Transactions of Nonferrous Metals Society of China* 26.2 (Feb. 2016), pp. 527–535. ISSN: 1003-6326. DOI: `10.1016/S1003-6326(16)64110-9`. URL: `https://www.sciencedirect.com/science/article/pii/S1003632616641109` (visited on 04/08/2022).

[15] Shih-Hao Chou, Yue-Lou Song, and Shu-San Hsiau. *A Study of the Mixing Index in Solid Particles*. 2017. URL: `https://www.jstage.jst.go.jp/article/kona/34/0/34_2017018/_article/-char/ja/` (visited on 05/16/2022).

[16] P.W. Cleary and M.D. Sinnott. "Assessing mixing characteristics of particle-mixing and granulation devices". English. In: *Particuology* 6.6 (2008), pp. 419–444. ISSN: 1674-2001. DOI: `10.1016/j.partic.2008.07.014`.

[17] Stephen Cole. *EDEM Simulation Run Time - EDEM - Altair Products - Altair Community*. Altair Community. Jan. 2022. URL: `https://community.altair.com/community?id=community_blog&sys_id=8fa2ba98dba32410e8863978f4961938` (visited on 09/27/2022).

[18] P. A. Cundall. "A Computer Model for Simulating Progressive, Large-scale Movement in Blocky Rock System". In: *Proceedings of the International Symposium on Rock Mechanics, 1971* (1971). URL: `https://ci.nii.ac.jp/naid/10018723276/` (visited on 03/09/2022).

[19] P. A. Cundall and O. D. L. Strack. "A discrete numerical model for granular assemblies". In: *Géotechnique* 29.1 (Mar. 1979). Publisher: ICE Publishing, pp. 47–65. ISSN: 0016-8505. DOI: `10.1680/geot.1979.29.1.47`. URL: `https://www.icevirtuallibrary.com/doi/abs/10.1680/geot.1979.29.1.47` (visited on 03/09/2022).

[20] S. Deng et al. "Radial mixing of metallurgical slag particles and steel balls in a horizontally rotating drum: A discussion of particle size distribution and mixing time". English. In: *Powder Technology* 378 (2021), pp. 441–454. ISSN: 0032-5910. DOI: `10.1016/j.powtec.2020.10.022`.

[21] M. Ebrahimi et al. "The effect of impeller configurations on particle mixing in an agitated paddle mixer". English. In: *Powder Technology* 332 (2018), pp. 158–170. ISSN: 0032-5910. DOI: `10.1016/j.powtec.2018.03.061`.

[22] Mohammadreza Ebrahimi et al. "Assessment of bi-disperse solid particles mixing in a horizontal paddle mixer through experiments and DEM". en. In: *Powder Technology* 381 (Mar. 2021), pp. 129–140. ISSN: 0032-5910. DOI: `10.1016/j.powtec.2020.11.041`. URL: `https://www.sciencedirect.com/science/article/pii/S0032591020310949` (visited on 02/01/2022).

[23] Z. Fang et al. "Structure optimization of plough blades in a ploughshare mixer using the DEM simulations". English. In: *Engineering Computations (Swansea, Wales)* 37.9 (2020), pp. 3455–3475. ISSN: 0264-4401. DOI: `10.1108/EC-01-2020-0032`.

[24] H.j. Feise and J.w. Carson. "The Evolution of Bulk Solids Technology Since 1982". de. In: *Chemical Engineering & Technology* 26.2 (2003), pp. 121–131. ISSN: 1521-4125. DOI: `10.1002/ceat.200390018`. URL: `https://onlinelibrary.wiley.com/doi/abs/10.1002/ceat.200390018` (visited on 03/09/2022).

[25] Halvor G. Forberg. "Twin Horizontal Axled Inwardly Rotating Paddle Mixer for Dry Ingredients". Mar. 1983.

[26] S. Golshan and B. Blais. "Insights into granular mixing in vertical ribbon mixers". English. In: *Canadian Journal of Chemical Engineering* 99.7 (2021), pp. 1570–1581. ISSN: 0008-4034. DOI: `10.1002/cjce.23965`.

[27] Andrew Grima. “Quantifying and modelling mechanisms of flow in cohesionless and cohesive granular materials”. In: *University of Wollongong Thesis Collection 1954-2016* (Jan. 2011). URL: `https://ro.uow.edu.au/theses/3425`.

[28] M. Halidan et al. “Prediction of the mixing behaviour of binary mixtures of particles in a bladed mixer”. en. In: *Chemical Engineering Science* 120 (Dec. 2014), pp. 37–48. ISSN: 0009-2509. DOI: `10.1016/j.ces.2014.08.048`. URL: `https://www.sciencedirect.com/science/article/pii/S0009250914004734` (visited on 04/14/2022).

[29] A. Hassanpour et al. “Analysis of particle motion in a paddle mixer using Discrete Element Method (DEM)”. English. In: *Powder Technology* 206.1-2 (2010), pp. 189–194. ISSN: 0032-5910. DOI: `10.1016/j.powtec.2010.07.025`.

[30] H. Hertz. “On the contact of elastic solids”. In: *Z. Reine Angew. Mathematik* 92 (1881), pp. 156–171. URL: `https://ci.nii.ac.jp/naid/10015562849/` (visited on 03/28/2022).

[31] Hosokawa Micron B.V. *Low Shear Batch Mixing Technology Webinar*. New Jersey, USA, July 2015. URL: `https://www.youtube.com/watch?v=In2af_40LKI` (visited on 02/28/2022).

[32] Behrooz Jadidi et al. “Investigation of Mixing Non-Spherical Particles in a Double Paddle Blender via Experiments and GPU-Based DEM Modeling”. en. In: *Engineering Proceedings* 19.1 (May 2022). Number: 1 Publisher: Multidisciplinary Digital Publishing Institute, p. 24. ISSN: 2673-4591. DOI: `10.3390/ECP2022-12661`. URL: `https://www.mdpi.com/2673-4591/19/1/24` (visited on 08/01/2022).

[33] Behrooz Jadidi et al. “Mixing and segregation assessment of bi-disperse solid particles in a double paddle mixer”. en. In: *Particuology* (July 2022). ISSN: 1674-2001. DOI: `10.1016/j.partic.2022.06.006`. URL: `https://www.sciencedirect.com/science/article/pii/S1674200122001298` (visited on 08/01/2022).

[34] Behrooz Jadidi et al. “Mixing performance analysis of non-cohesive particles in a double paddle blender using DEM and experiments”. en. In: *Powder Technology* 397 (Jan. 2022), p. 117122. ISSN: 0032-5910. DOI: `10.1016/j.powtec.2022.117122`. (Visited on 02/01/2022).

[35] Nitin Jain, Julio M. Ottino, and Richard M. Lueptow. “Regimes of segregation and mixing in combined size and density granular systems: an experimental study”. en. In: *Granular Matter* 7.2 (July 2005), pp. 69–81. ISSN: 1434-7636. DOI: `10.1007/s10035-005-0198-x`. URL: `https://doi.org/10.1007/s10035-005-0198-x` (visited on 10/31/2022).

[36] Alvaro Janda and Jin Y. Ooi. “DEM modeling of cone penetration and unconfined compression in cohesive solids”. en. In: *Powder Technology*. Particle Modelling with the Discrete Element Method A success story of PARDEM (www.pardem.eu) 293 (May 2016), pp. 60–68. ISSN: 0032-5910. DOI: `10.1016/j.powtec.2015.05.034`. URL: `https://www.sciencedirect.com/science/article/pii/S0032591015004209` (visited on 05/23/2022).

[37] X. Jin et al. “DEM investigation of mixing indices in a ribbon mixer”. English. In: *Particuology* 60 (2022), pp. 37–47. ISSN: 1674-2001. DOI: `10.1016/j.partic.2021.03.005`.

[38] R. Kapelle. “Calibration and Verification experiments for Discrete Element Modeling of cohesive materials - Kalibratie en verificatie experimenten voor het Discreet Element Modelleren van cohesieve materialen”. en. In: (2015). URL: `https://repository.tudelft.nl/islandora/object/uuid%3A23e93669-09b1-4f83-b8f1-d302edeb596a` (visited on 03/28/2022).

[39] P. M. C. Lacey. “Developments in the theory of particle mixing”. en. In: *Journal of Applied Chemistry* 4.5 (1954), pp. 257–268. ISSN: 1934-998X. DOI: `10.1002/jctb.5010040504`. URL: `https://onlinelibrary.wiley.com/doi/abs/10.1002/jctb.5010040504` (visited on 03/15/2022).

[40] J. Li, C. Wassgren, and J.D. Litster. “Multi-scale modeling of a spray coating process in a paddle mixer/coater: The effect of particle size distribution on particle segregation and coating uniformity”. English. In: *Chemical Engineering Science* 95 (2013), pp. 203–210. ISSN: 0009-2509. DOI: `10.1016/j.ces.2013.03.014`.

[41] Stef Lommen, Dingena Schott, and Gabriel Lodewijks. “DEM speedup: Stiffness effects on behavior of bulk material”. en. In: *Particuology*. Special issue on conveying and handling of particulate solids – Challenges of discrete element simulation, application and calibration 12 (Feb. 2014), pp. 107–112. ISSN: 1674-2001. DOI: `10.1016/j.partic.2013.03.006`. URL: `https://www.sciencedirect.com/science/article/pii/S1674200113001387` (visited on 05/31/2022).

[42] J. Long et al. “Discrete element simulation for mixing performances and power consumption in a twin-blade planetary mixer with non-cohesive particles”. English. In: *Advanced Powder Technology* 33.2 (2022). ISSN: 0921-8831. DOI: `10.1016/j.apt.2022.103437`.

[43] G. Lu, J. R. Third, and C. R. Müller. “Discrete element models for non-spherical particle systems: From theoretical developments to applications”. en. In: *Chemical Engineering Science* 127 (May 2015), pp. 425–465. ISSN: 0009-2509. DOI: `10.1016/j.ces.2014.11.050`. URL: `https://www.sciencedirect.com/science/article/pii/S0009250914007040` (visited on 03/14/2022).

[44] M. Marigo et al. “A numerical comparison of mixing efficiencies of solids in a cylindrical vessel subject to a range of motions”. English. In: *Powder Technology* 217 (2012), pp. 540–547. ISSN: 1873-328X. DOI: `10.1016/j.powtec.2011.11.016`.

[45] Michele Marigo. “Discrete element method modelling of complex granular motion in mixing vessels: evaluation and validation”. English. d_en. University of Birmingham, July 2012. URL: `https://etheses.bham.ac.uk/id/eprint/3402/` (visited on 03/10/2022).

[46] Michele Marigo and Edmund Hugh Stitt. “Discrete Element Method (DEM) for Industrial Applications: Comments on Calibration and Validation for the Modelling of Cylindrical Pellets”. en. In: *KONA Powder and Particle Journal* 32.0 (2015), pp. 236–252. ISSN: 0288-4534, 2187-5537. DOI: `10.14356/kona.2015016`. URL: `https://www.jstage.jst.go.jp/article/kona/32/0/32_2015016/_article` (visited on 03/25/2022).

[47] R. D. Mindlin and H. Deresiewicz. “Elastic Spheres in Contact Under Varying Oblique Forces”. In: *Journal of Applied Mechanics* 20.3 (1953), pp. 327–344. ISSN: 0021-8936. DOI: `10.1115/1.4010702`. URL: `https://doi.org/10.1115/1.4010702` (visited on 03/28/2022).

[48] John Paul Morrissey. “Discrete element modelling of iron ore pellets to include the effects of moisture and fines”. en. In: (Nov. 2013). Accepted: 2013-12-11T09:53:00Z Publisher: The University of Edinburgh. URL: `https://era.ed.ac.uk/handle/1842/8270` (visited on 03/28/2022).

[49] S. Nadimi et al. “Numerical modelling of rough particle contacts subject to normal and tangential loading”. en. In: *Granular Matter* 21.4 (Nov. 2019), p. 108. ISSN: 1434-5021, 1434-7636. DOI: `10.1007/s10035-019-0970-y`. URL: `http://link.springer.com/10.1007/s10035-019-0970-y` (visited on 10/26/2022).

[50] D. J Parker et al. “Positron emission particle tracking using the new Birmingham positron camera”. en. In: *Nuclear Instruments and Methods in Physics Research Section A: Accelerators, Spectrometers, Detectors and Associated Equipment*. 5th Int. Conf. on Position-Sensitive Detectors 477.1 (Jan. 2002), pp. 540–545. ISSN: 0168-9002. DOI: `10.1016/S0168-9002(01)01919-2`. URL: `https://www.sciencedirect.com/science/article/pii/S0168900201019192` (visited on 03/10/2022).

[51] M. Pasha et al. “A comparative analysis of particle tracking in a mixer by discrete element method and positron emission particle tracking”. English. In: *Powder Technology* 270.PB (2015), pp. 569–574. ISSN: 0032-5910. DOI: `10.1016/j.powtec.2014.09.007`.

[52] Edward L. Paul, Victor A. Atiemo-Obeng, and Suzanne M. Kresta. *Handbook of Industrial Mixing: Science and Practice*. en. Google-Books-ID: jzuZDwAAQBAJ. John Wiley & Sons, Nov. 2003. ISBN: 978-0-471-26919-9.

[53] Eric Perkins and John R. Williams. “A fast contact detection algorithm insensitive to object sizes”. In: *Engineering Computations* 18.1/2 (Jan. 2001). Publisher: MCB UP Ltd, pp. 48–62. ISSN: 0264-4401. DOI: `10.1108/02644400110365770`. URL: `https://doi.org/10.1108/02644400110365770` (visited on 03/29/2022).

[54] M. Poux et al. “Powder mixing: Some practical rules applied to agitated systems”. en. In: *Powder Technology* 68.3 (Dec. 1991), pp. 213–234. ISSN: 0032-5910. DOI: `10.1016/0032-5910(91)80047-M`. URL: `https://www.sciencedirect.com/science/article/pii/003259109180047M` (visited on 02/23/2022).

[55] L Vu-Quoc, X Zhang, and O. R Walton. “A 3-D discrete-element method for dry granular flows of ellipsoidal particles”. en. In: *Computer Methods in Applied Mechanics and Engineering* 187.3 (July 2000), pp. 483–528. ISSN: 0045-7825. DOI: `10.1016/S0045-7825(99)00337-0`. URL: `https://www.sciencedirect.com/science/article/pii/S0045782599003370` (visited on 03/29/2022).

[56] Aman Rastogi. “Using baffle to improve axial mixing in double cone blenders: dry impregnation process”. eng. PhD thesis. Rutgers University - School of Graduate Studies, 2018. DOI: `10.7282/t3-8zcj-pj04`. URL: `https://rucore.libraries.rutgers.edu/rutgers-lib/59194/` (visited on 03/24/2022).

[57] B. Remy, B.J. Glasser, and J.G. Khinast. “The effect of mixer properties and fill level on granular flow in a bladed mixer”. English. In: *AIChE Journal* 56.2 (2010), pp. 336–353. ISSN: 1547-5905. DOI: `10.1002/aic.11979`.

[58] Martin J. Rhodes. *Introduction to Particle Technology*. en. Google-Books-ID: P9Qgvh7kMP8C. John Wiley & Sons, June 2008. ISBN: 978-0-470-01427-1.

[59] Dingena Schott. *Discrete Element Method Simulations; Lecture 1 - DEM a particle based method*. 2021.

[60] Dietmar Schulze. *Powders and bulk solids: behavior, characterization, storage and flow*. en. OCLC: ocn166372537. Berlin ; New York: Springer, 2008. ISBN: 978-3-540-73767-4.

[61] Pooja Shenoy et al. “Dry mixing of food powders: Effect of water content and composition on mixture quality of binary mixtures”. en. In: *Journal of Food Engineering* 149 (Mar. 2015), pp. 229–236. ISSN: 0260-8774. DOI: `10.1016/j.jfoodeng.2014.10.019`. URL: `https://www.sciencedirect.com/science/article/pii/S0260877414004397` (visited on 03/15/2022).

[62] Pooja Shenoy et al. “Effect of powder densities, particle size and shape on mixture quality of binary food powder mixtures”. en. In: *Powder Technology* 272 (Mar. 2015), pp. 165–172. ISSN: 0032-5910. DOI: `10.1016/j.powtec.2014.11.023`. URL: `https://www.sciencedirect.com/science/article/pii/S0032591014009334` (visited on 04/19/2022).

[63] Sunil R. de Silva, Are Dyrøy, and Gisle G. Enstad. “Segregation Mechanisms and Their Quantification Using Segregation Testers”. en. In: *IUTAM Symposium on Segregation in Granular Flows*. Ed. by Anthony D. Rosato and Denis L. Blackmore. Solid Mechanics and Its Applications. Dordrecht: Springer Netherlands, 2000, pp. 11–29. ISBN: 978-94-015-9498-1. DOI: `10.1007/978-94-015-9498-1_2`.

[64] . *Stainless Steel - Grade 304 (UNS S30400)*. en. Section: Materials Article. Oct. 2001. URL: `https://www.azom.com/article.aspx?ArticleID=965` (visited on 12/07/2022).

[65] Parisa Tahvildarian, Farhad Ein-Mozaffari, and Simant R. Upreti. “Circulation intensity and axial dispersion of non-cohesive solid particles in a V-blender via DEM simulation”. en. In: *Particuology* 11.6 (Dec. 2013), pp. 619–626. ISSN: 1674-2001. DOI: `10.1016/j.partic.2012.12.010`. URL: `https://www.sciencedirect.com/science/article/pii/S1674200113001041` (visited on 03/24/2022).

[66] Y. Tsugeno et al. “DEM simulation for optimal design of powder mixing in a ribbon mixer”. English. In: *Advanced Powder Technology* (2021). ISSN: 0921-8831. DOI: `10.1016/j.apt.2021.03.026`.

[67] Yugong Wu, Zhigang Fan, and Yuzhu Lu. “Bulk and interior packing densities of random close packing of hard spheres”. en. In: *Journal of Materials Science* 38.9 (May 2003), pp. 2019–2025. ISSN: 1573-4803. DOI: `10.1023/A:1023597707363`. URL: `https://doi.org/10.1023/A:1023597707363` (visited on 06/01/2022).

[68] Z. Yang et al. “Multiple-particle tracking—an improvement for positron particle tracking”. en. In: *Nuclear Instruments and Methods in Physics Research Section A: Accelerators, Spectrometers, Detectors and Associated Equipment* 564.1 (Aug. 2006), pp. 332–338. ISSN: 0168-9002. DOI: `10.1016/j.nima.2006.04.054`. URL: `https://www.sciencedirect.com/science/article/pii/S0168900206006942` (visited on 03/10/2022).

[69] A. Yaraghi et al. “Mixing assessment of non-cohesive particles in a paddle mixer through experiments and discrete element method (DEM)”. English. In: *Advanced Powder Technology* 29.11 (2018), pp. 2693–2706. ISSN: 0921-8831. DOI: `10.1016/j.apt.2018.07.019`.

[70] Y. You et al. “Numerical simulation of particle mixing behavior in high speed shear mixer and cylinder mixer”. English. In: *ISIJ International* 61.7 (2021), pp. 2059–2065. ISSN: 0915-1559. DOI: `10.2355/isijinternational.ISIJINT-2020-768`.

[71] Q. Yuan et al. “The effect of paddle configurations on particle mixing in a soil-fertilizer continuous mixing device”. English. In: *Powder Technology* 391 (2021), pp. 292–300. ISSN: 0032-5910. DOI: `10.1016/j.powtec.2021.06.022`.

[72] D. Zhang and W. J. Whiten. “The calculation of contact forces between particles using spring and damping models”. en. In: *Powder Technology*. Research of Powder Technology in Australia 88.1 (July 1996), pp. 59–64. ISSN: 0032-5910. DOI: `10.1016/0032-5910(96)03104-X`. URL: `https://www.sciencedirect.com/science/article/pii/003259109603104X` (visited on 03/28/2022).

[73] Y C Zhou, A B Yu, and J Bridgwater. “Segregation of binary mixture of particles in a bladed mixer”. en. In: *Journal of Chemical Technology & Biotechnology* 78.2-3 (2003), pp. 187–193. ISSN: 1097-4660. DOI: `10.1002/jctb.731`. URL: `https://onlinelibrary.wiley.com/doi/abs/10.1002/jctb.731` (visited on 04/14/2022).

A

Research paper

The research paper starts on next page.

Parametric analysis of a double shaft batch-type paddle mixer - A DEM study

J.V. Emmerink[1], A.H. Hadi[1], C. Cleven[2], J. Jovanova[1], D.L. Schott[1]
[1]Delft University of Technology, Department of Maritime and Transport Technology, Delft, Netherlands
[2]Dinnissen B.V., Sevenum, Netherlands

Abstract **– The Discrete Element Method (DEM) in combination with an One Factor At a Time (OFAT) experimental simulation plan were employed to investigate the effect of a selection of factors on the mixing performance of a double shaft, batch-type paddle mixer. Most influential factors on the mixing performance of the paddle mixer are desired for optimization purposes. Selected factors are the three material characteristics (particle size, particle density, composition), three operational conditions (initial filling pattern, fill level, impeller rotational speed) and three geometric characteristics (paddle size, paddle angle and paddle number). The Relative Standard Deviation (RSD) is used to evaluate the degree of mixing. Also, two KPIs were defined which are the mixing effectiveness (mixture quality after 30 seconds) and the mixing efficiency (time it takes to reach a RSD smaller than or equal to 0.2). The particle size and particle density have a significant effect on the final mixture quality after 30 seconds of mixing (KPI 1). Moreover, the composition, initial filling pattern, fill level, impeller rotational speed and paddle size have a significant effect on how fast a steady-state mixture quality is reached (KPI 2). Finally, the paddle angle and paddle number have a significant effect on both KPIs and therefore holds most potential with respect to optimization purposes.**

Keywords **– Double shaft paddle mixer, Discrete Element Method, Free-flowing particles, Batch mixing**

NOMENCLATURE

a	Particle size ratio [-]
b	Particle density ratio [-]
c	Volume composition ratio [-]
C_n	Normal contact damping coefficient $[kg/s]$
C_R	Coefficient of Restitution (CoR) [-]
C_t	Tangential contact damping coefficient $[kg/s]$
d_p	Particle diameter $[mm]$
e	Fill level of mixing chamber [-]
E	Young's modulus $[N/m^2]$
E^*	Equivalent Young's modulus $[N/m^2]$
$F_{n,ij}$	Normal component of the contact force $[N]$
$F_{t,ij}$	Tangential component of the contact force $[N]$
f	Impeller rotational speed $[rpm]$
$F_{g,i}$	Gravitational force on particle i $[N]$
g	Paddle size [-]
G	Shear modulus $[Pa]$
G^*	Equivalent shear modulus $[Pa]$
i	Paddle number [-]
I_i	Moment of Inertia of particle i $[kg \cdot m^2]$
k_n	Normal contact stiffness coefficient $[N \cdot m^{-3/2}]$
k_t	Tangential contact stiffness coefficient $[Pa \cdot m]$
m_i	Mass of particle i $[kg]$
m^*	Equivalent mass $[kg]$
$M_{t,ij}$	Rotational torque $[Nm]$
$M_{r,ij}$	Rolling resistance torque $[Nm]$
M_2	Average mass concentration of component 2 [-]
$M_{2,i}$	Mass concentration of component 2 in bin i [-]
N	Number of bins [-]
N_c	Number of particles in contact with particle i [-]
p	Initial filling pattern [-]
R^*	Equivalent radius $[m]$
R_i	Radius of particle i $[m]$
R_{min}	Smallest particle radius in system $[m]$
R_{nbr}	Neighborhood radius $[m]$
s	Standard deviation [-]
v_i	Translational velocity of particle i $[m/s]$
V_p	Total volume particles of granular material $[m^3]$
α_1	Paddle angle general paddle $[deg]$
$\delta_{n,ij}$	Normal overlap $[m]$
$\delta'_{n,ij}$	Normal velocity $[m/s]$
$\delta_{t,ij}$	Tangential overlap $[m]$
$\delta'_{t,ij}$	Tangential velocity $[m/s]$
Δt	Simulation time step [s]
ζ	Damping coefficient [-]
ν	Poisson's ratio [-]
ρ_p	Particle density $[g/cm^3]$
ω_i	Angular velocity of particle i $[s^{-1}]$

I. INTRODUCTION

Mixing granular materials is a common practice in many industries like food, pharmaceutical and chemical. Many different mixing applications exist like gravity-controlled mixers, high shear mixers and agitated blenders [16]. One application that belongs to the latter class is the double shaft, batch-type paddle mixer. Its geometric characteristics are based upon a design invented in the 70's by Halvor Forberg [9]. Since then, trial and error techniques and other empirical methods are employed to determine the influence of factors on the mixing performance of the system. However, this approach is rather costly and time-consuming. Therefore, the Discrete Element Method (DEM) offers a great solution that will be explained later.

Until now the paddle mixer has not been subjected to thorough research. Although, the limited amount of research that is available will be discussed in chronological order. Ebrahimi et al. [6] investigated impeller configurations on mixing performance in a single shaft, horizontal batch-type paddle mixer. Following that, Ebrahimi et al. [7] and Yaraghi et al. [21] also investigated rotational speed, fill level and initial loading pattern of both mono-sized and bi-disperse particles for a single shaft paddle mixer. Both DEM and experimental measurements were used to assess the mixing performance of the mixer. Concerning double-shaft, batch-type paddle mixer only a few DEM-based studies have been published. Hassanpour et al. [11] was the first to investigate this particular system with DEM. They carried out an analysis of particle motion by using experiments in the form of Positron Emmission Particle Tracking (PEPT) and DEM simulations. In 2013, Li et al. [14] looked into the effect of Particle Size Distribution (PSD) on segregation and coating uniformity. Subsequently, as a follow up study on the research done by Hassanpour et al. [11] a more thorough research was done by tracking multiple particles with PEPT and DEM simulations [15]. Furthermore, Shenoy et al. [17, 18] utilized a custom built, lab-scale double shaft paddle mixer to investigate the effect of particle density, particle size, particle shape, water content and composition on a binary food powder mixture. Recently Jadidi et al. [12] investigated the mixing performance of a double shaft, paddle mixer by a sensitivity analysis on the impeller speed, initial loading pattern and fill level. Additionally, they also touched upon the influence of particle shape on the mixing performance.

Only the effect of the operational factors impeller rotational speed, initial filling pattern and fill level on the mixing performance of a double shaft, batch-type paddle mixer are investigated. But, the significance of material characteristics (e.g. particle shape, particle size, particle density) and geometric properties (e.g. paddle size, mixing chamber shape, paddle number) is not yet clearly understood for this particular mixing application. Consequently, in practice long lasting trial and error procedures are conducted according to the customer's demands to make sure desired mixture quality will be achieved.

A. Research objectives & Scope

While the operational conditions (initial filling pattern, fill level and impeller rotational speed) are investigated with regard to a similar double shaft paddle mixer, the influence of the material properties (particle size, particle density and composition) and geometric characteristics (paddle size, paddle angle and number of paddles) on the mixing performance of the double shaft paddle mixer is missing in literature. This motivates the author to conduct a research with the aim to obtain new insights on factor significance from a material and geometry perspective. The two research objectives are:

1. Develop a model that can present flow behaviour and mixing patterns inside the paddle mixer
2. Identify and evaluate the influence of material, operational condition and design factors on the mixing performance of a double shaft batch-type paddle mixer.

The paddle mixer under investigation is commonly deployed in industry. In order to achieve reliable results, all the parameters were taken from Jadidi et al. [12] which have been already validated in their study. The material model consists of free-flowing, bi-disperse spherical glass beads. The adopted input parameters are utilized to construct the filling process and mixing process. Furthermore, the filling process was subjected to a stability analysis to ensure a robust and fit-for-purpose simulation. According to a predetermined mixing time the mixing performance will be analysed. Handling prior to and after batch mixing is not considered. The mixing process simulations are started from a stationary initial particle bed and mixing of additives (extremely small amount of mixture components) is excluded.

Research is conducted by using the Discrete Element Method (DEM) as this allows to model granular material. Performing DEM simulations instead of physical experiments is the most time and cost efficient way to fulfill the research objectives. First a fit-for-purpose simulation model is being built (objective 1). Then, the experimental simulation plan is designed and executed (objective 2). It consists of an One Factor At a Time (OFAT) approach, where selected factors are subjected to a parametric analysis to assess the mixing performance of the paddle mixer. The mixing performance is assessed both quantitatively and qualitatively.

- **Quantitative analysis**: In related literature, to assess quantitatively the performance of a mix application is by calculating a so-called mixing index. Most suitable mixing index for this particular research is the Relative Standard Deviation (RSD) ([4]). To assess both the mixing efficiency and mixing effectiveness, two KPI's are defined:

  KPI 1: The mixing index RSD after 30 seconds of mixing

  KPI 2: The time it takes to reach a RSD smaller than or equal to 0.2
- **Qualitative analysis**: To be able to understand the mixing mechanisms and patterns inside the paddle mixer, screenshots are taken of the particle bed in x, y and z directions. Additionally, in same directions heat maps are created to assess the local mixture quality. The normalised mass concentration in every bin in the local grid system is being visualised by a color based upon a fixed color bar.

This paper is structured as follows. First the modelling method DEM is explained in Chapter II. followed by the simulation model setup in Chapter III. Then, in Chapter IV. all selected factor levels and the experimental design diagram are explicated. The mixing assessment method is elaborated in Chapter V. Finally, results are discussed in Chapter VI. and conclusions drawn in Chapter VII.

II. DISCRETE ELEMENT METHOD (DEM)

The Discrete Element Method (DEM) is utilized to simulate the mixing mechanisms and flow patterns inside the paddle mixer. The method has been successfully employed in many areas such as mining engineering, agricultural technology, chemical engineering, pharmaceutical industry, food industry and process engineering [3, 8].

Particles experience two types of motions during simulation: Rotational and Translational. Both are governed by Newton's laws of motion. The forces and torques on

---

[0] Screenshots and heat maps are not included to keep the document concise

an individual particle are caused by interaction with other particles or the system's boundaries. In Equation 1 and Equation 2, the translational and rotational equations of motion are formulated. In Figure 1, a two-dimensional particle-particle interaction is illustrated with corresponding parameters introduced in the equations of motion [5]. Furthermore, the Hertz-Mindlin contact model is used to model the interaction between the free-flowing particles and the interaction between particles and geometry. Normal and tangential contact forces are calculated by Equation 3 and Equation 10.

$$m_i \frac{dv_i}{dt} = \sum_{j}^{N_c} (F_{n,ij} - F_{t,ij}) + F_{g,i} \tag{1}$$

where:

m_i is the mass of particle i
v_i is the translational velocity of particle i
N_c is the number of particles in contact with particle i
$F_{n,ij}$ is the normal component of the contact force between particle i and j
$F_{t,ij}$ is the tangential component of the contact force between particle i and j
$F_{g,i}$ is the gravitational force on particle i

$$I_i \frac{d\omega_i}{dt} = \sum_{j}^{N_c} (M_{t,ij} + M_{r,ij}) \tag{2}$$

where:
I_i is the moment of inertia of particle i
ω_i is the angular velocity of particle i
N_c is the number of particles in contact with particle i
$M_{t,ij}$ is the rotational torque between particle i and j
$M_{r,ij}$ is the rolling resistance torque between particle i and j

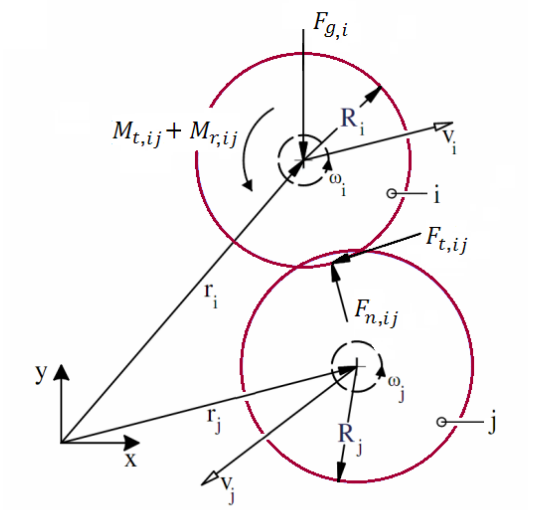

Fig. 1. Two-dimensional particle-particle interaction with forces acting on particle i from contacting particle j. Reprinted from [10] and adjusted.

$$F_{n,ij} = k_n \cdot \delta_{n,ij}^{\frac{3}{2}} + C_n \cdot \delta'_{n,ij} \tag{3}$$

$$k_n = \frac{4}{3} \cdot E^* \cdot \sqrt{R^*} \tag{4}$$

$$C_n = -2 \cdot \sqrt{\frac{5}{6}} \cdot \zeta \cdot \sqrt{m^*} \tag{5}$$

$$\frac{1}{E^*} = \frac{(1-\nu_i^2)}{E_i} + \frac{(1-\nu_j^2)}{E_j} \tag{6}$$

$$R^* = \frac{1}{\frac{1}{R_i} + \frac{1}{R_j}} \tag{7}$$

$$m^* = \frac{m_i m_j}{m_i + m_j} \tag{8}$$

$$\zeta = \frac{ln(C_R)}{\sqrt{ln^2(C_R) + \pi^2}} \tag{9}$$

where:
$F_{n,ij}$ is the normal component of the contact force between particle i and j
k_n is the normal contact stiffness coefficient
E^* is the equivalent Young's modulus
R^* is the equivalent radius
$\delta_{n,ij}$ is the normal overlap between particle i and j
C_n is the normal contact damping coefficient
$\delta'_{n,ij}$ is the normal velocity between particle i and j
E is the Young's modulus
ν_i is the Poisson's ratio of particle i
R_i is the radius of particle i
m^* is the equivalent mass
m_i is the mass of particle i
ζ is the damping coefficient
C_R is the Coefficient of Restitution (CoR)

$$F_{t,ij} = k_t \cdot \delta_{t,ij} + C_t \cdot \delta'_{t,ij} \tag{10}$$

$$k_t = 8 \cdot G^* \cdot \sqrt{R^* \cdot \delta_{n,ij}} \tag{11}$$

$$C_t = -2 \cdot \sqrt{\frac{5}{6}} \cdot \zeta \cdot \sqrt{m^*} \tag{12}$$

$$\frac{1}{G^*} = \frac{(2-\nu_i)}{G_i} + \frac{(2-\nu_j)}{G_j} \tag{13}$$

where
$F_{t,ij}$ is the tangential component of the contact force between particle i and j
k_t is the tangential contact stiffness coefficient
$\delta_{t,ij}$ is the tangential overlap
C_t is the tangential contact damping coefficient
$\delta'_{t,ij}$ is the tangential velocity between particle i and j
G^* is the equivalent shear modulus
G is the shear modulus
R^* is the equivalent radius
$\delta_{n,ij}$ is the normal overlap between particle i and j

The simulations were conducted on parallel mode using 14 CPUs and 1 GPU of a High-Performance-Computer (Intel(R) Xeon(R) W-2275 CPU @ 3.30GHz, 3312 Mhz, 14 Core(s), 28 Logical Processor(s)) for each run.

III. SIMULATION MODEL SETUP

In Figure 2 the 175L paddle mixer is shown which is based upon the first created design by Forberg [9]. The shafts are positioned horizontally, each with 14 paddles evenly distributed over four radial quadrants. The double teardrop-shaped chamber in combination with counter-rotating shafts forces the bulk material towards the center of the chamber, just above the shafts, as illustrated in Figure 3. At this location, a so-called fluidized zone is formed [9]. Here, two or multiple material components are blended together as one bulk material by reconfiguration of the individual particles, hereby dictating the system's performance. Additionally, the paddles are configured in such a way that they force the granular material to move in a circular pattern through the chamber [11].

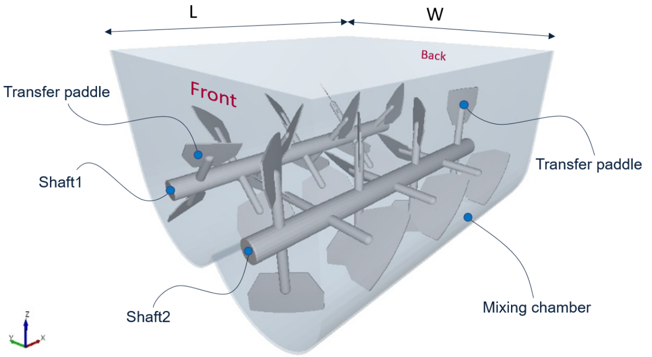

Fig. 2. Isometric view of the double shaft paddle mixer with names and dimensions.

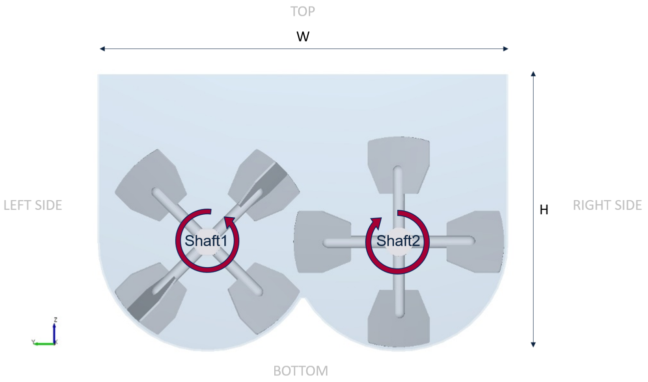

Fig. 3. Front view of double shaft paddle mixer with dimensions and rotational directions of shafts.

To avoid accumulation in the corners of the mixing chamber, the last paddle pair is positioned under a -15deg-angle and functions as 'transfer' paddles (Figure 2). To avoid collisions between the paddles of shaft1 and shaft2, a phase angle of 45deg is applied between the two shafts (Figure 3).

TABLE I

Dimensions of paddle mixer.

Parameter	Unit	Value
L	mm	900
W	mm	850
H	mm	570

Initial material characteristics are adopted from the material model of Jadidi et al. [12] as shown in Table II. Moreover, a time step of 4.74378e-5 s and shear modulus of 1e6 Pa are used for all simulations in the experimental simulation plan. The values are the result of the stability analysis conducted with the aim to create a robust and fit-for-purpose DEM simulation of the model [1]. The geometric properties are based upon the material stainless steel 304 [20].

The reference case is presented in Table III. The parameters are explained in detail in Chapter IV.

TABLE II

Initial simulation input parameters used in DEM simulations [12].

Parameter	Unit	Value
Poisson's ratio ν_p	-	0.3
Shear modulus G_p	Pa	1e6
Particle-particle CoR	-	0.75
Particle-particle CoSF	-	0.5
Particle-particle CoDF	-	0.01
Geometry density ρ_w	$\mathrm{kg\,m^{-3}}$	7850
Poisson's ratio ν_w	-	0.265
Shear modulus G_w	Pa	7.4e10
Particle-geometry CoR	-	0.75
Particle-geometry CoSF	-	0.35
Particle-geometry CoDF	-	0.005
Simulation time	s	30
Time step t	s	4.74378e-5

TABLE III

Characteristics of reference case.

Parameter	Unit	Value
Diameter particle 1 $d_{p,1}$	mm	10
Diameter particle 2 $d_{p,2}$	mm	5
Density particle 1 $\rho_{p,1}$	$\mathrm{kg\,m^{-3}}$	2500
Density particle 2 $\rho_{p,2}$	$\mathrm{kg\,m^{-3}}$	357
Composition c	-	80/20
Initial filling pattern p	-	Front-Back
Fill level e	%	100
Impeller rotational speed f	rpm	60
Paddle size g	-	1.0 (Original)
Paddle angle α_1	deg	45
Paddle number i	-	14
Number of particle 1	-	149,427
Number of particle 2	-	298,855
Total number of particles	-	448,282

---

[1] Stability analysis not included in this document

IV. EXPERIMENTAL SIMULATION PLAN

The factors for the parametric analysis with factor levels are shown in Table IV where the '0' column represents the reference case. The initial filling pattern abbreviations mean Top-Bottom (TB), Front-Back (FB) and Side-by-Side (SS). Furthermore, an One Factor at a Time (OFAT) experimental simulation plan is designed. Because research on a relatively high number of factors could become cluttered, simplicity of the experimental simulation plan is key. Generated results should be easy to understand. Decisive criteria is the ability to evaluate the particle bed in a qualitative way, preferably by visual observations of the particle bed. Results of the OFAT experimental simulation plan are assumed to be a good starting point for further research. Finally, the experimental simulation plan consists of 19 simulations as shown in Table V. The first run is the reference case, followed by 18 runs where each factor is varied according to OFAT. It is determined to not repeat the simulations. Minor deviations were observed after an analysis on the reference case concerning number of repetitions.

TABLE IV

Overview of all selected factors with corresponding levels for screening procedure.

Factor	Unit	-1	0	1
a - Particle size ratio	[-]	1	2	3
b - Particle density ratio	[-]	1	7	20
c - Composition	[-]	99/1	80/20	50/50
p - Initial filling pattern	[-]	TB	FB	SS
e - Fill level	[%]	40	100	140
f - Impeller rotational speed	[rpm]	40	60	80
g - Paddle size	[-]	0.67	1.00	1.50
α_1 - Paddle angle	[deg]	30	45	60
i - Paddle number	[#]	7	14	28

The effect of the particle size will be investigated by the particle size ratio between the two components of the mixture (Equation 14). The diameter of particle 1 varies between 5 *mm* and 15 *mm*.

$$a = \frac{d_{p,1}}{d_{p,2}} \tag{14}$$

where:

a is the particle size ratio
$d_{p,1}$ is the diameter of particle 1
$d_{p,2}$ is the diameter of particle 2

The effect of the particle density will be investigated by the particle density ratio between two components of the mixture (Equation 15). The density of particle 1 varies between 125 kg/m^3 and 2500 kg/m^3.

$$b = \frac{\rho_{p,1}}{\rho_{p,2}} \tag{15}$$

where:

b is the particle density ratio
$\rho_{p,1}$ is the density of particle 1
$\rho_{p,2}$ is the density of particle 2

The effect of composition will be investigated by the ratio between the total particle volumes of component 1 and component 2 (Equation 16). An illustration is provided in Figure 4.

$$c = \frac{V_{p,1}}{V_{p,2}} \tag{16}$$

where:

c is the total particle volume ratio

$V_{p,1}$ is the particle volume of component 1

$V_{p,2}$ is the particle volume of component 2

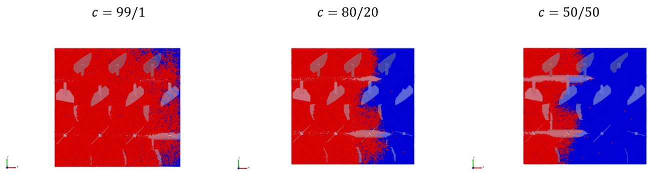

Fig. 4. Illustration of the three different compositions.

The three different initial filling patterns are Top-Bottom (TB), Front-Back (FB) and Side-by-Side (SS). An illustration is provided in Figure 5.

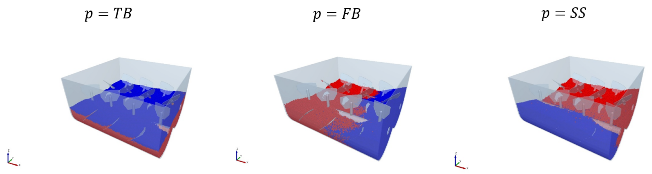

Fig. 5. Illustration of the three different initial filling patterns.

The fill level is illustrated in Figure 6.

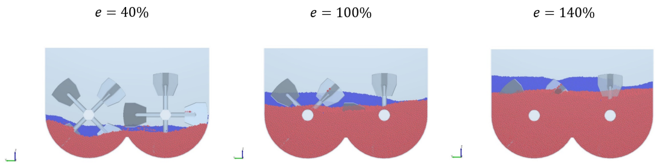

Fig. 6. Illustration of the three different fill levels.

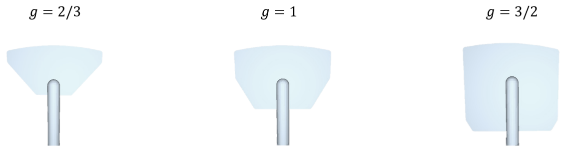

Fig. 7. Illustration of the three different paddle sizes.

With respect to the paddle size, the lower level value is equal to 2/3 times the effective surface of the original paddle size. And the upper level equal to 3/2 times the original paddle size. In Figure 7 an illustration is provided.

Figure 8 an illustration provided.

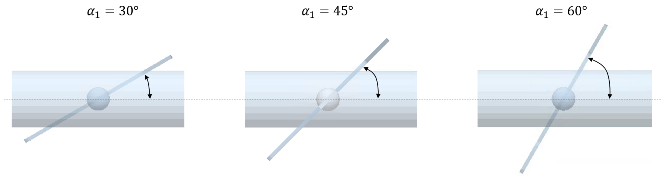

Fig. 8. Illustration of the three different paddle angles.

TABLE V
Experimental simulation plan with factor levels and number of particles (particle1, particle2 and total)

Run	a	b	c	p	e	f	g	α_1	i	Particle1	Particle2	Total
Ref.	2	7	80/20	FB	100%	60	1	45deg	14	149,427	298,855	448,282
2	**1**	7	80/20	FB	100%	60	1	45deg	14	1,195,419	298,855	1,494,274
3	**3**	7	80/20	FB	100%	60	1	45deg	14	44,275	298,855	343,130
4	2	**1**	80/20	FB	100%	60	1	45deg	14	149,427	298,855	448,282
5	2	**20**	80/20	FB	100%	60	1	45deg	14	149,427	298,855	448,282
6	2	7	**99/1**	FB	100%	60	1	45deg	14	184,916	14,943	199,859
7	2	7	**50/50**	FB	100%	60	1	45deg	14	93,392	747,137	840,529
8	2	7	80/20	**TB**	100%	60	1	45deg	14	149,427	298,855	448,282
9	2	7	80/20	**SS**	100%	60	1	45deg	14	149,427	298,855	448,282
10	2	7	80/20	FB	**40%**	60	1	45deg	14	59,771	119,542	179,313
11	2	7	80/20	FB	**140%**	60	1	45deg	14	209,198	418,397	627,595
12	2	7	80/20	FB	100%	**40**	1	45deg	14	149,427	298,855	448,282
13	2	7	80/20	FB	100%	**80**	1	45deg	14	149,427	298,855	448,282
14	2	7	80/20	FB	100%	60	**0.67**	45deg	14	149,427	298,855	448,282
15	2	7	80/20	FB	100%	60	**1.5**	45deg	14	149,427	298,855	448,282
16	2	7	80/20	FB	100%	60	1	**30deg**	14	149,427	298,855	448,282
17	2	7	80/20	FB	100%	60	1	**60deg**	14	149,427	298,855	448,282
18	2	7	80/20	FB	100%	60	1	45deg	**7**	149,427	298,855	448,282
19	2	7	80/20	FB	100%	60	1	45deg	**28**	149,427	298,855	448,282

Figure 9 illustrates the three different paddle numbers.

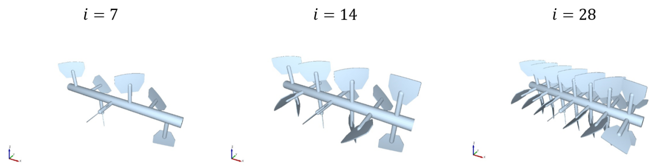

Fig. 9. Illustration of the three different paddle numbers. Shaft2 is used for the illustration.

V. MIXING PERFORMANCE ASSESSMENT

The Relative Standard Deviation (RSD) is utilized to assess the mixing performance of the paddle mixer in a quantitative manner. The RSD is one of the most frequently used mixing index [1, 2, 6, 12] and is calculated by Equation 17.

$$RSD = \frac{s}{M_2} \tag{17}$$

The standard deviation s can be calculated by Equation 18 .

$$s = \sqrt{\frac{\sum_{i=1}^{N}(M_{2,i} - M_2)^2}{N-1}} \tag{18}$$

where:

RSD is the mixing index Relative Standard Deviation
s is the standard deviation over all evaluated bins
M_2 is the average mass concentration of component 2 over all taken samples
$M_{2,i}$ is the mass concentration of component 2 in bin i
N is the number of bins

Theoretically, a RSD of one means the two mixture components are completely segregated. On the other hand, a RSD of zero means the components are perfectly mixed. Ideally, the RSD over time should follow a global trend from high to low. Specifically, as the bins would always capture the interface of a two-component mixture already a number of bins is filled with both components. Consequently, the RSD should begin from a value slightly lower than one and start decreasing the moment the shafts are beginning to rotate. Depending on the mixing configuration of the system, eventually the RSD should reach a steady-state value.

To calculate the RSD a grid system is required. The number of bins and bin size affects the RSD [4], thus multiple grid systems are evaluated (Table VI). The factors 4, 5 and 6 times the largest particle diameter d_p (equal to 15 mm) are chosen as it is suggested by Jadidi et al. [12] to keep a bin size of $> 4{*}d_p$. Besides a slight discrepancy in steady-state RSD values (Figure 10) the 14x14x9 grid system in the x, y and z directions is chosen, respectively.

What can be observed from Figure 10 is the RSD reaching a value of > 1 caused by the wide spread in mass concentration values of component 2 over the evaluated bins. As the graph shows the expected trend after approx. 3.8 seconds, the part where the RSD exceeds a value of one is not considered.

The selection of bins to calculate standard deviation s is dependent on the total mass present in the bin. In case the

---

[1] As the composition of the 80/20 center point value is based upon volume, the mass concentration is determined by converting the volume fraction into a mass fraction.

total mass is lower than the average mass in a bin, the bin is eliminated from the calculation.

TABLE VI
Analysis on grid system with number of bins, average number of particles in each cell and the RSD.

Bin size	Grid	Bin number	Particles per bin	RSD (30s)
6*d_p	9x9x6	486	351	0.105
5*d_p	11x11x7	847	201	0.131
4*d_p	14x14x9	1764	97	0.167

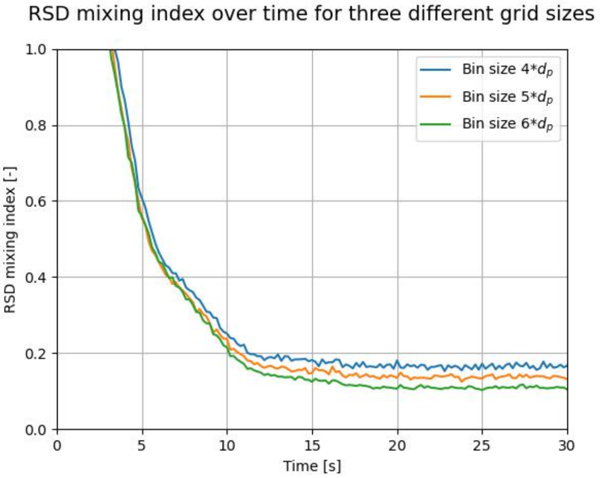

Fig. 10. RSD mixing index over time for different grid sizes.

Based upon the RSD calculation, the following two KPI's are determined tailored to this particular mixing application:

KPI 1: The (steady-state) RSD after 30 seconds of mixing - The first KPI indicate the mixing effectiveness of the system for investigated factor level.

KPI 2: Time it takes to reach a RSD smaller than or equal to 0.2 - The second KPI indicate the mixing efficiency towards the steady-state RSD value. In other words, how fast does the mixture quality of one factor level evolve over time compared to another.

VI. RESULTS & DISCUSSION

Generated results explicate the main effect of every factor on the system's response. Consequently, drawn conclusions about factors are valid with all other values fixed at their center point values, as shown in Table IV. The material factors (particle size, particle density and composition) are discussed first, followed by the operational condition factors (initial filling pattern, fill level and impeller rotational speed) and the geometry factors (paddle size, paddle angle and paddle number). Only results that provide new insights are discussed in detail.

A. Particle size

The influence of the particle size on the mixing performance of the paddle mixer is shown in Figure 11.

It can observed that the particle size ratios a=1 and a=3 perform comparable, and the particle size ratio a=2 performs slightly better than the other two when steady-state is reached. The results are not in line with the hypothesis which states an increase in particle size ratio would cause a decrease in mixture quality due to segregation (de-mixing) mechanisms. The observed phenomenon can be explained by the interplay between different segregation mechanisms. With respect to the particle size ratio a=1, it is assumed the push-away effect [19] is the most dominant segregation mechanism present according to visual observations of the particle bed. The difference in particle density causing the heavier particles to push away the lighter particles towards the sides of the mixing chamber. With respect to particle size ratios a=2 and a=3, the accumulation of component 2 at the wall edges is less. Now that the particle size differs between the two components, it is assumed the percolation segregation mechanism becomes the more dominant mixing mechanism [16] where the larger particles accumulate at the top of the particle bed. Moreover, another segregation mechanism that interact with the push-away and percolation is the buoyancy mechanism [13]. These three mentioned segregation mechanism interact with each other because of the difference in particle density for the center point simulation and the simultaneously varied particle size ratio. In what way the mentioned mechanisms percolation, buoyancy and push-away contribute for this particular type of mixing application is not yet known and needs further research.

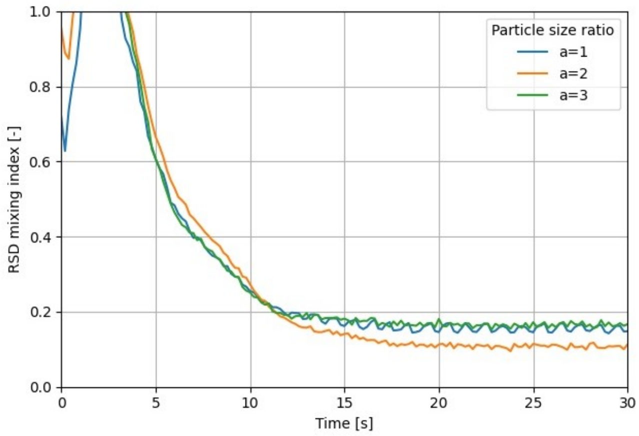

Fig. 11. RSD mixing index over time for different particle size ratios.

B. Particle density

The influence of the particle density on the mixing performance of the paddle mixer is shown in Figure 12. The figure shows that all three investigated levels show a more or less equal development of the mixing quality over time and end up approximately on the same RSD after 30 seconds of mixing. As already mentioned, it is assumed the three segregation mechanisms buoyancy, percolation and push- away are working simultaneously, one more dominant than the other. It is not yet clearly understood which one is more dominant over the others.

C. Composition

According to Figure 13, the *c*=80/20 and *c*=50/50 compositions perform better than the *c*=99/1 composition, as was expected upfront. However, the substantial difference in final steady-state mixture qualities of *c*=99/1 compared to *c*=80/20 and *c*=50/50 raises some questions. Because the grid

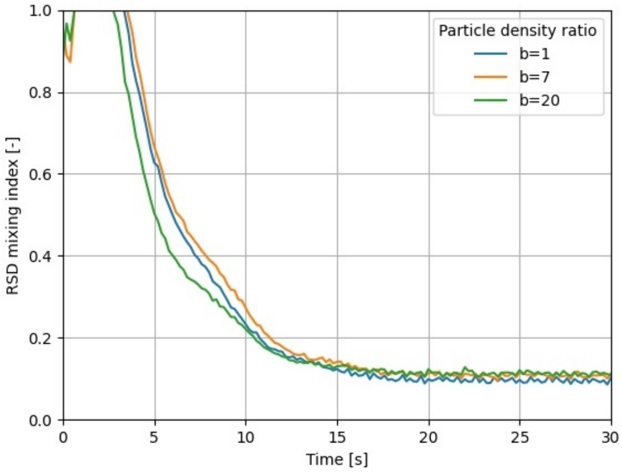

Fig. 12. RSD mixing index over time for different particle density ratios.

system analysis is performed with *c*=80/20, it could be for the *c*=99/1 too few particles of component 2 are present in each bin to obtain an accurate RSD.

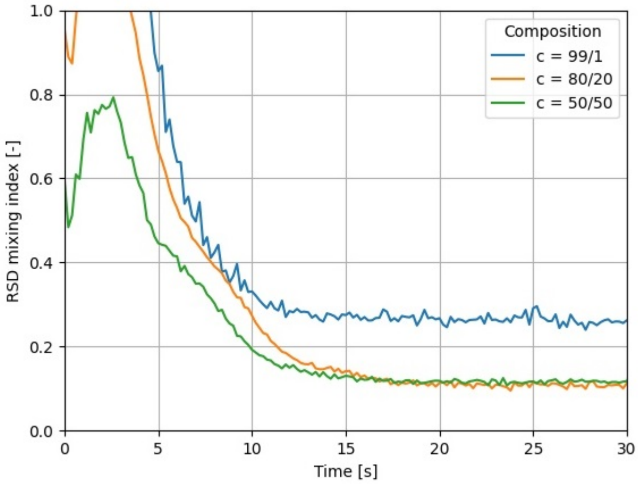

Fig. 13. RSD mixing index over time for different compositions.

In Figure 14, the grid system has an effect on the RSD over time for all three composition levels which is in line with the statement that the RSD is grid dependent. Furthermore, the *c*=99/1 steady state RSD lays closer to the other two levels. The larger bins in the 7x7x4 grid system results in more particles per bin. This is beneficial for the analysis on the *c*=99/1 simulation, as the results can be assumed more accurate from a statistical point of view. However, further research is required to proof the *c*=99/1 simulation converges to the other two composition levels when the bin size further increases. As all other factors besides the composition should be evaluated with the same grid system to compare KPIs, further analysis is not included.

D. Initial filling pattern

The influence of the initial filling pattern on the mixing performance of the paddle mixer is shown in Figure 15.

Looking at the figure, the TB initial filling pattern is the best performing pattern followed by SS and FB filling patterns. This result is in line what is found in literature [12]. All three levels reach the same steady-state RSD which underline the presence of both axial and radial mix mechanisms caused by the angled paddles. The latter can be confirmed by research from Hassanpour et al. [11].

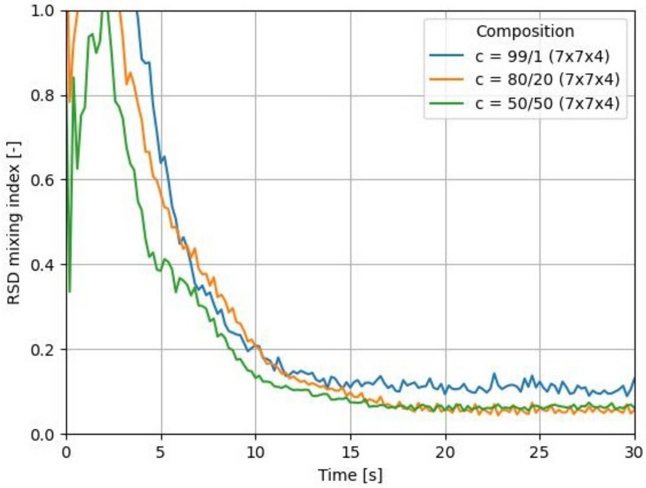

Fig. 14. RSD mixing index over time for different compositions with a grid system consisting of 7x7x4 bins

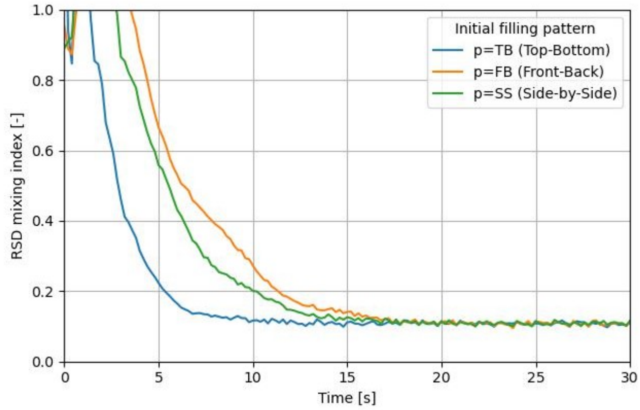

Fig. 15. RSD mixing index over time for different initial filling patterns.

E. Fill level

The influence of the fill level on the mixing performance of the paddle mixer is shown in Figure 16.

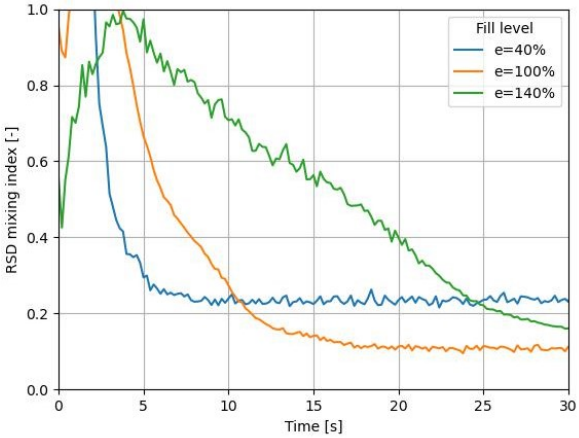

Fig. 16. RSD mixing index over time for different fill levels.

Considering the results presented in Figure 16, a higher fill level resulted in slower mixing. However, the steady-state mixture quality reached by e=40% fill level is unforeseen. Moreover, the mixing time for the e=140% level is too small to draw accurate conclusions, as it did not reach the steady-state RSD yet. Nevertheless, the graph suggests the e=140% level is approaching the e=100% level.

According to Jadidi et al. [12], the fill level does not have a significant impact on the mixing performance. They investigated 40%, 50% and 60% fill levels with impeller rotational speeds of 10 rpm, 40 rpm and 70 rpm. All levels performed more or less equal in terms of mixing speed and final steady-state mixture quality. However, concerning the broad range of fill levels selected for this research (40%, 100% and 140%) compared to Jadidi's research, it was expected the fill level does have influence on the mixing performance of the system. The hypothesis is based upon the number of particles that have to be relocated which would lead to an increase in time before reaching a steady state mixture quality. Hereby, it is assumed that the fill level range investigated by Jadidi was too narrow to observe any variation in mixing performance.

Comparison between Figure 17 and the original Figure 16, one can observe the e=40% level converges towards the e=100% level. Still, the steady-state mixture qualities are not identical. Whether the present discrepancy of steady-state mixture quality between the 40% level and e=100% is caused by the grid system or other factors is unknown. Further analysis is not part of this research.

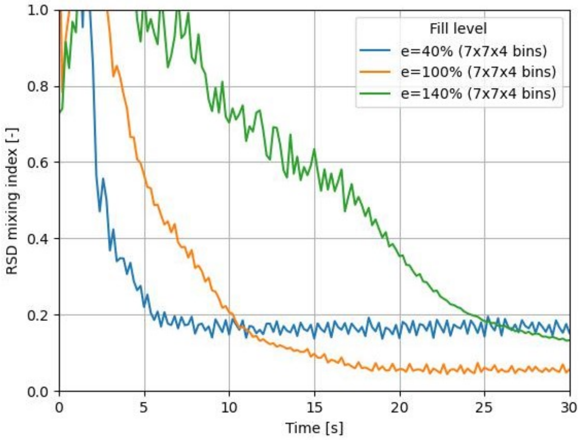

Fig. 17. RSD mixing index over time for different fill levels with a grid system consisting of 7x7x4 bins.

Moreover, what can also be perceived is the considerable fluctuations of the RSD over time for both the 40% level and the 140%. Fluctuations in each level is believed to originate from different sources. The fluctuations in the 40% level can be explained by the highly diffusive behaviour of particles in the mixing chamber. The particles do have enough space in the fluidized zone of the mixing chamber to move freely, as can be seen from Figure 18 where the particle velocity is displayed at t=30s. Consequently, concentration of particle 2 in every evaluated bin changes rapidly in time causing variation in RSD.

With respect to the e=140% level, the origin of the fluctuations probably lays at the alteration of mixing mechanism dominance. The freedom of movement of particles in the fluidized zone is decreased causing a deterioration of the diffusive mixing mechanism. As a result, the convective mixing mechanism plays a more dominant role in the mixing process. In other words, groups of particles are relocated by the paddles. As the paddle pairs are welded onto the shaft in an 90deg alternating fashion, not all particle groups are transported equally smooth through the mixing chamber causing observed fluctuations.

Finally, Figure 18 clearly shows for e=140% fill level the stagnant fluidized zone in the center of the mixing chamber with particle velocities equal to zero. This is not conducive for the mixing performance of the system as shown in Figure 17 where the mixing efficiency is substantially lower for the e=140% fill level compared to the e=40% and e=100% fill levels.

F. Impeller rotational speed

The influence of the impeller rotational speed on the mixing performance of the paddle mixer is shown in Figure 19.

Looking at Figure 19, the steady-state RSD is reached quicker with increasing the impeller rotational speed, but all three end up at the same mixture quality. The positive correlation between impeller rotational speed and mixing efficiency is in line with literature [12]. The phenomenon can be explained by the amount of momentum imposed on the particles that increases with a higher impeller rotational speed. A higher impeller rotational speed stimulates the diffusive movement of particles in the fluidized zone of the mixing chamber which is the main reason for the improvement of mixing efficiency in the initial stage of mixing.

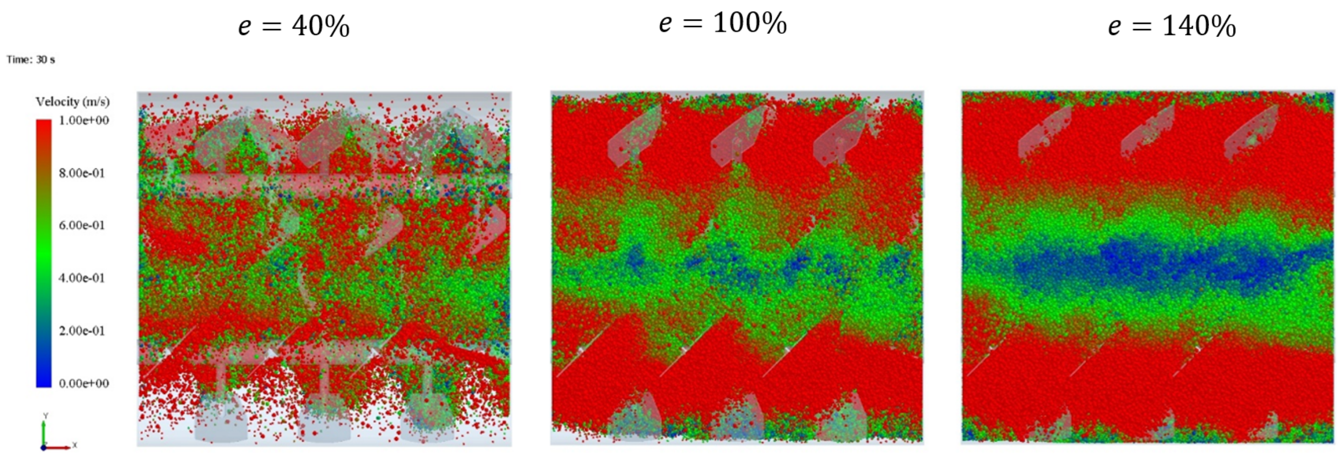

Fig. 18. Velocity of particles from top view for all three fill levels at time=31s.

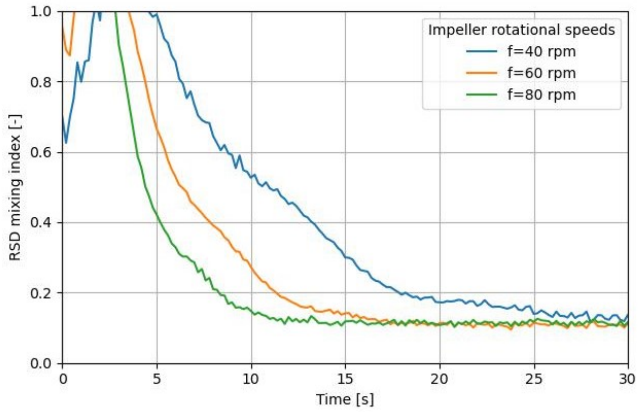

Fig. 19. RSD mixing index over time for different impeller rotational speeds.

G. Paddle size

The influence of the paddle size on the mixing performance of the paddle mixer is shown in Figure 20.

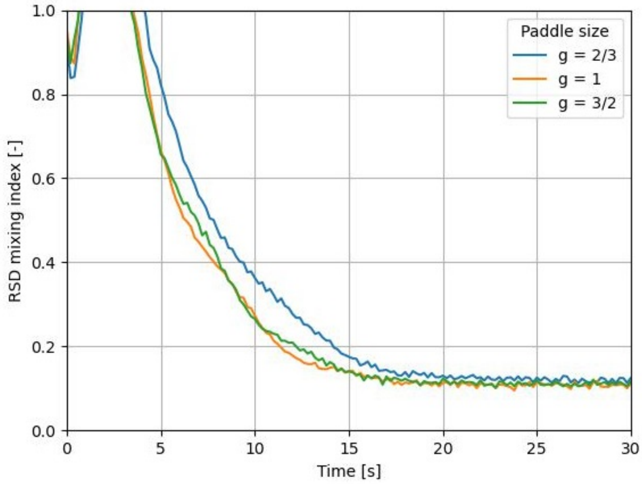

Fig. 20. RSD mixing index over time for different paddle sizes.

According to Figure 20, a smaller paddle size results in a slower mixing process. It can also be observed that the paddle size g=1 and g=3/2 perform equally well. In literature, no research has (yet) been conducted on the effect of the paddle size on the mixing performance of the paddle mixer. As explained in Section F.a highly dynamic and diffusive fluidized zone is beneficial for the mixing performance of the system. The paddle part that contributes most to such a fluidized zone is the outermost part of the paddle near the inner wall of the mixing chamber, because the centrifugal force is highest at this position, indirectly increasing particle velocity. As the material that is added or removed from the original paddle size is done inside out meaning in radial direction outwards, the paddle size does not affect the mixing performance significantly. The final steady-state RSD is similar for all three levels.

H. Paddle angle

The influence of the paddle size on the mixing performance of the paddle mixer is shown in Figure 22.

Looking at Figure 22, it can be stated the paddle angle equal to α_1=45deg is the best performing one. This paddle angle outperforms the α_1=30deg paddle angle in terms of mixing efficiency, and does the same for the α_1=60deg paddle angle in terms of final steady-state mixing quality.

In literature, Jadidi et al. [12] used a paddle mixer with fixed, 0deg-angled paddles. Consequently, radial mixing was the dominant mixing mechanism compared to the axial mixing mechanism. In 2018, Ebrahimi et al. [6] investigated the impeller configuration of a single shaft paddle mixer. From the five different impeller configurations (0deg, 30deg, 45deg, 60deg and rectangular impellers) the 30deg-angled paddle resulted in the best performing paddle followed by the 45deg-angled paddle.

With respect to the double shaft paddle mixer a similar result was expected. On the one hand, a 0deg-angled paddle configuration lacks the ability to stimulate axial mixing. On the other hand, an angle approaching 90deg would be disadvantageous for radial mixing. The optimum paddle angle will lay in between these two extremes.

An interesting observation is the difference in final steady-state mixture quality between the 60deg paddle angle compared to the α_1=30deg and α_1=45deg paddle angles. The paddle mixer with α_1=60deg paddles is not able to perform

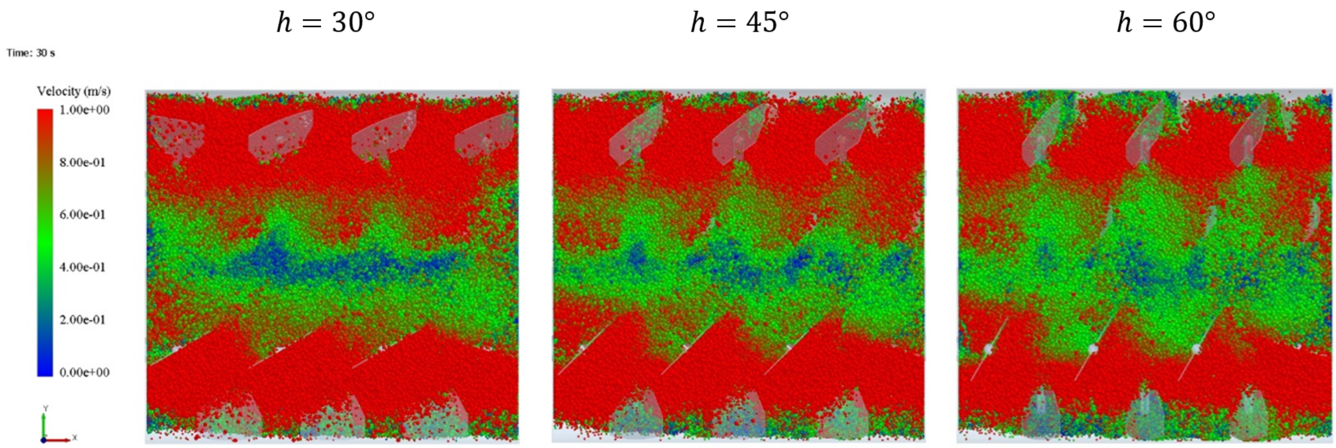

Fig. 21. Velocity of particles from top view for all three paddle angles at time=31s.

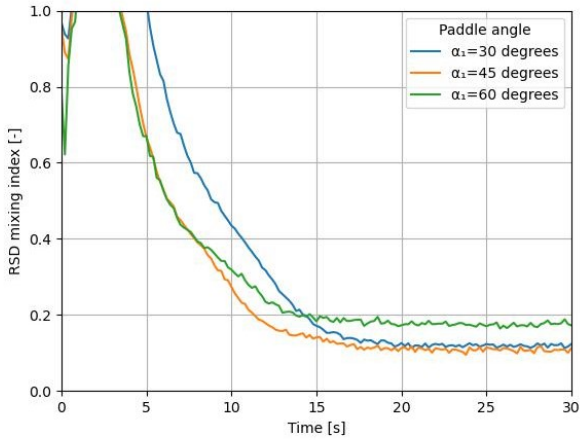

Fig. 22. RSD mixing index over time for different paddle angles.

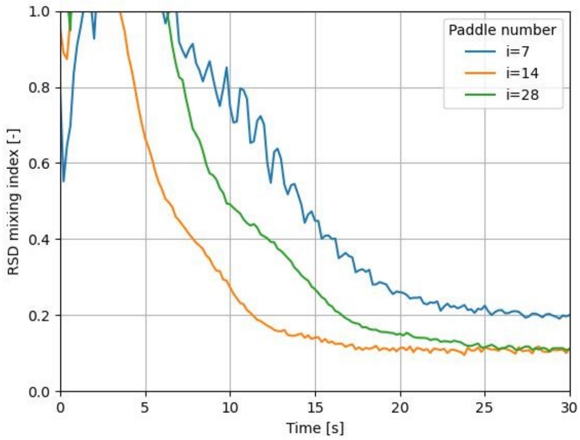

Fig. 23. RSD mixing index over time for different paddle numbers.

equally well compared to the other two configurations. Figure 21 depict the origin of the problem. At the left and right walls of the mixing machine, many particle velocities are equal to zero or close to zero. The α_1=60deg angled paddles are not able to grab all particles near the walls resulting in a lower steady-state RSD eventually.

I. Paddle number

The influence of the paddle number on the mixing performance of the paddle mixer is shown in Figure 23.

Looking at Figure 23, the paddle number does have an influence on both the mixing efficiency (KPI 2) and mixing effectiveness (KPI 1). Less paddles compared to the original paddle number (equal to 14), would mean less particles will be relocated over time and thus slower mixing. With respect to mixing efficiency, a paddle number of 28 did not lead to expected result. More paddles do not contribute to reaching the steady-state RSD quicker. The creation of a stagnant fluidized zone is causing the slower mixing mechanism compared to the *i*=14 level (indicated by the blue color in Figure 25).

After the first analysis it is decided to also investigate two variants of the paddle number *i*=7, which can be seen in Figure 26. In Figure 24 the results are presented.

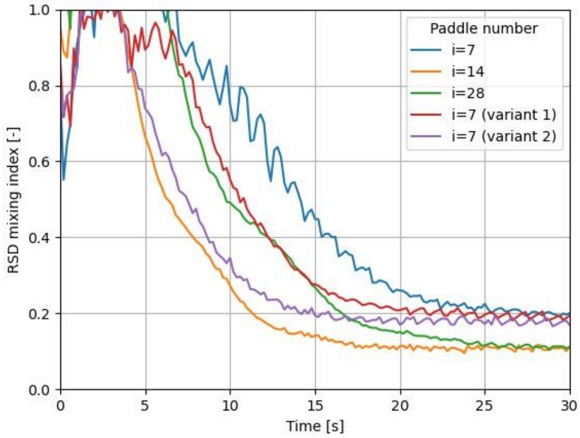

Fig. 24. RSD mixing index over time for different paddle numbers, including variant 1 and variant 2 of the paddle number equal to 7.

As can be concluded from Figure 24, different configurations of the paddle number *i*=7 leads to different results, but eventually an identical steady-state RSD value is reached for all three variants of the *i*=7 level.

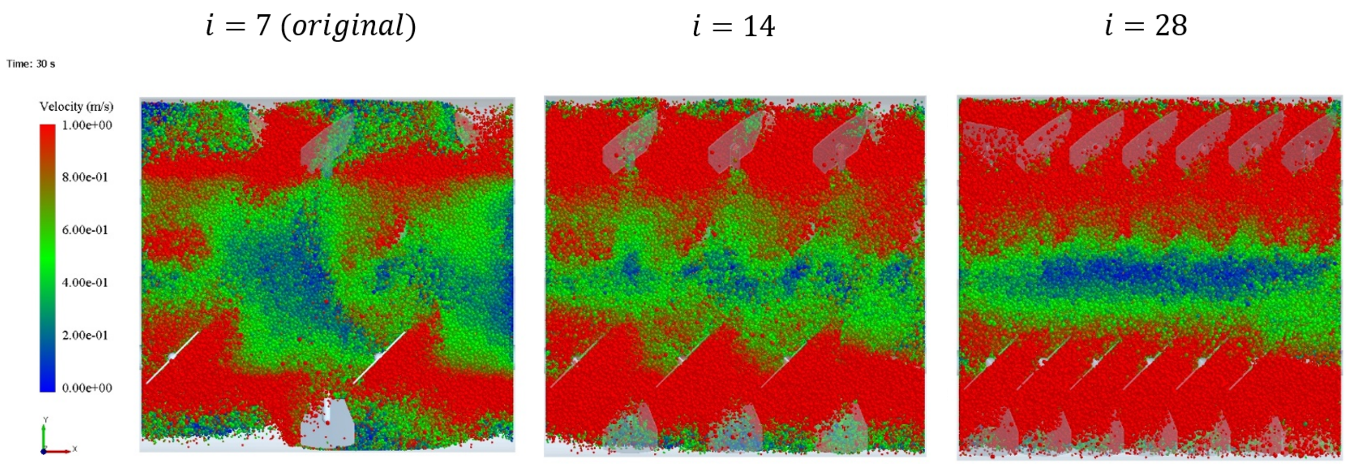

Fig. 25. Velocity of particles from top view for all three paddle numbers at time=31s.

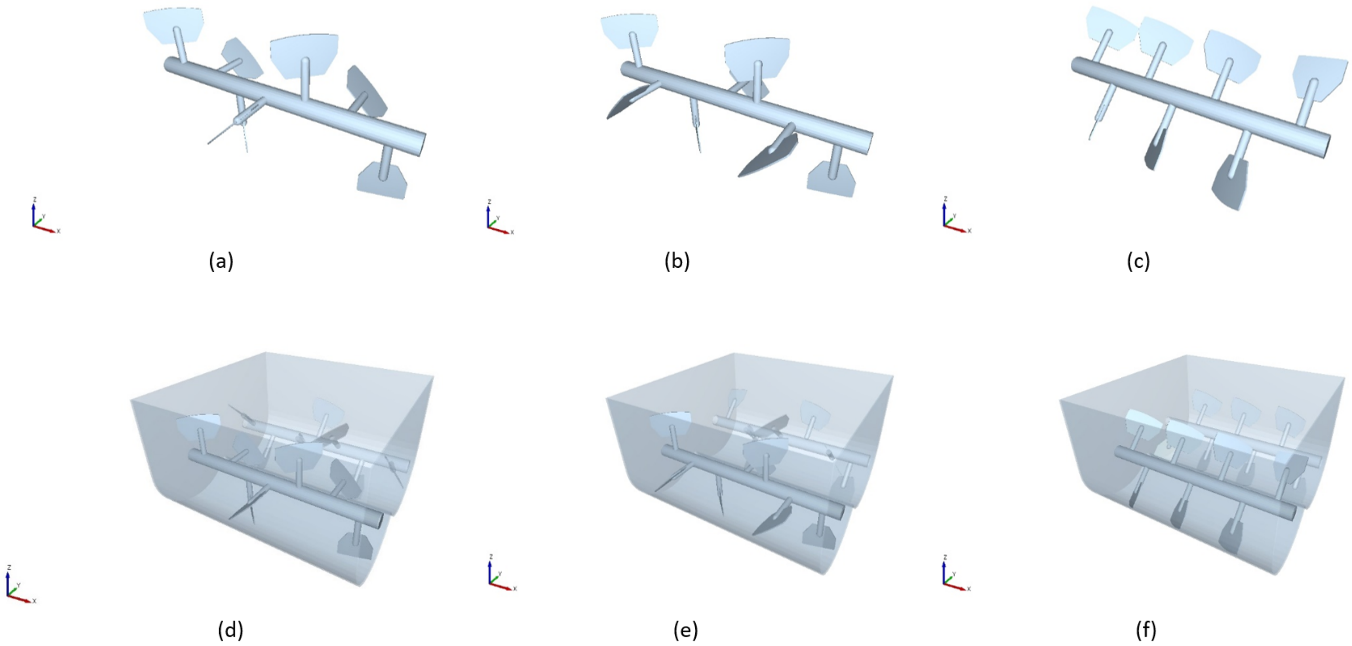

Fig. 26. (a) Original paddle number of 7, (b) variant 1, (c) variant 2, (d) Original shaft configuration, (e) shaft configuration for variant 1 and (f) shaft configuration of variant 2.

VII. CONCLUSIONS

The discrete element method (DEM) in combination with an One Factor At a Time (OFAT) experimental simulation plan were employed to investigate the effect of a selection of factors on the mixing performance of a double shaft, batch-type paddle mixer. The factors are three material characteristics (particle size, particle density and composition), three operational conditions (initial filling pattern, fill level and impeller rotational speed) and three geometric characteristics (paddle size, paddle angle and paddle number). A two-component adopted material model consisting of free-flowing, spherical glass beads was used as starting point. Based upon the mixing index Relative Standard Deviation (RSD), two Key Performance Indicators (KPIs) were defined tailored to the paddle mixer to assess the mixing performance of the system in terms of mixing effectiveness (KPI 1) and mixing efficiency (KPI 2).

The mixing performance is evaluated on mixing effectiveness (KPI 1) and mixing efficiency (KPI 2). An overview of all results is shown in Figure 27. The partially greyed out plots of the composition and fill level are not considered. The c=99/1 composition results are affected by the designed 14x14x9 grid system, even as the e=40% fill level and require further research to draw valid conclusions. The e=140% fill level did not reach a steady-state RSD after 30 seconds of mixing and is therefore excluded.

With respect to the mixing effectiveness (KPI 1) as shown in Figure 27, the factors particle size, particle density, paddle angle and paddle number have a significant influence on the final steady-state RSD value reached after 30 seconds of mixing.

Furthermore, it can be observed that all factors have a

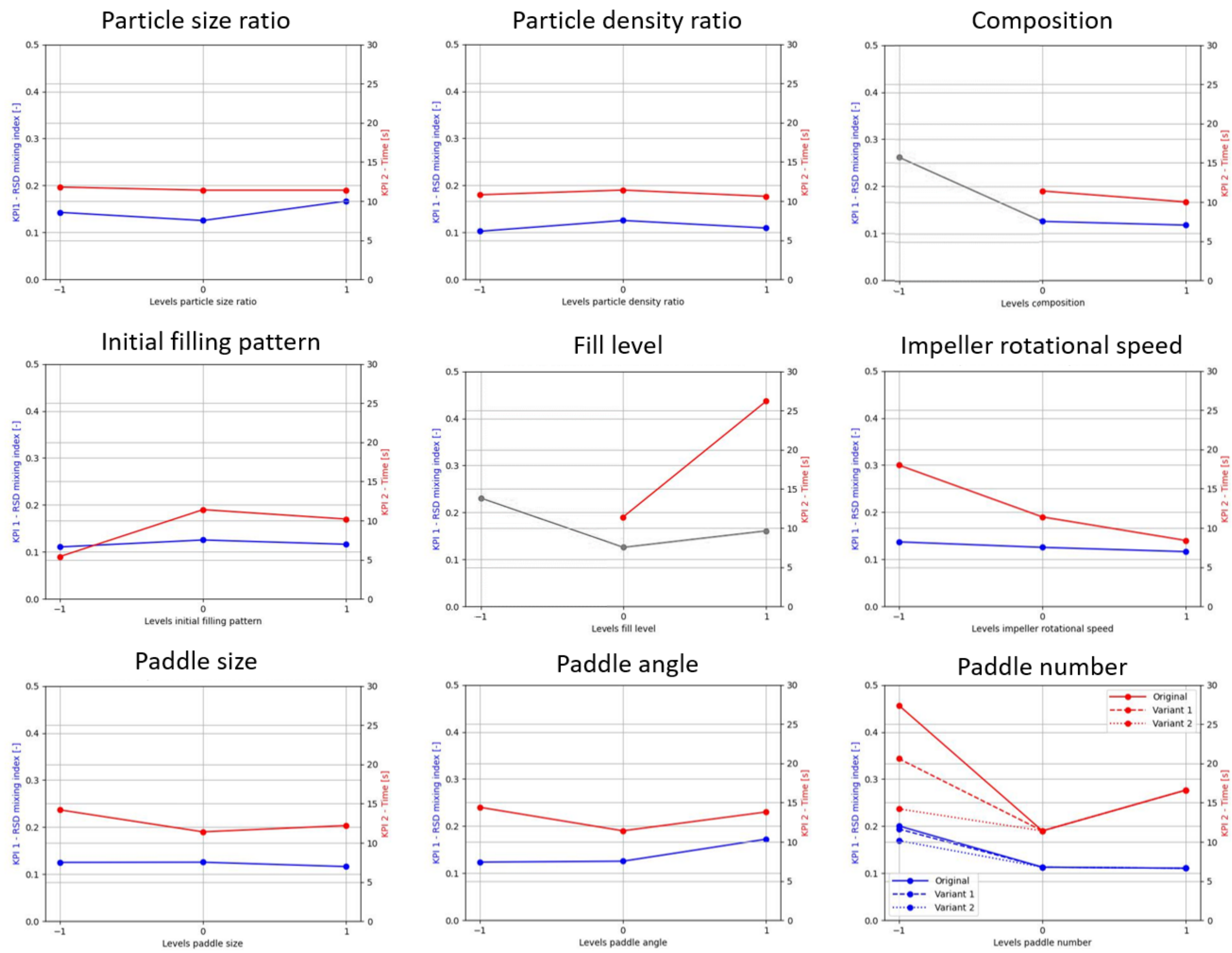

Fig. 27. Overview of the influence of all factors on KPI and KPI 2. Greyed out plots of the composition and fill levels are not considered.

nonlinear relation (besides particle density) with evaluated KPI 1. Initially it was expected that an increase in particle size ratio would cause an increase in KPI 1. However, as can be seen in Figure 27 this is not true. Literature suggest that interplay of particle size and particle density can cause mixing to be enhanced or attenuated. Therefore, the non-linearity of the particle size is expected to originate from the interaction with the particle density.

With respect to the paddle angle, an optimal configuration exists between the 30 and 60 degrees. Thus, it can be concluded that the radial mixing and the axial mixing mechanisms both contribute to the mixing performance of the paddle mixer. Increasing the number of paddles will improve the mixing effectiveness up to a certain point. Eventually, the extra surface that relocates the granular material will not add value anymore. What the tipping point is concerning the addition of paddles needs further investigation. Besides, how the paddles are assembled onto the shaft could also have an effect on KPI 1 as can be seen by the different variants of the paddle number equal to 7 (Figure 27).

With respect to the mixing efficiency (KPI 2) as shown in Figure 27, the factors initial filling pattern, fill level, impeller rotational speed and paddle number have a major influence. The factors composition, paddle size and paddle angle have a substantial influence.

Moreover, the factors paddle size, paddle angle and paddle number do have a nonlinear relation with KPI 2. The initial filling pattern is excluded here since it is a categorical factor. But, it can be stated that the Top-Bottom (TB) initial filling pattern performs best compared to the Front-Back (FB) and Side-by-Side (SS) patterns. Additionally, increasing the impeller rotational speed results in a decrease of KPI 2. In other words, mixing of the product occurs faster. Finally, the effect of the paddle number on KPI 2 is significant. Irrespective of the i=7 paddle variants, it can be observed that the mixing efficiency does not improve when eliminating 7 paddles or adding 14 paddles to the original paddle number of i=14.

In Figure 28, the factor significance on the mixing performance is shown. The particle size and particle density have a significant effect on the final mixture quality after 30 seconds of mixing (KPI 1: Mixing effectiveness). The composition, initial filling pattern, fill level, impeller rotational speed and paddle size have a significant effect on how fast a steady-state mixture quality is reached (KPI 2: Mixing efficiency). The paddle angle and paddle number have a significant effect on both KPIs and therefore holds most potential with respect to optimization purposes.

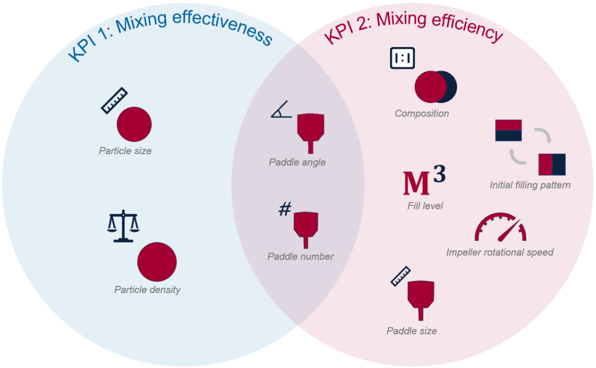

Fig. 28. Venn diagram of factor significance with regard to KPI 1: Mixing effectiveness and KPI 2: Mixing efficiency.

It should be noted the research findings only explicate main effects of selected factors on the mixing performance of a double shaft batch-type paddle mixer and no factor interactions are captured. Accordingly, conclusions drawn about every individual factor in this chapter are valid when all other factors are fixed at their center point values (Table IV). Validation of the retrieved results by means of real-world physical experiments is required.

To make a deliberate choice in which factors are most suitable for further analysis, more simulations are required. Depending on the number of factors, it is recommended to use a statistics-based Design of Experiments (DoE) simulation plan. With a minimum number of runs the main effect of factors and low-level interactions between factors can be captured by DoE. Moreover, obtained results are only valid for bi-disperse, free-flowing spherical glass beads. The effect of cohesion between particles or particle shape could be interesting research directions.

BIBLIOGRAPHY

[1] Basel Alchikh-Sulaiman, Farhad Ein-Mozaffari, and Ali Lohi. “Evaluation of poly-disperse solid particles mixing in a slant cone mixer using discrete element method”. en. In: *Chemical Engineering Research and Design* 96 (Apr. 2015), pp. 196–213. ISSN: 0263-8762. DOI: `10.1016/j.cherd.2015.02.020`. URL: `https://www.sciencedirect.com/science/article/pii/S0263876215000623` (visited on 04/14/2022).

[2] Meysam Alian, Farhad Ein-Mozaffari, and Simant R. Upreti. “Analysis of the mixing of solid particles in a plowshare mixer via discrete element method (DEM)”. en. In: *Powder Technology* 274 (Apr. 2015), pp. 77–87. ISSN: 0032-5910. DOI: `10.1016/j.powtec.2015.01.012`. URL: `https://www.sciencedirect.com/science/article/pii/S0032591015000224` (visited on 04/19/2022).

[3] F. Bertrand, L. -A. Leclaire, and G. Levecque. “DEM-based models for the mixing of granular materials”. en. In: *Chemical Engineering Science*. 5th International Symposium on Mixing in Industrial Processes (ISMIP5) 60.8 (Apr. 2005), pp. 2517–2531. ISSN: 0009-2509. DOI: `10.1016/j.ces.2004.11.048`. URL: `https://www.sciencedirect.com/science/article/pii/S0009250904009492` (visited on 03/08/2022).

[4] Pooja Bhalode and Marianthi Ierapetritou. “A review of existing mixing indices in solid-based continuous blending operations”. en. In: *Powder Technology* 373 (Aug. 2020), pp. 195–209. ISSN: 0032-5910. DOI: `10.1016/j.powtec.2020.06.043`. URL: `https://www.sciencedirect.com/science/article/pii/S0032591020305635` (visited on 03/22/2022).

[5] P. A. Cundall and O. D. L. Strack. “A discrete numerical model for granular assemblies”. In: *Géotechnique* 29.1 (Mar. 1979). Publisher: ICE Publishing, pp. 47–65. ISSN: 0016-8505. DOI: `10.1680/geot.1979.29.1.47`. URL: `https://www.icevirtuallibrary.com/doi/abs/10.1680/geot.1979.29.1.47` (visited on 03/09/2022).

[6] M. Ebrahimi et al. “The effect of impeller configurations on particle mixing in an agitated paddle mixer”. English. In: *Powder Technology* 332 (2018), pp. 158–170. ISSN: 0032-5910. DOI: `10.1016/j.powtec.2018.03.061`.

[7] Mohammadreza Ebrahimi et al. “Assessment of bi-disperse solid particles mixing in a horizontal paddle mixer through experiments and DEM”. en. In: *Powder Technology* 381 (Mar. 2021), pp. 129–140. ISSN: 0032-5910. DOI: `10.1016/j.powtec.2020.11.041`. URL: `https://www.sciencedirect.com/science/article/pii/S0032591020310949` (visited on 02/01/2022).

[8] H.j. Feise and J.w. Carson. "The Evolution of Bulk Solids Technology Since 1982". de. In: *Chemical Engineering & Technology* 26.2 (2003), pp. 121–131. ISSN: 1521-4125. DOI: `10.1002/ceat.200390018`. URL: `https://onlinelibrary.wiley.com/doi/abs/10.1002/ceat.200390018` (visited on 03/09/2022).

[9] Halvor G. Forberg. "Twin Horizontal Axled Inwardly Rotating Paddle Mixer for Dry Ingredients". Mar. 1983.

[10] Andrew Grima. "Quantifying and modelling mechanisms of flow in cohesionless and cohesive granular materials". In: *University of Wollongong Thesis Collection 1954-2016* (Jan. 2011). URL: `https://ro.uow.edu.au/theses/3425`.

[11] A. Hassanpour et al. "Analysis of particle motion in a paddle mixer using Discrete Element Method (DEM)". English. In: *Powder Technology* 206.1-2 (2010), pp. 189–194. ISSN: 0032-5910. DOI: `10.1016/j.powtec.2010.07.025`.

[12] Behrooz Jadidi et al. "Mixing performance analysis of non-cohesive particles in a double paddle blender using DEM and experiments". en. In: *Powder Technology* 397 (Jan. 2022), p. 117122. ISSN: 0032-5910. DOI: `10.1016/j.powtec.2022.117122`. (Visited on 02/01/2022).

[13] Nitin Jain, Julio M. Ottino, and Richard M. Lueptow. "Regimes of segregation and mixing in combined size and density granular systems: an experimental study". en. In: *Granular Matter* 7.2 (July 2005), pp. 69–81. ISSN: 1434-7636. DOI: `10.1007/s10035-005-0198-x`. URL: `https://doi.org/10.1007/s10035-005-0198-x` (visited on 10/31/2022).

[14] J. Li, C. Wassgren, and J.D. Litster. "Multi-scale modeling of a spray coating process in a paddle mixer/coater: The effect of particle size distribution on particle segregation and coating uniformity". English. In: *Chemical Engineering Science* 95 (2013), pp. 203–210. ISSN: 0009-2509. DOI: `10.1016/j.ces.2013.03.014`.

[15] M. Pasha et al. "A comparative analysis of particle tracking in a mixer by discrete element method and positron emission particle tracking". English. In: *Powder Technology* 270.PB (2015), pp. 569–574. ISSN: 0032-5910. DOI: `10.1016/j.powtec.2014.09.007`.

[16] Martin J. Rhodes. *Introduction to Particle Technology*. en. Google-Books-ID: P9Qgvh7kMP8C. John Wiley & Sons, June 2008. ISBN: 978-0-470-01427-1.

[17] Pooja Shenoy et al. "Dry mixing of food powders: Effect of water content and composition on mixture quality of binary mixtures". en. In: *Journal of Food Engineering* 149 (Mar. 2015), pp. 229–236. ISSN: 0260-8774. DOI: `10.1016/j.jfoodeng.2014.10.019`. URL: `https://www.sciencedirect.com/science/article/pii/S0260877414004397` (visited on 03/15/2022).

[18] Pooja Shenoy et al. "Effect of powder densities, particle size and shape on mixture quality of binary food powder mixtures". en. In: *Powder Technology* 272 (Mar. 2015), pp. 165–172. ISSN: 0032-5910. DOI: `10.1016/j.powtec.2014.11.023`. URL: `https://www.sciencedirect.com/science/article/pii/S0032591014009334` (visited on 04/19/2022).

[19] Sunil R. de Silva, Are Dyrøy, and Gisle G. Enstad. "Segregation Mechanisms and Their Quantification Using Segregation Testers". en. In: *IUTAM Symposium on Segregation in Granular Flows*. Ed. by Anthony D. Rosato and Denis L. Blackmore. Solid Mechanics and Its Applications. Dordrecht: Springer Netherlands, 2000, pp. 11–29. ISBN: 978-94-015-9498-1. DOI: `10.1007/978-94-015-9498-1_2`.

[20] . *Stainless Steel - Grade 304 (UNS S30400)*. en. Section: Materials Article. Oct. 2001. URL: `https://www.azom.com/article.aspx?ArticleID=965` (visited on 12/07/2022).

[21] A. Yaraghi et al. "Mixing assessment of non-cohesive particles in a paddle mixer through experiments and discrete element method (DEM)". English. In: *Advanced Powder Technology* 29.11 (2018), pp. 2693–2706. ISSN: 0921-8831. DOI: `10.1016/j.apt.2018.07.019`.

B

Simulation Model

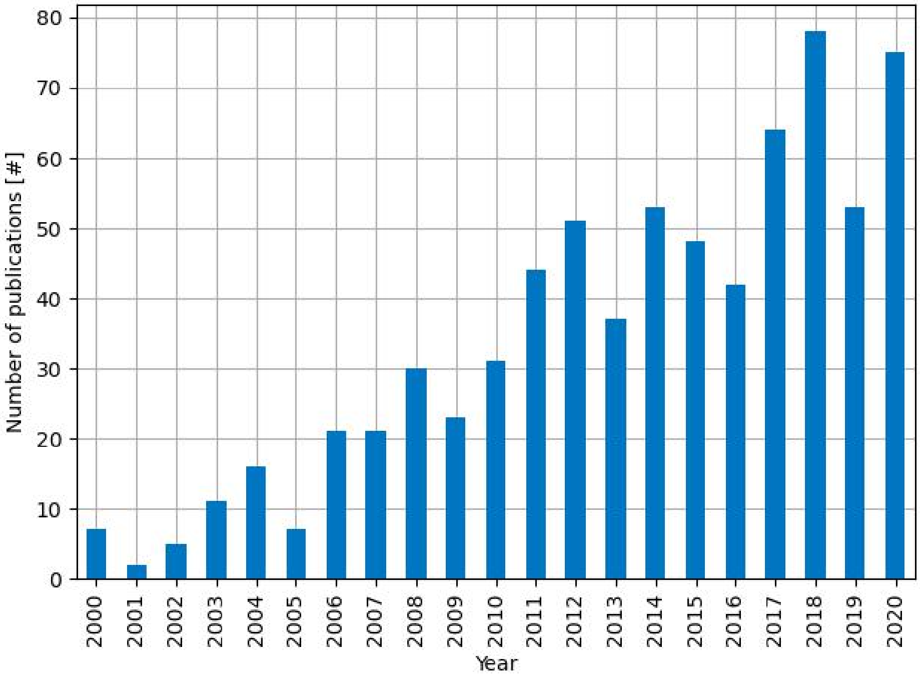

Figure B.1: Number of publications for the last two decades with keywords ”Discrete Element Method”, ”Discrete Element Model”, ”Discrete Particle Simulation”, ”Discrete Particle Simulation”, ”Discrete Particle Method” and ”Granular dynamic simulation” on search engine Scopus.

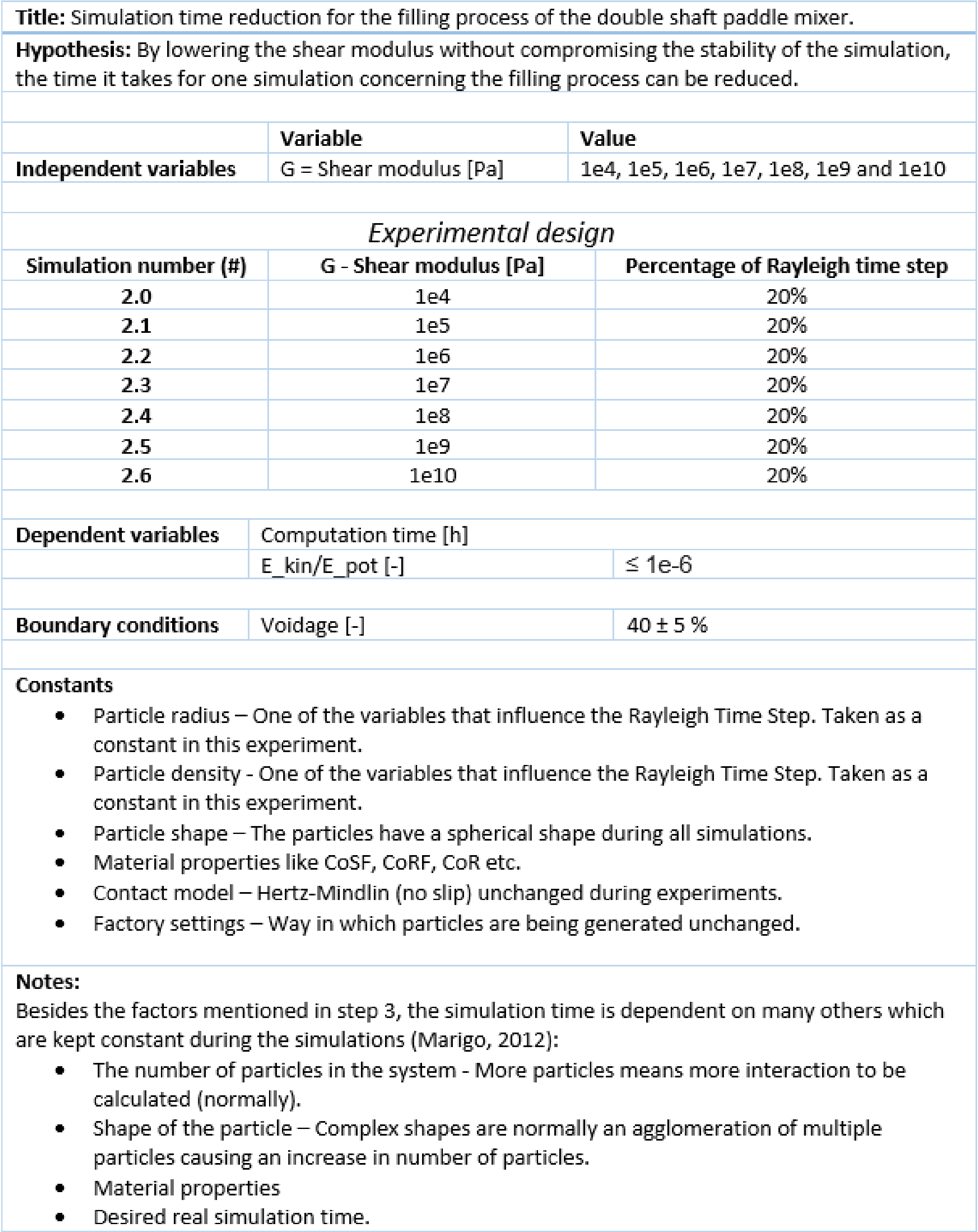

Title: Simulation time reduction for the filling process of the double shaft paddle mixer.

Hypothesis: By lowering the shear modulus without compromising the stability of the simulation, the time it takes for one simulation concerning the filling process can be reduced.

	Variable	**Value**
Independent variables	G = Shear modulus [Pa]	1e4, 1e5, 1e6, 1e7, 1e8, 1e9 and 1e10

Experimental design

Simulation number (#)	**G - Shear modulus [Pa]**	**Percentage of Rayleigh time step**
2.0	1e4	20%
2.1	1e5	20%
2.2	1e6	20%
2.3	1e7	20%
2.4	1e8	20%
2.5	1e9	20%
2.6	1e10	20%

Dependent variables	Computation time [h]	
	E_kin/E_pot [-]	≤ 1e-6
Boundary conditions	Voidage [-]	40 ± 5 %

Constants

- Particle radius – One of the variables that influence the Rayleigh Time Step. Taken as a constant in this experiment.
- Particle density - One of the variables that influence the Rayleigh Time Step. Taken as a constant in this experiment.
- Particle shape – The particles have a spherical shape during all simulations.
- Material properties like CoSF, CoRF, CoR etc.
- Contact model – Hertz-Mindlin (no slip) unchanged during experiments.
- Factory settings – Way in which particles are being generated unchanged.

Notes:

Besides the factors mentioned in step 3, the simulation time is dependent on many others which are kept constant during the simulations (Marigo, 2012):

- The number of particles in the system - More particles means more interaction to be calculated (normally).
- Shape of the particle – Complex shapes are normally an agglomeration of multiple particles causing an increase in number of particles.
- Material properties
- Desired real simulation time.

Figure B.2: Step 1 of simulation plan for filling process of 'worst-case scenario' simulation.

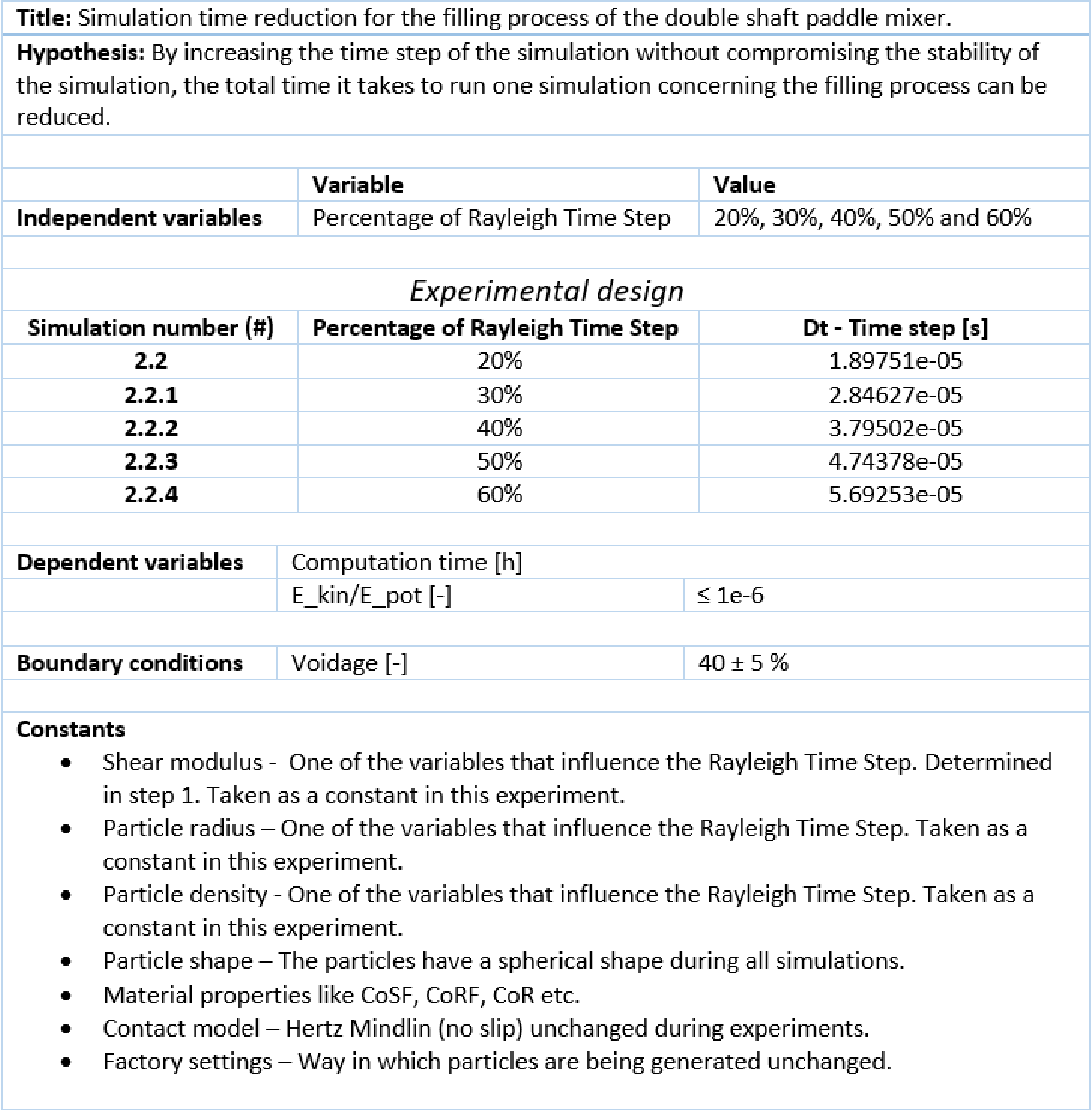

Title: Simulation time reduction for the filling process of the double shaft paddle mixer.

Hypothesis: By increasing the time step of the simulation without compromising the stability of the simulation, the total time it takes to run one simulation concerning the filling process can be reduced.

	Variable	Value
Independent variables	Percentage of Rayleigh Time Step	20%, 30%, 40%, 50% and 60%

Experimental design

Simulation number (#)	Percentage of Rayleigh Time Step	Dt - Time step [s]
2.2	20%	1.89751e-05
2.2.1	30%	2.84627e-05
2.2.2	40%	3.79502e-05
2.2.3	50%	4.74378e-05
2.2.4	60%	5.69253e-05

Dependent variables	Computation time [h]	
	E_kin/E_pot [-]	≤ 1e-6
Boundary conditions	Voidage [-]	40 ± 5 %

Constants

- Shear modulus - One of the variables that influence the Rayleigh Time Step. Determined in step 1. Taken as a constant in this experiment.
- Particle radius – One of the variables that influence the Rayleigh Time Step. Taken as a constant in this experiment.
- Particle density - One of the variables that influence the Rayleigh Time Step. Taken as a constant in this experiment.
- Particle shape – The particles have a spherical shape during all simulations.
- Material properties like CoSF, CoRF, CoR etc.
- Contact model – Hertz Mindlin (no slip) unchanged during experiments.
- Factory settings – Way in which particles are being generated unchanged.

Figure B.3: Step 2 of simulation plan for filling process of ’worst-case scenario’ simulation.

C

Grid system

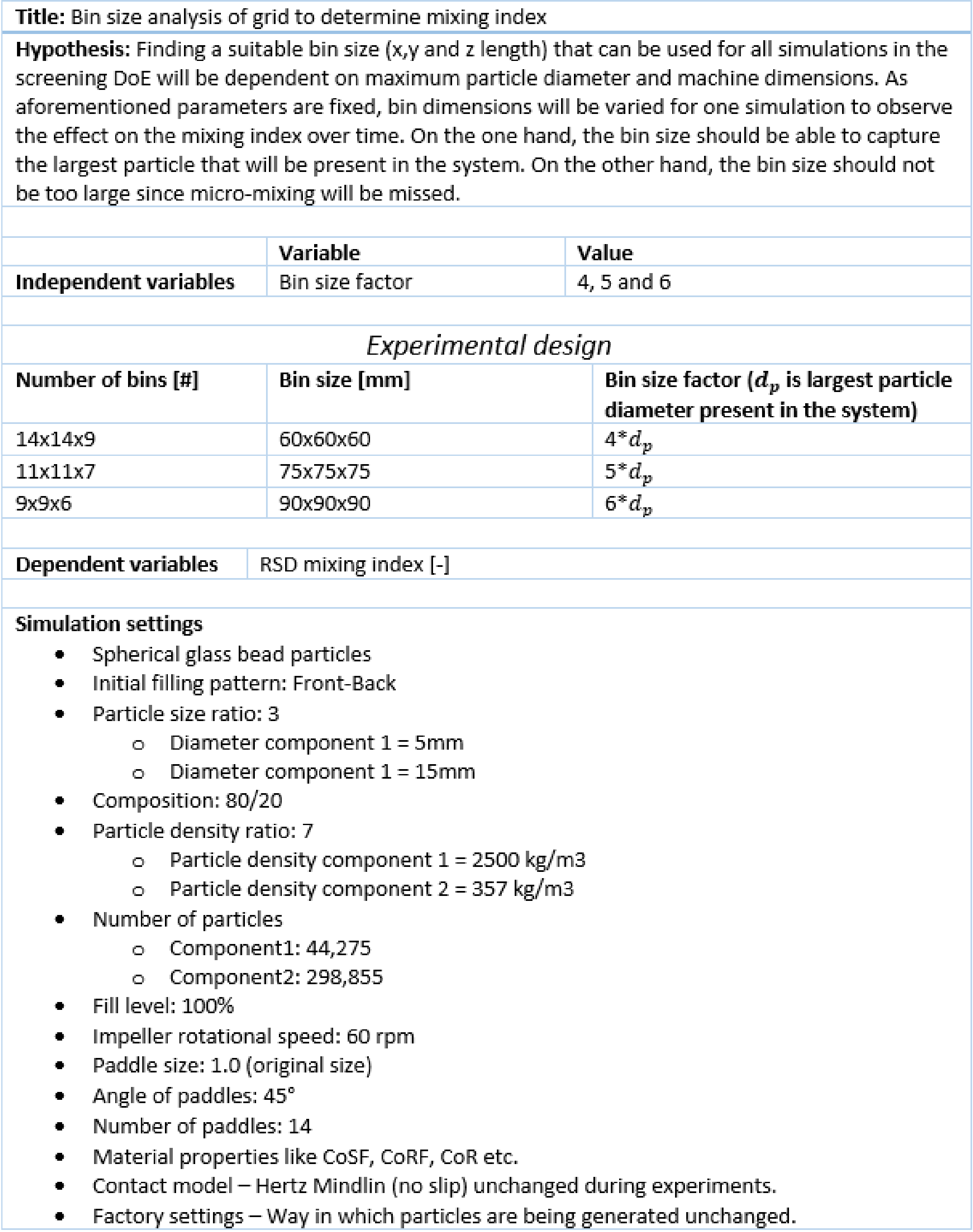

Title: Bin size analysis of grid to determine mixing index

Hypothesis: Finding a suitable bin size (x,y and z length) that can be used for all simulations in the screening DoE will be dependent on maximum particle diameter and machine dimensions. As aforementioned parameters are fixed, bin dimensions will be varied for one simulation to observe the effect on the mixing index over time. On the one hand, the bin size should be able to capture the largest particle that will be present in the system. On the other hand, the bin size should not be too large since micro-mixing will be missed.

	Variable	**Value**
Independent variables	Bin size factor	4, 5 and 6

Experimental design

Number of bins [#]	**Bin size [mm]**	**Bin size factor (d_p is largest particle diameter present in the system)**
14x14x9	60x60x60	$4*d_p$
11x11x7	75x75x75	$5*d_p$
9x9x6	90x90x90	$6*d_p$

Dependent variables	RSD mixing index [-]

Simulation settings

- Spherical glass bead particles
- Initial filling pattern: Front-Back
- Particle size ratio: 3
  - Diameter component 1 = 5mm
  - Diameter component 1 = 15mm
- Composition: 80/20
- Particle density ratio: 7
  - Particle density component 1 = 2500 kg/m3
  - Particle density component 2 = 357 kg/m3
- Number of particles
  - Component1: 44,275
  - Component2: 298,855
- Fill level: 100%
- Impeller rotational speed: 60 rpm
- Paddle size: 1.0 (original size)
- Angle of paddles: 45°
- Number of paddles: 14
- Material properties like CoSF, CoRF, CoR etc.
- Contact model – Hertz Mindlin (no slip) unchanged during experiments.
- Factory settings – Way in which particles are being generated unchanged.

Figure C.1: Simulation plan for determination suitable bin size of grid bin system.

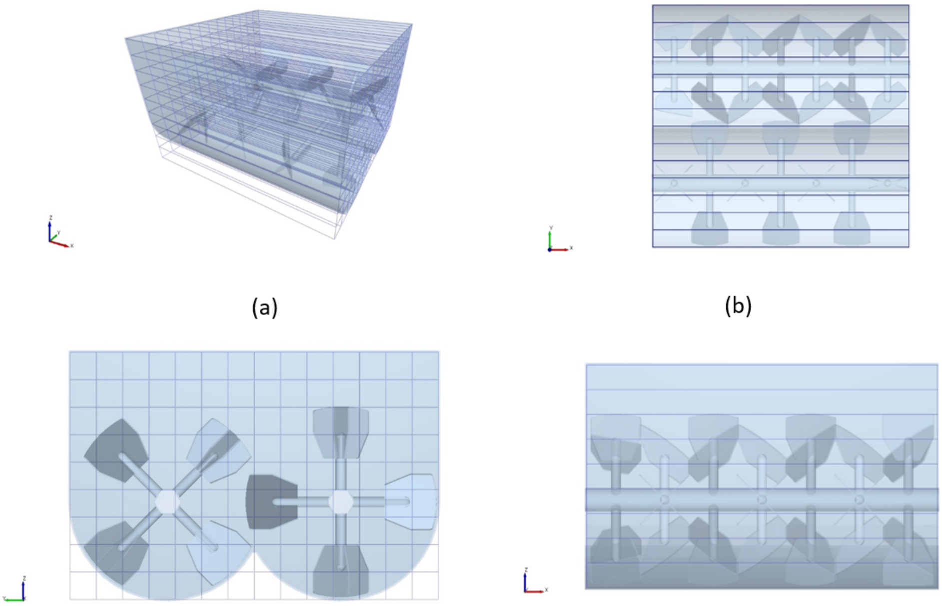

Figure C.2: (a) Isometric view, (b) top view, (c) front view and (d) right side view of 1x14x9 local grid system in x-direction.

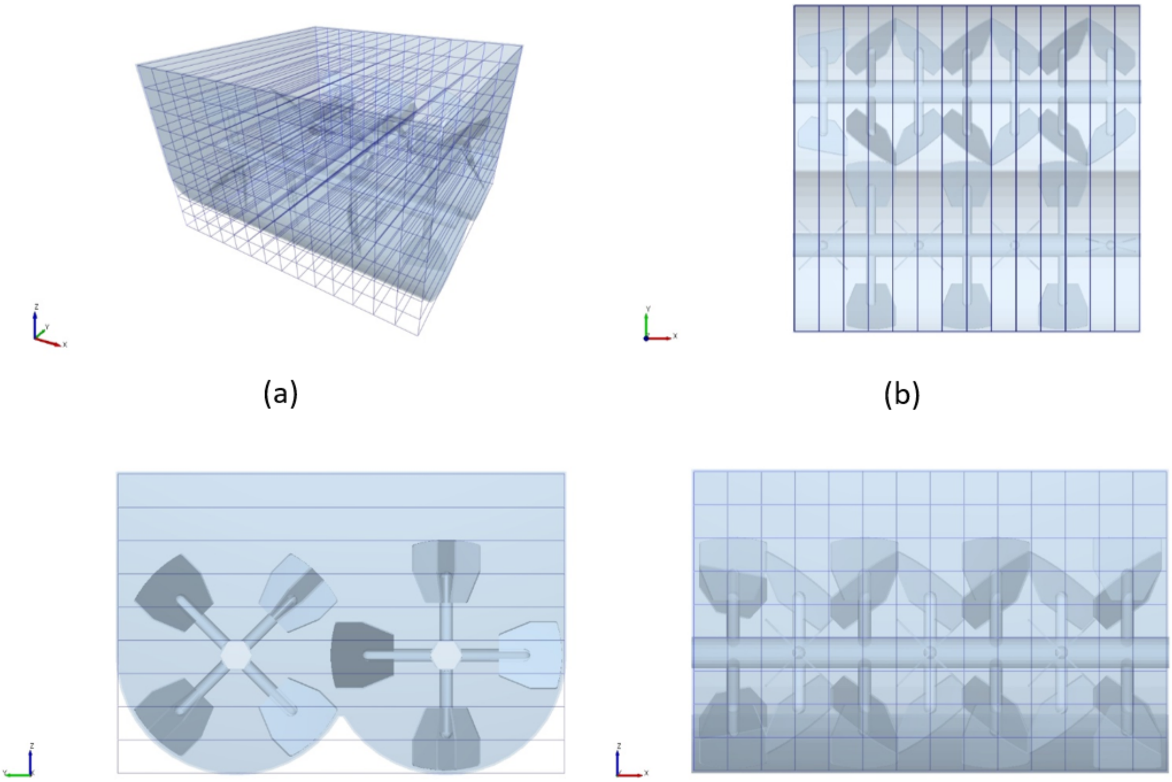

Figure C.3: (a) Isometric view, (b) top view, (c) front view and (d) right side view of 14x1x9 local grid system in y-direction.

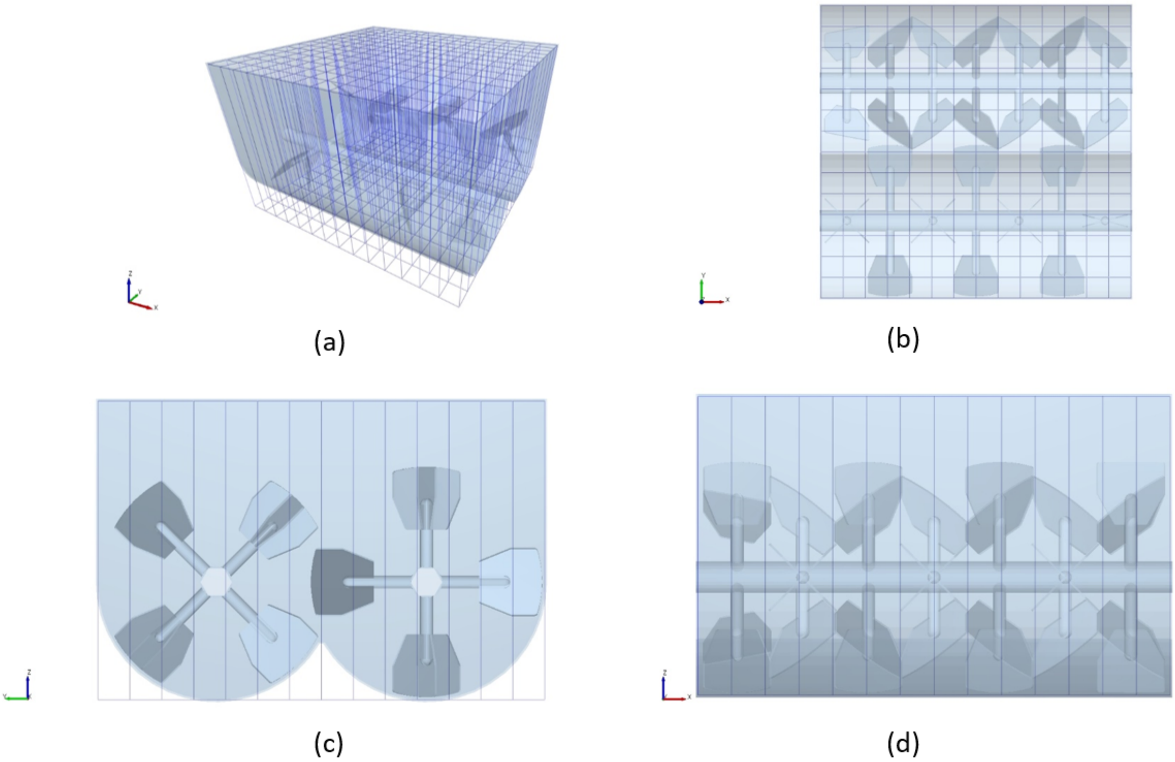

Figure C.4: (a) Isometric view, (b) top view, (c) front view and (d) right side view of 14x14x1 local grid system in z-direction.

D

Results

In this appendix, all results are presented in tabular and graphical form. Values of KPI 1 and KPI 2 are shown in Table D.1, Table D.2 and Table D.3. Additional screenshots and heat maps are displayed for every simulation separately.

Table D.1: Values KPI 1 and KPI 2 for all simulations.

Run	Factor	Level	KPI 1	KPI 2
1	Ref.	-	0.113	11.4
2	a	1	0.113	11.8
3		3	0.167	11.4
4	b	1	0.102	10.8
5		20	0.109	10.6
6	c	99/1	0.262	-
7		50/50	0.118	10
8	p	TB	0.111	5.4
9		SS	0.116	10.2
10	e	40%	0.231	-
11		140%	0.160	26.2
12	f	40 rpm	0.137	18
13		80 rpm	0.116	8.4
14	g	2/3	0.125	14.2
15		3/2	0.116	12.2
16	α_1	30°	0.123	14.4
17		60°	0.123	13.8
18	i	7	0.201	27.4
19		28	0.111	16.6

Table D.2: Values KPI 1 and KPI 2 for simulations 6, 7, 10 and 11 with adjusted grid system consisting of 7x7x4 bins instead of 14x14x9 bins.

Run	Factor	Level	KPI 1	KPI 2
1	Ref.	-	0.057	10.4
6	c	99/1	0.131	9.6
7		50/50	0.062	8.8
10	e	40%	0.151	5.6
11		140%	0.133	24.4

Table D.3: Values KPI 1 and KPI 2 for simulations 1, 18 (including two variants) and 19.

Run	Factor	Level	KPI 1	KPI 2
1	Ref.	-	0.132	11.4
18	i	7	0.201	27.4
18 (variant 1)		7	0.194	20.6
18 (variant 2)		7	0.169	14.2
19		28	0.111	16.6

D.1. Simulation 1 - Center point

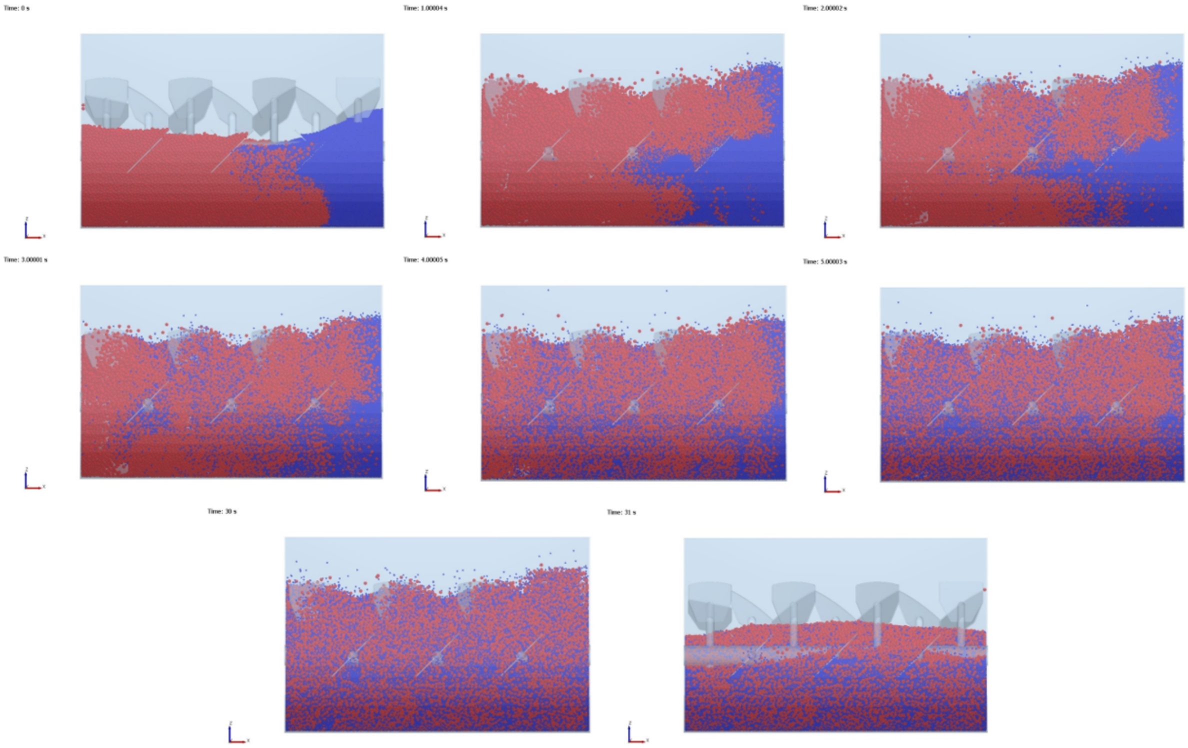

Figure D.1: Side view of simulation 1 - Center point for time step t=0s, t=1s, t=2s, t=3s, t=4s, t=5s, t=30s and t=31s.

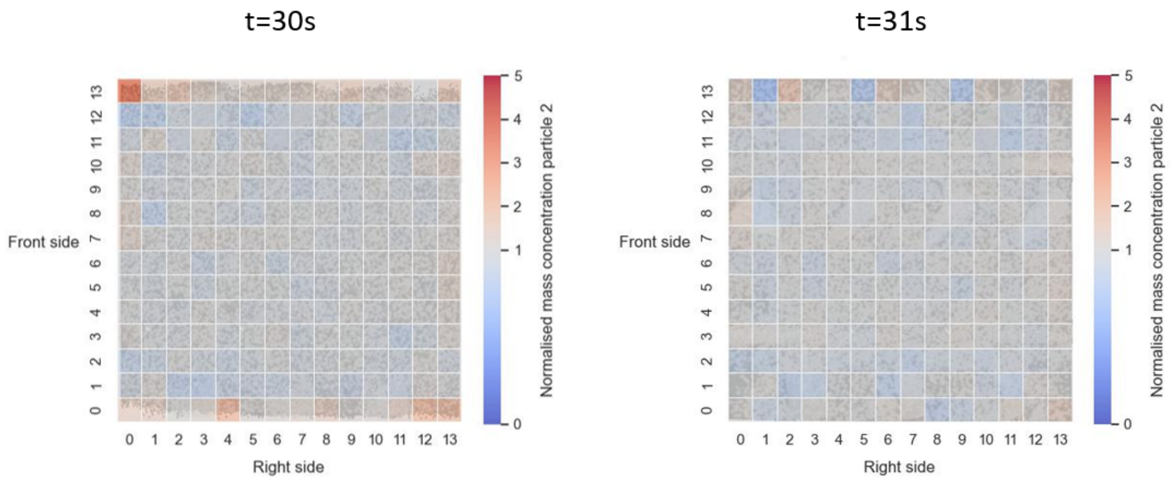

Figure D.2: Simulation 1 - Heat map of 14x14x1 grid with normalized concentrations of particle 2 at time=30s and t=31s.

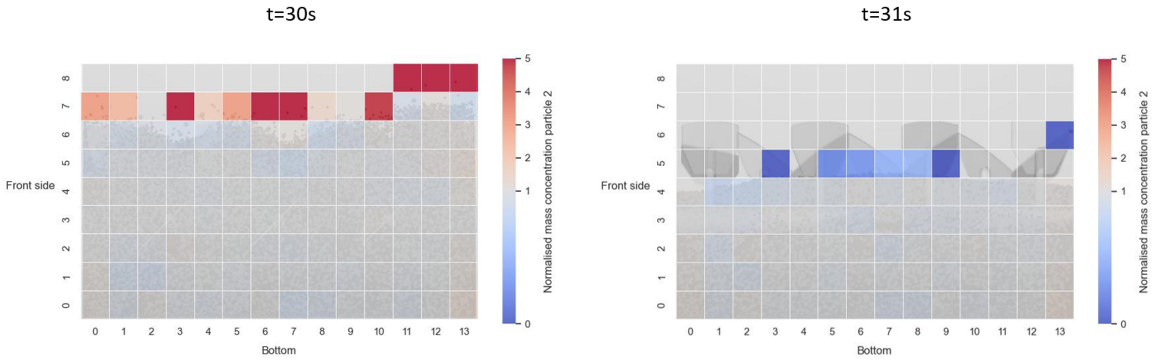

Figure D.3: Simulation 1 - Heat map of 14x1x9 grid with normalized concentrations of particle 2 at time=30s and t=31s.

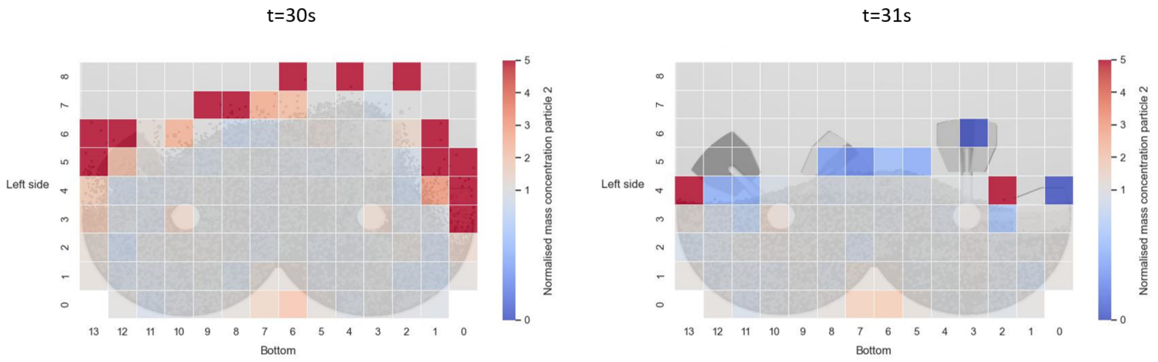

Figure D.4: Simulation 1 - Heat map of 1x14x9 grid with normalized concentrations of particle 2 at time=30s and t=31s.

D.2. Simulation 2 - Particle size ratio (-1)

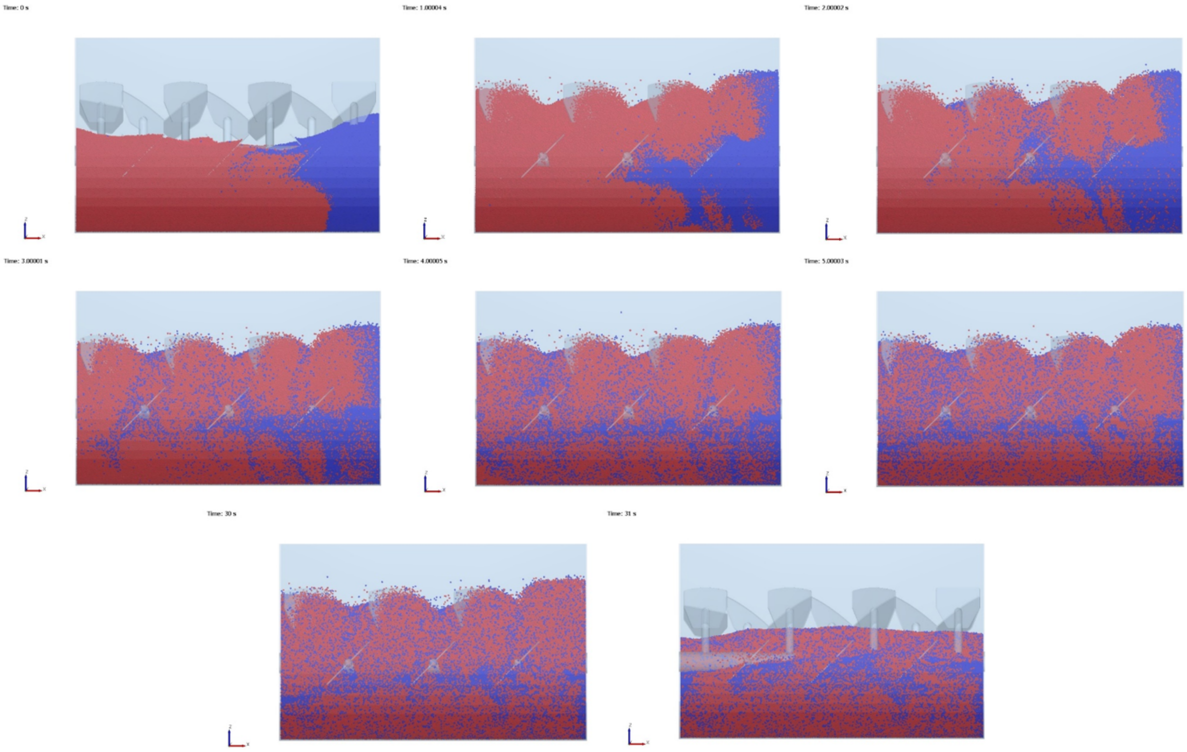

Figure D.5: Side view of simulation 2 - Particle size ratio (α=1) for time step t=0s, t=1s, t=2s, t=3s, t=4s, t=5s, t=30s and t=31s.

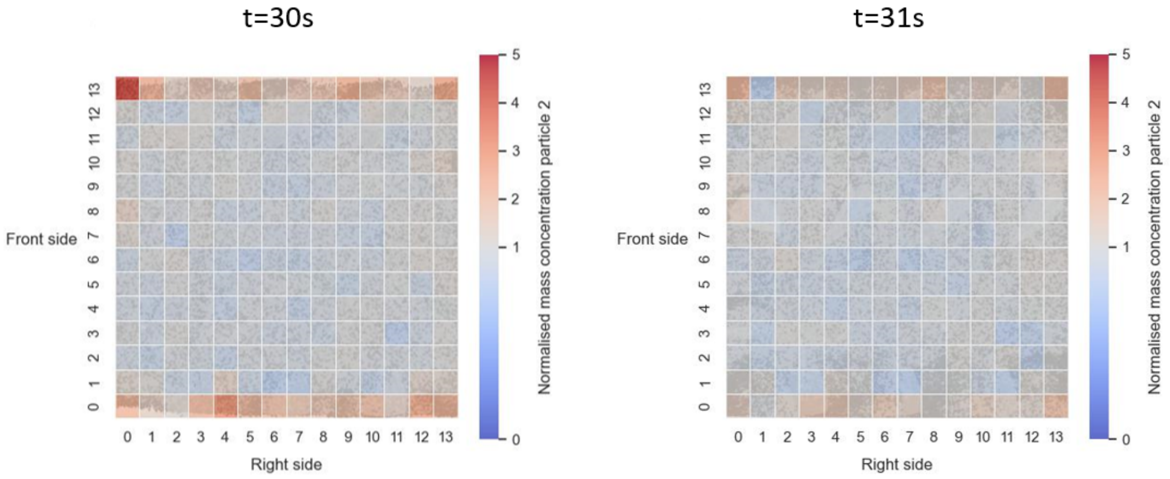

Figure D.6: Simulation 2 - Heat map of 14x14x1 grid with normalized concentrations of particle 2 at time=30s and t=31s.

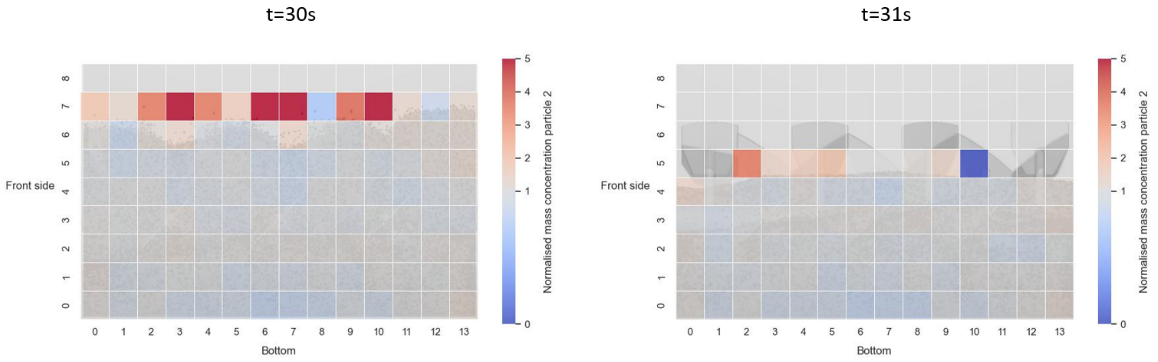
t=30s

t=31s

Figure D.7: Simulation 2 - Heat map of 14x1x9 grid with normalized concentrations of particle 2 at time=30s and t=31s.

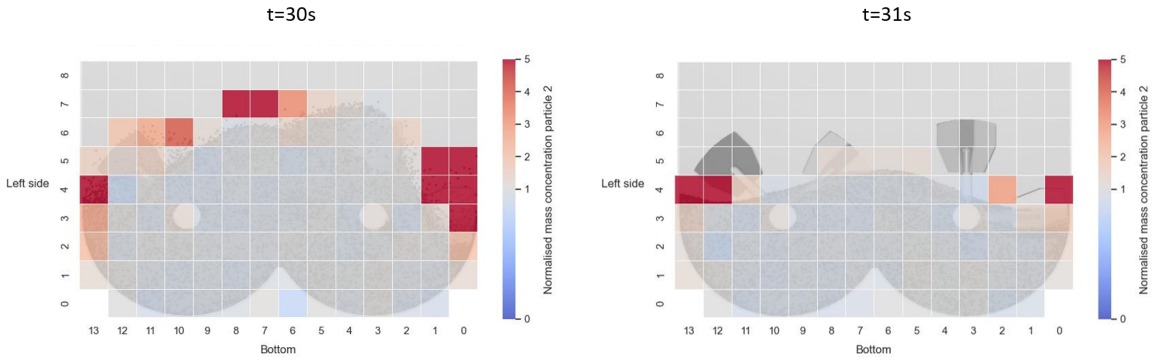
t=30s

t=31s

Figure D.8: Simulation 2 - Heat map of 1x14x9 grid with normalized concentrations of particle 2 at time=30s and t=31s.

D.3. Simulation 3 - Particle size ratio (+1)

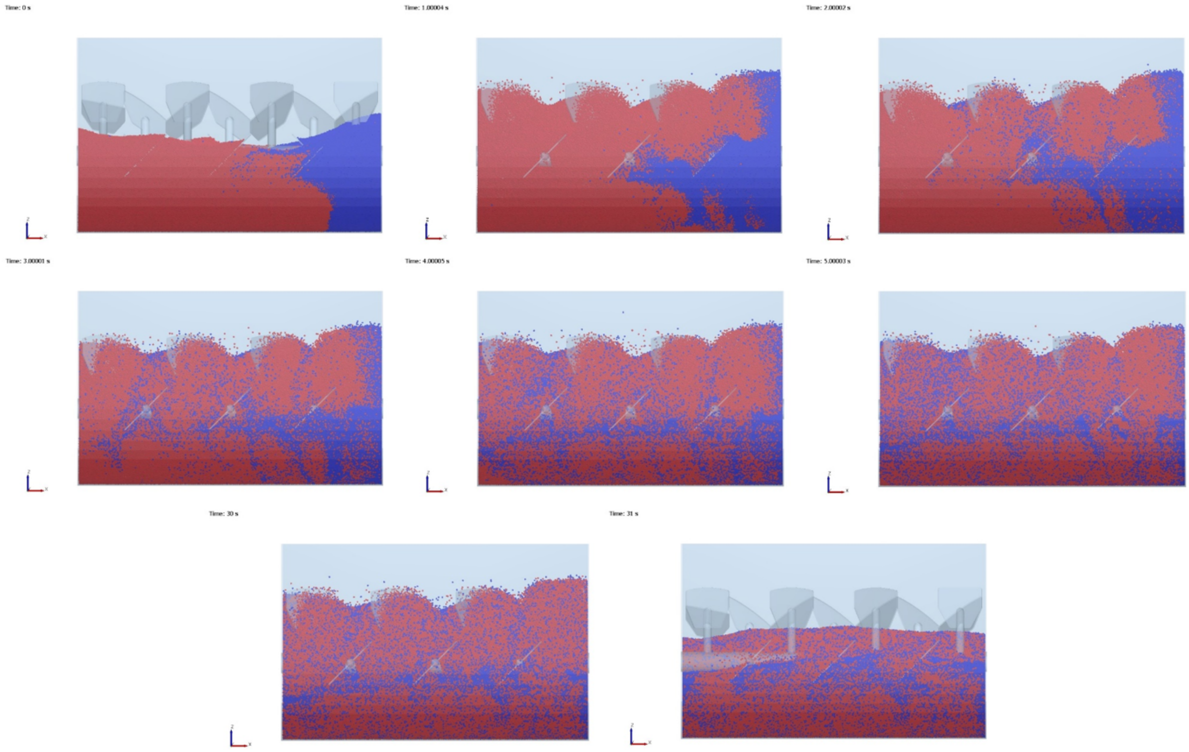

Figure D.9: Side view of simulation 3 - Particle size ratio (α=3) for time step t=0s, t=1s, t=2s, t=3s, t=4s, t=5s, t=30s and t=31s.

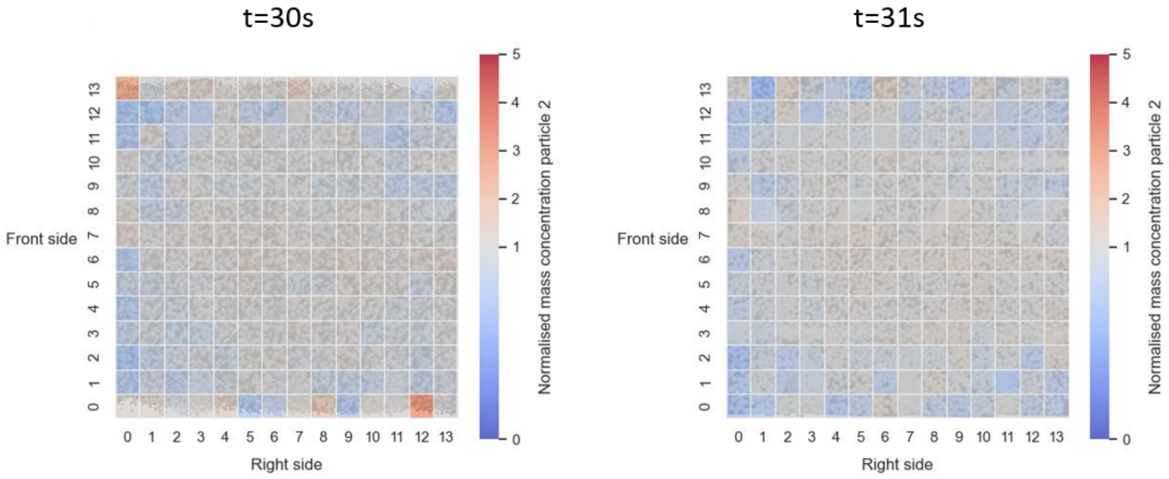

Figure D.10: Simulation 3 - Heat map of 14x14x1 grid with normalized concentrations of particle 2 at time=30s and t=31s.

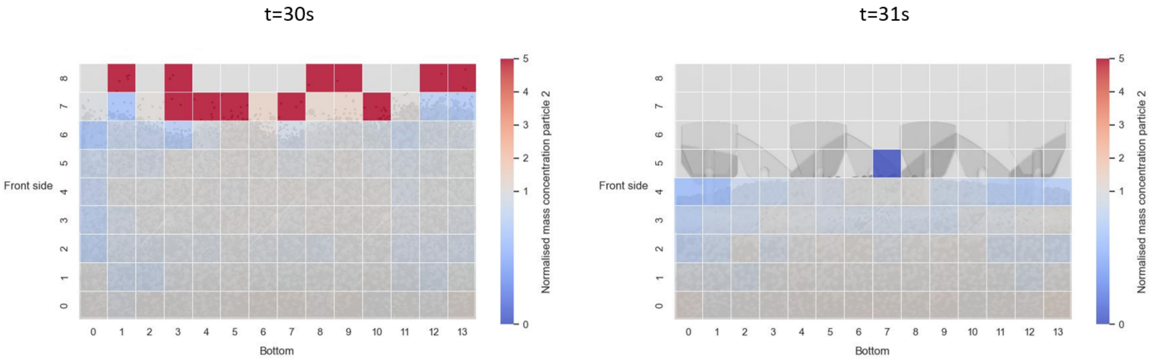

Figure D.11: Simulation 3 - Heat map of 14x1x9 grid with normalized concentrations of particle 2 at time=30s and t=31s.

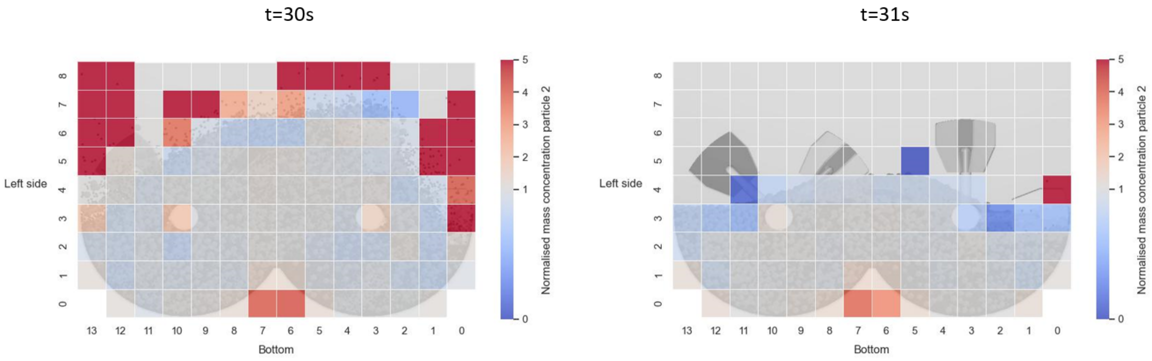

Figure D.12: Simulation 3 - Heat map of 1x14x9 grid with normalized concentrations of particle 2 at time=30s and t=31s.

D.4. Simulation 4 - Particle density ratio (-1)

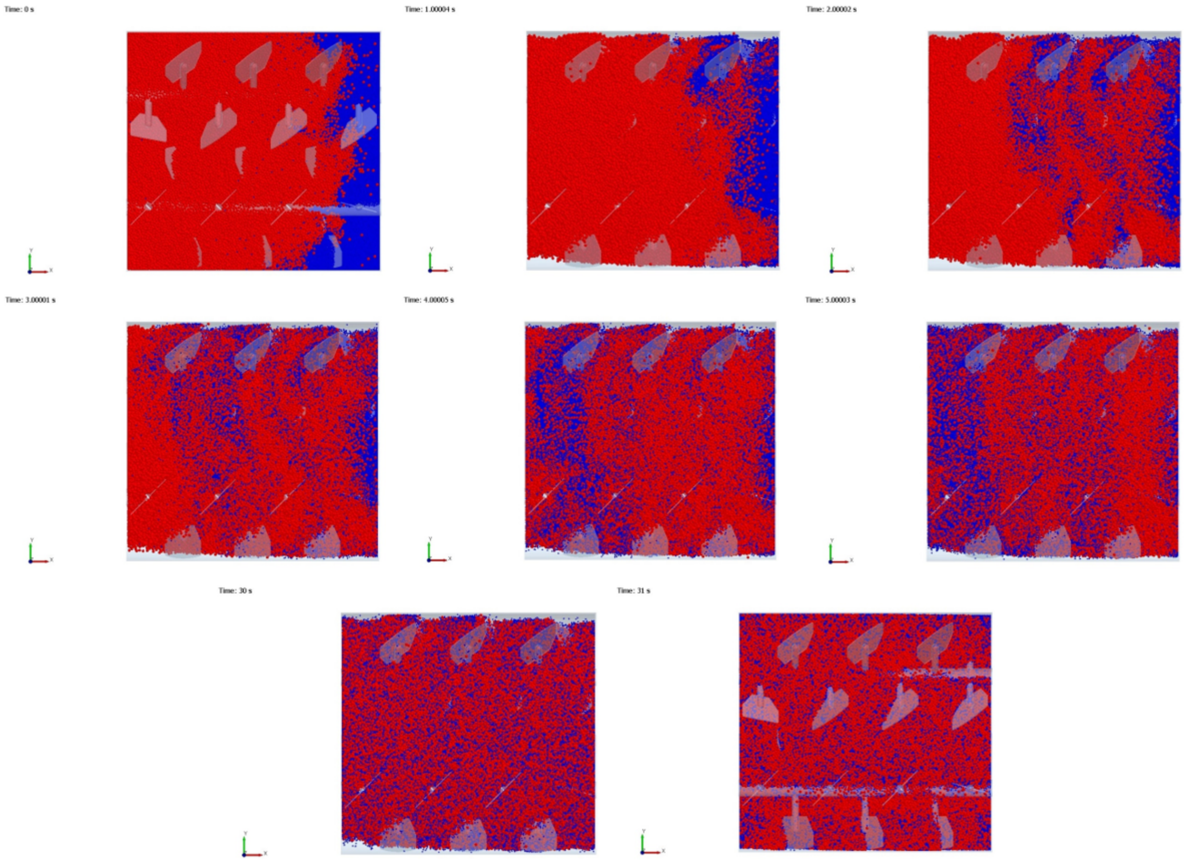

Figure D.13: Top view of simulation 4 - Particle density ratio (*b*=1) for time step t=0s, t=1s, t=2s, t=3s, t=4s, t=5s, t=30s and t=31s.

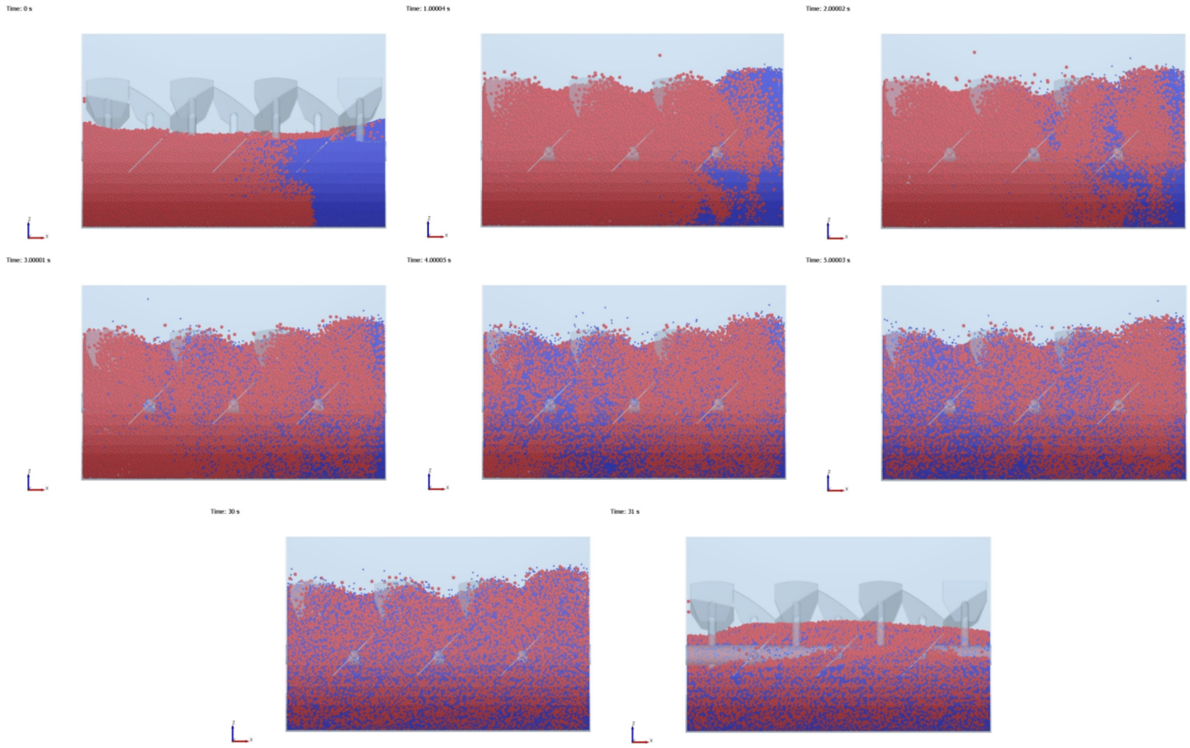

Figure D.14: Side view of simulation 4 - Particle density ratio (b=1) for time step t=0s, t=1s, t=2s, t=3s, t=4s, t=5s, t=30s and t=31s.

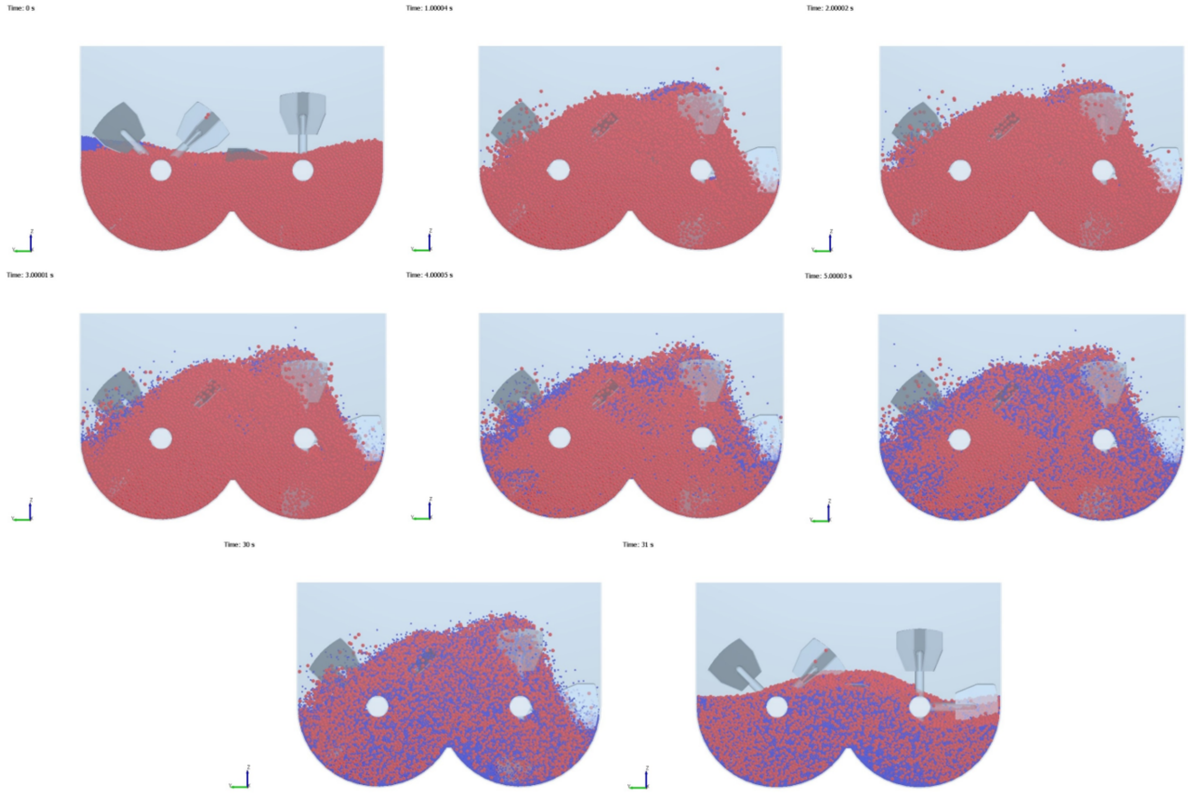

Figure D.15: Front view of simulation 4 - Particle density ratio (b=1) for time step t=0s, t=1s, t=2s, t=3s, t=4s, t=5s, t=30s and t=31s.

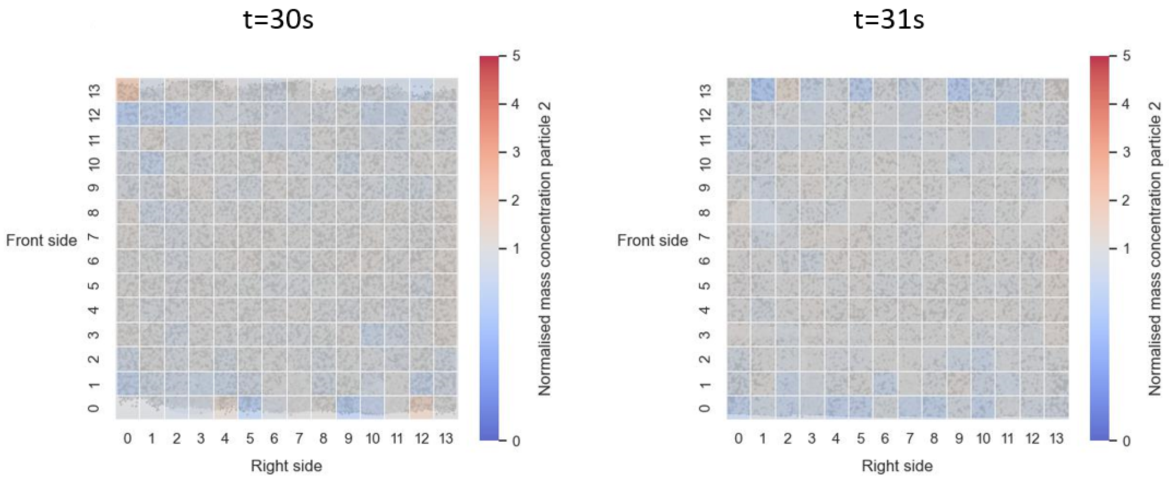

Figure D.16: Simulation 4 - Heat map of 14x14x1 grid with normalized concentrations of particle 2 at time=30s and t=31s.

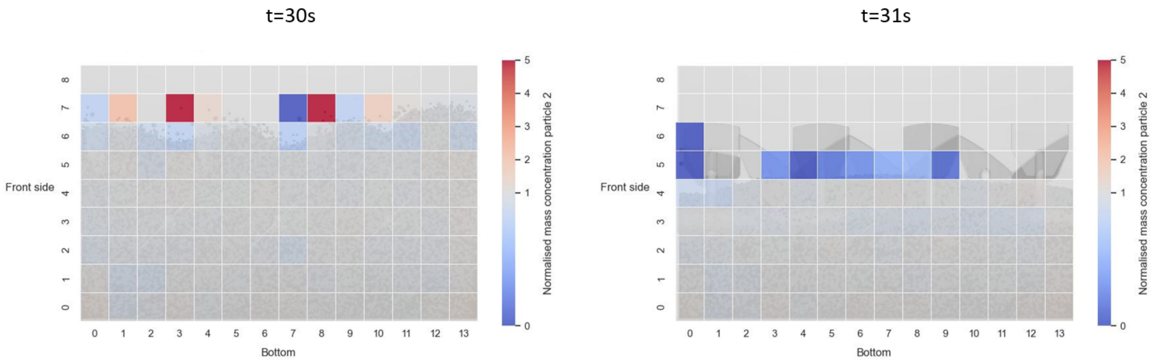

Figure D.17: Simulation 4 - Heat map of 14x1x9 grid with normalized concentrations of particle 2 at time=30s and t=31s.

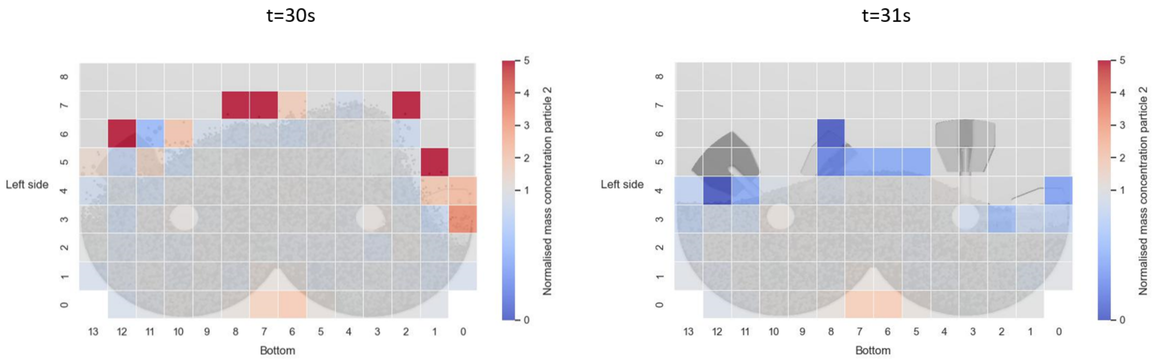

Figure D.18: Simulation 4 - Heat map of 1x14x9 grid with normalized concentrations of particle 2 at time=30s and t=31s.

D.5. Simulation 5 - Particle density ratio (+1)

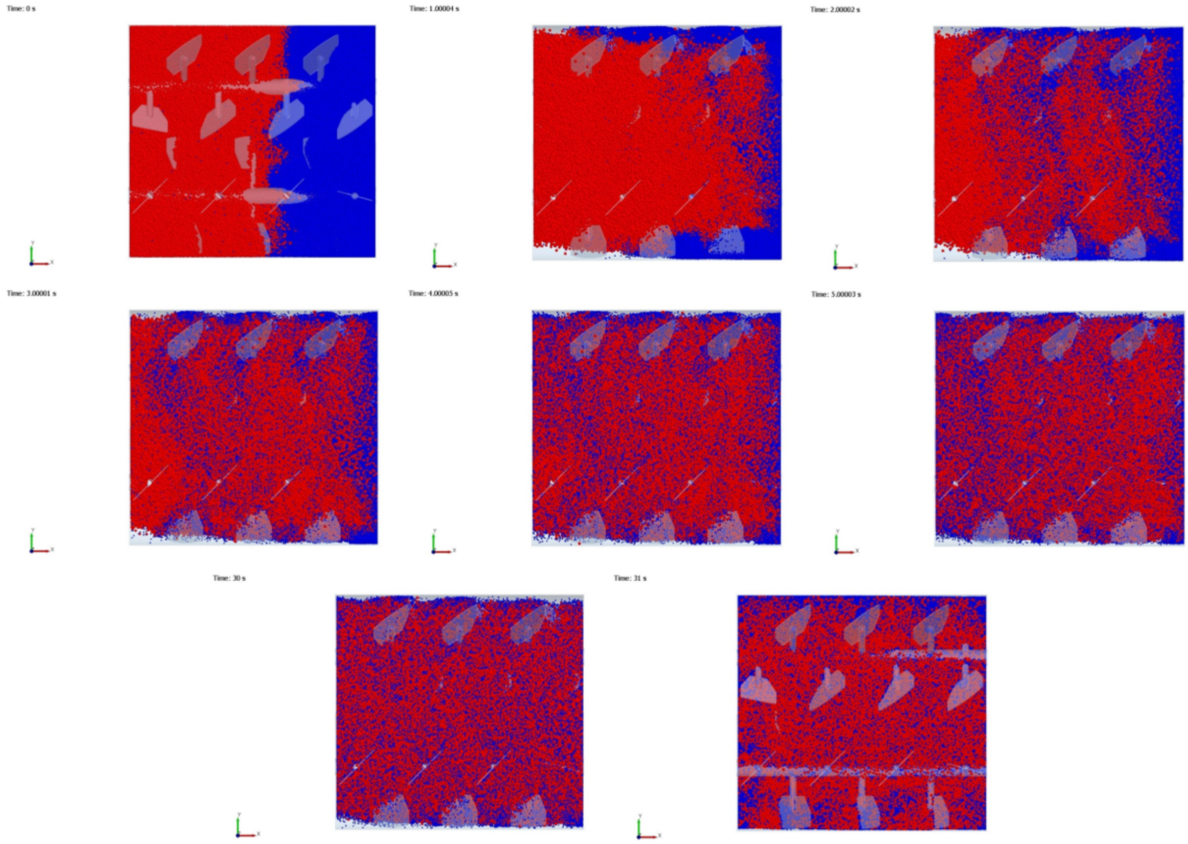

Figure D.19: Top view of simulation 5 - Particle density ratio (b=20) for time step t=0s, t=1s, t=2s, t=3s, t=4s, t=5s, t=30s and t=31s.

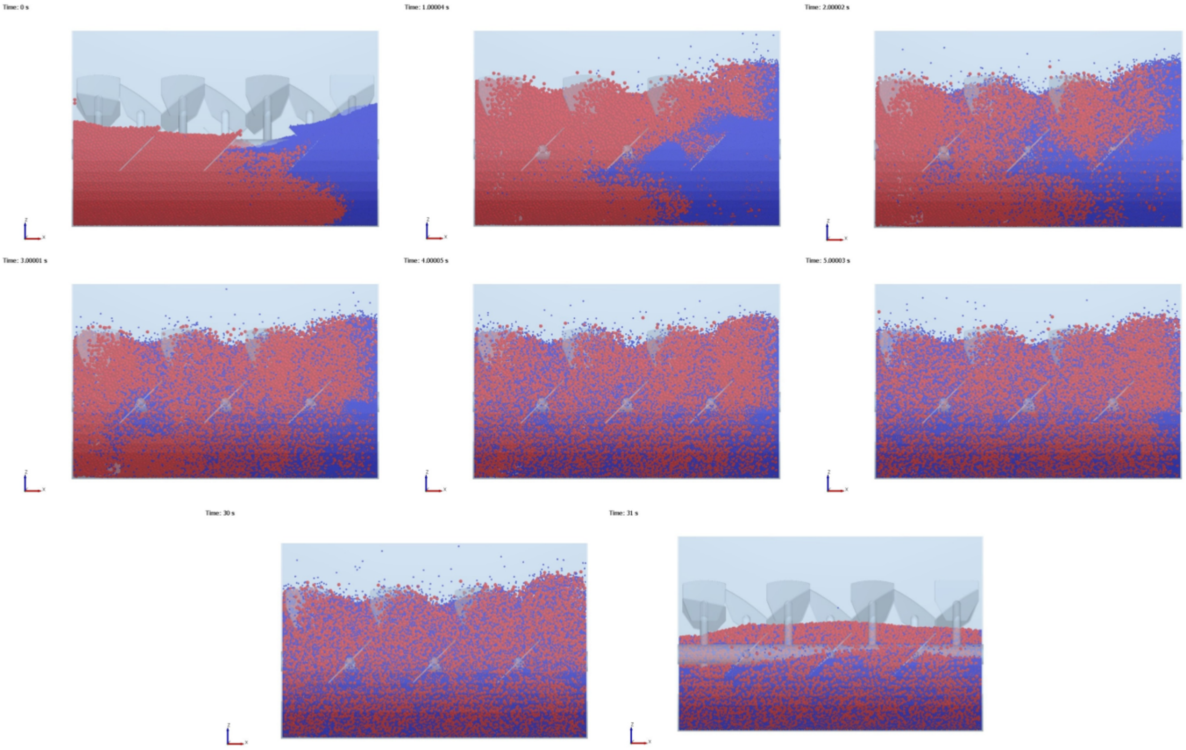

Figure D.20: Side view of simulation 5 - Particle density ratio (b=20) for time step t=0s, t=1s, t=2s, t=3s, t=4s, t=5s, t=30s and t=31s.

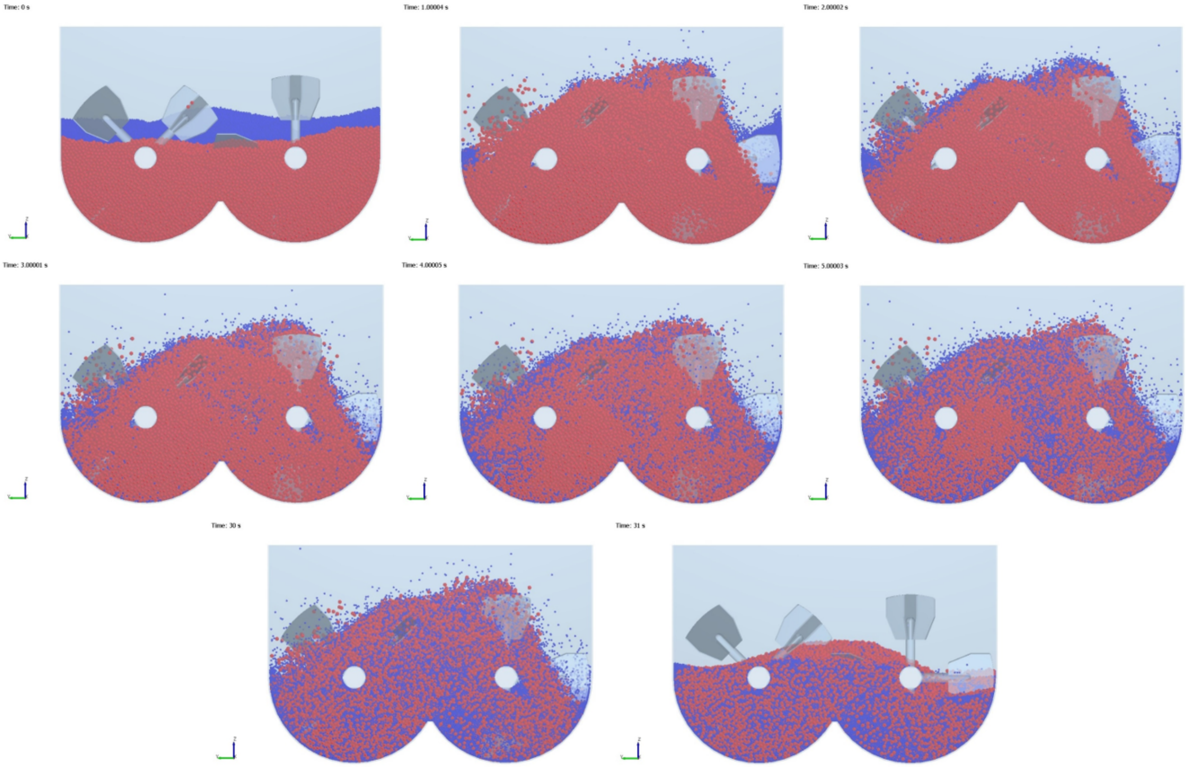

Figure D.21: Front view of simulation 5 - Particle density ratio (b=20) for time step t=0s, t=1s, t=2s, t=3s, t=4s, t=5s, t=30s and t=31s.

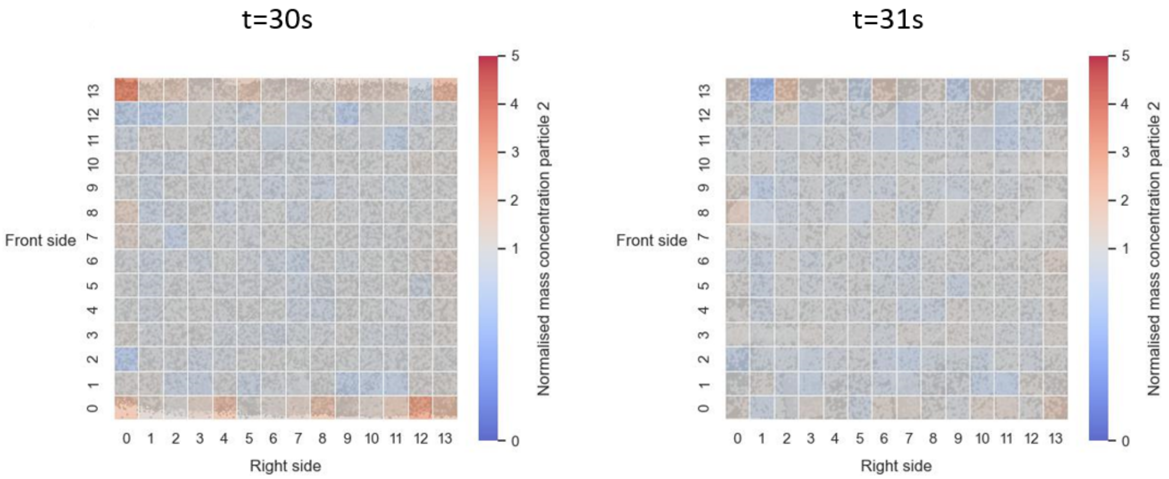

Figure D.22: Simulation 5 - Heat map of 14x14x1 grid with normalized concentrations of particle 2 at time=30s and t=31s.

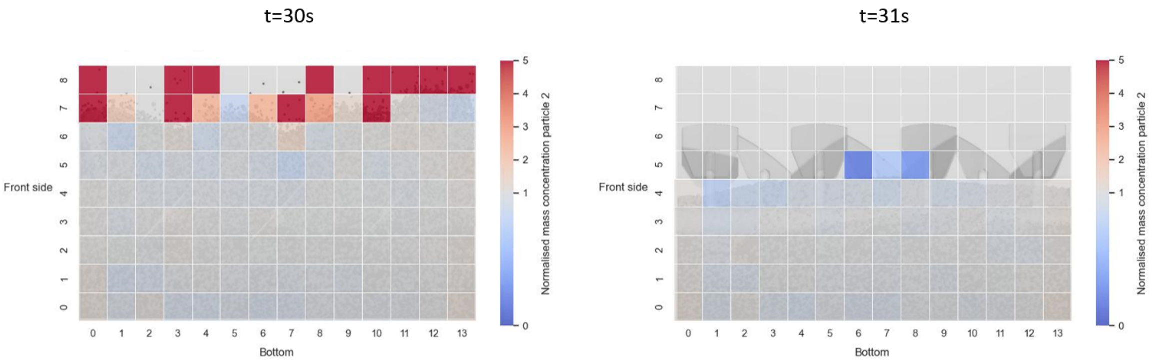

Figure D.23: Simulation 5 - Heat map of 14x1x9 grid with normalized concentrations of particle 2 at time=30s and t=31s.

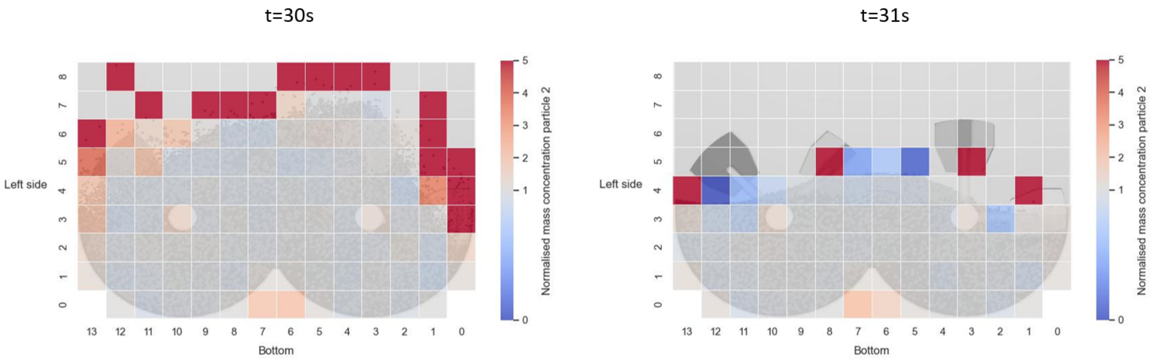

Figure D.24: Simulation 5 - Heat map of 1x14x9 grid with normalized concentrations of particle 2 at time=30s and t=31s.

D.6. Simulation 6 - Composition (-1)

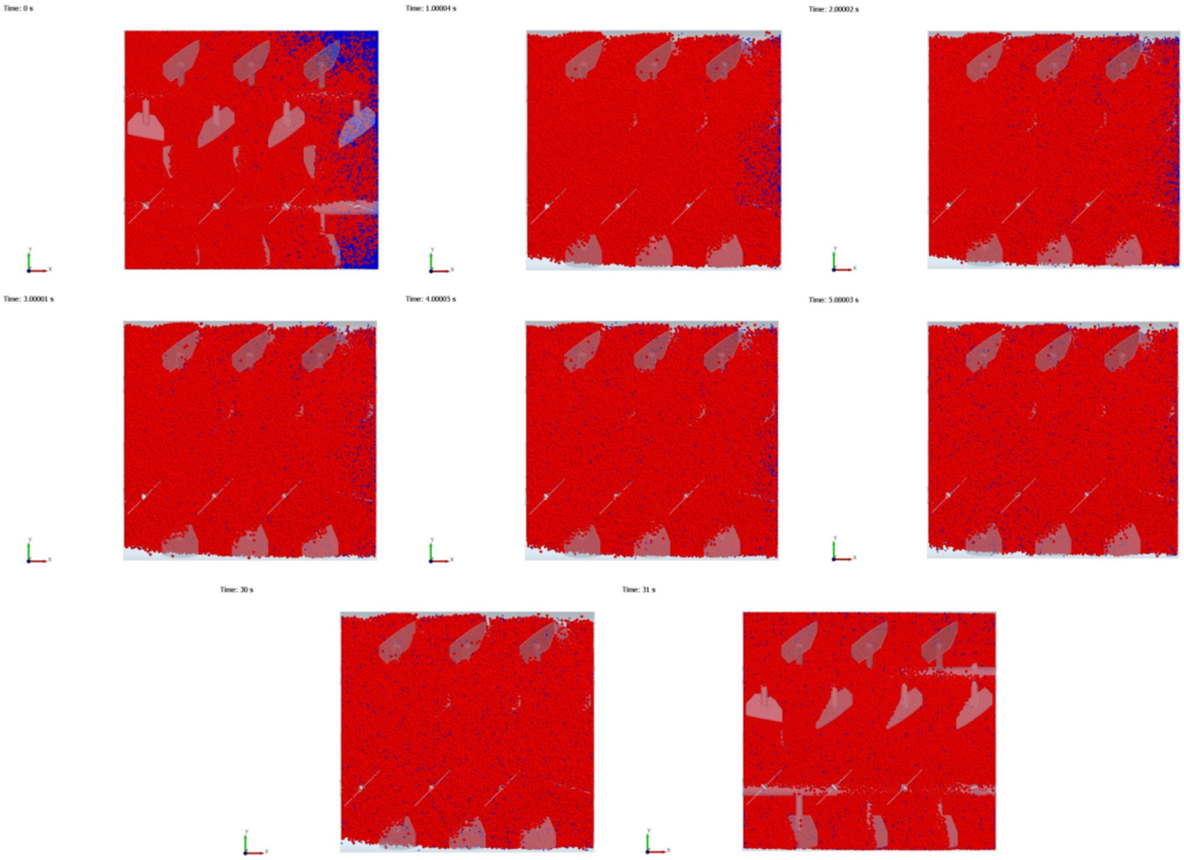

Figure D.25: Top view of simulation 6 - Composition (c=99/1) for time step t=0s, t=1s, t=2s, t=3s, t=4s, t=5s, t=30s and t=31s.

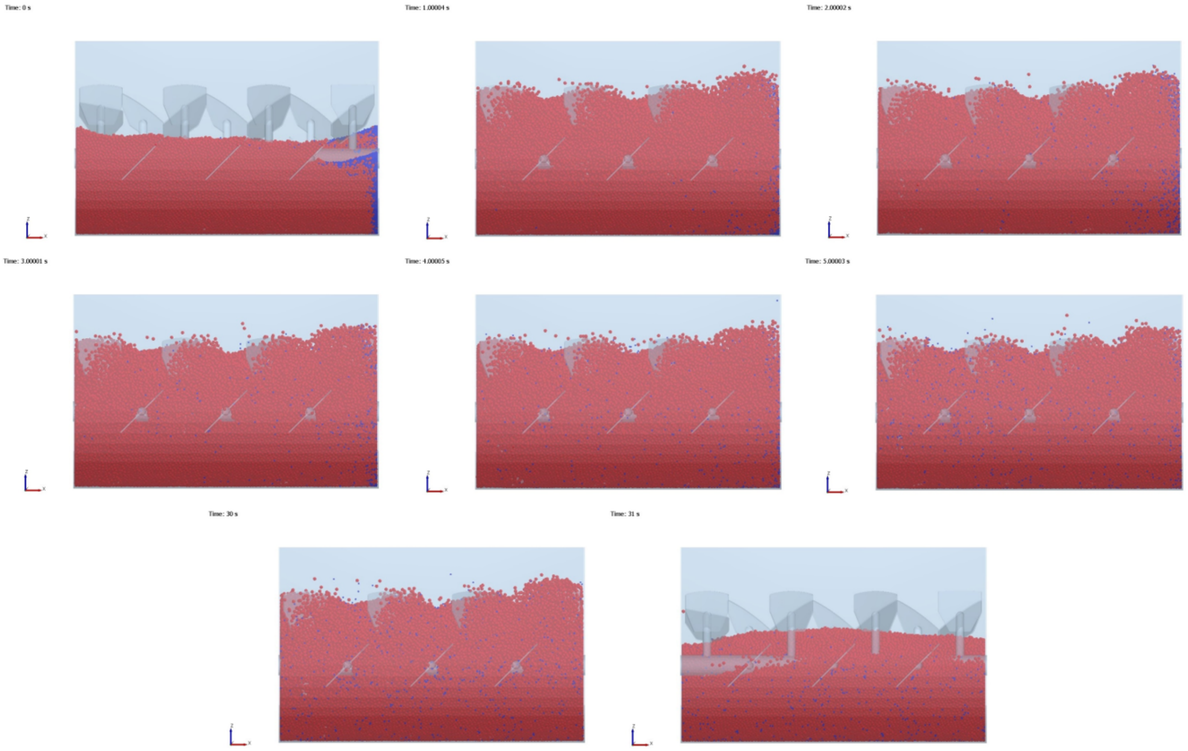

Figure D.26: Side view of simulation 6 - Composition (c=99/1) for time step t=0s, t=1s, t=2s, t=3s, t=4s, t=5s, t=30s and t=31s.

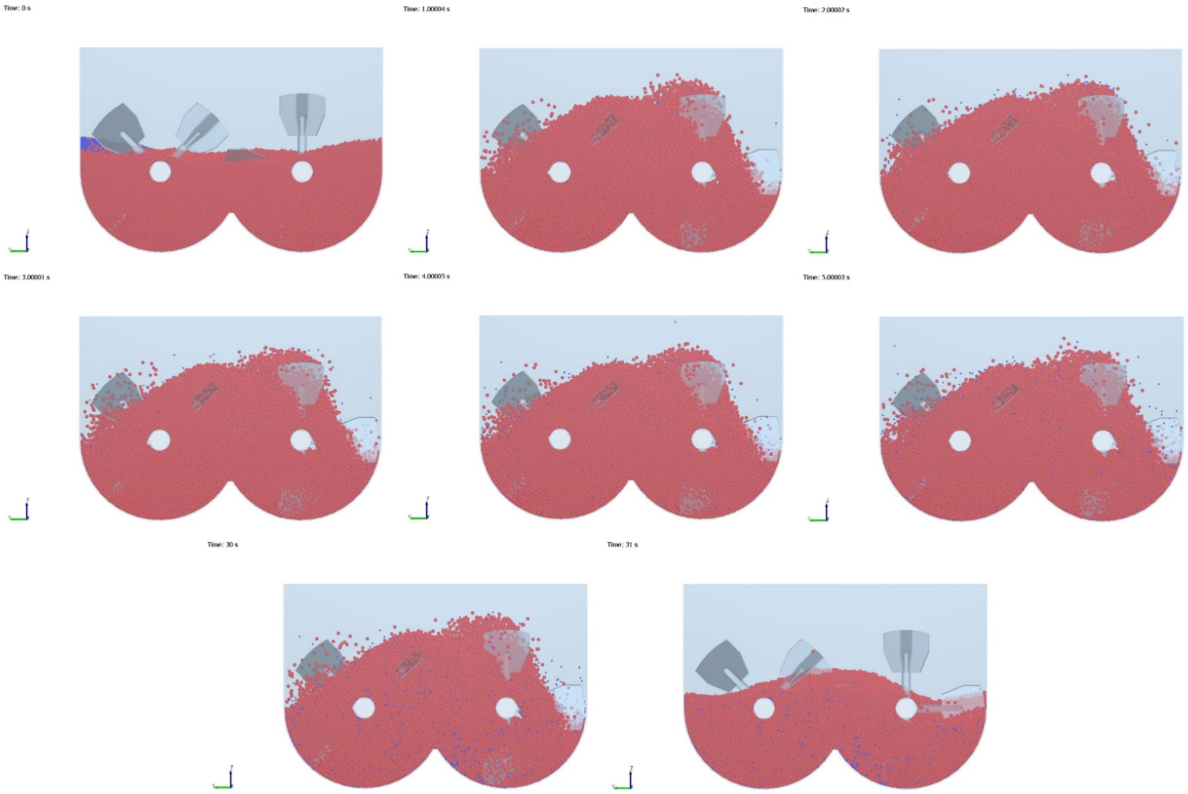

Figure D.27: Front view of simulation 6 - Composition (c=99/1) for time step t=0s, t=1s, t=2s, t=3s, t=4s, t=5s, t=30s and t=31s.

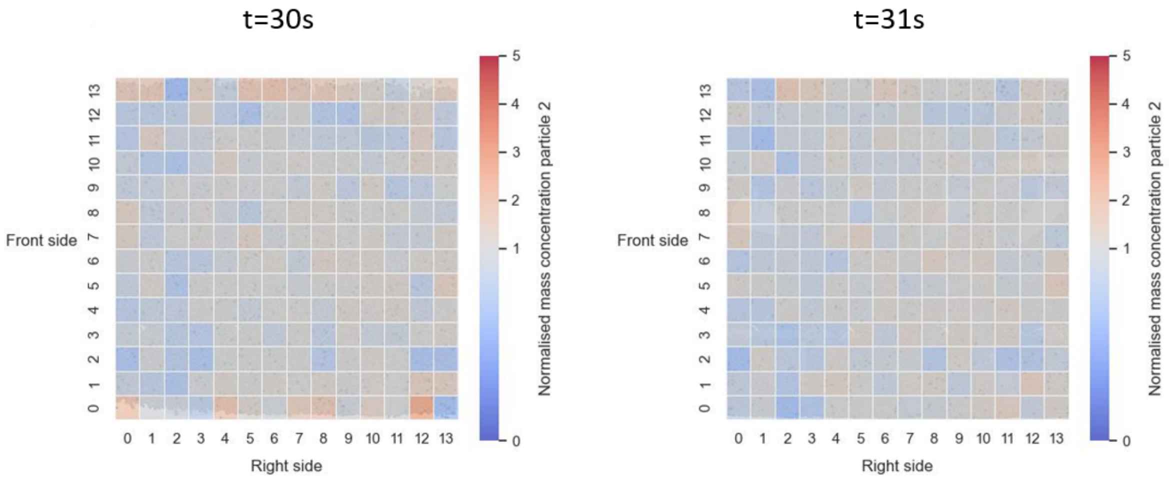

Figure D.28: Simulation 6 - Heat map of 14x14x1 grid with normalized concentrations of particle 2 at time=30s and t=31s.

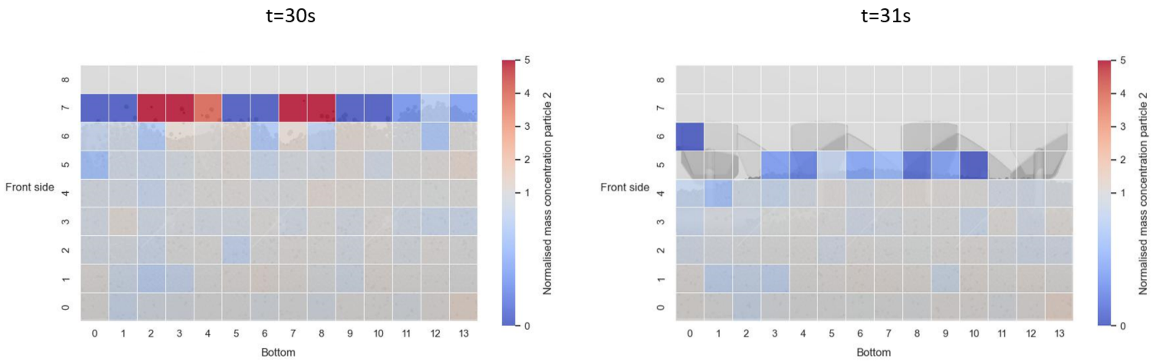

Figure D.29: Simulation 6 - Heat map of 14x1x9 grid with normalized concentrations of particle 2 at time=30s and t=31s.

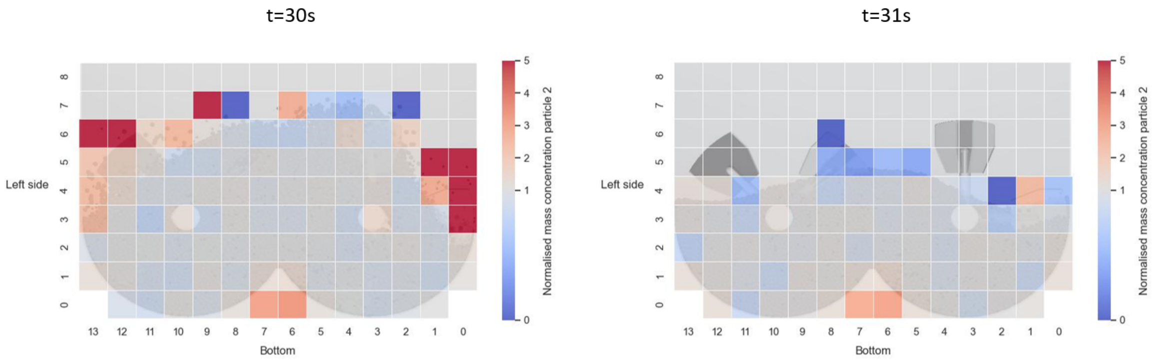

Figure D.30: Simulation 6 - Heat map of 1x14x9 grid with normalized concentrations of particle 2 at time=30s and t=31s.

D.7. Simulation 7 - Composition (+1)

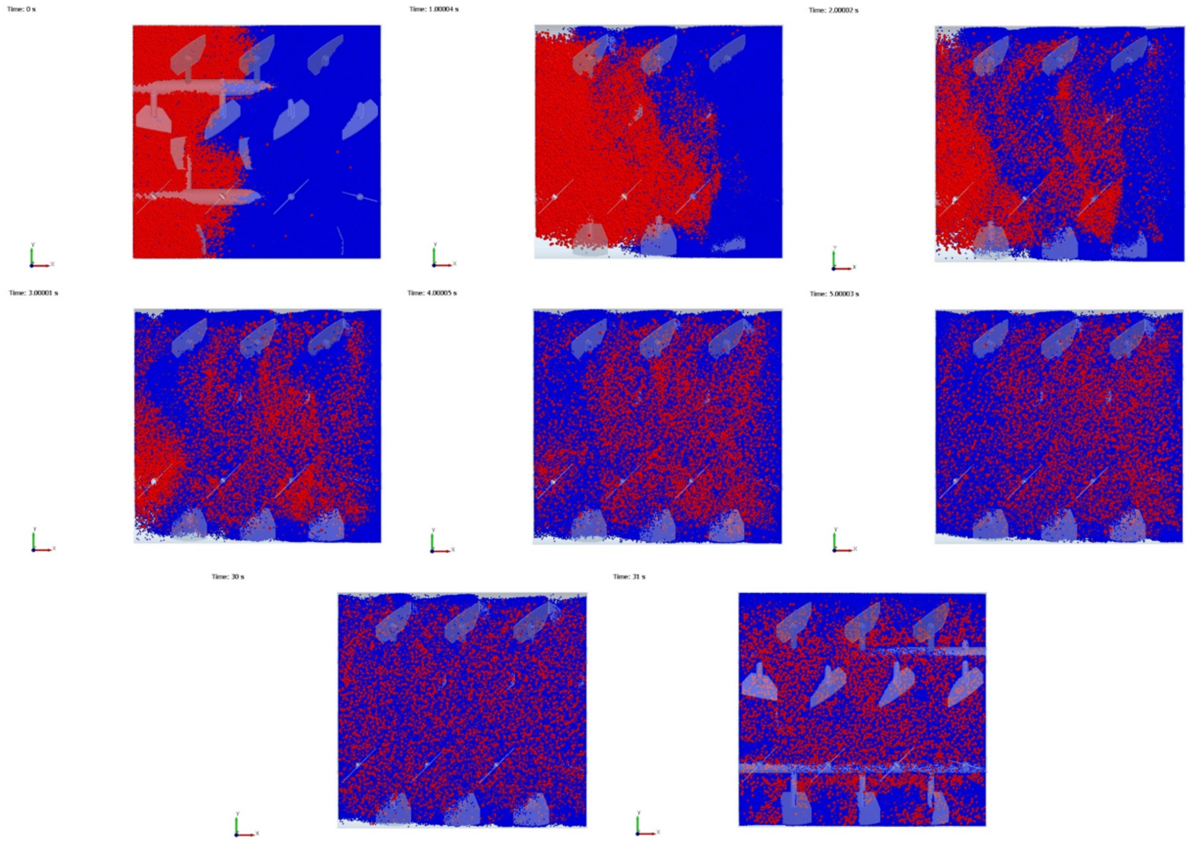

Figure D.31: Top view of simulation 7 - Composition (c=50/50) for time step t=0s, t=1s, t=2s, t=3s, t=4s, t=5s, t=30s and t=31s.

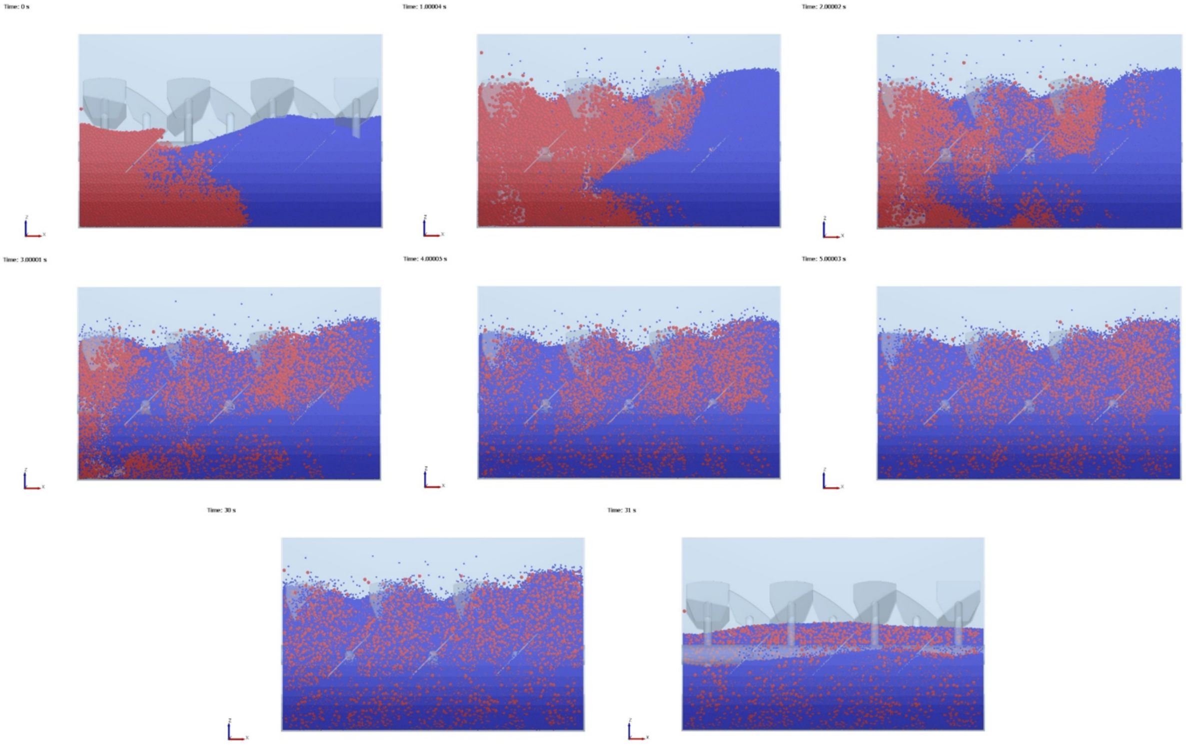

Figure D.32: Side view of simulation 7 - Composition (c=50/50) for time step t=0s, t=1s, t=2s, t=3s, t=4s, t=5s, t=30s and t=31s.

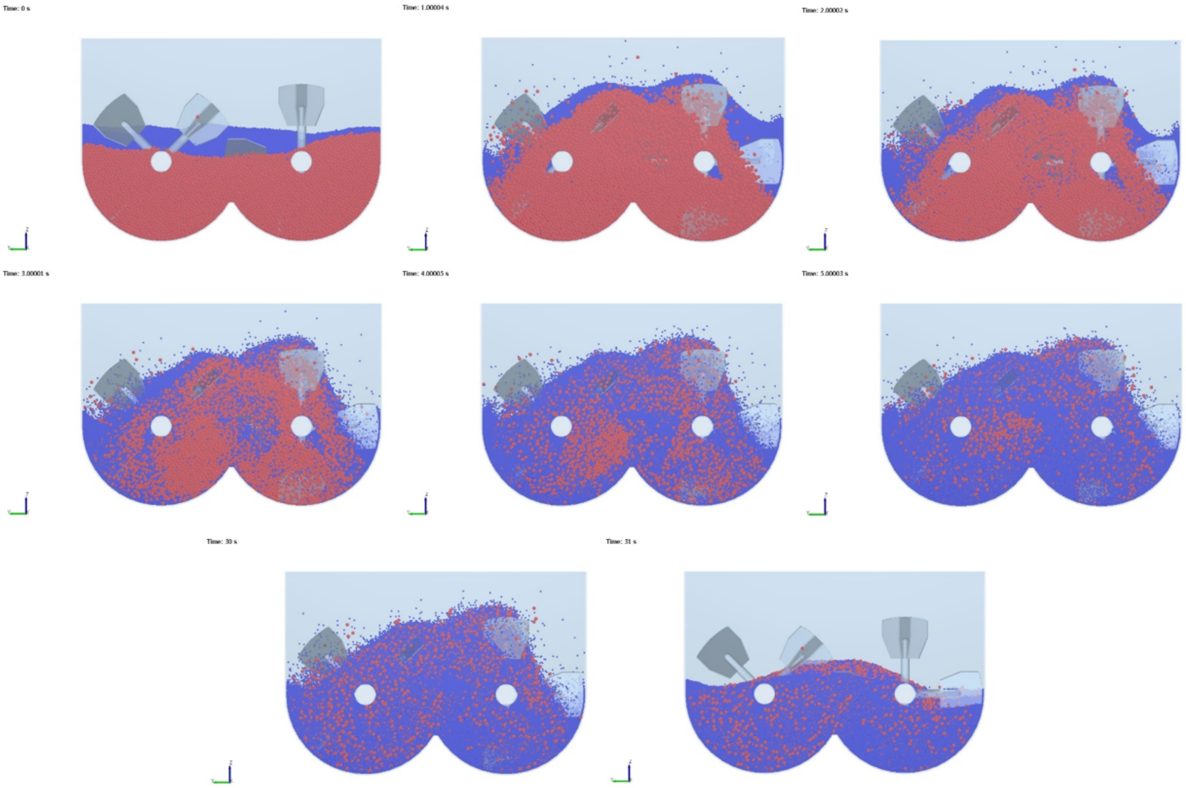

Figure D.33: Front view of simulation 7 - Composition (c=50/50) for time step t=0s, t=1s, t=2s, t=3s, t=4s, t=5s, t=30s and t=31s.

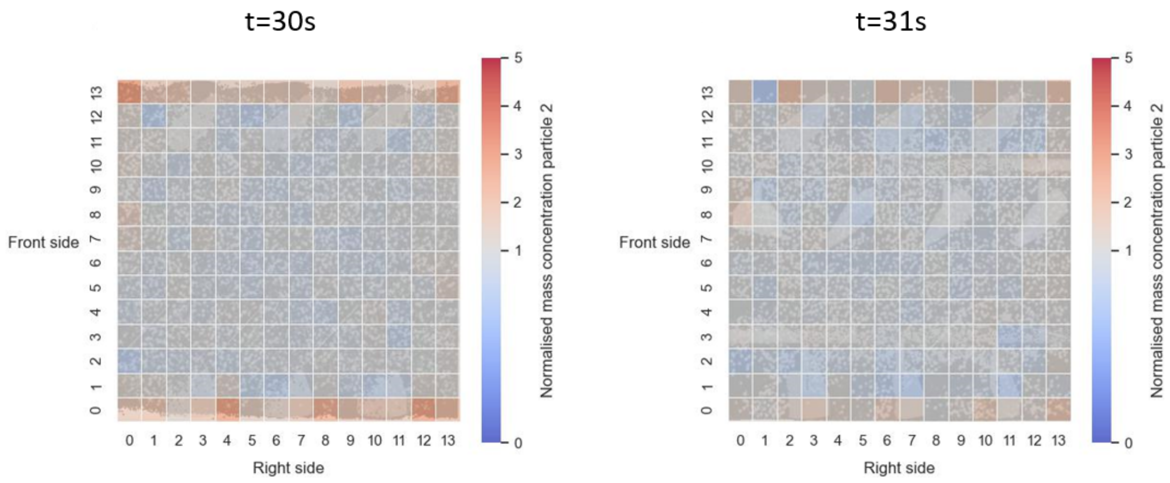

Figure D.34: Simulation 7 - Heat map of 14x14x1 grid with normalized concentrations of particle 2 at time=30s and t=31s.

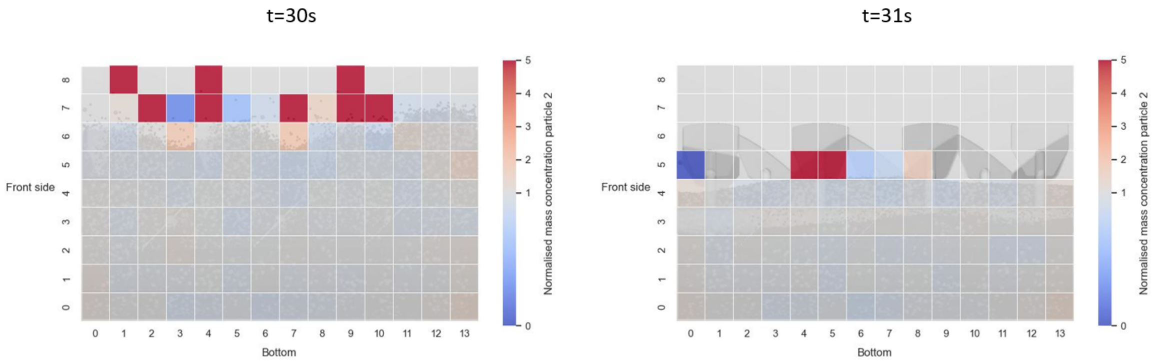

Figure D.35: Simulation 7 - Heat map of 14x1x9 grid with normalized concentrations of particle 2 at time=30s and t=31s.

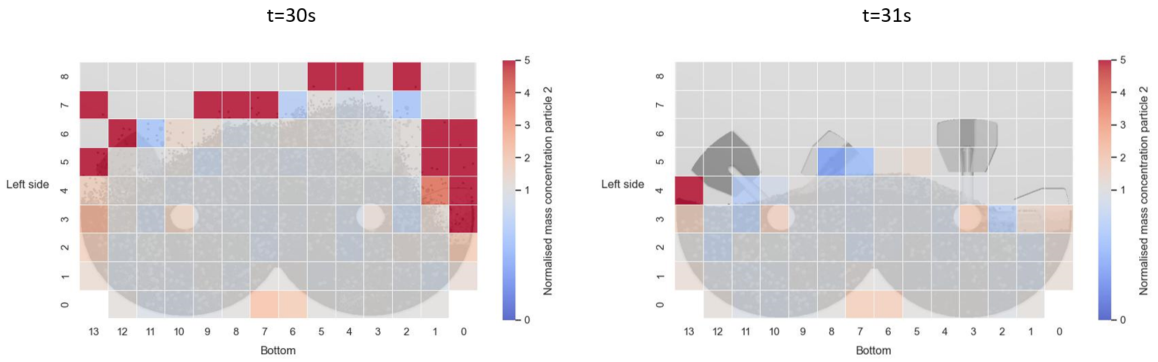

Figure D.36: Simulation 7 - Heat map of 1x14x9 grid with normalized concentrations of particle 2 at time=30s and t=31s.

D.8. Simulation 8 - Initial filling pattern (-1)

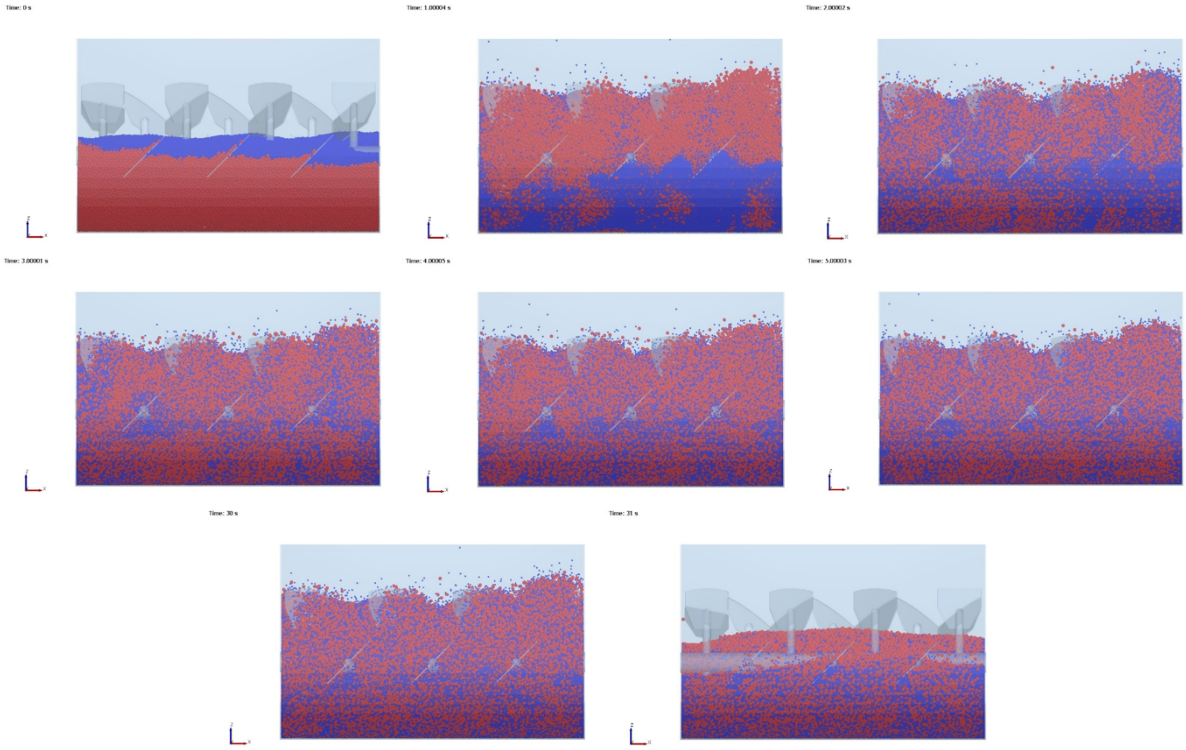

Figure D.37: Side view of simulation 8 - Initial filling pattern (d=TB) for time step t=0s, t=1s, t=2s, t=3s, t=4s, t=5s, t=30s and t=31s.

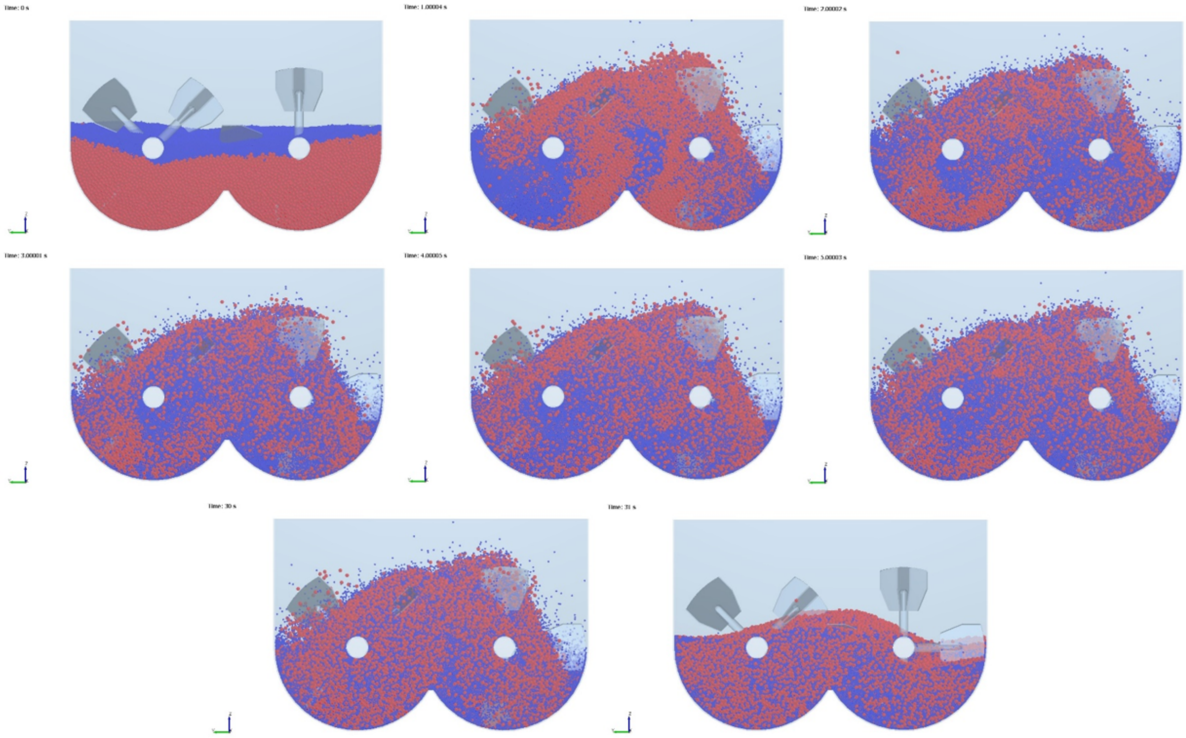

Figure D.38: Front view of simulation 8 - Initial filling pattern (d=TB) for time step t=0s, t=1s, t=2s, t=3s, t=4s, t=5s, t=30s and t=31s.

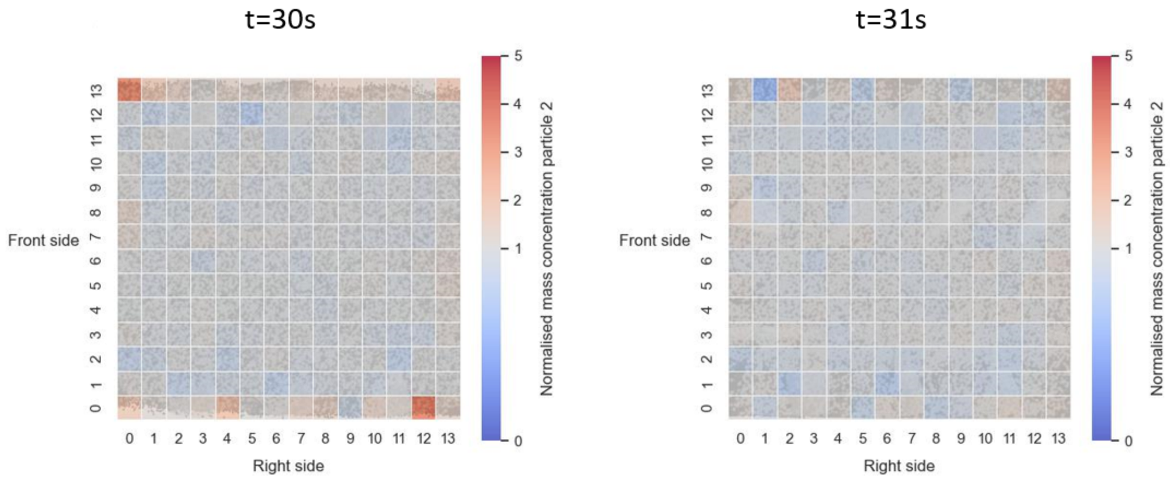

Figure D.39: Simulation 8 - Heat map of 14x14x1 grid with normalized concentrations of particle 2 at time=30s and t=31s.

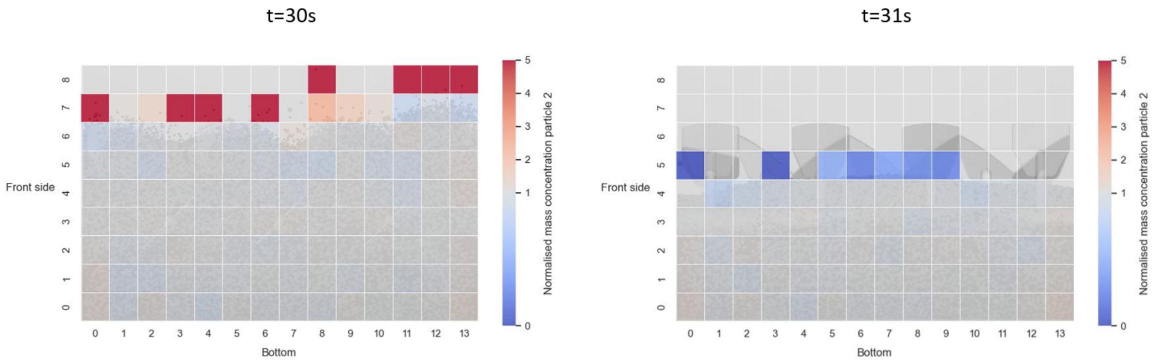

Figure D.40: Simulation 8 - Heat map of 14x1x9 grid with normalized concentrations of particle 2 at time=30s and t=31s.

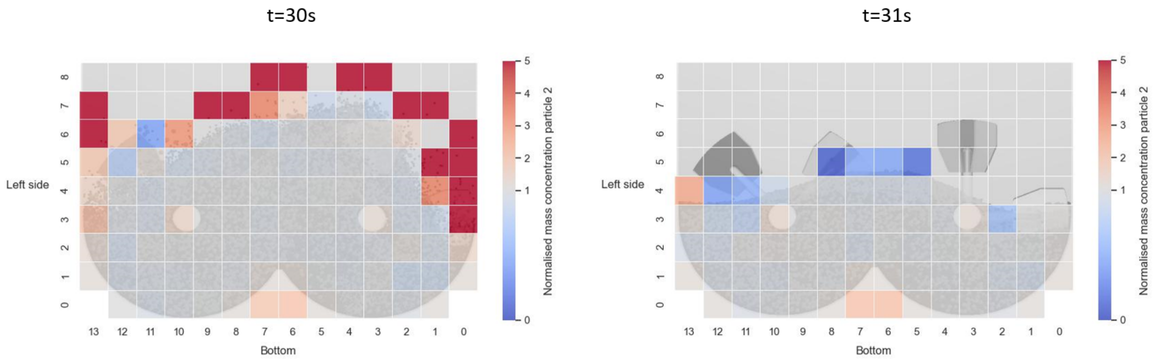

Figure D.41: Simulation 8 - Heat map of 1x14x9 grid with normalized concentrations of particle 2 at time=30s and t=31s.

D.9. Simulation 9 - Initial filling pattern (+1)

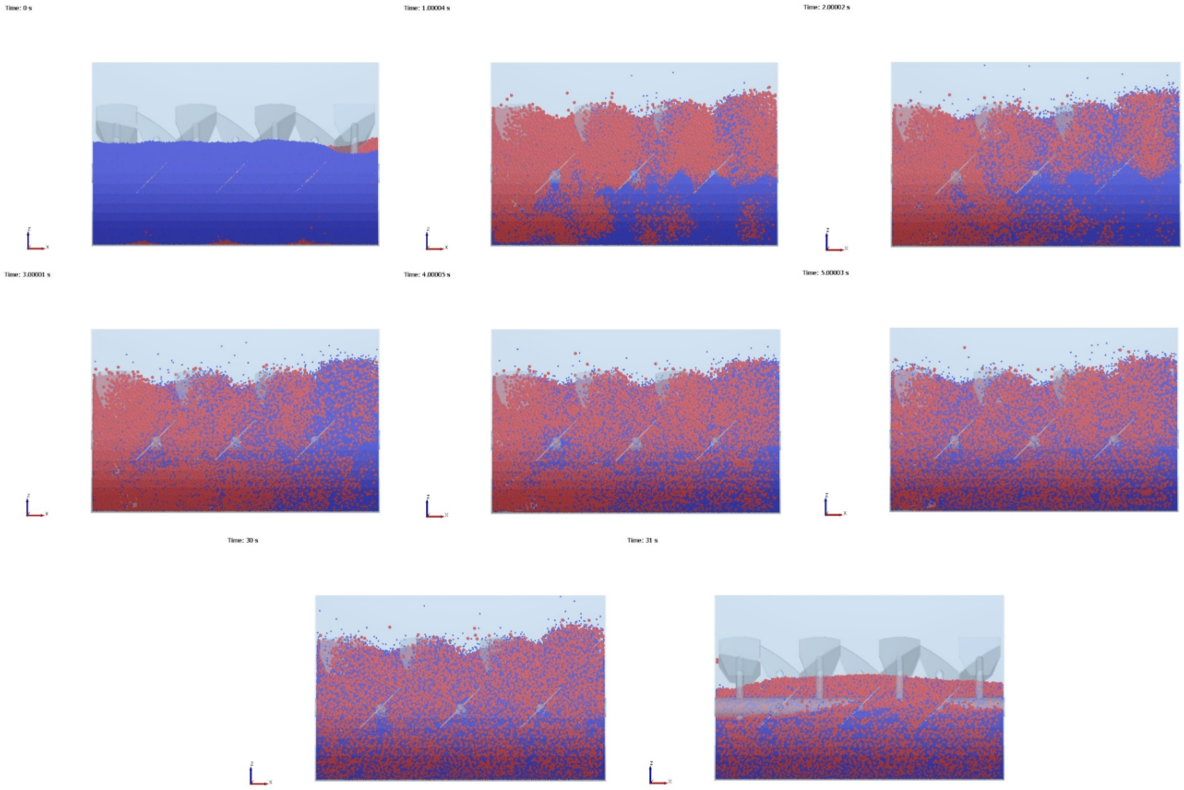

Figure D.42: Side view of simulation 9 - Initial filling pattern (d=SS) for time step t=0s, t=1s, t=2s, t=3s, t=4s, t=5s, t=30s and t=31s.

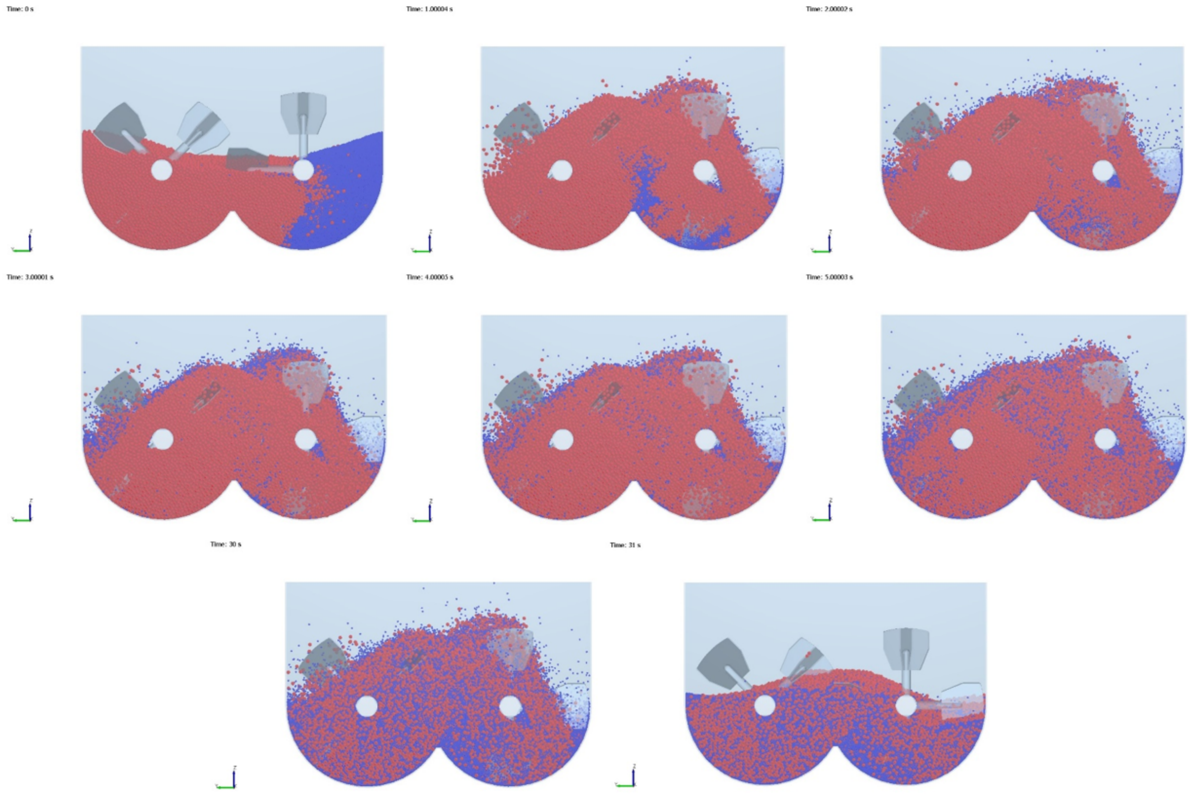

Figure D.43: Front view of simulation 9 - Initial filling pattern (d=SS) for time step t=0s, t=1s, t=2s, t=3s, t=4s, t=5s, t=30s and t=31s.

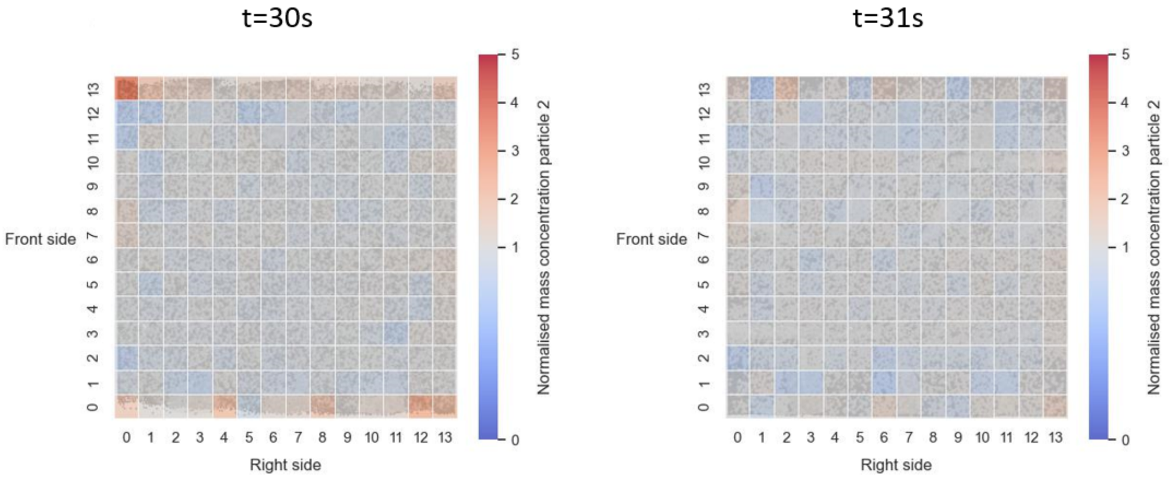

Figure D.44: Simulation 9 - Heat map of 14x14x1 grid with normalized concentrations of particle 2 at time=30s and t=31s.

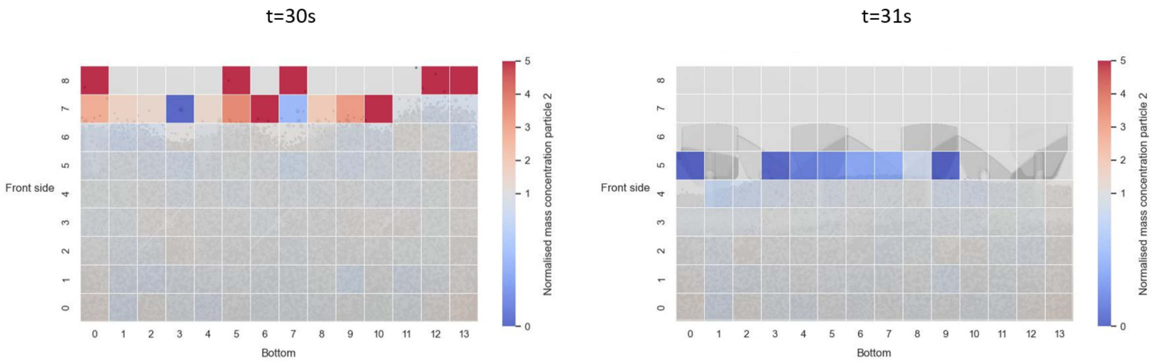

Figure D.45: Simulation 9 - Heat map of 14x1x9 grid with normalized concentrations of particle 2 at time=30s and t=31s.

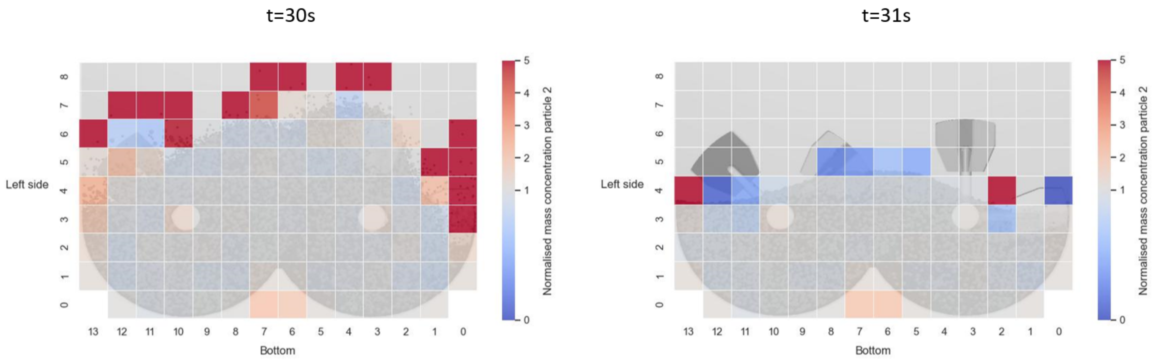

Figure D.46: Simulation 9 - Heat map of 1x14x9 grid with normalized concentrations of particle 2 at time=30s and t=31s.

D.10. Simulation 10 - Fill level (-1)

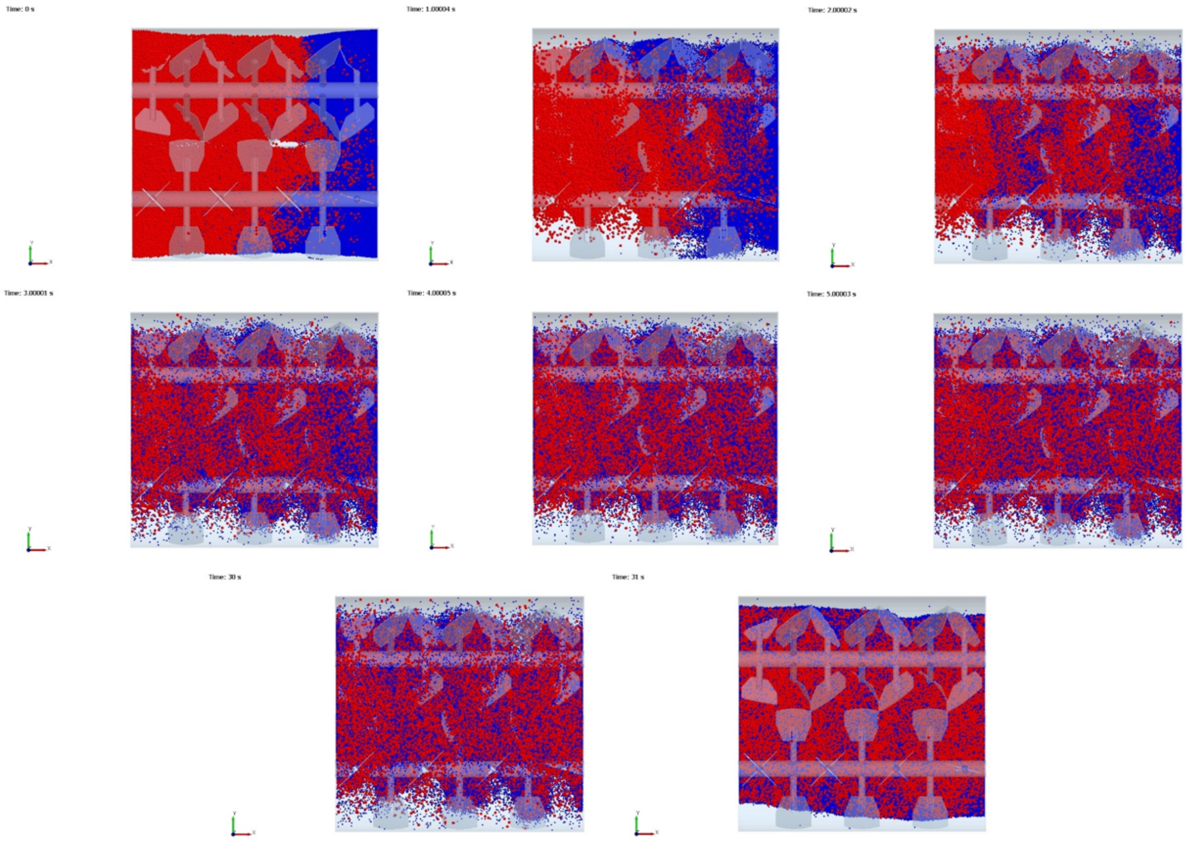

Figure D.47: Top view of simulation 10 - Fill level (e=40%) for time step t=0s, t=1s, t=2s, t=3s, t=4s, t=5s, t=30s and t=31s.

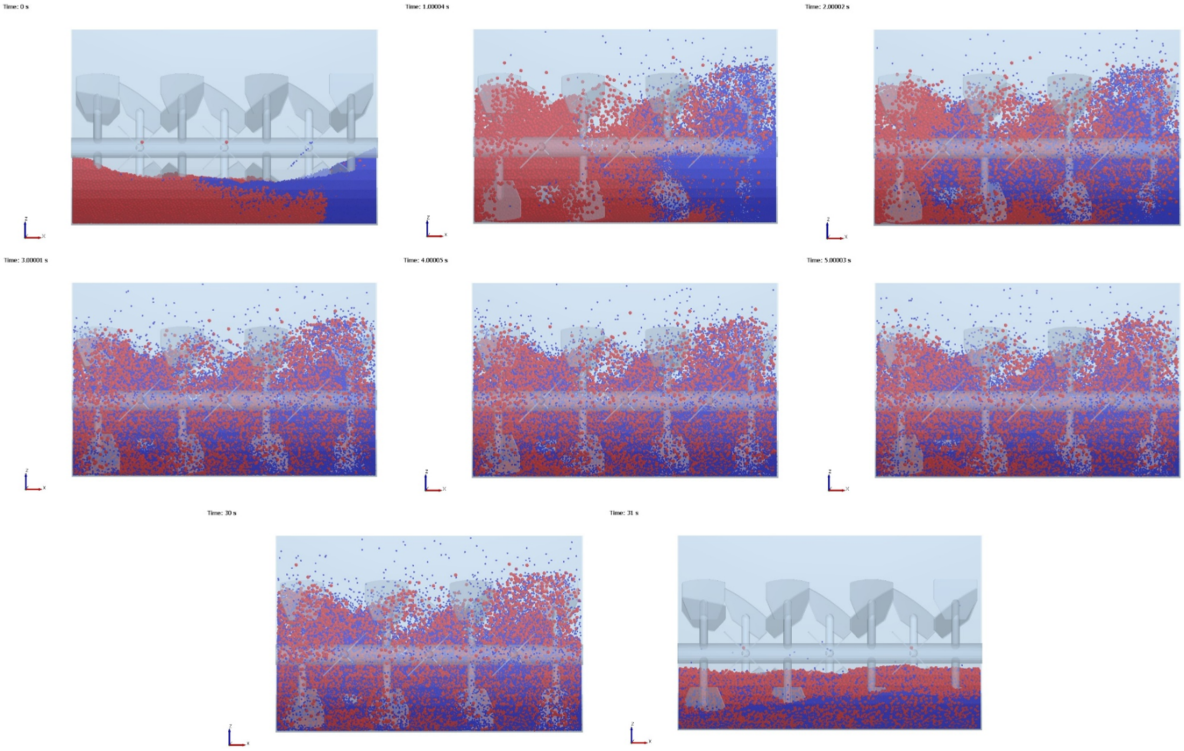

Figure D.48: Side view of simulation 10 - Fill level (e=40%) for time step t=0s, t=1s, t=2s, t=3s, t=4s, t=5s, t=30s and t=31s.

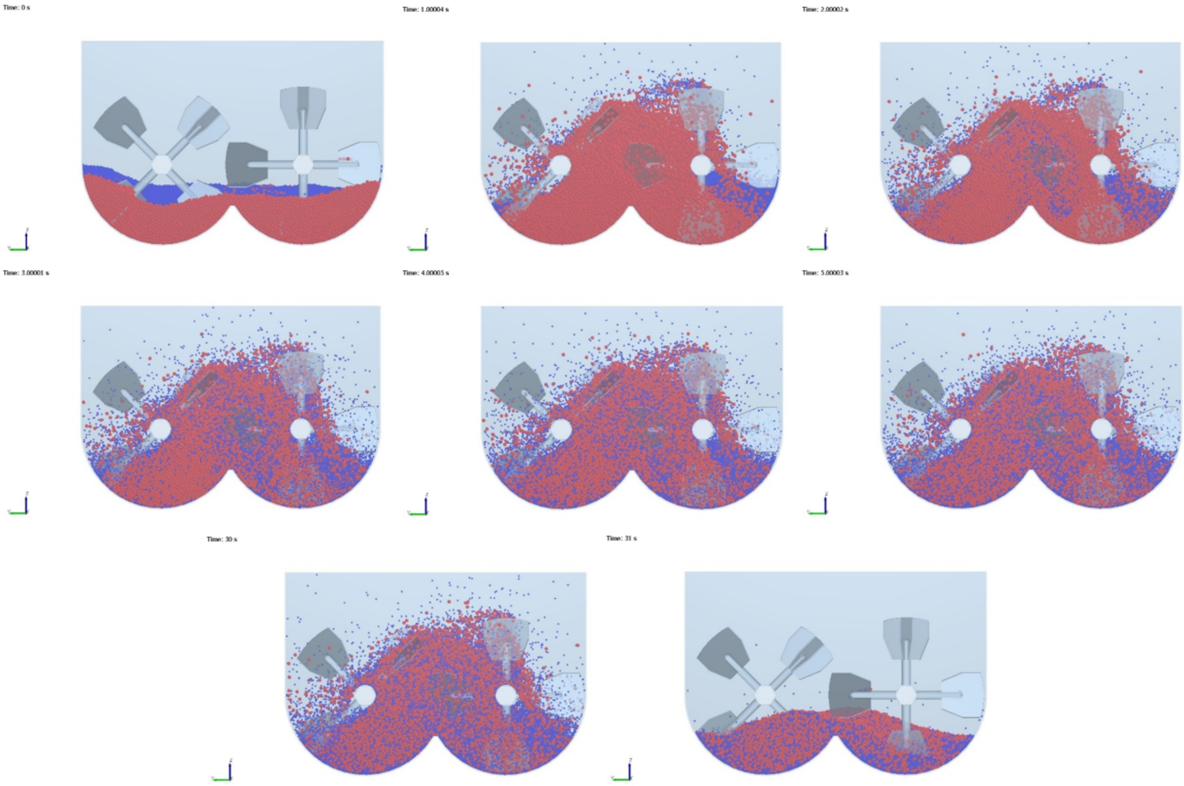

Figure D.49: Front view of simulation 10 - Fill level (e=40%) for time step t=0s, t=1s, t=2s, t=3s, t=4s, t=5s, t=30s and t=31s.

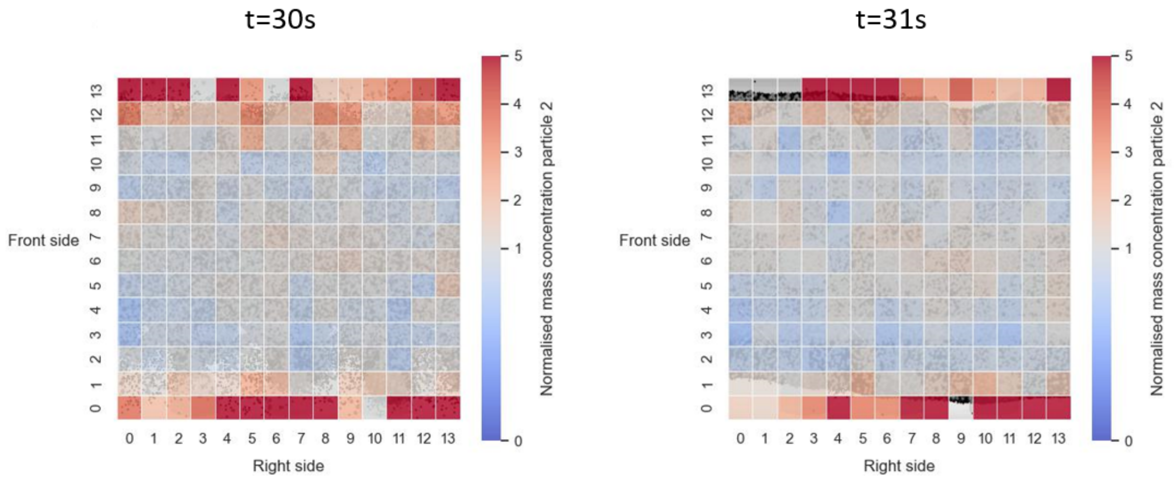

Figure D.50: Simulation 10 - Heat map of 14x14x1 grid with normalized concentrations of particle 2 at time=30s and t=31s.

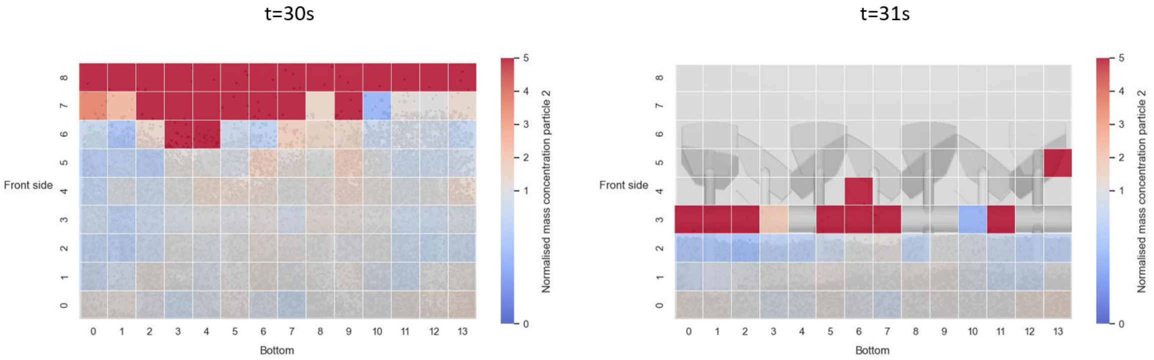

Figure D.51: Simulation 10 - Heat map of 14x1x9 grid with normalized concentrations of particle 2 at time=30s and t=31s.

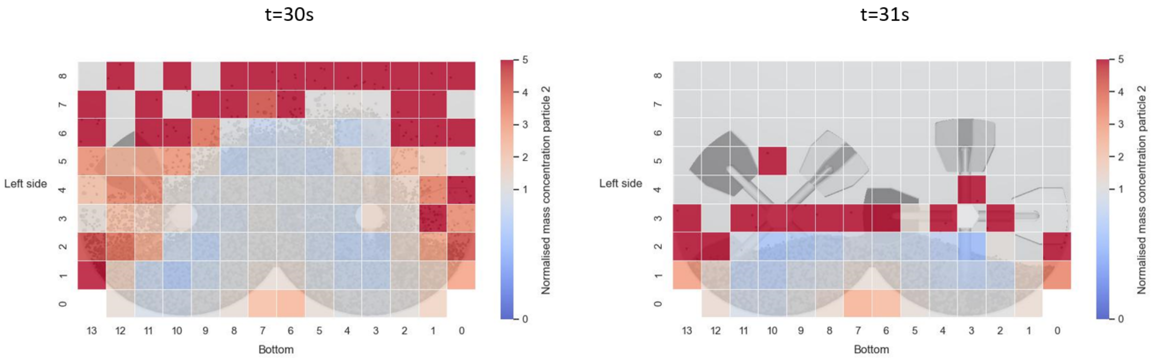

Figure D.52: Simulation 10 - Heat map of 1x14x9 grid with normalized concentrations of particle 2 at time=30s and t=31s.

D.11. Simulation 11 - Fill level (+1)

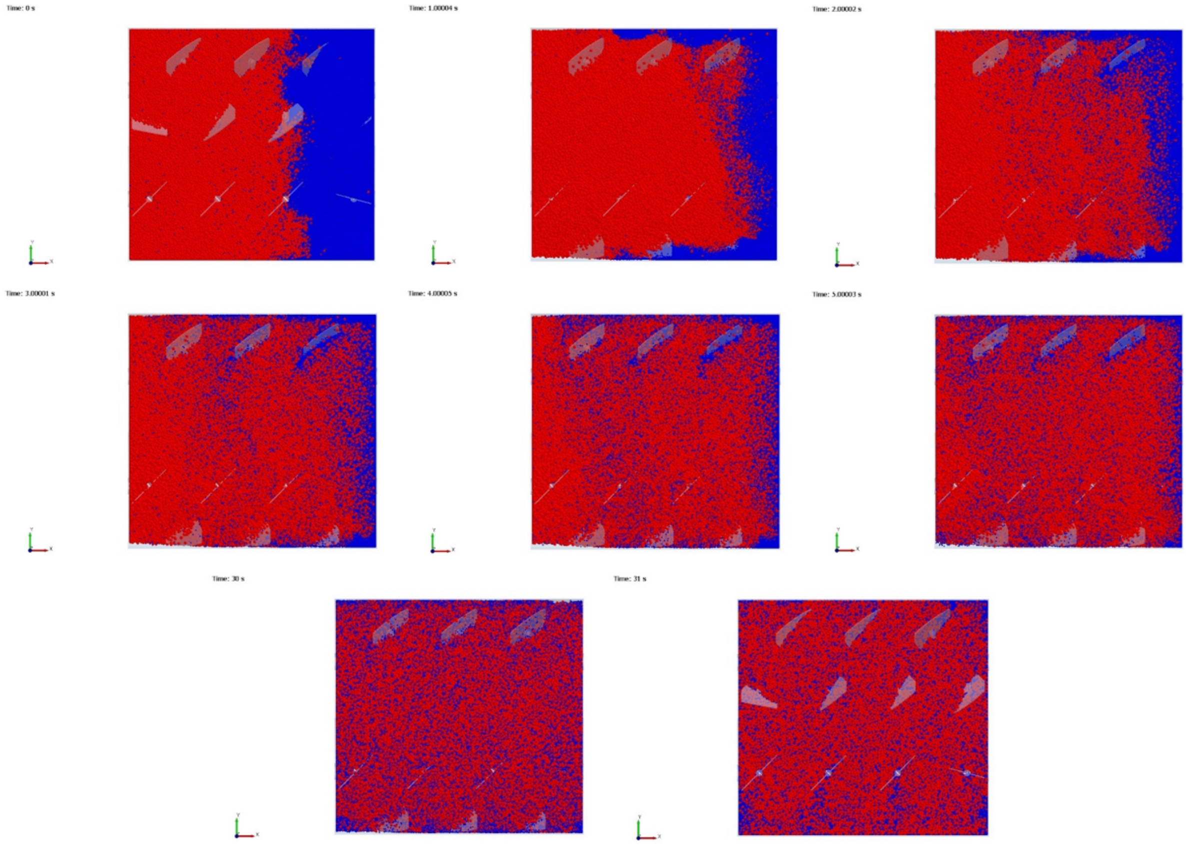

Figure D.53: Top view of simulation 11 - Fill level (e=140%) for time step t=0s, t=1s, t=2s, t=3s, t=4s, t=5s, t=30s and t=31s.

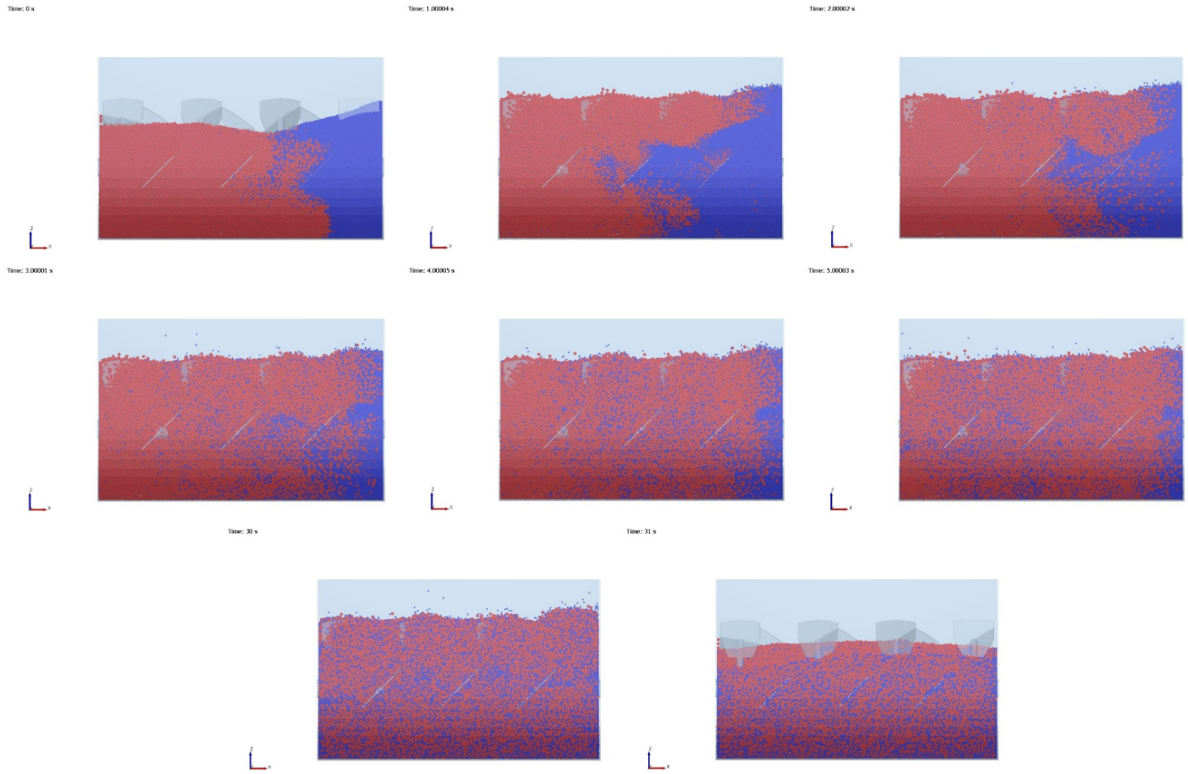

Figure D.54: Side view of simulation 11 - Fill level (e=140%) for time step t=0s, t=1s, t=2s, t=3s, t=4s, t=5s, t=30s and t=31s.

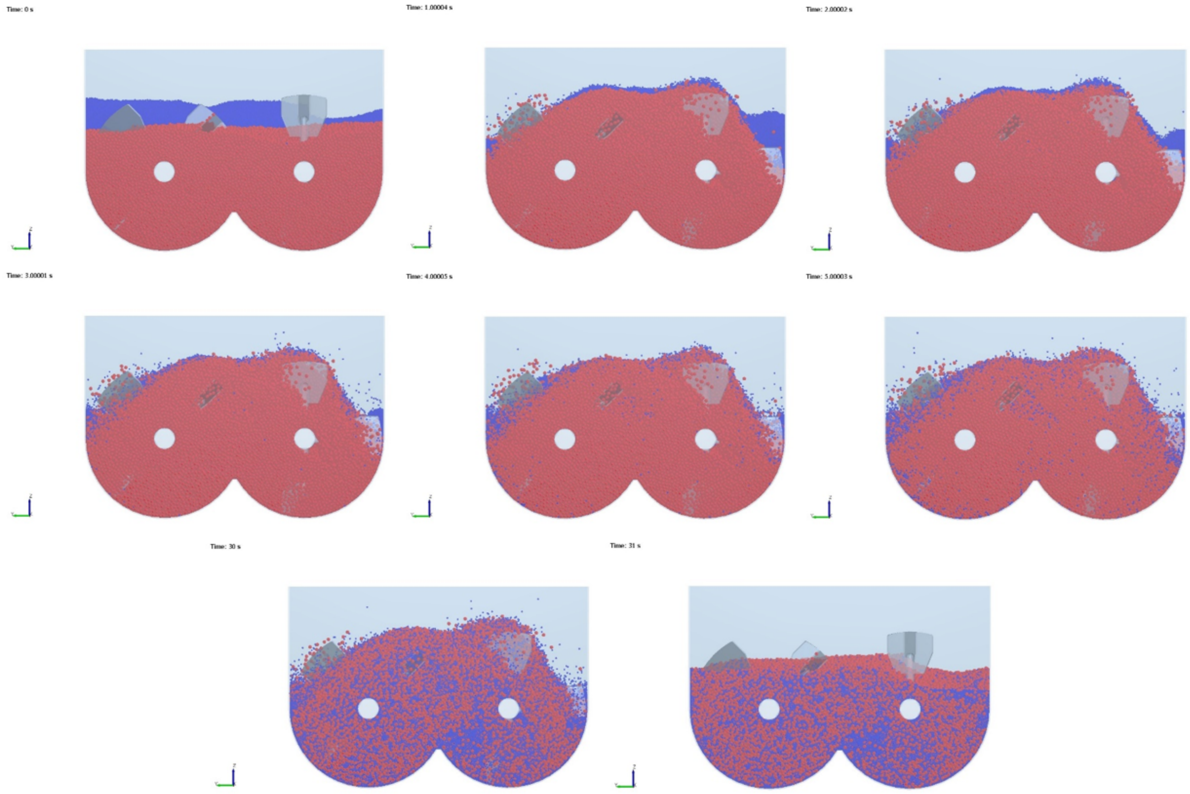

Figure D.55: Front view of simulation 11 - Fill level (e=140%) for time step t=0s, t=1s, t=2s, t=3s, t=4s, t=5s, t=30s and t=31s.

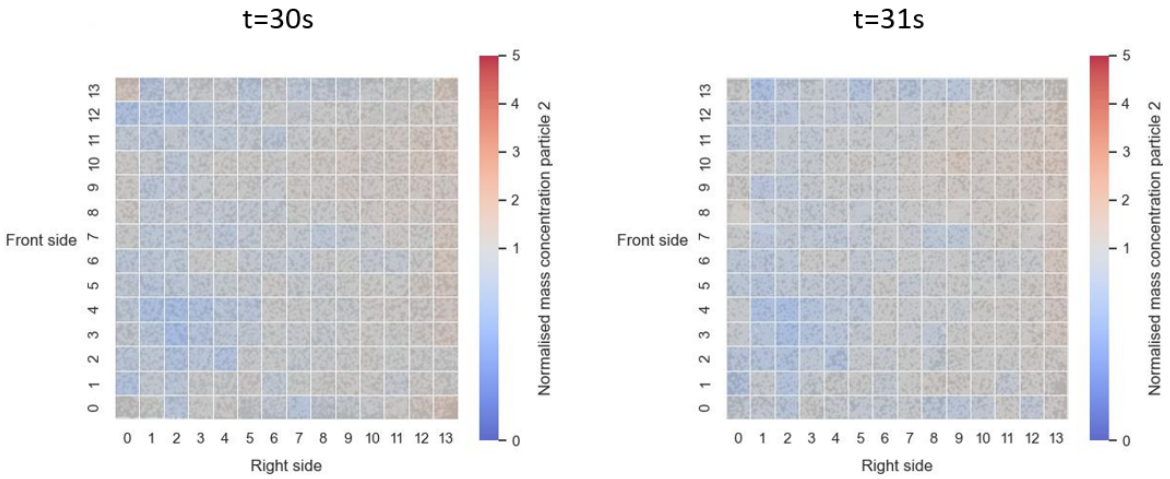
t=30s

t=31s

Figure D.56: Simulation 11 - Heat map of 14x14x1 grid with normalized concentrations of particle 2 at time=30s and t=31s.

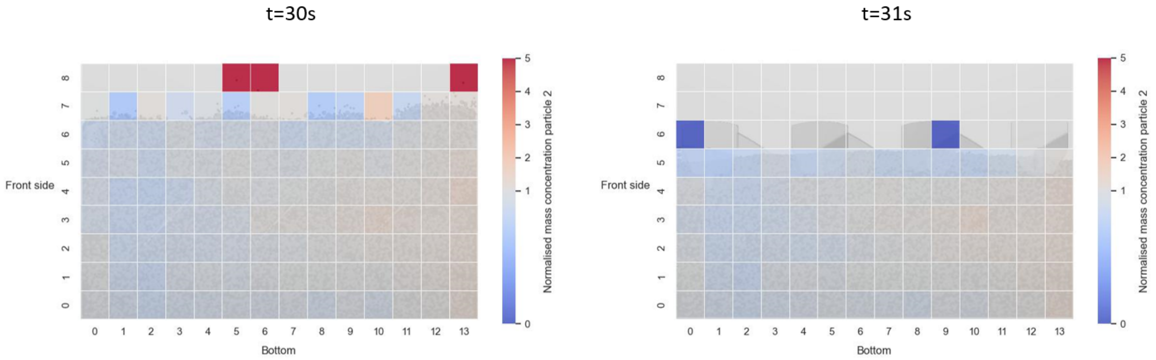
t=30s

t=31s

Figure D.57: Simulation 11 - Heat map of 14x1x9 grid with normalized concentrations of particle 2 at time=30s and t=31s.

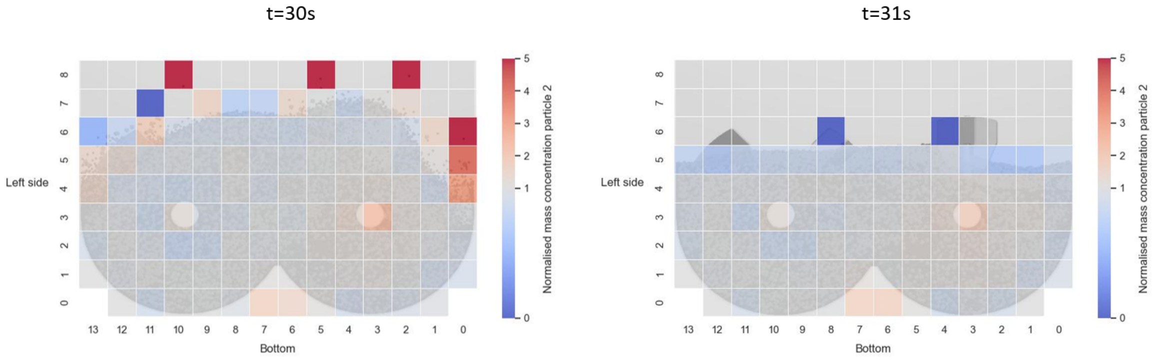
t=30s

t=31s

Figure D.58: Simulation 11 - Heat map of 1x14x9 grid with normalized concentrations of particle 2 at time=30s and t=31s.

D.12. Simulation 12 - Impeller rotational speed (-1)

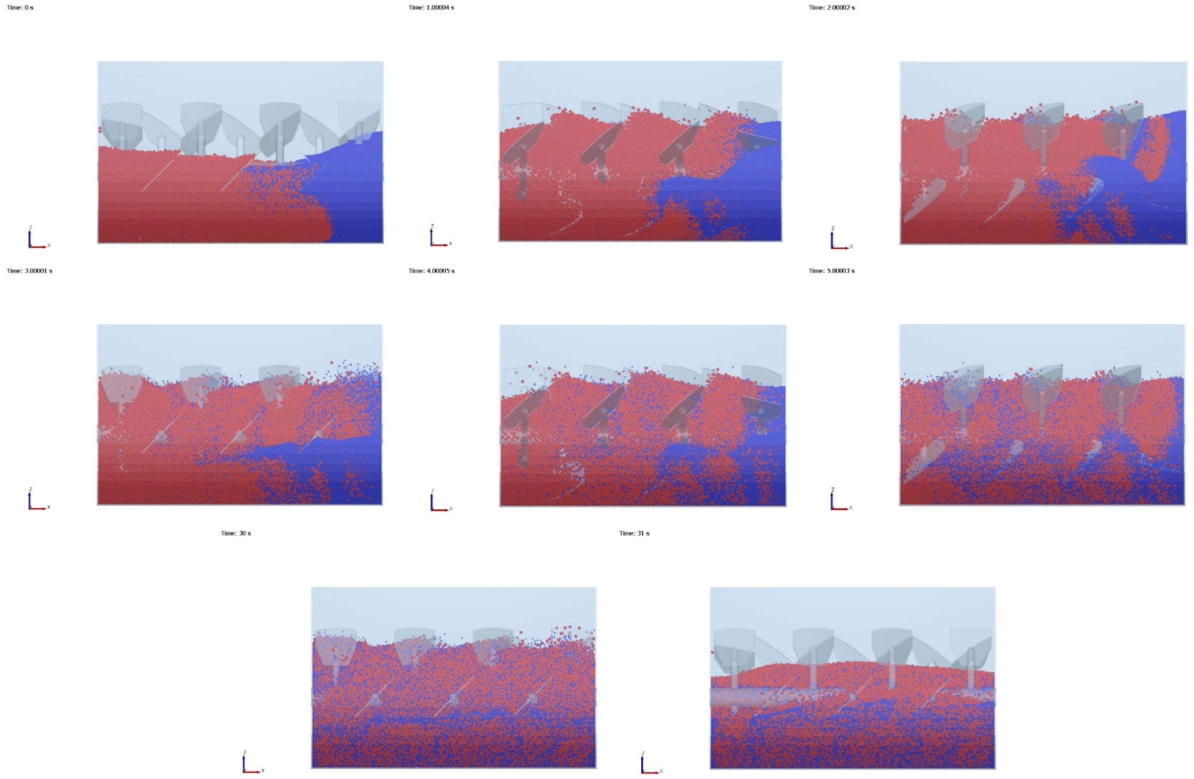

Figure D.59: Side view of simulation 12 - Impeller rotational speed (f=40 rpm) for time step t=0s, t=1s, t=2s, t=3s, t=4s, t=5s, t=30s and t=31s.

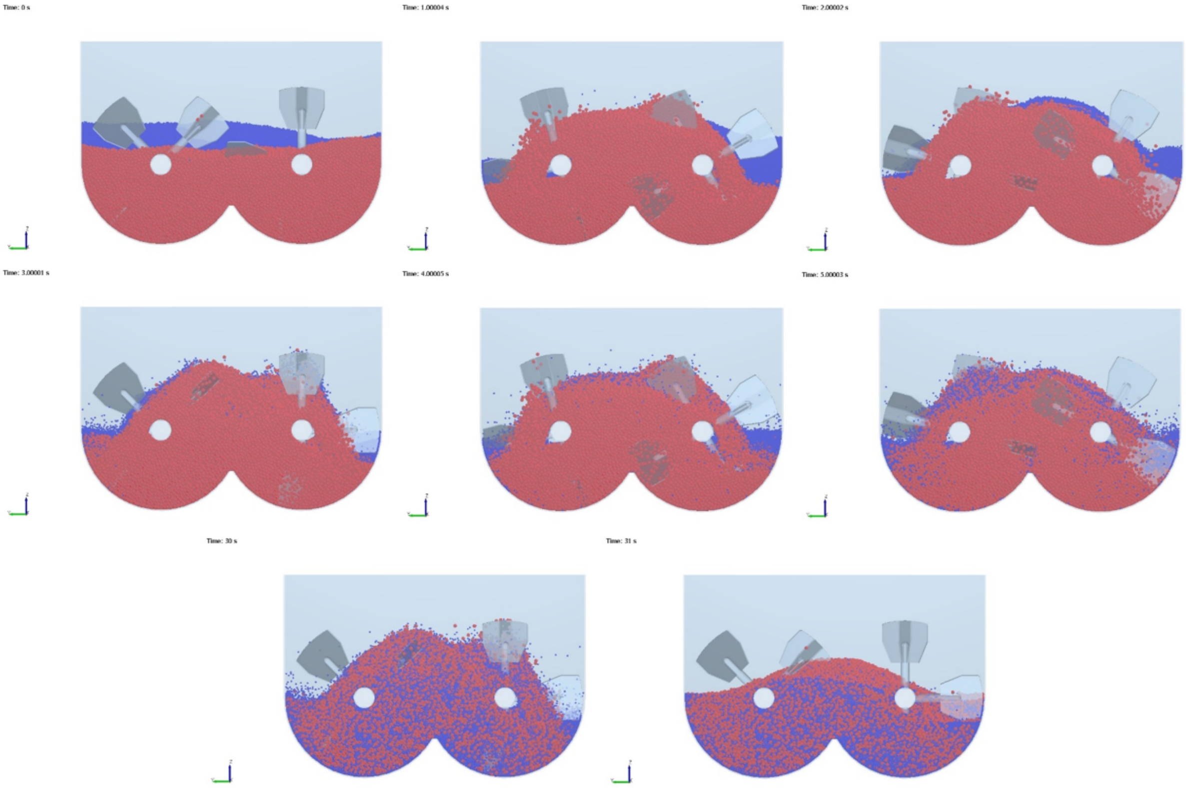

Figure D.60: Front view of simulation 12 - Impeller rotational speed (f=40 rpm) for time step t=0s, t=1s, t=2s, t=3s, t=4s, t=5s, t=30s and t=31s.

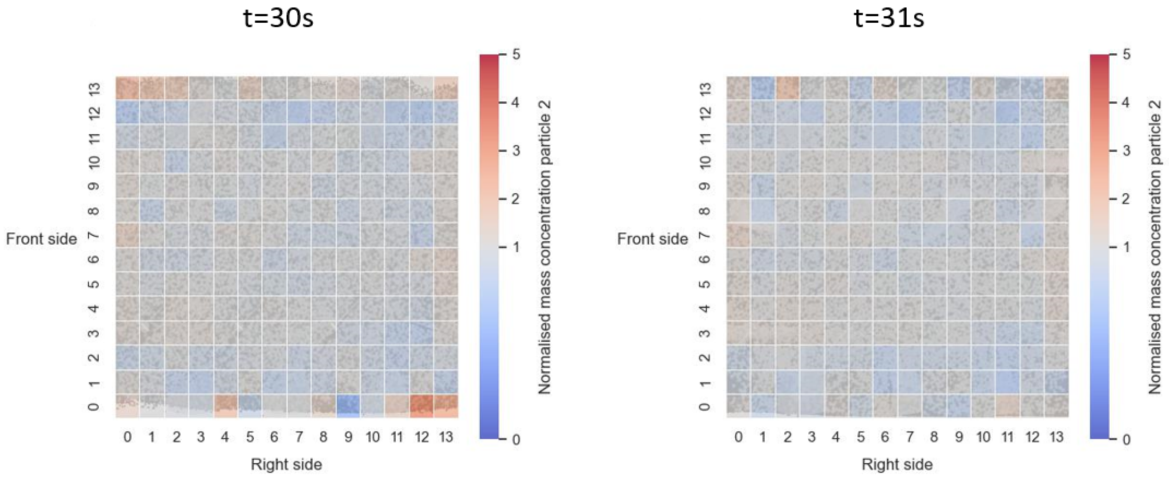

Figure D.61: Simulation 12 - Heat map of 14x14x1 grid with normalized concentrations of particle 2 at time=30s and t=31s.

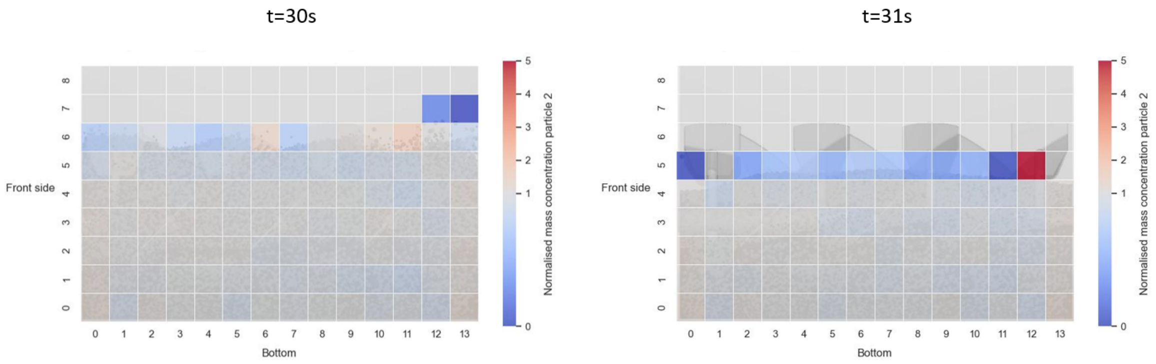

Figure D.62: Simulation 12 - Heat map of 14x1x9 grid with normalized concentrations of particle 2 at time=30s and t=31s.

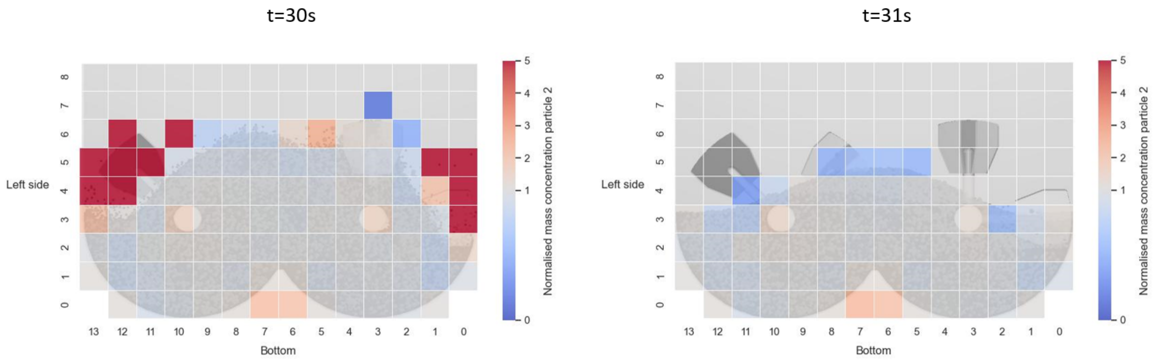

Figure D.63: Simulation 12 - Heat map of 1x14x9 grid with normalized concentrations of particle 2 at time=30s and t=31s.

D.13. Simulation 13 - Impeller rotational speed (+1)

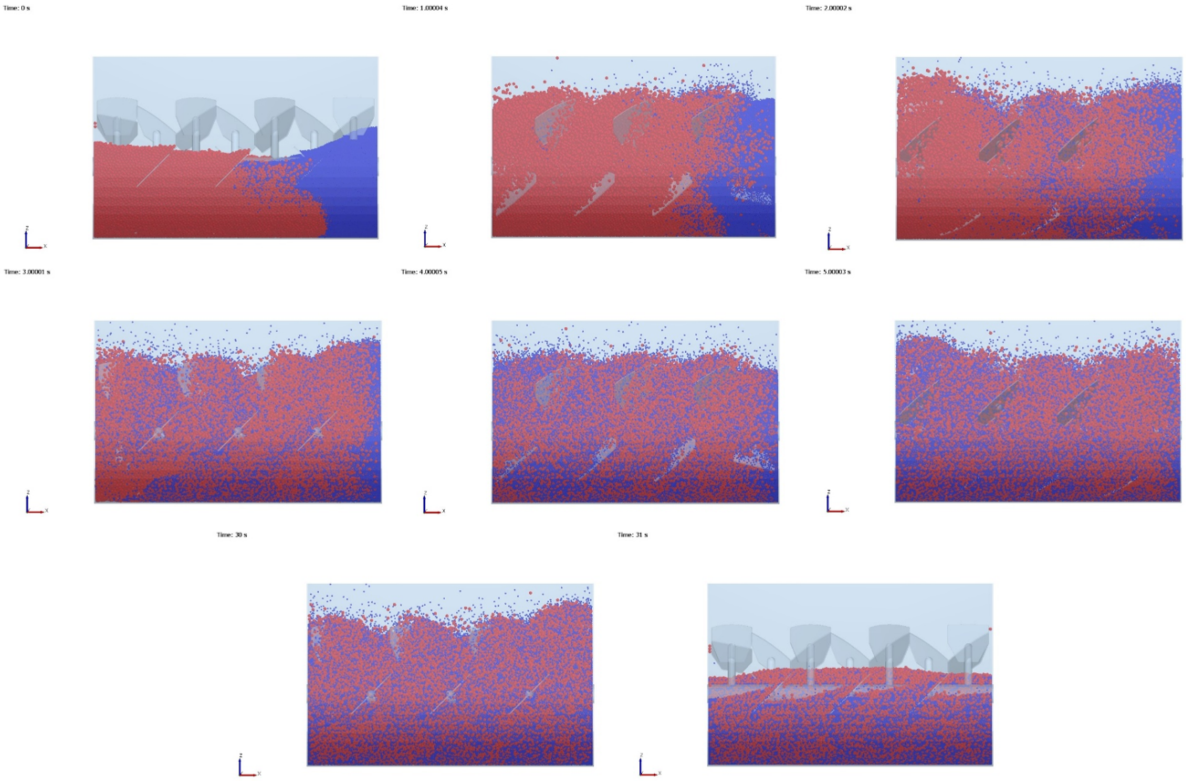

Figure D.64: Side view of simulation 13 - Impeller rotational speed (f=80 rpm) for time step t=0s, t=1s, t=2s, t=3s, t=4s, t=5s, t=30s and t=31s.

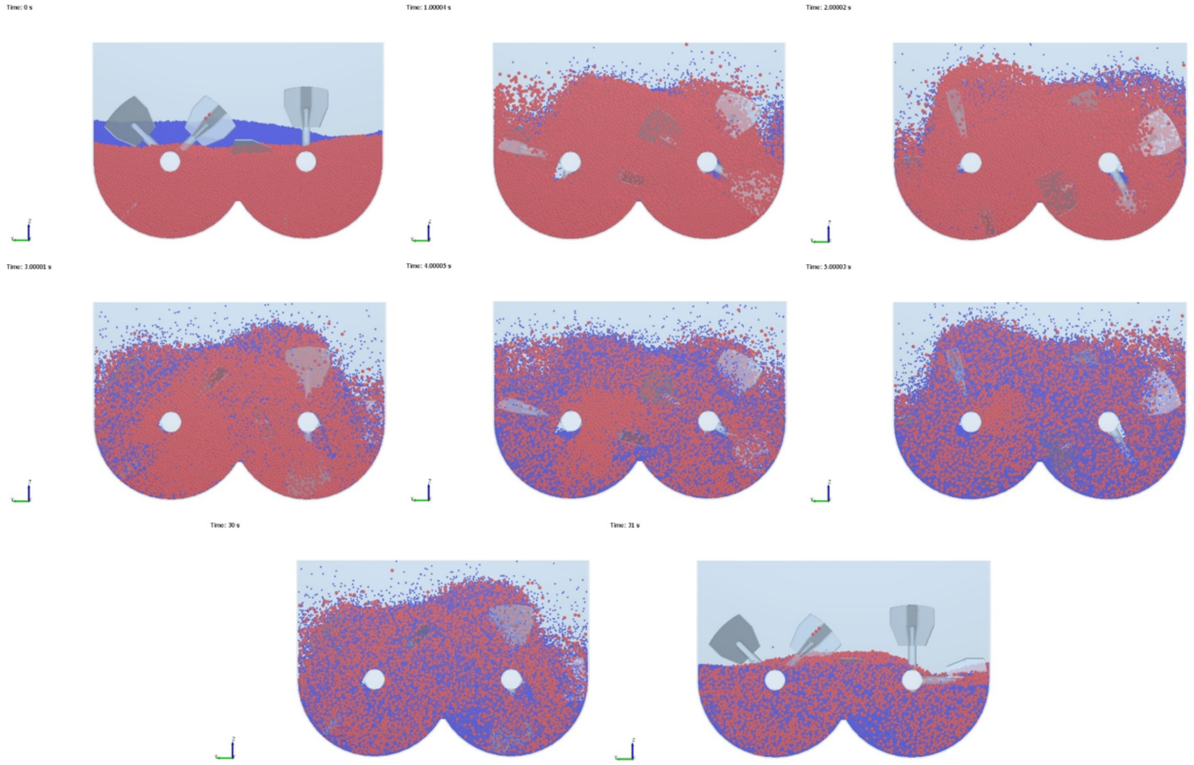

Figure D.65: Front view of simulation 13 - Impeller rotational speed (f=80 rpm) for time step t=0s, t=1s, t=2s, t=3s, t=4s, t=5s, t=30s and t=31s.

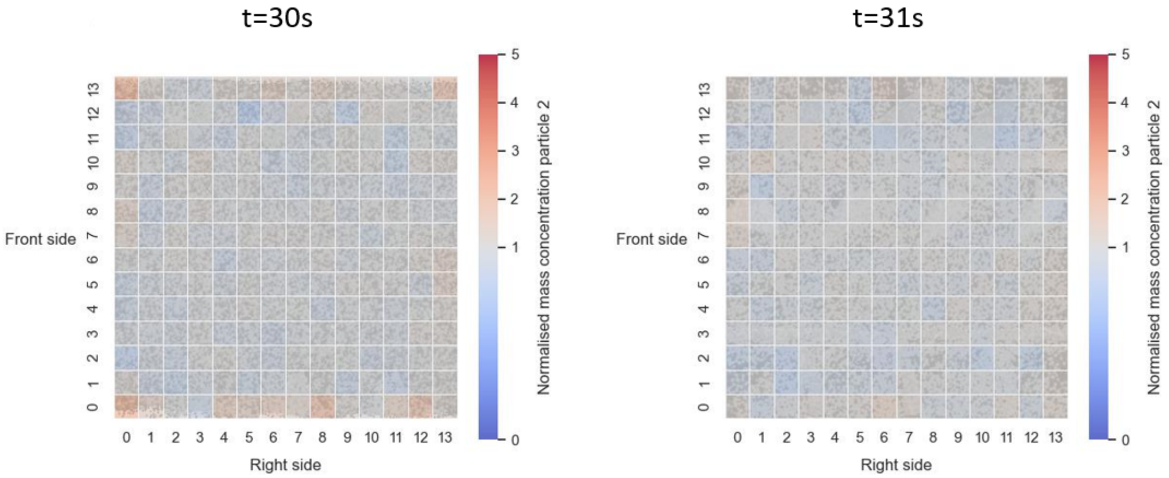

Figure D.66: Simulation 13 - Heat map of 14x14x1 grid with normalized concentrations of particle 2 at time=30s and t=31s.

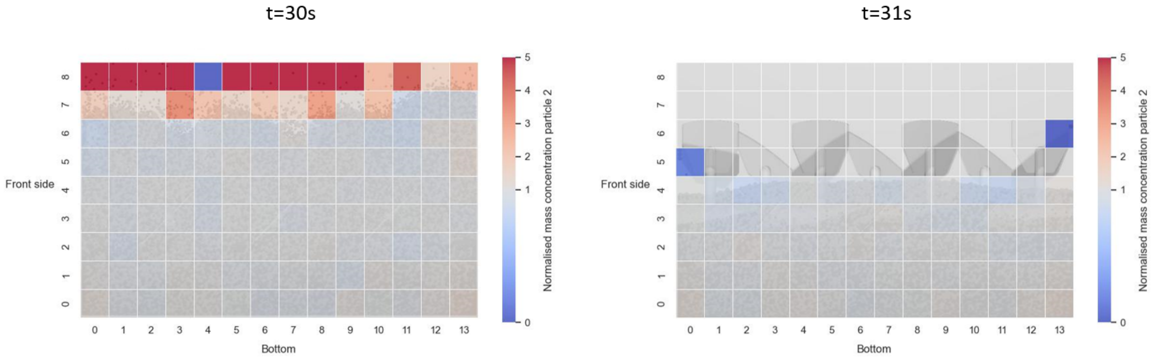

Figure D.67: Simulation 13 - Heat map of 14x1x9 grid with normalized concentrations of particle 2 at time=30s and t=31s.

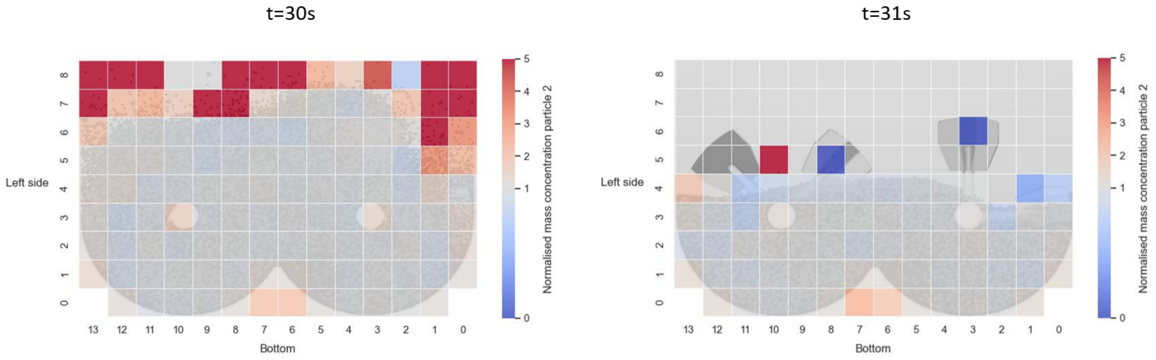

Figure D.68: Simulation 13 - Heat map of 1x14x9 grid with normalized concentrations of particle 2 at time=30s and t=31s.

D.14. Simulation 14 - Paddle size (-1)

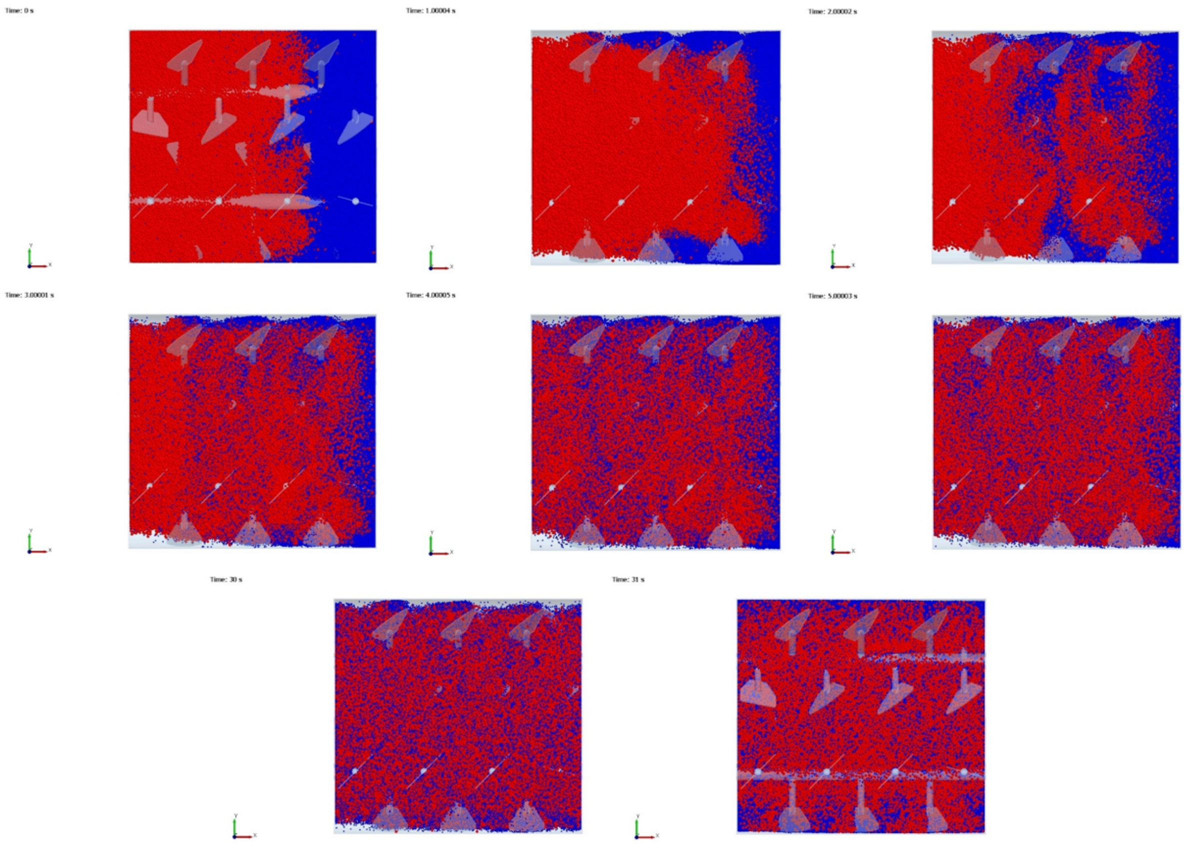

Figure D.69: Top view of simulation 14 - Paddle size (g=2/3) for time step t=0s, t=1s, t=2s, t=3s, t=4s, t=5s, t=30s and t=31s.

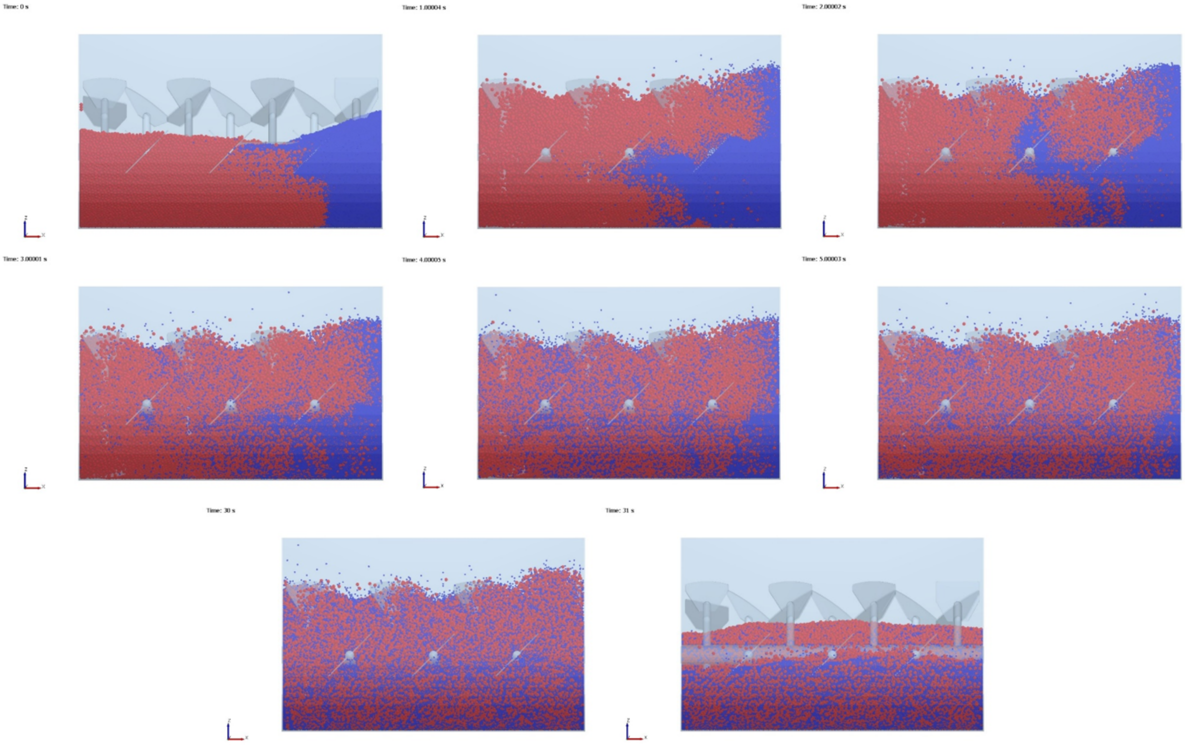

Figure D.70: Side view of simulation 14 - Paddle size (g=2/3) for time step t=0s, t=1s, t=2s, t=3s, t=4s, t=5s, t=30s and t=31s.

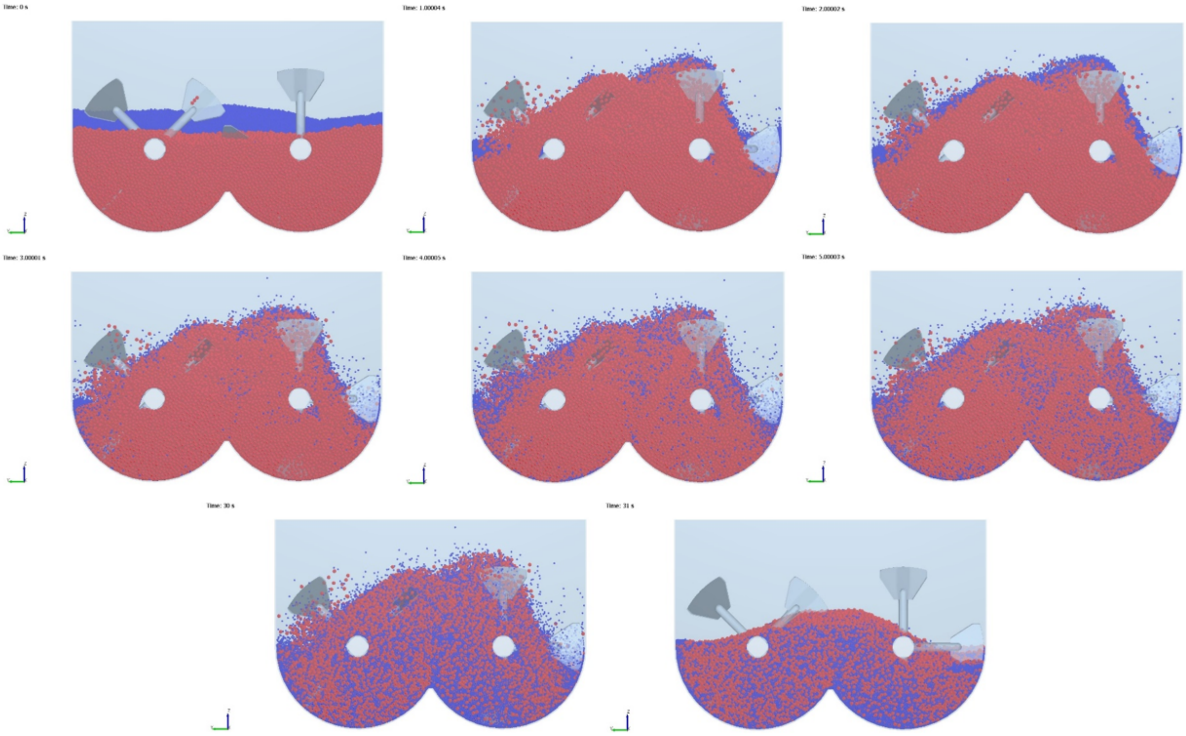

Figure D.71: Front view of simulation 14 - Paddle size (g=2/3) for time step t=0s, t=1s, t=2s, t=3s, t=4s, t=5s, t=30s and t=31s.

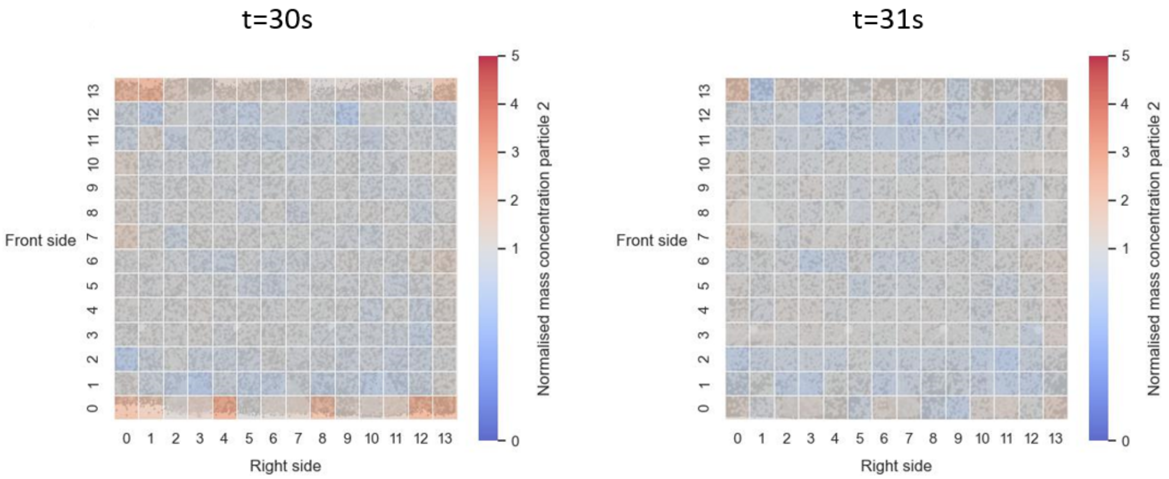

Figure D.72: Simulation 14 - Heat map of 14x14x1 grid with normalized concentrations of particle 2 at time=30s and t=31s.

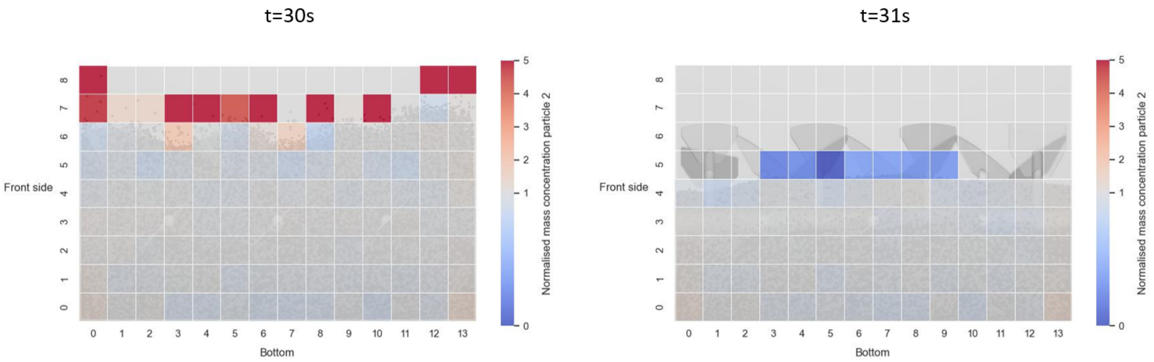

Figure D.73: Simulation 14 - Heat map of 14x1x9 grid with normalized concentrations of particle 2 at time=30s and t=31s.

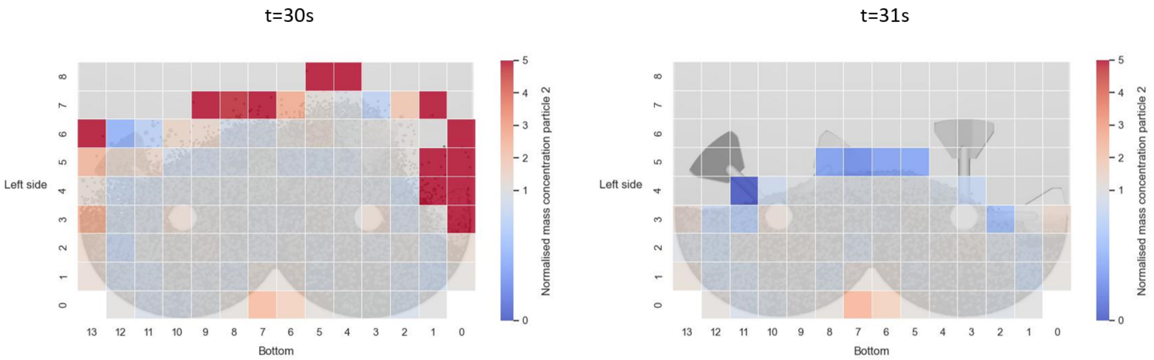

Figure D.74: Simulation 14 - Heat map of 1x14x9 grid with normalized concentrations of particle 2 at time=30s and t=31s.

D.15. Simulation 15 - Paddle size (+1)

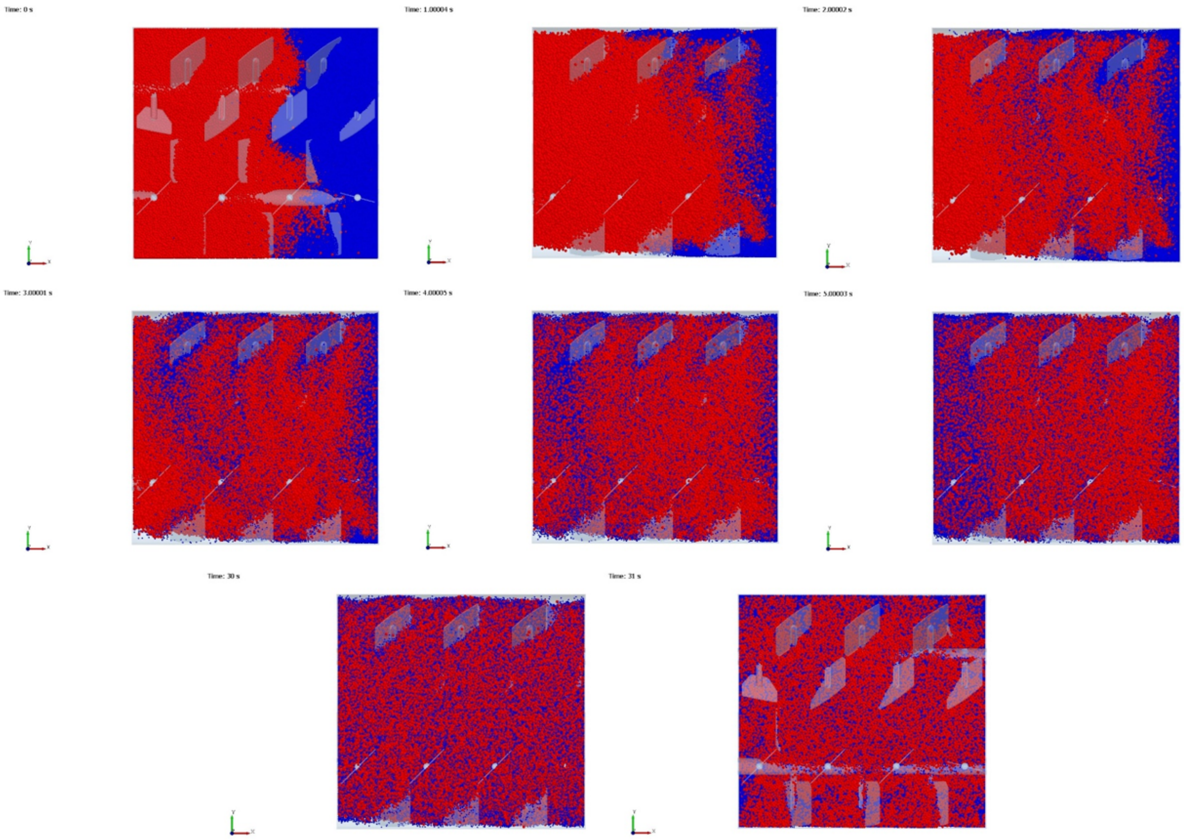

Figure D.75: Top view of simulation 15 - Paddle size (g=3/2) for time step t=0s, t=1s, t=2s, t=3s, t=4s, t=5s, t=30s and t=31s.

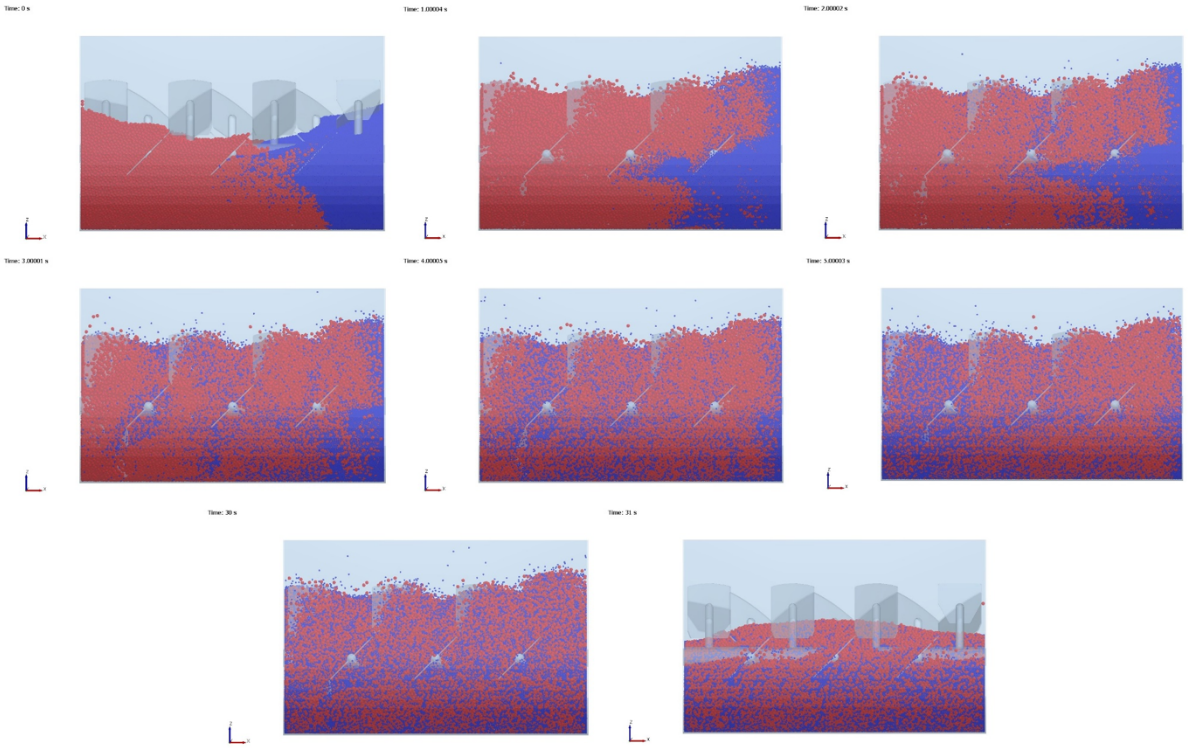

Figure D.76: Side view of simulation 15 - Paddle size (g=3/2) for time step t=0s, t=1s, t=2s, t=3s, t=4s, t=5s, t=30s and t=31s.

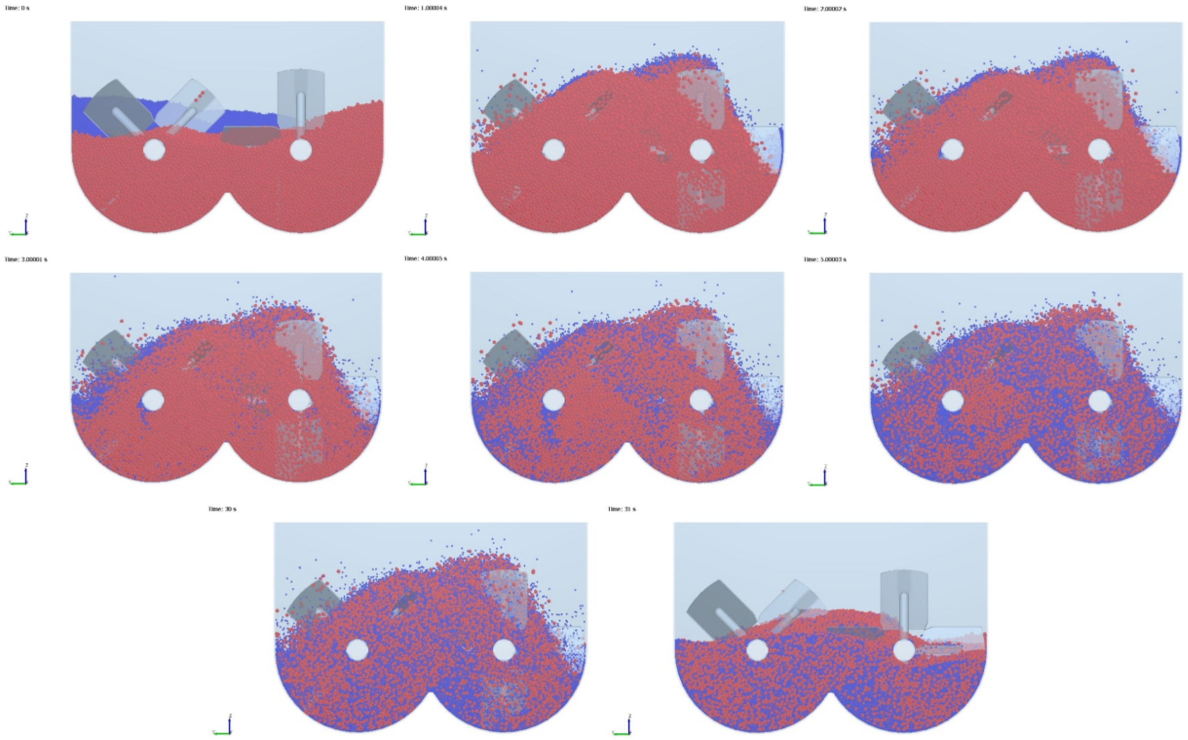

Figure D.77: Front view of simulation 15 - Paddle size (g=3/2) for time step t=0s, t=1s, t=2s, t=3s, t=4s, t=5s, t=30s and t=31s.

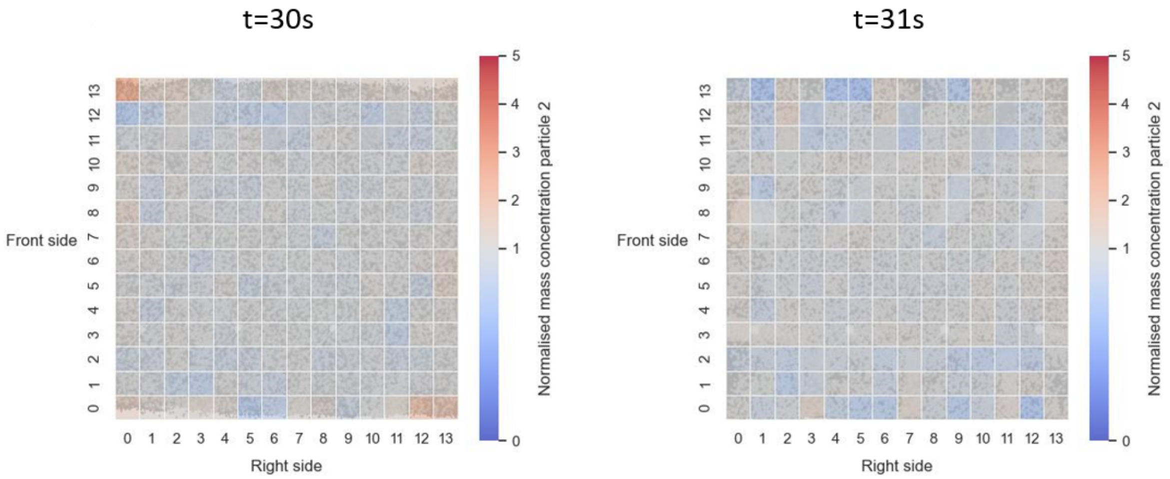

Figure D.78: Simulation 15 - Heat map of 14x14x1 grid with normalized concentrations of particle 2 at time=30s and t=31s.

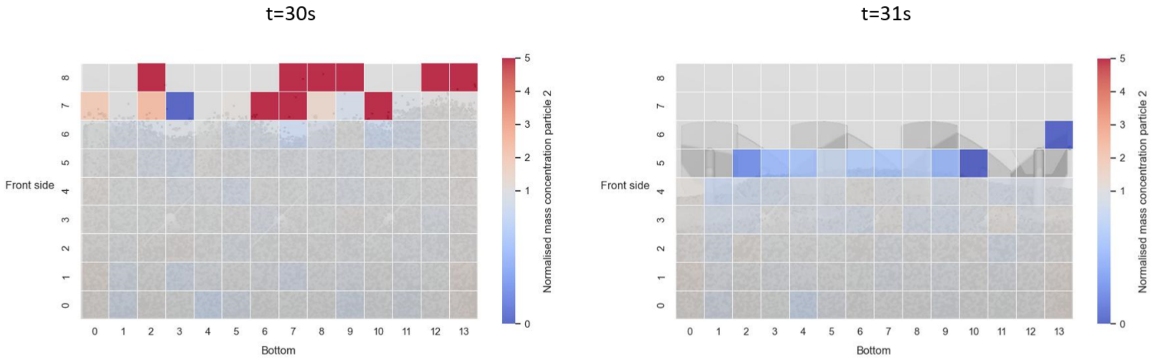

Figure D.79: Simulation 15 - Heat map of 14x1x9 grid with normalized concentrations of particle 2 at time=30s and t=31s.

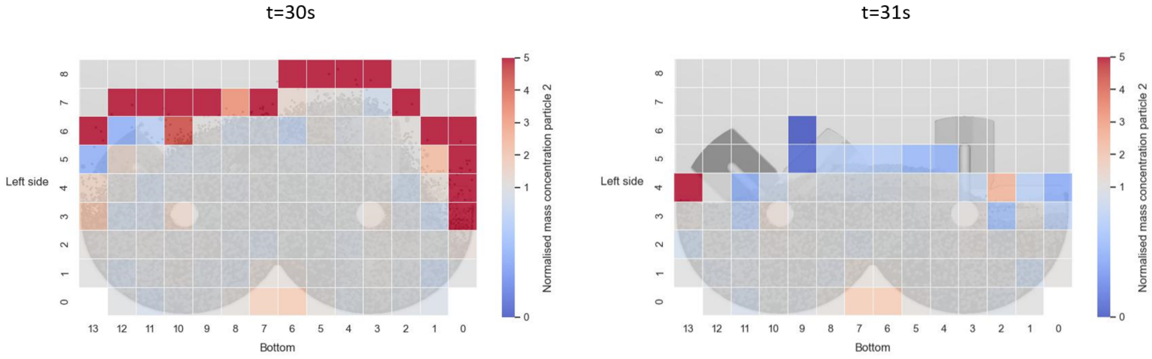

Figure D.80: Simulation 15 - Heat map of 1x14x9 grid with normalized concentrations of particle 2 at time=30s and t=31s.

D.16. Simulation 16 - Paddle angle (-1)

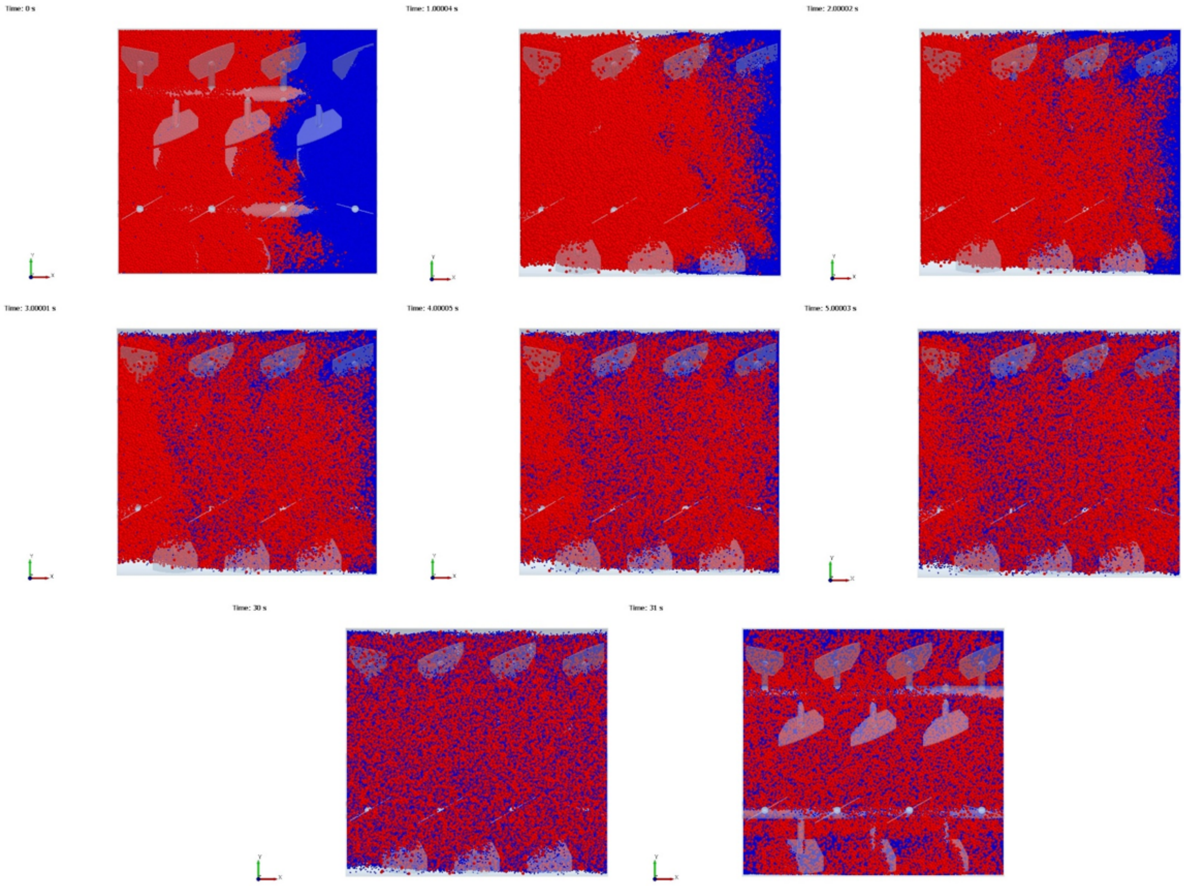

Figure D.81: Top view of simulation 16 - Paddle angle (h=30°) for time step t=0s, t=1s, t=2s, t=3s, t=4s, t=5s, t=30s and t=31s.

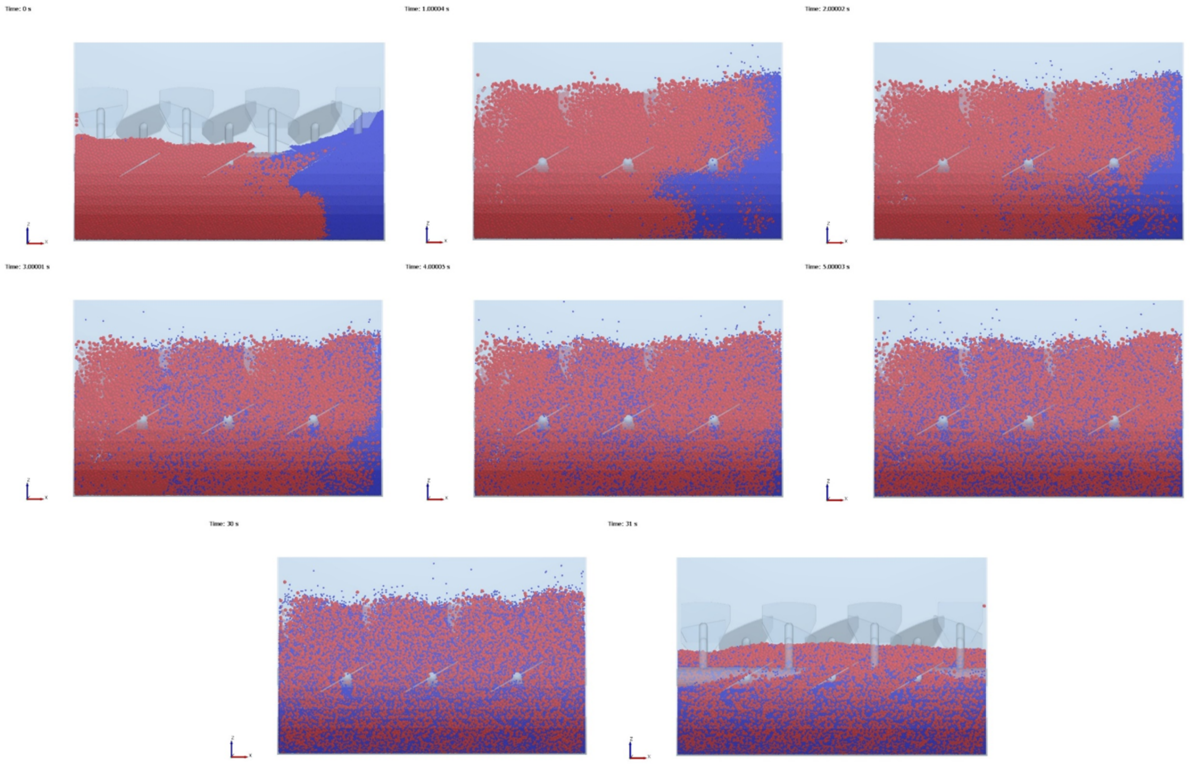

Figure D.82: Side view of simulation 16 - Paddle angle (h=30°) for time step t=0s, t=1s, t=2s, t=3s, t=4s, t=5s, t=30s and t=31s.

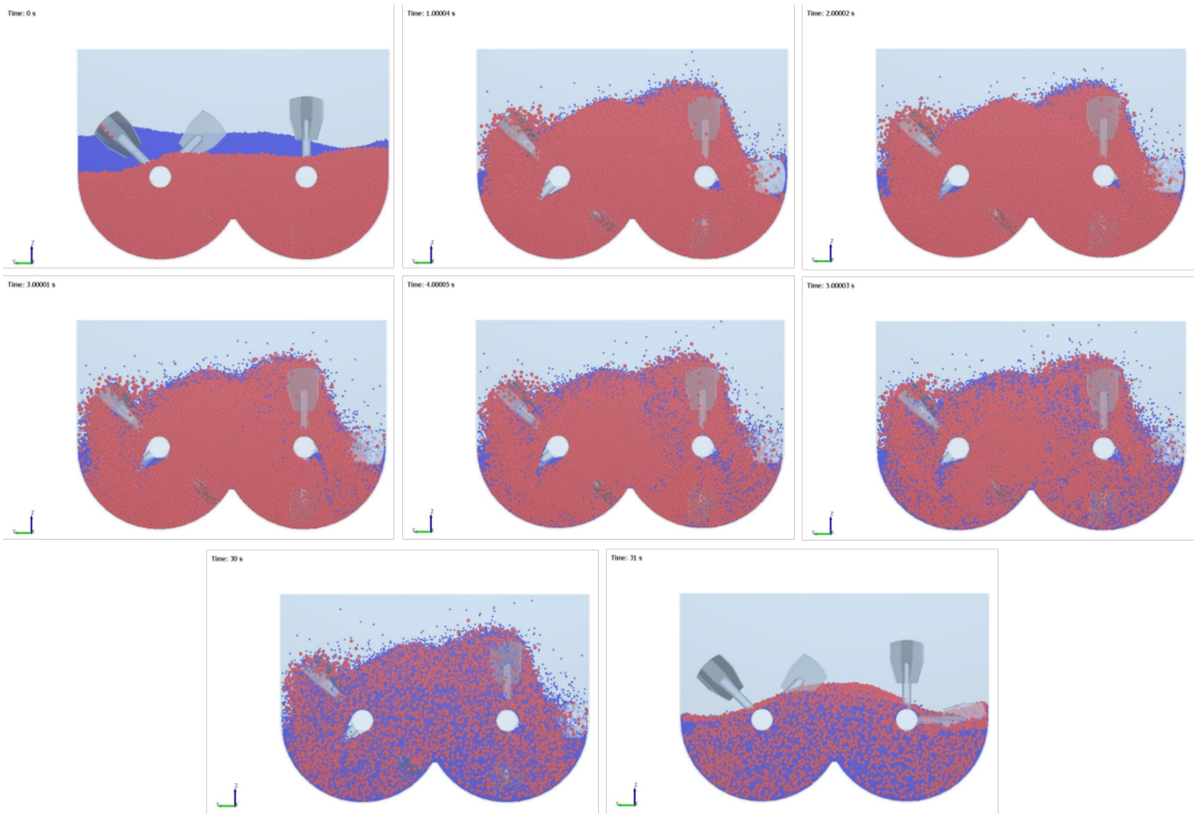

Figure D.83: Front view of simulation 16 - Paddle angle (h=30°) for time step t=0s, t=1s, t=2s, t=3s, t=4s, t=5s, t=30s and t=31s.

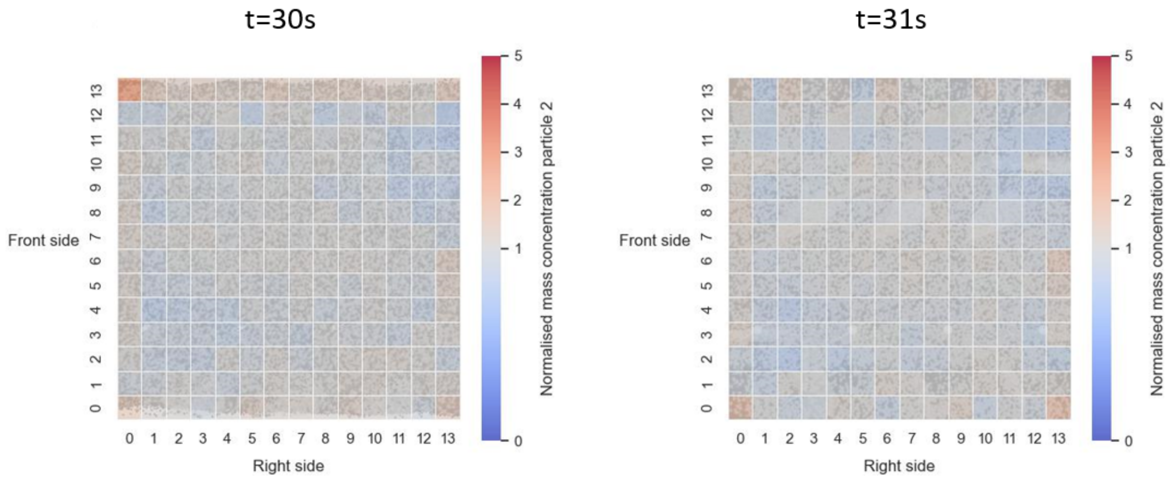

Figure D.84: Simulation 16 - Heat map of 14x14x1 grid with normalized concentrations of particle 2 at time=30s and t=31s.

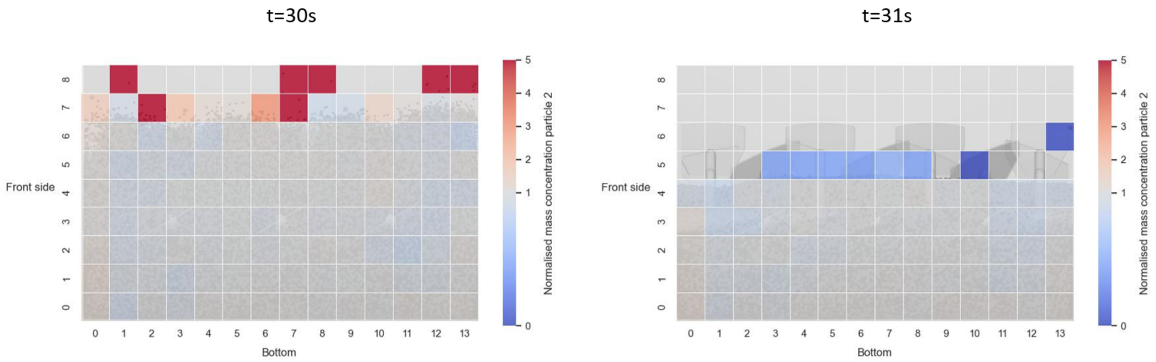

Figure D.85: Simulation 16 - Heat map of 14x1x9 grid with normalized concentrations of particle 2 at time=30s and t=31s.

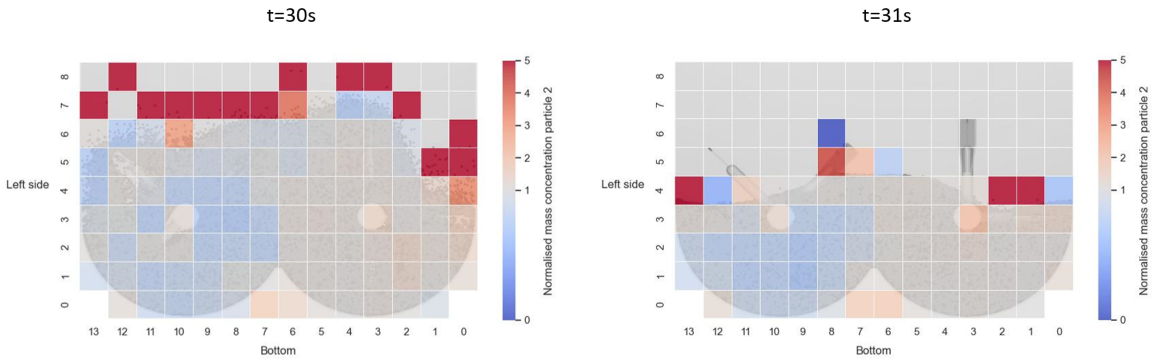

Figure D.86: Simulation 16 - Heat map of 1x14x9 grid with normalized concentrations of particle 2 at time=30s and t=31s.

D.17. Simulation 17 - Paddle angle (+1)

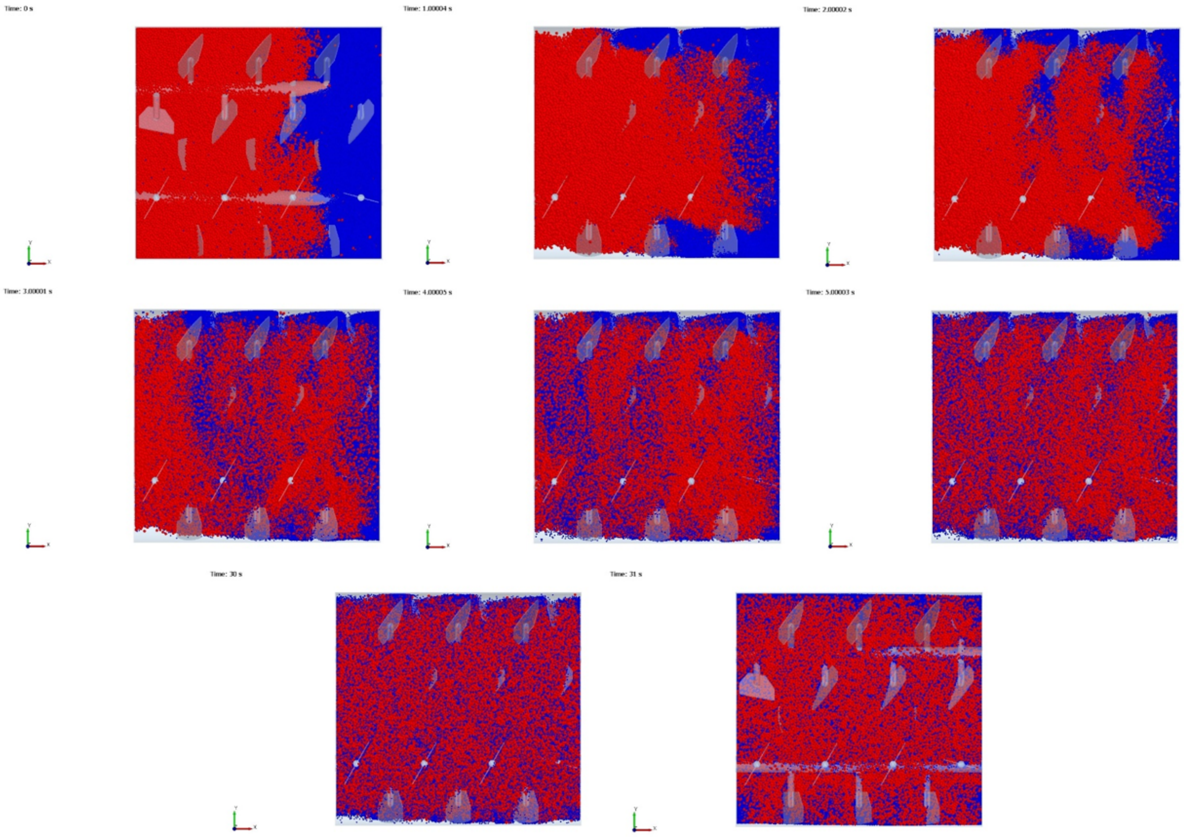

Figure D.87: Top view of simulation 17 - Paddle angle (h=60°) for time step t=0s, t=1s, t=2s, t=3s, t=4s, t=5s, t=30s and t=31s.

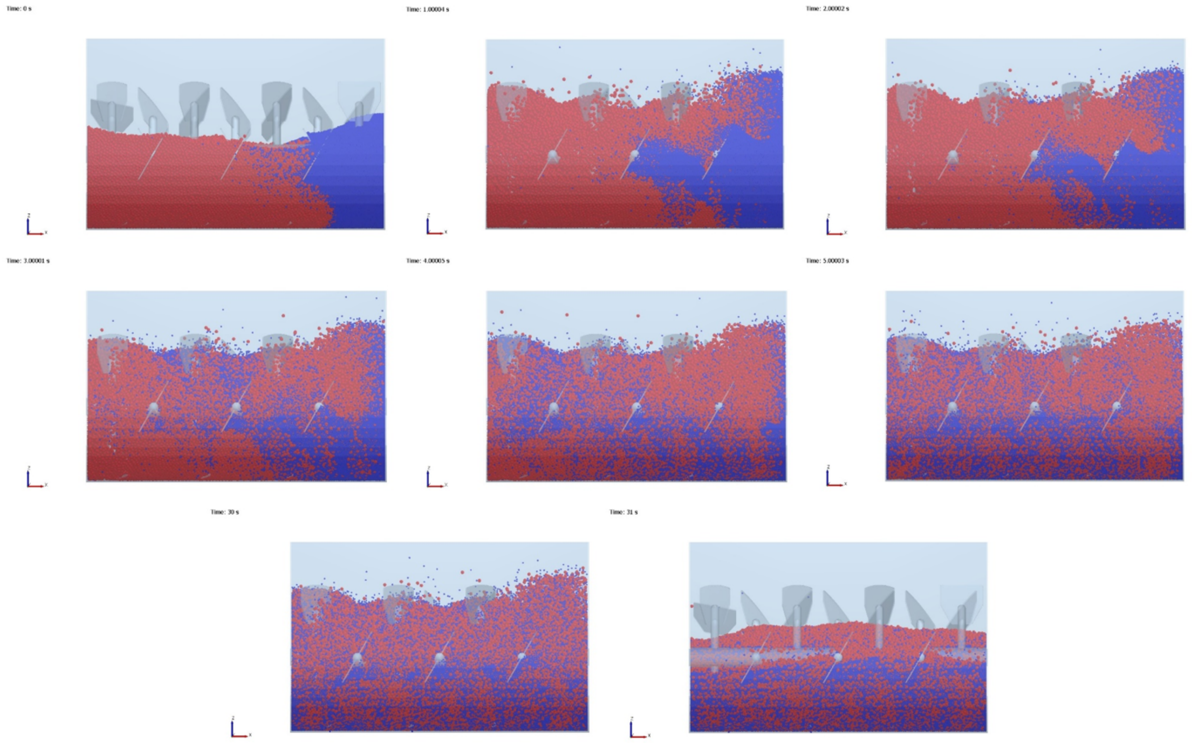

Figure D.88: Side view of simulation 17 - Paddle angle (h=60°) for time step t=0s, t=1s, t=2s, t=3s, t=4s, t=5s, t=30s and t=31s.

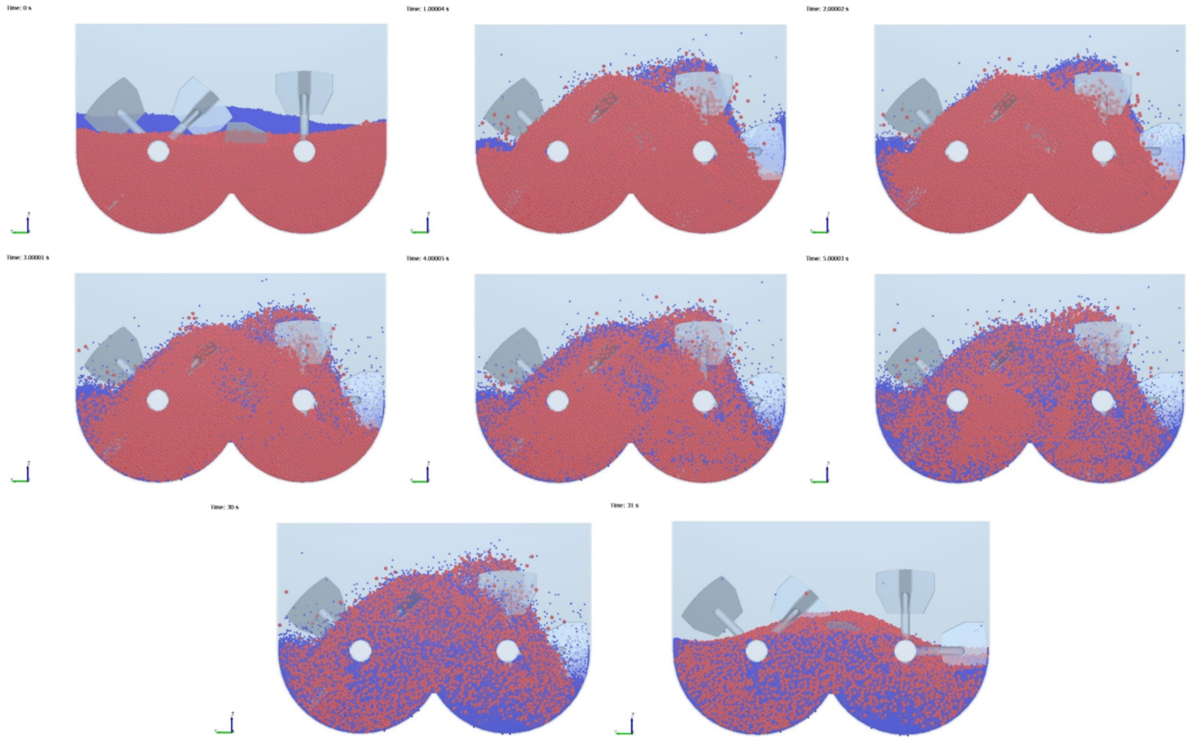

Figure D.89: Front view of simulation 17 - Paddle angle (h=60°) for time step t=0s, t=1s, t=2s, t=3s, t=4s, t=5s, t=30s and t=31s.

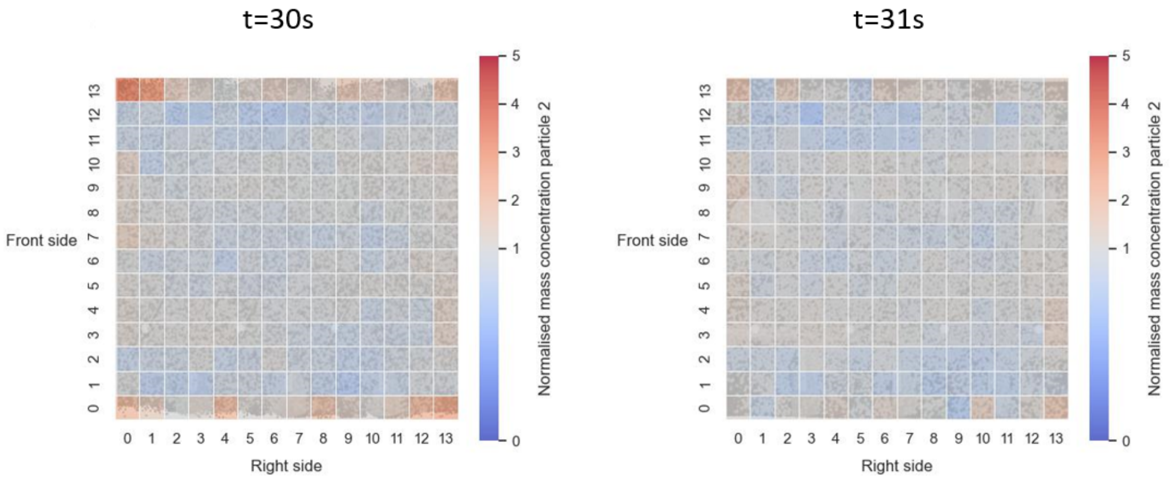

Figure D.90: Simulation 17 - Heat map of 14x14x1 grid with normalized concentrations of particle 2 at time=30s and t=31s.

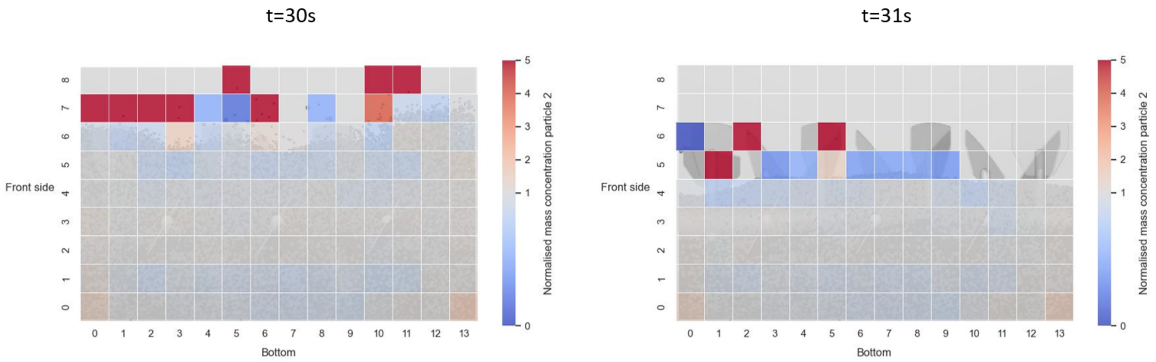

Figure D.91: Simulation 17 - Heat map of 14x1x9 grid with normalized concentrations of particle 2 at time=30s and t=31s.

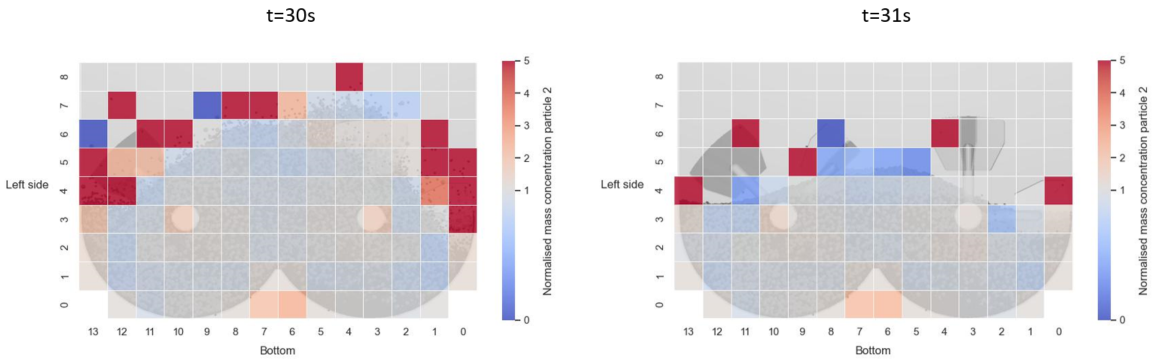

Figure D.92: Simulation 17 - Heat map of 1x14x9 grid with normalized concentrations of particle 2 at time=30s and t=31s.

D.18. Simulation 18 - Paddle number (-1)

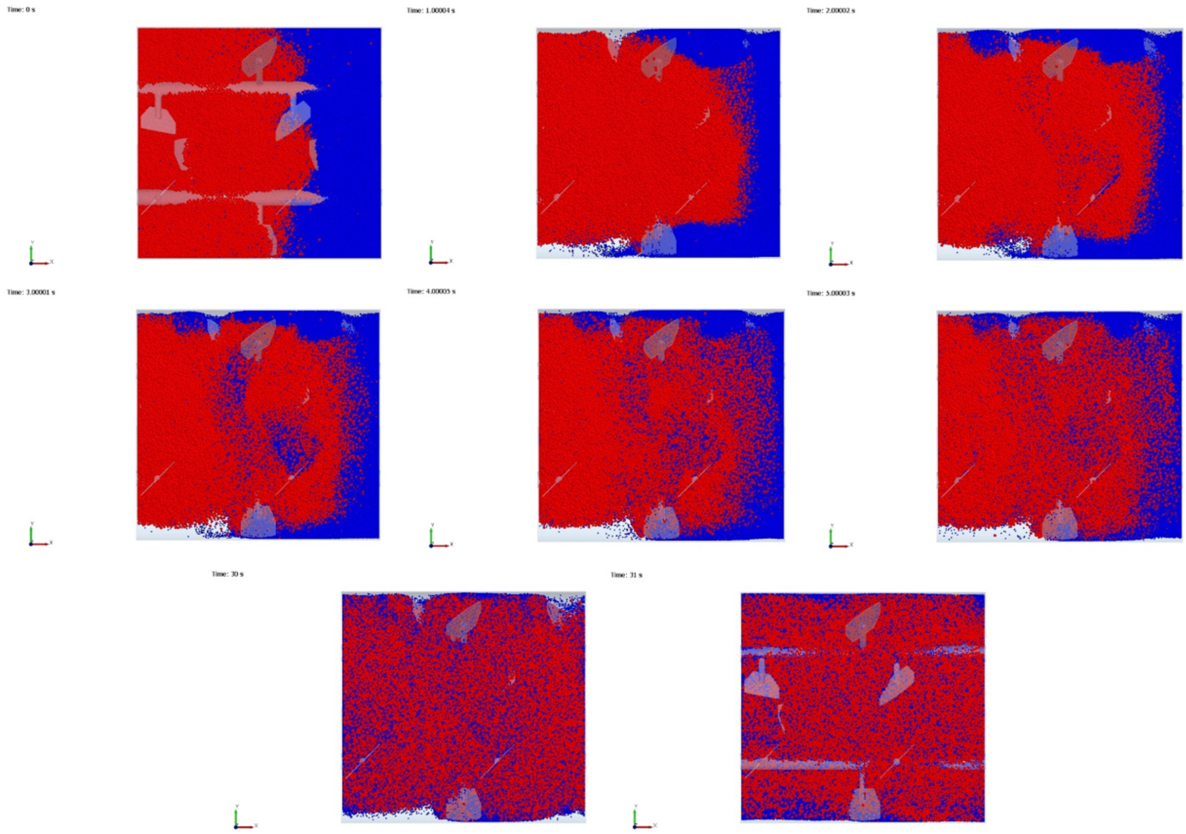

Figure D.93: Top view of simulation 18 - Paddle number (i=7) for time step t=0s, t=1s, t=2s, t=3s, t=4s, t=5s, t=30s and t=31s.

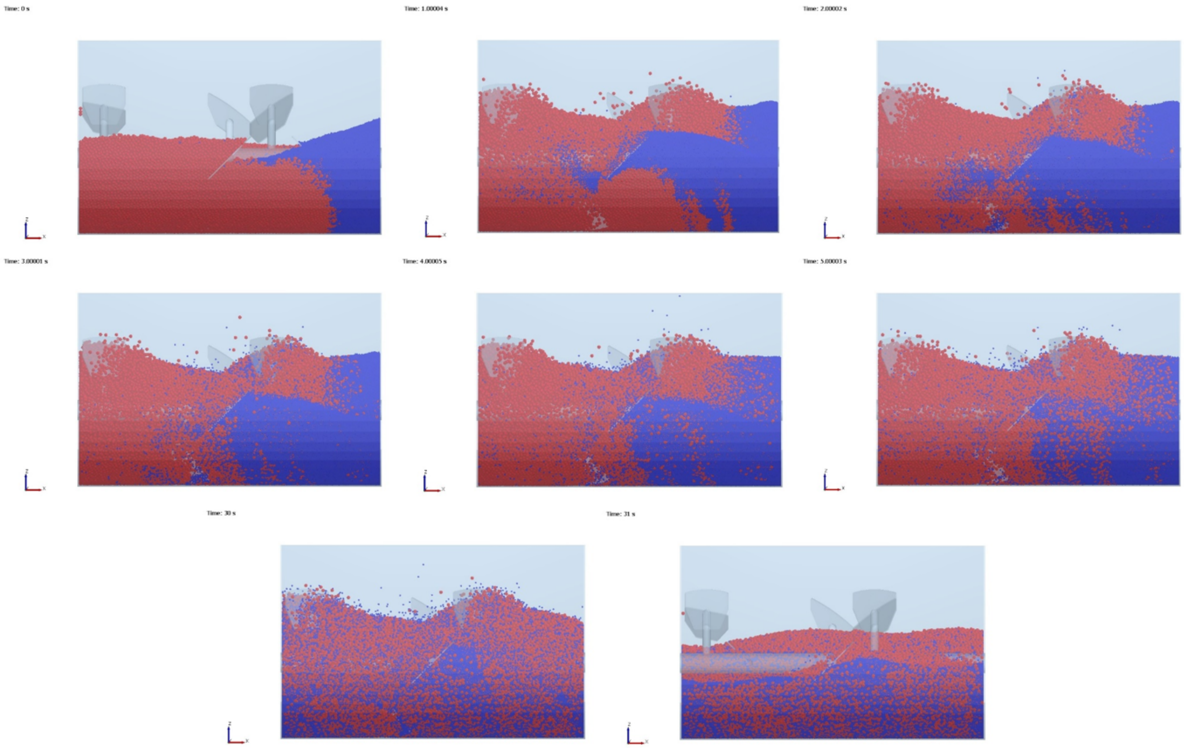

Figure D.94: Side view of simulation 18 - Paddle number (i=7) for time step t=0s, t=1s, t=2s, t=3s, t=4s, t=5s, t=30s and t=31s.

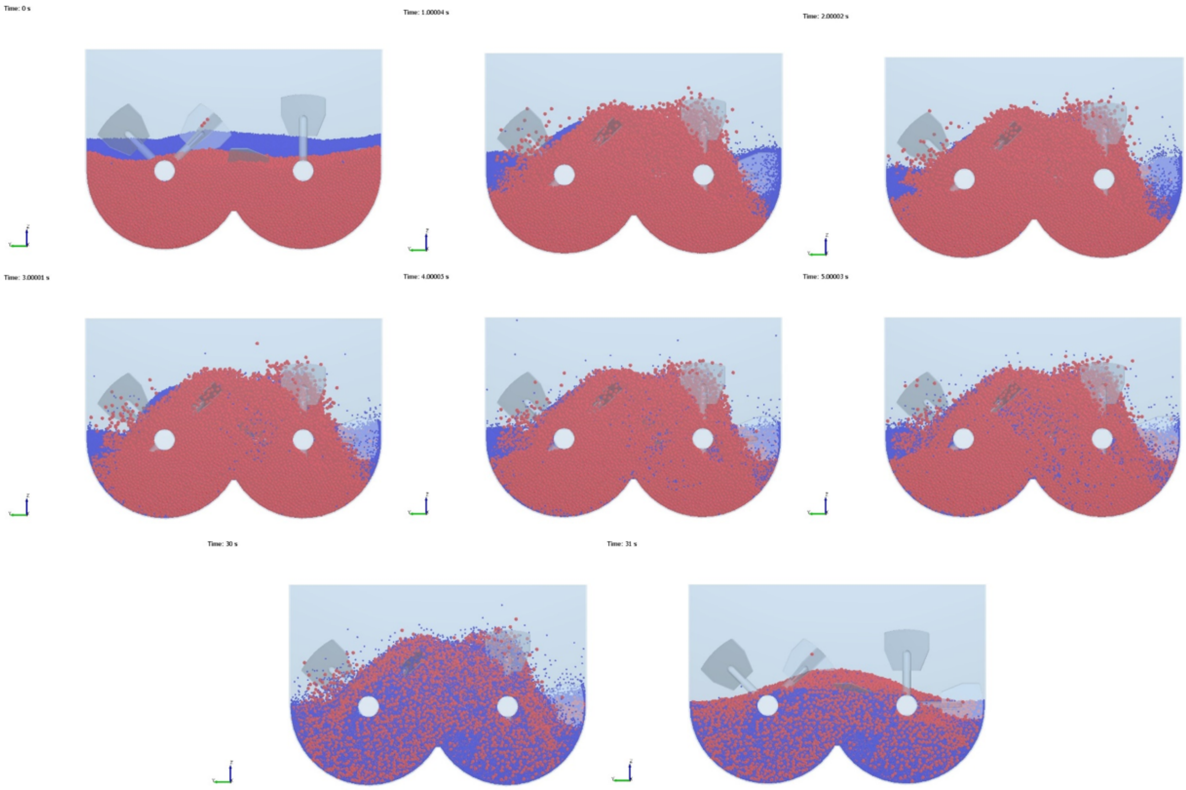

Figure D.95: Front view of simulation 18 - Paddle number (i=7) for time step t=0s, t=1s, t=2s, t=3s, t=4s, t=5s, t=30s and t=31s.

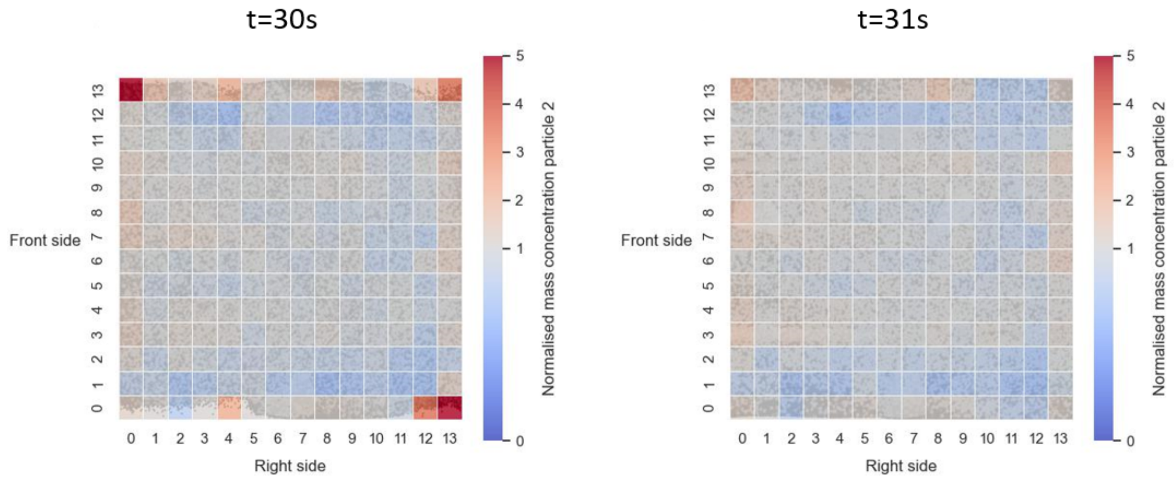

Figure D.96: Simulation 18 - Heat map of 14x14x1 grid with normalized concentrations of particle 2 at time=30s and t=31s.

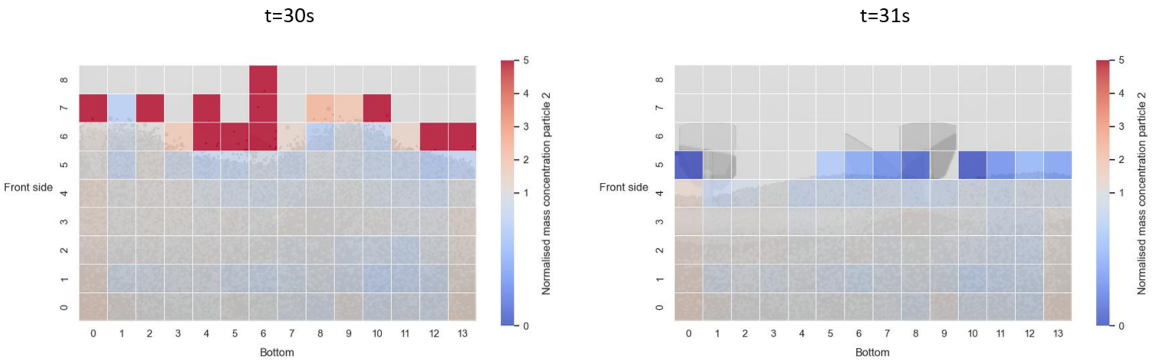

Figure D.97: Simulation 18 - Heat map of 14x1x9 grid with normalized concentrations of particle 2 at time=30s and t=31s.

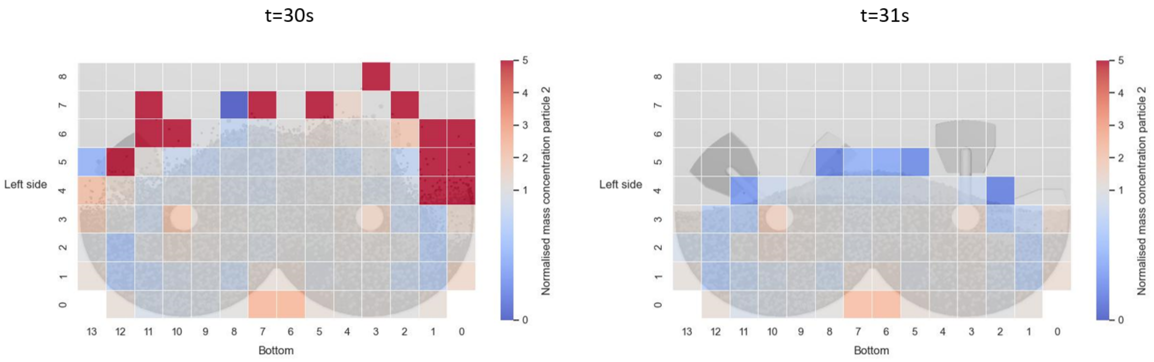

Figure D.98: Simulation 18 - Heat map of 1x14x9 grid with normalized concentrations of particle 2 at time=30s and t=31s.

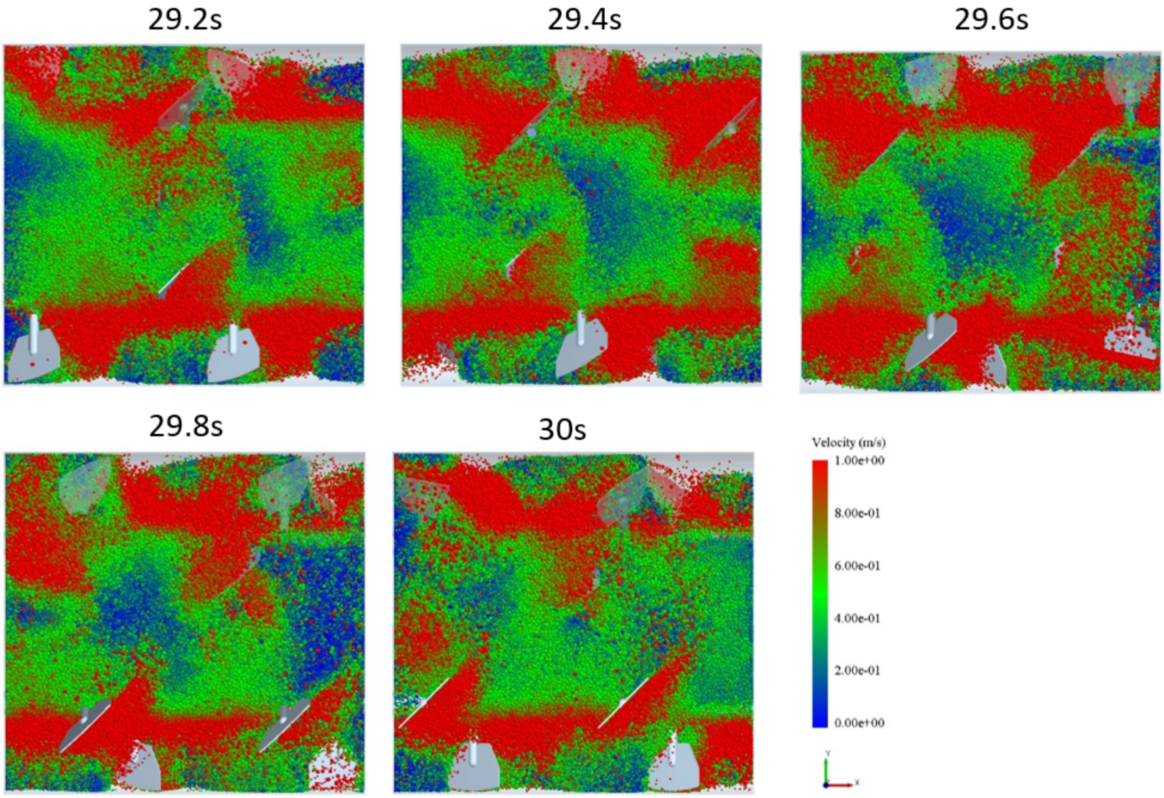

Figure D.99: Simulation 18 - Velocity of particles from top view for the paddle number i=7 (variant 1) for time period 29.2-30s.

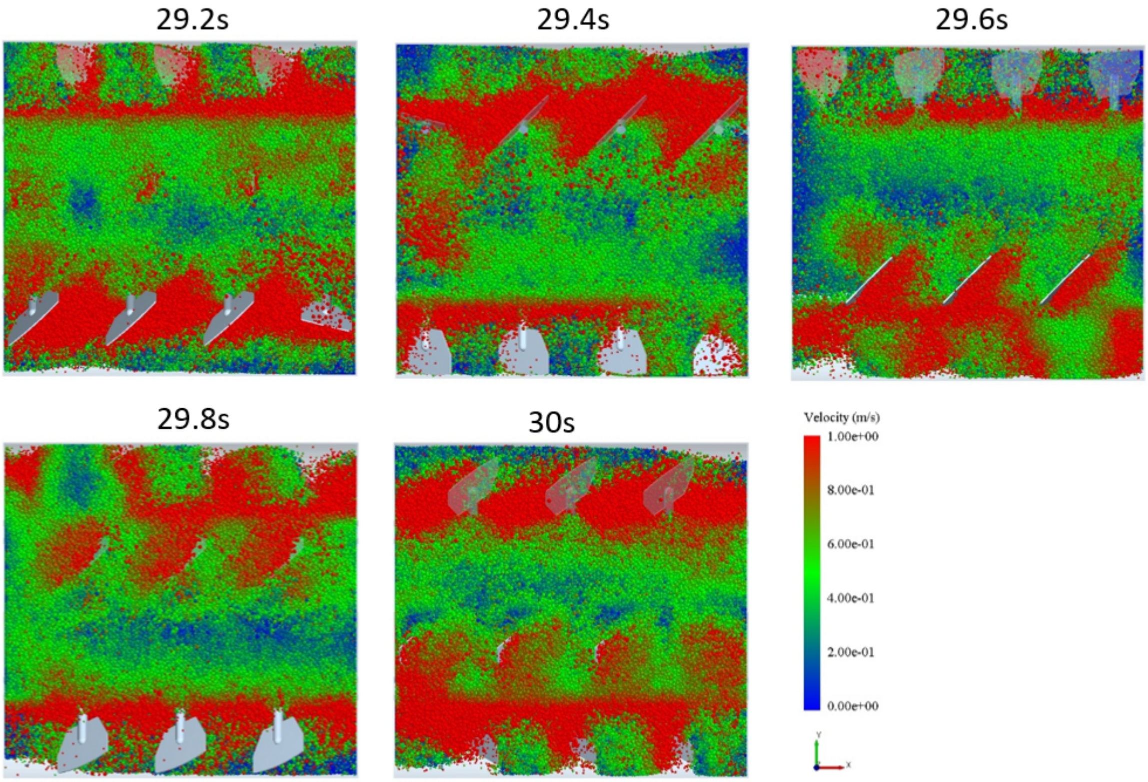

Figure D.100: Simulation 18 - Velocity of particles from top view for the paddle number i=7 (variant 2) for time period 29.2-30s.

D.19. Simulation 19 - Paddle number (+1)

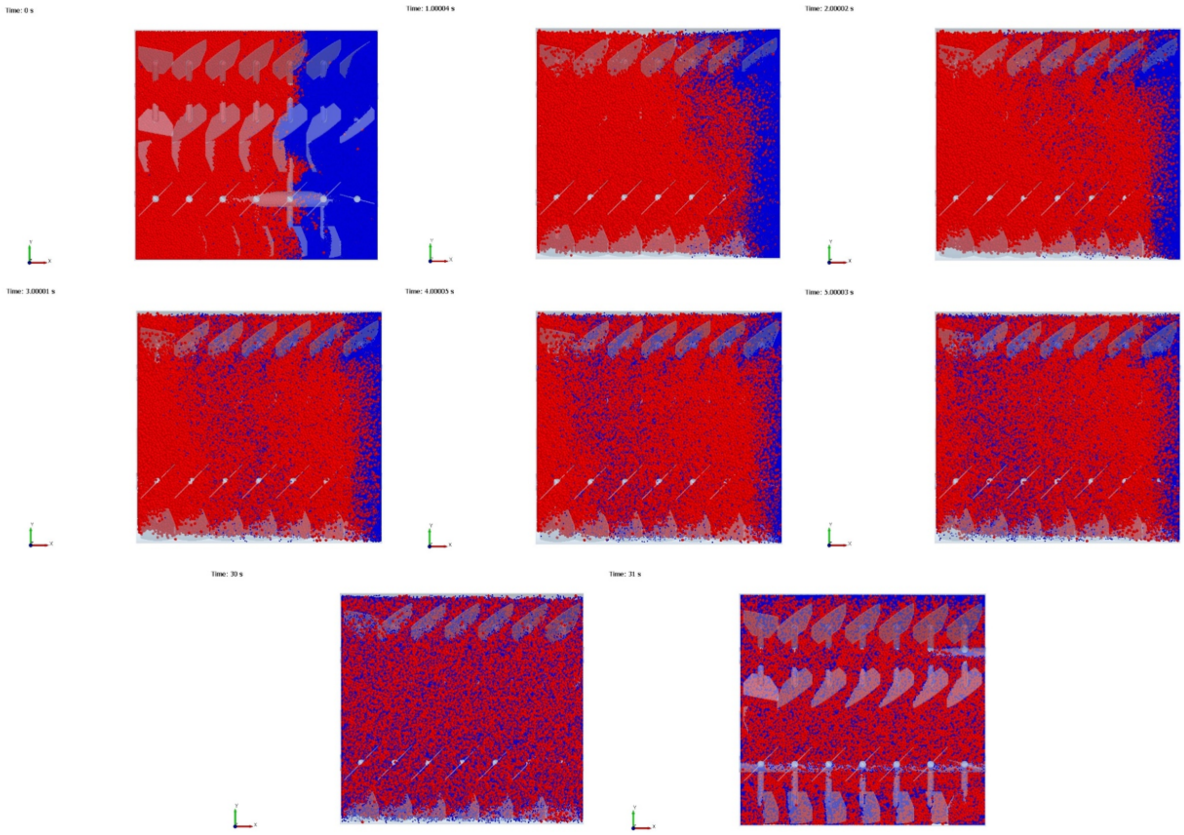

Figure D.101: Top view of simulation 19 - Paddle number (i=28) for time step t=0s, t=1s, t=2s, t=3s, t=4s, t=5s, t=30s and t=31s.

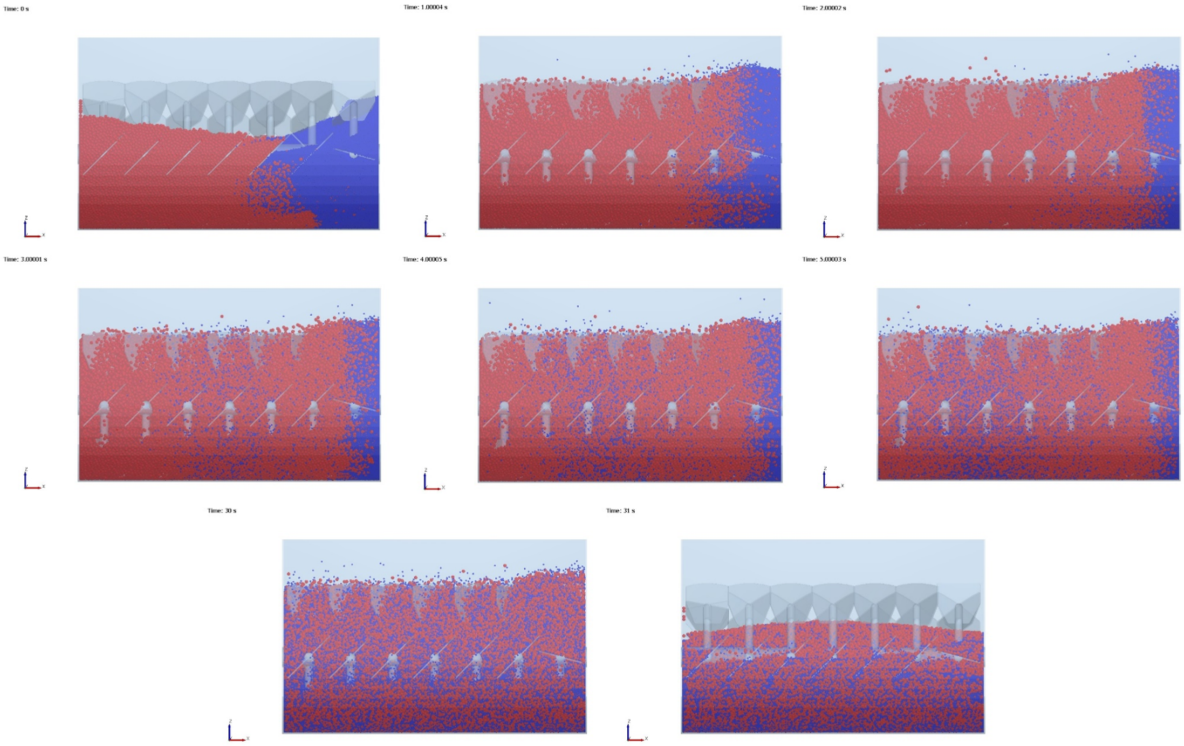

Figure D.102: Side view of simulation 19 - Paddle number (i=28) for time step t=0s, t=1s, t=2s, t=3s, t=4s, t=5s, t=30s and t=31s.

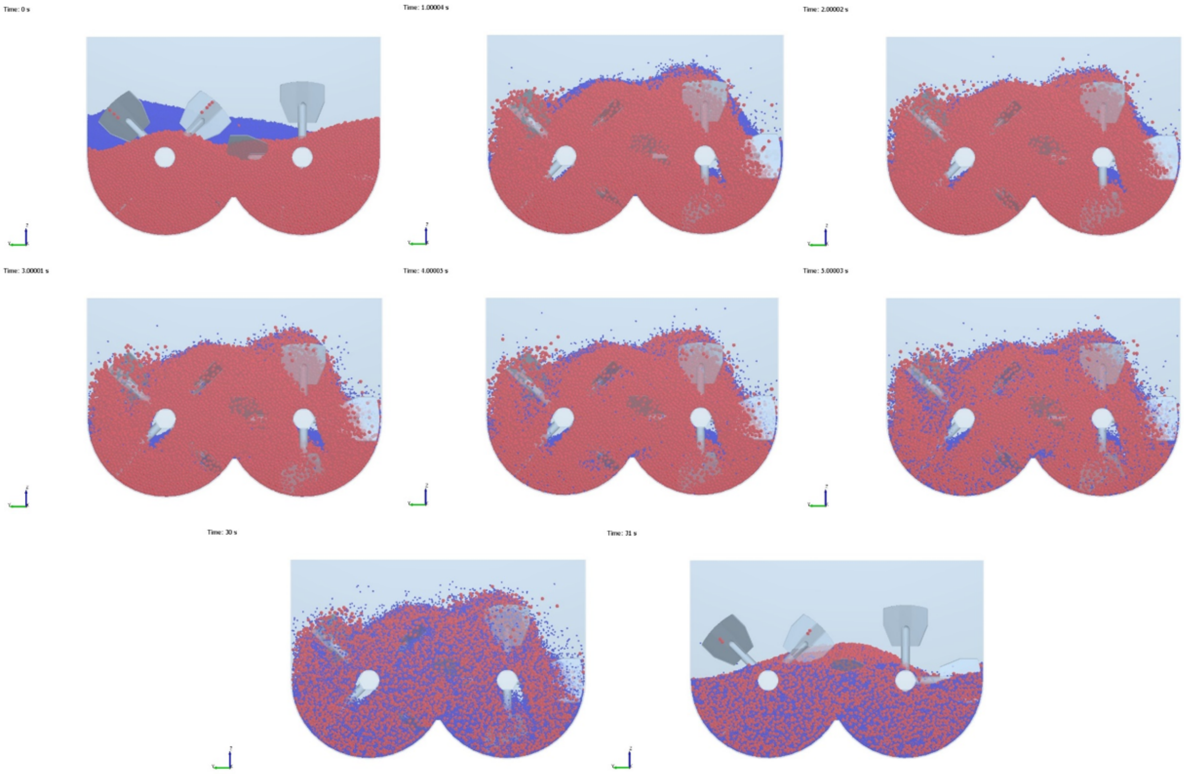

Figure D.103: Front view of simulation 19 - Paddle number (i=28) for time step t=0s, t=1s, t=2s, t=3s, t=4s, t=5s, t=30s and t=31s.

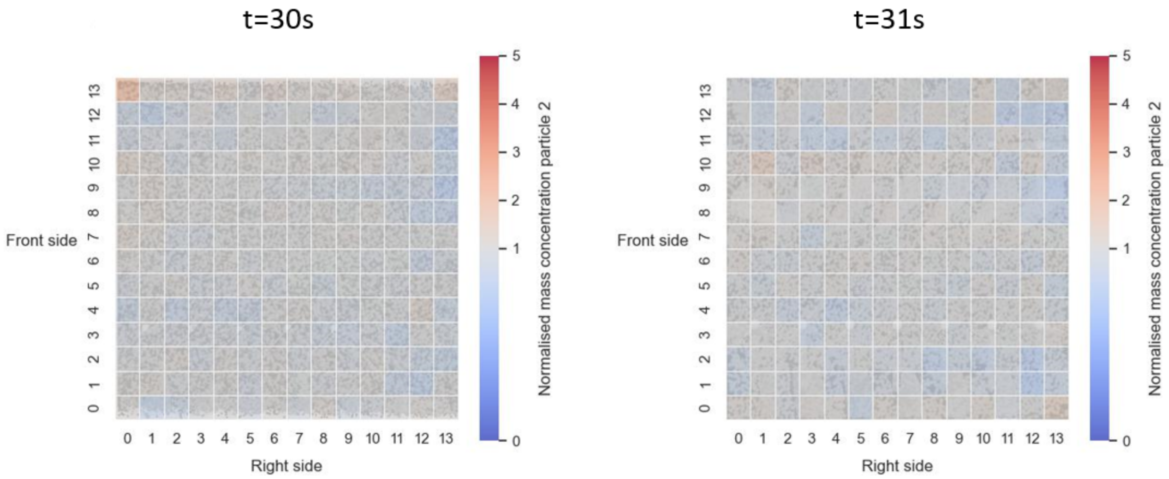

Figure D.104: Simulation 19 - Heat map of 14x14x1 grid with normalized concentrations of particle 2 at time=30s and t=31s.

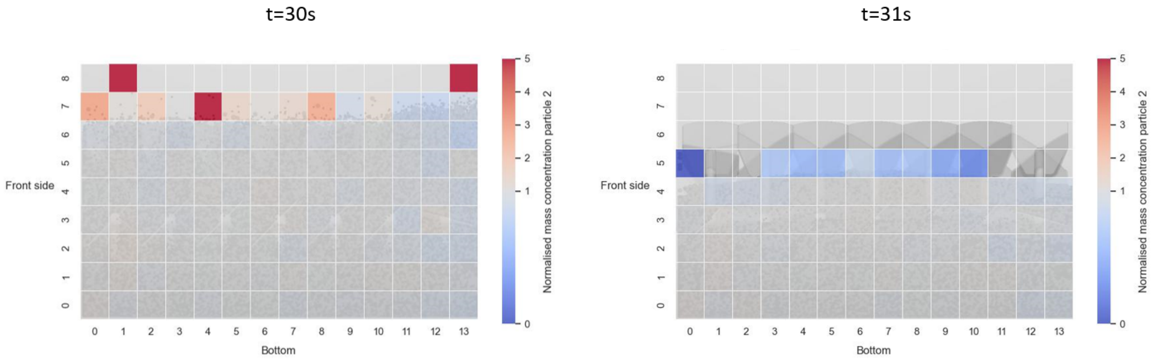

Figure D.105: Simulation 19 - Heat map of 14x1x9 grid with normalized concentrations of particle 2 at time=30s and t=31s.

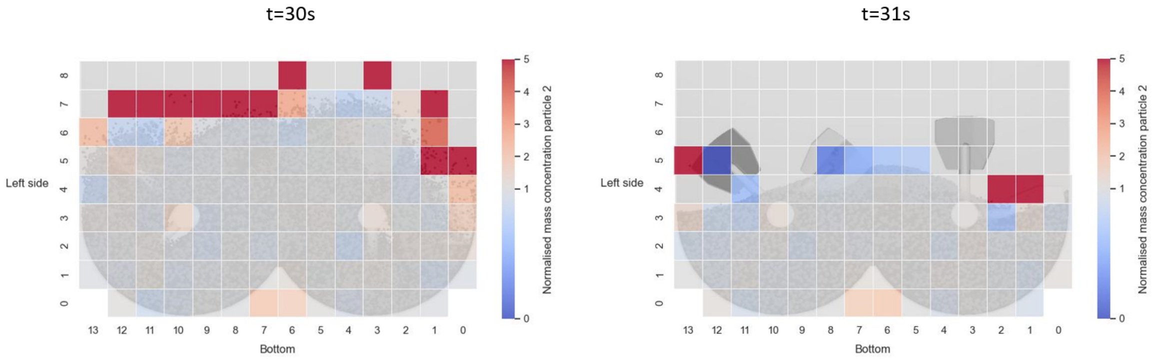

Figure D.106: Simulation 19 - Heat map of 1x14x9 grid with normalized concentrations of particle 2 at time=30s and t=31s.

E

Torque data

In this appendix, the torque data for every factor is presented.

Table E.1: Average, maximum and minimum torque for all simulations at time period 1-30s.

Run	Factor	Level	Torque avg	Torque max	Torque min
1	Ref.	-	0.000326	0.297	0
2	a	1	0.000190	0.040	0
3		3	0.000398	0.482	0
4	b	1	0.000395	0.162	0
5		20	0.000308	0.237	0
6	c	99/1	0.000434	0.281	0
7		50/50	0.000182	0.136	0
8	p	TB	0.000333	0.227	0
9		SS	0.000332	0.148	0
10	e	40%	0.000110	0.107	0
11		140%	0.000524	0.391	0
12	f	40 rpm	0.000327	0.213	0
13		80 rpm	0.000323	0.182	0
14	g	2/3	0.000220	0.096	-0.055
15		3/2	0.000079	0.160	-0.101
16	α_1	30°	0.000042	0.235	-0.082
17		60°	0.000345	0.422	0
18	i	7	0.000535	0.304	0
19		28	0.000253	0.115	0

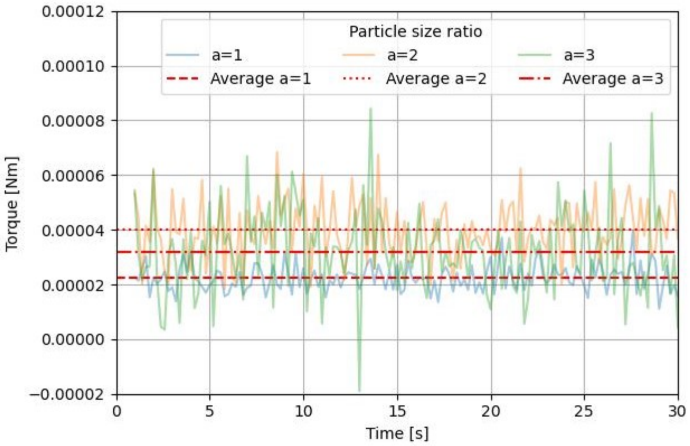

Figure E.1: Torque average over time for different particle size ratios.

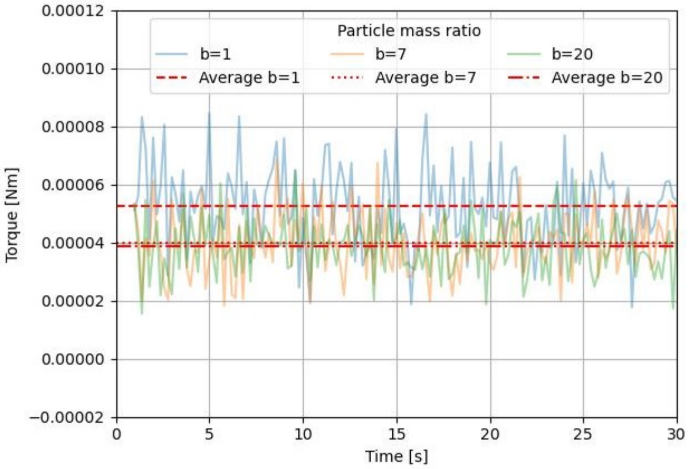

Figure E.2: Torque average over time for different particle density ratios.

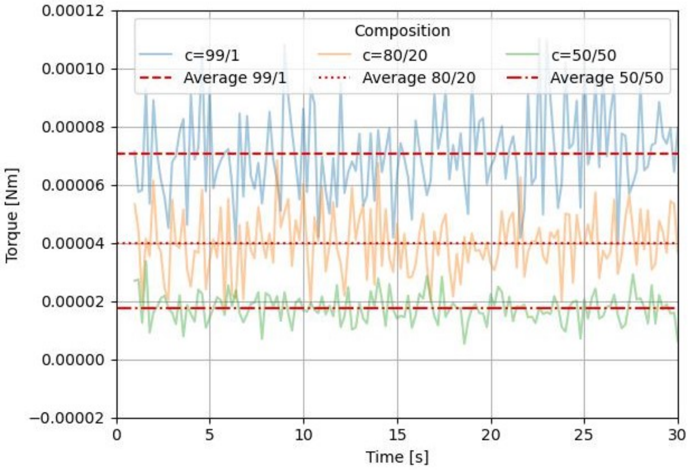

Figure E.3: Torque average over time for different compositions.

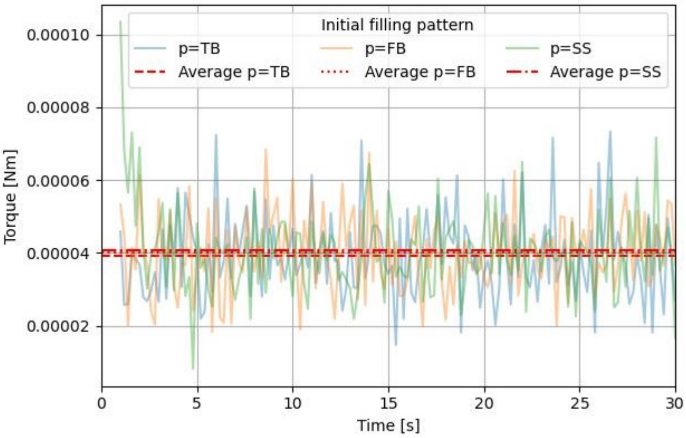

Figure E.4: Torque average over time for different initial filling patterns

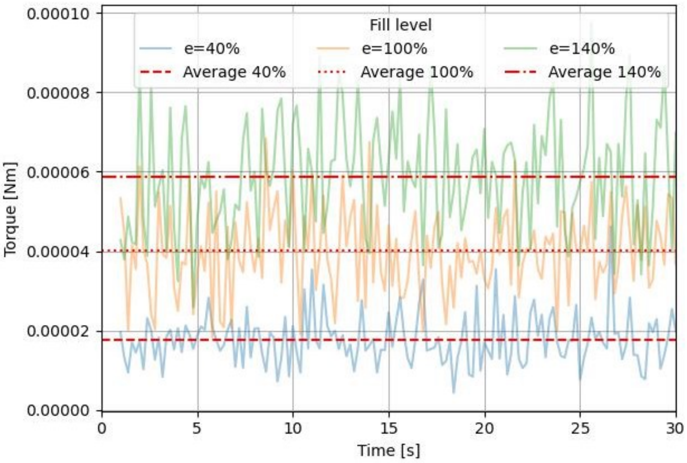

Figure E.5: Torque average over time for different fill levels.

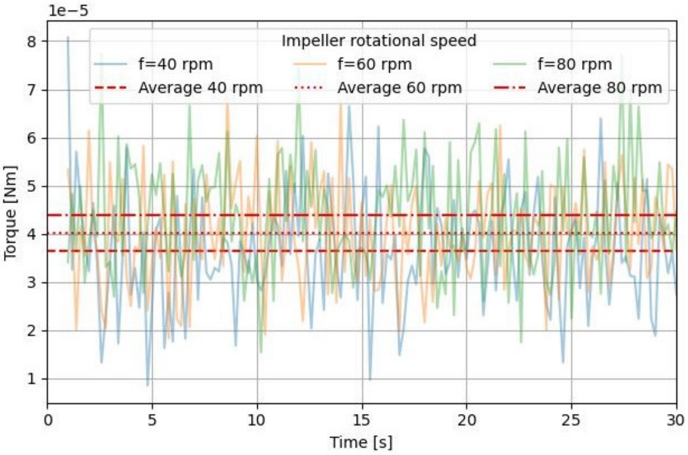

Figure E.6: Torque average over time for different impeller rotational speeds.

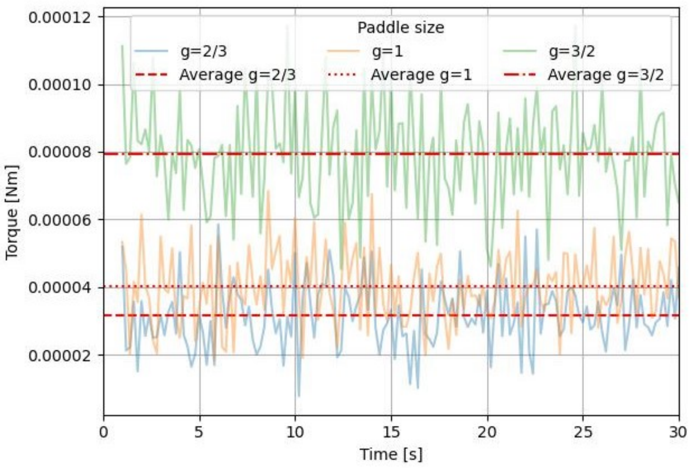

Figure E.7: Torque average over time for different paddle sizes.

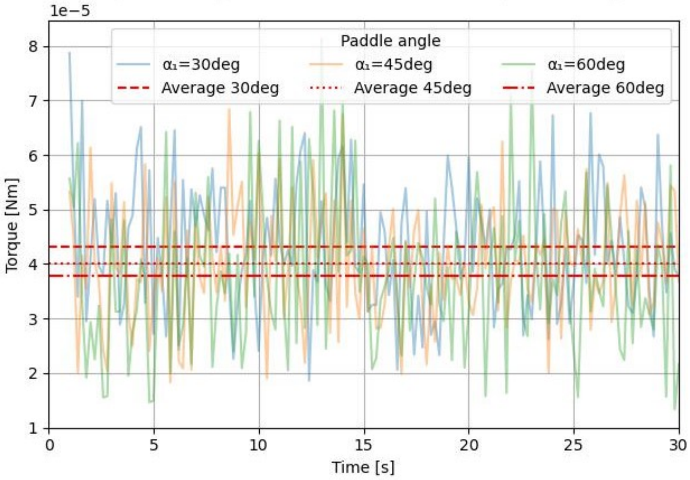

Figure E.8: Torque average over time for different paddle angles.

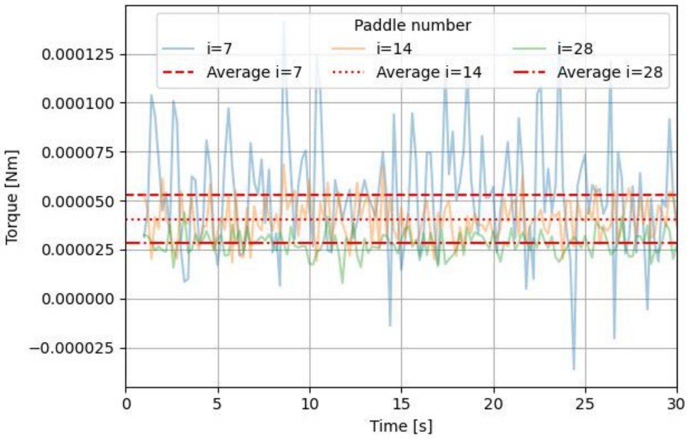

Figure E.9: Torque average over time for different paddle numbers.